UNIVERSITÉ DU QUÉBEC À MONTRÉAL

EXPLOITATION DU TRANSPORT DE MASSE PAR MICROSCOPIE À CELLULE ÉLECTROCHIMIQUE À BALAYAGE (SECCM) POUR DES MESURES CINÉTIQUES À L'ÉCHELLE NANOMÉTRIQUE

THÈSE

PRÉSENTÉE

COMME EXIGENCE PARTIELLE

DU DOCTORAT EN CHIMIE

PAR

SAMANEH SALEK ESFAHANI

DÉCEMBRE 2025

UNIVERSITÉ DU QUÉBEC À MONTRÉAL

LEVERAGING MASS TRANSPORT WITH SCANNING ELECTROCHEMICAL CELL MICROSCOPY (SECCM) FOR NANOSCALE KINETIC MEASUREMENTS

THESIS

PRESENTED

AS A PARTIAL REQUIREMENT

DOCTORATE IN CHEMISTRY

BY

SAMANEH SALEK ESFAHANI

DECEMBER 2025

ACKNOWLEDGMENT

First and foremost, I would like to express my gratitude to my supervisor, Joshua Byers, who believed in me from the very first day. His support, encouragement, and guidance shaped me into the enthusiastic scientist I am today. Thank you for your invaluable mentorship, your advice in every aspect of my journey, and for always pushing me to grow.

I am sincerely grateful to the members of my thesis committee Ana Tavares, Steen Schougaard, and Guillaume Goubert for accepting to evaluate my work and for dedicating their time and expertise.

My heartfelt thanks go to every member of Josh's group, who have supported me from the very beginning of my research journey as a master's student through to my PhD, especially Tao, Romaric, Alec, Ahmed, Marwa, and Romain. I may not name everyone, but I want to thank all those at UQAM who encouraged me, supported me, and helped me overcome challenges, making this journey more enjoyable. I am also especially thankful to my dear friend Maryam for her companionship.

More than anyone else, I owe my PhD to my family. To my husband Amir, and my beloved daughters Sophia and Lia, who have been my daily motivation. You are not only my reason to breathe but also the reason I strive to become a better version of myself. To my sister Sara, thank you for always being there for me in every possible way. To my father in heaven, and my mom, whom I miss every single day. Your love and memory have always carried me forward.

Along this journey, I had the great honor of receiving the Women in Science Award, which allowed me to meet and be inspired by many extraordinary women in science. I am also grateful to FRQNT (https://doi.org/10.69777/349841) for their financial support throughout my studies.

Finally, I thank God for granting me the strength, patience, and perseverance to complete this challenging chapter of my life, and for always lighting my path.

DEDICATION

To all the kind souls whose only mission is to spread love,
peace, and goodness in this world

TABLE OF CONTENT

LIST OF FIGURES

LIST OF TABLES

LIST OF ABBREVIATIONS, INITIALISMS, AND ACRONYMS

BSE	Backscattered electrons
CDV	Chemical vapor deposition
CO_2RR	CO_2 reduction reaction
DC	Direct current
EBSD	Electron backscatter diffraction
ECSA	Electrochemically active surface area
EDS/EDX	Energy dispersive X-ray
FEG	Field emission guns
FEM	Finite element method
FET	Floating electrode techniques
GDE	Gas diffusion electrode
HER	Hydrogen evolution reaction
HOR	Hydrogen oxidation reaction
MEA	Membrane electrode assembly
NP	Nanoparticle
OER	Oxygen evolution reaction
OHP	Outer Helmholtz plane
PXRD	Powder X-ray diffraction
QRCE	Quasi reference-counter electrode

RDE	Rotating disk electrode
RHE	Reversible hydrogen electrode
SE	Secondary electrons
SECCM	Scanning electrochemical cell microscopy
SEE	Single-entity electrochemistry
SEM	Scanning electron microscopy
STEM	Scanning transmission electron microscopy
TEM	Transmission electron microscopy
XRD	X-ray diffraction

LIST OF SYMBOLS AND UNITS

a	Activity
C	Concentration
D	Diffusioncoefficient
D	Distance
E	Potential
E^0	Standard potential
F	Faraday constant
I	Current
I_{hemi}	Hemisphere microelectrode current
I_{seccm}	SECCM current
j	Current density
j_0	Exchange current density
k^o	Standard rate constant
λ	Wavelength
M	Molar
m_o	Mass transfer coefficient
n	Number of electron
n	Order of reflection
nm	nanometer
ν	Scan rate

pA	Picoampere
R	Radius of droplet
R	Gas constant
r_p	Radius of micropipet
s	second
T	Temperature
V	volt
θ	Glancing angle
γ	Half angle of the micropipet
ρ	Radial coordinate
ΔG	Change in Gibbs free

RÉSUMÉ

L'électrocatalyse à l'échelle nanométrique est gouvernée non seulement par les propriétés intrinsèques des matériaux, mais également par la structure et la taille des particules électrocatalytiques. Dans ce travail, la microscopie à cellule électrochimique à balayage (SECCM), combinée à la microscopie électronique à balayage (MEB), est exploitée pour étudier quantitativement l'activité électrocatalytique à l'échelle de mono particules. À travers trois études complémentaires, nous démontrons comment la SECCM permet des mesures cinétiques détaillées en tenant compte des effets du transport de masse sur les réactions.

Dans la première étude, des particules d'argent de taille comprise entre 100 et 500 nm de rayon ont été électrodéposées sur un substrat et étudiées individuellement pour leur activité de la réaction de réduction l'oxygène (ORR). Les résultats révèlent une dépendance claire à la taille, les particules plus petites présentant des densités de courant plus élevées en raison d'un transport de masse amélioré. Cette observation souligne l'influence de la taille des particules sur le transport de masse et offre de nouvelles perspectives pour l'interprétation des performances électrocatalytiques dans les systèmes hétérogènes.

La deuxième étude porte sur des particules de platine, de 90 à 500 nm de rayon, afin d'examiner à la fois la réaction d'évolution de l'hydrogène (HER) et la réduction de l'oxygène (ORR) à l'aide de mesures SECCM. En tirant parti des variations du transport de masse dues à la taille des particules, les paramètres cinétiques tels que la constante de vitesse apparente (k^0_{app}) et la densité de courant d'échange apparente (j^0_{app}) ont été extraits pour chaque particule. Notamment, les plus petites particules de Pt ont montré des potentiels à mi-onde ($E_{1/2}$) plus négatifs pour l'ORR, indiquant des limitations cinétiques, tandis que pour la HER, elles ont présenté des j^0_{app}plus élevés et des surtensions plus faibles. Ces tendances illustrent comment un meilleur transport de masse pour les petites particules peut réduire les limitations de diffusion, permettant ainsi une évaluation plus précise de la cinétique intrinsèque.

La troisième étude étend l'utilisation de la SECCM à la voltampérométrie en régime stationnaire dans le liquide ionique [EMIM][BF_4], où des voltammogrammes à balayage linéaire (LSV) ont été enregistrés à l'aide de pipets de diamètre de pointe variable afin de contrôler le transport de masse. Cette approche a permis d'extraire de manière fiable le coefficient de diffusion et la constante hétérogène de vitesse (k^o) à l'aide de l'analyse de Koutecký–Levich et de modélisations numériques, donnant des valeurs cohérentes avec celles de la littérature. De plus, l'ajustement analytique des LSV à très faible courant a permis de cartographier k^o à l'échelle submicronique.

Ensemble, ces études démontrent les capacités puissantes de la SECCM pour l'analyse électrochimique à l'échelle nanométrique, permettant des mesures cinétiques localisées prenant en compte les variations de transport de masse. Ce travail met en lumière l'utilisation de la SECCM comme un outil quantitatif en électrochimie des entités uniques, ouvrant de nouvelles voies pour les études catalytiques et la cartographie électrochimique de surface.

Mots clés : Microscopie à cellule électrochimique à balayage (SECCM), électrocatalyse, électrochimie des particules individuelles, réaction d'évolution de l'hydrogène (HER), réduction de l'oxygène (ORR), transport de masse, constante de vitesse hétérogène, analyse cinétique.

ABSTRACT

Electrocatalysis at the nanoscale is controlled not only by intrinsic properties of materials but also by structure and size of the electrocatalytic particles. In this work, Scanning Electrochemical Cell Microscopy (SECCM), combined with Scanning Electron Microscopy (SEM) is leveraged to quantitatively investigate electrocatalytic activity at the level of individual particles. Through three complementary studies, we demonstrate how SECCM enables detailed kinetic measurements by mass transport effect on the overall reactions.

In the first study, silver particles ranging in size from 100 to 500 nm in radius were electrodeposited onto a substrate and studied individually for their oxygen reduction reaction (ORR) activity. The results reveal a clear size dependence, with smaller particles demonstrating higher current densities due to enhanced mass transport. This finding highlights the influence of particle size on mass transport and offers new perspectives for interpreting electrocatalytic performance in heterogeneous systems.

The second study focuses on platinum particles, with radii between 90 and 500 nm, to examine both the hydrogen evolution reaction (HER) and ORR using SECCM measurements. Leveraging the variations in mass transport arising from particle size differences, kinetic parameters such as the apparent standard rate constant (k^0_{app}) and apparent exchange current density (j^0_{app}) were extracted for individual particles. Notably, smaller Pt particles showed more negative ORR half-wave potentials ($E_{1/2}$), indicating kinetic limitations, while for HER, they exhibited higher j^0_{app} and lower overpotentials. These trends highlight how enhanced mass transport at smaller particles can reduce diffusion limitations, allowing for more accurate assessment of intrinsic kinetics.

The third study extends SECCM to steady-state voltammetry in the ionic liquid [EMIM][BF_4], where linear sweep voltammograms (LSVs) were recorded using pipets of varying tip diameter to control mass transport. This approach enabled the reliable extraction of the diffusion coefficient and heterogeneous rate constant (k^o) using both Koutecký–Levich analysis and numerical modeling, resulting in values consistent with the literature. Moreover, analytical fitting of ultralow current LSVs allowed mapping of k^o at the submicron scale.

Together, these studies demonstrate the powerful capabilities of SECCM for nanoscale electrochemical analysis, enabling spatially resolved kinetic measurements that account for mass transport variations. This work highlights the application of SECCM as a quantitative tool in single-entity electrochemistry, opening new way in catalytic studies and electrochemical surface mapping.

Keywords : Scanning Electrochemical Cell Microscopy (SECCM), electrocatalysis, single particle electrochemistry, hydrogen evolution reaction (HER), oxygen reduction reaction (ORR), mass transport, heterogenous rate constant, kinetic analysis.

CHAPTER 1 INTRODUCTION

1.1 Background

1.1.1 Electrocatalysis

The water cycle is a fundamental concept in energy systems. It relies on the conversion of hydrogen (H_2) and oxygen (O_2) through electrochemical reactions. In fuel cells, hydrogen and oxygen combine to produce water (H_2O) and electricity, while in reverse, water electrolysis uses electricity to split water into hydrogen and oxygen. This cycle is crucial to the development of hydrogen-based energy technologies. Water electrolysis requires an electrical energy input to drive the following reaction:

$$2H_2O \rightarrow 2H_2 + O_2 \quad (1.1)$$

which is governed by the standard free-energy relationship $\Delta G^0 = -nFE^0$, where E^0 is equal to 1.23 V vs RHE (Lee, J. *et al.*, 2013; Stamenkovic *et al.*, 2017).

The success of the hydrogen economy depends on efficient hydrogen production and its application in energy systems. Water electrolysis offers a sustainable and clean method of producing hydrogen and oxygen. The hydrogen and oxygen produced can subsequently be used in fuel cells to produce electricity. Reactions involving in water cycles are Hydrogen Evolution Reaction (HER) and Oxygen Evolution Reaction (OER) in water electrolysis, Hydrogen Oxidation Reaction (HOR), and Oxygen Reduction Reaction (ORR) in fuel cells which is a more complex reaction. The efficiency of these reactions is often evaluated through current density at fixed potentials that can be evaluated through techniques like cyclic voltammetry. Understanding these processes at a fundamental level is crucial for optimizing hydrogen and oxygen electrochemistry and advancing energy storage and conversion technologies (Stamenkovic *et al.*, 2017).

The efficiency of water electrolysis and fuel cells remains below their thermodynamic limits. The primary limitation in both systems is the high overpotential required for the water cycle reactions, which originates from catalytic inefficiencies. Advancing electrocatalysis research is essential to

improve reaction kinetics, extend electrode material lifespans, and develop cost-effective alternatives to noble metal catalysts.

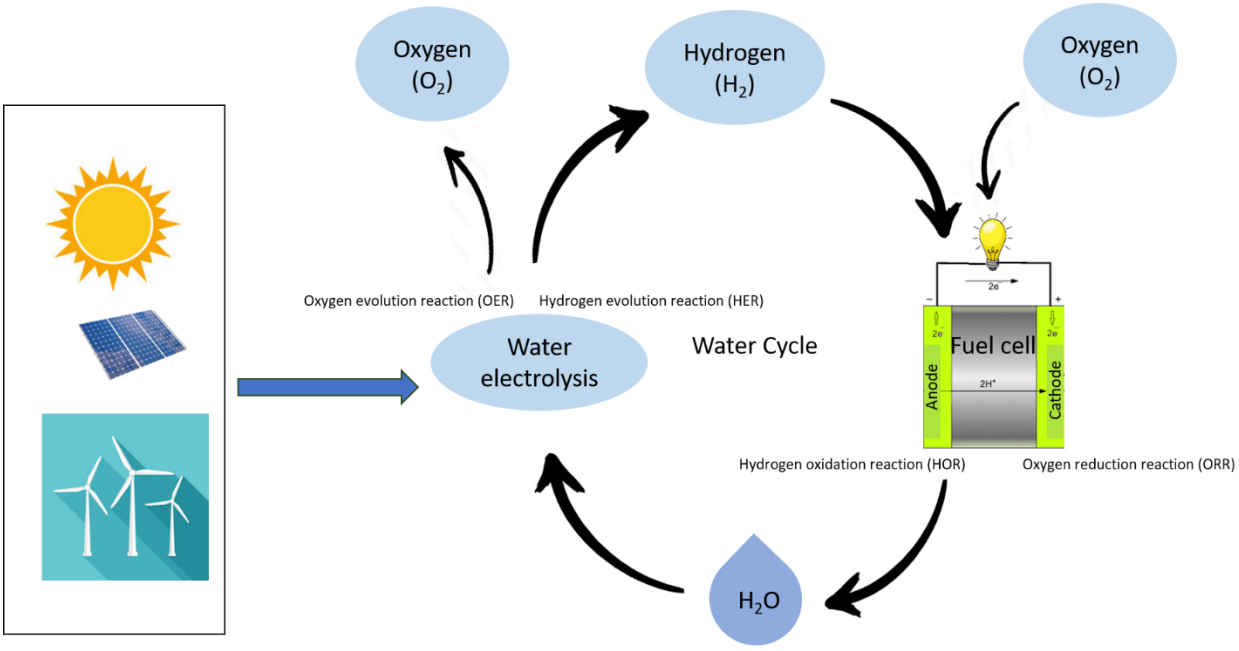

Figure 1.1 Schematic of water cycle where water uses as both reactant and product for a sustainable source of energy. Converting wind and solar energy into hydrogen enables long-term energy storage. Unlike other storage methods, hydrogen retains its energy indefinitely, making it a reliable solution for balancing supply and demand in renewable energy systems.

1.1.2 Oxygen Reduction Reaction

The Oxygen Reduction Reaction (ORR) is the cathodic process that occurs in low-temperature fuel cells and metal air batteries. These fuel cells convert the chemical energy of hydrogen fuel into electrical energy through an electrochemical reaction, making them a major technology for hydrogen-powered transportation and alternative energy systems. Despite their promise, the ORR is hindered by slow reaction kinetics leading to significant overpotentials that reduce efficiency. To overcome this challenge and make low temperature fuel cells more applicable, extensive research has focused on developing ORR electrocatalysts that are active and durable (Trindell et al., 2020).

The ORR can follow two distinct pathways including a two-electron or a four-electron process. In the two-electron pathway (equation 1.2), molecular oxygen (O_2) undergoes partial reduction, producing hydrogen peroxide (H_2O_2). However, in energy conversion technologies, the four-electron pathway (equation 1.3), which directly reduces oxygen to water (H_2O) is preferred due to its higher energy efficiency (Lee, J. *et al.*, 2013; Trindell *et al.*, 2020).

$$O_2 + 2H^+ + 2e^- \rightarrow H_2O_2 \qquad E^0 = 0.7 \text{ V vs RHE} \tag{1.2}$$

$$O_2 + 4H^+ + 4e^- \rightarrow 2H_2O \qquad E^0 = 1.23 \text{ V vs RHE} \tag{1.3}$$

1.1.3 Hydrogen Evolution Reaction

The hydrogen evolution reaction (HER) is a classic two-electron transfer process. LO

$$2H^+ + 2e^- \rightarrow H_2 \qquad E^0 = 0 \text{ V vs RHE} \tag{1.4}$$

The overall reaction rate is largely governed by the free energy of hydrogen adsorption. Platinum is considered the benchmark catalyst for HER, as it sits near the top of the hydrogen activity volcano plot with an almost thermoneutral ΔG_{H+}. This optimal binding energy allows platinum to achieve high reaction rates with negligible overpotentials in acidic environments, making it the one most effective catalyst for HER (Benck et al., 2014).

1.2 Scanning Electrochemical Cell Microscopy (SECCM)

Scanning Electrochemical Cell Microscopy (SECCM) is a high-resolution technique to map electrochemical activity at interface on the nanoscale with high resolution. This method involves creating a localized electrochemical cell at the end of a micro/(nano)pipet filled with an electrolyte solution. The electrolyte at the pipet tip creates a droplet that contacts the substrate surface, defining the confined area where measurements are performed. The working electrode is the area of the substrate in contact with the electrolyte, while there is a quasi-reference counter electrodes (QRCEs) in the pipet (Figure 1.2) (Anderson et Edwards, 2023).

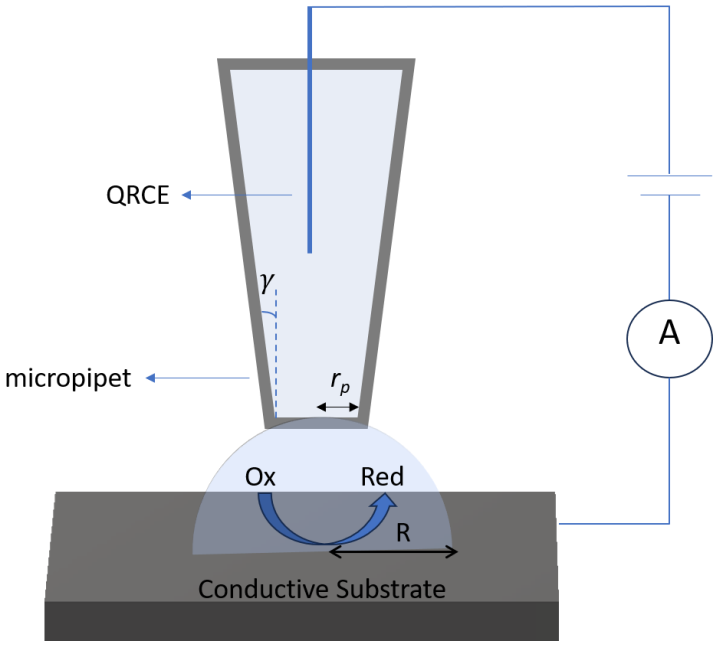

Figure 1.2 Scanning Electrochemical Cell Microscopy (SECCM) configuration. A micro/(nano)pipet filled with the electrolyte containing a quasi reference-counter electrode (QRCE). r_p is the radius of the pipet while R is the radius of the droplet on the surface of the substrate which is the working electrode. γ is the half angle of the micropipet.

1.2.1 Operational Principles of SECCM

Electrochemical measurements, such as voltammetry, are performed by applying a potential versus QRCE and monitoring the current at the substrate surface. The system is equipped with piezoelectric positioners that allow precise movement of the pipet or substrate in three dimensions (xyz). This setup enables spatially resolved electrochemical measurements across the substrate, creating detailed electrochemical maps (Ebejer, N. *et al.*, 2013). When using SECCM, droplet-surface contact is detected by the current which flows when the electrochemical circuit is completed and forming a two-electrode electrochemical cell between the QRCE and the working electrode which is the wetting surface area of the substrate in contact with droplet. In hopping mode, electrochemical measurements are conducted by systematically mapping the activity across the surface. In this approach, the pipet first makes contact with the substrate (Figure 1.3A), allowing the voltammetric measurement to be performed (Figure 1.3B). Once the measurement is completed,

the pipet is gradually retracted from the surface, causing the electrolyte droplet to detach. As the distance between the pipet tip and the substrate increases, the measured current progressively decreases. Retraction continues until no current is detected (Figure 1.3C). This method enables spatially resolved electrochemical analysis while minimizing surface interference (Bentley, Cameron L., 2022; Ebejer, Neil *et al.*, 2010). By sequentially positioning the pipet at various points on the substrate, SECCM can perform electrochemical characterizations at each location, generating nanoscale maps of activity. This approach allows for the direct correlation of topographical features, such as individual grains and grain boundaries, with their electrochemical behavior. Moreover, these measurements can be integrated with ex-situ measurements of spectroscopy or microscopy techniques, enabling simultaneous structural and functional analysis of the substrate (Snowden, Michael E. *et al.*, 2012).

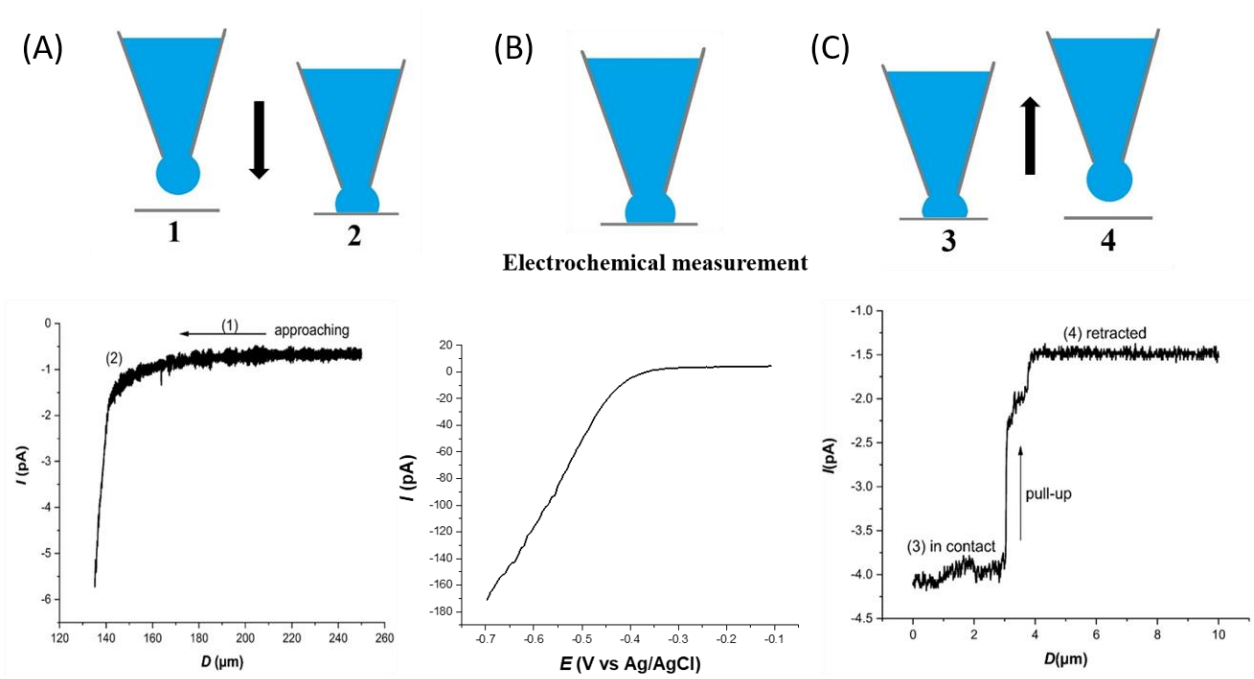

Figure 1.3 Schematic of SECCM pipet and the corresponding graphs in hopping mode (A) Current-distance graph while approaching (B) Voltammogram in contact moment (C) Current-distance graph during the retraction till no current is detected.

1.2.2 Applications of SECCM

SECCM's ability to perform localized measurements within a microscale electrochemical cell makes it an invaluable tool for investigating surface features and resolving their activity with nanoscale precision. Through its combination of spatial resolution, automated mapping, and compatibility with other characterization methods, SECCM provides unique insights into the relationships between structure and electrochemical performance and applied to many studies such as electrocatalysis (Bentley, Cameron L., 2022), electrochemical heterogeneity studies to map the facet affect reactivity (Gaudin, Lachlan F. *et al.*, 2024), energy conversion materials (Strange et al., 2023) , and also single entity measurements (Choi *et al.*, 2020; Clarke *et al.*, 2024; Lu, Xiaoxi *et al.*, 2021).

1.2.3 SECCM for Electrocatalysis

Traditional techniques like the rotating disk electrode (RDE) are widely used to evaluate electrocatalysts for fuel cells and water electrolyzers, mostly in the early stages of catalyst development when only small quantities of materials are available (Lazaridis *et al.*, 2022; Trogisch *et al.*, 2024; Xing *et al.*, 2014). However, RDE measurements often fail to reproduce the real operating conditions of membrane electrode assemblies (MEAs) used in practical devices. This difference arises due to fundamental differences in mass transport, catalyst layer structure, and environmental factors between the two systems (Lazaridis *et al.*, 2022).

In an RDE setup, the catalyst layer is thin (0.1–2 μm) and fully immersed in liquid electrolyte, where diffusion across a micrometer scale liquid boundary layer controls mass transport. This configuration leads to significant limitations in oxygen or hydrogen availability for reactions like the oxygen reduction reaction (ORR) or the hydrogen evolution reaction (HER). Conversely, MEAs feature thicker (5–20 μm) porous catalyst layers, where gas-phase diffusion plays a dominant role. These differences result in lower specific and geometric current densities in RDE experiments and can lead to under or overestimation of catalyst performance (Lazaridis *et al.*, 2022). The limitations of RDE, particularly its inability to provide realistic mass transport conditions and the challenges associated with gas bubble removal during gas-evolving reactions, highlight the need for alternative methodologies. Techniques like gas diffusion electrodes (GDEs) and floating electrode techniques (FETs) are emerging as promising intermediate approaches, offering better

alignment with MEA conditions. Another useful method is Scanning Electrochemical Cell Microscopy (SECCM) which offers a significant advantage in electrocatalysis. SECCM provides localized electrochemical measurements, enabling the study of individual catalyst particles or well-defined regions of a surface under highly controlled conditions (Mariano *et al.*, 2021b; Mariano, Ruperto G. *et al.*, 2022; Zhang, L. *et al.*, 2024). Unlike RDE, SECCM is not limited by the bulk liquid diffusion, as it operates at the nanoscale with a confined droplet. This allows for the investigation of intrinsic catalyst properties, such as activity, selectivity, and stability in environments that can more closely imitate those in MEAs. Moreover, SECCM is able to map electrochemical activity across surfaces with nanoscale resolution, so it provides unique insights into catalyst heterogeneity (Chen, C.-H. *et al.*, 2014; Choi *et al.*, 2020; Kang *et al.*, 2023; Mariano *et al.*, 2017b; Mariano, Ruperto G. *et al.*, 2022; Quast, Thomas *et al.*, 2021). This is mostly important for understanding how variations in particle size, shape, or support interactions influence performance. By correlating these measurements with complementary (in-situ/ex-situ) techniques like scanning electron microscopy (SEM), SECCM enables the direct correlation of structural and electrochemical properties, overcoming many of the challenges faced in traditional ensemble techniques like RDE. Furthermore, the particular approach of SECCM allows for fast mass transport within the nanopipet, making it ideal for studying rapid electrode kinetics (Anderson, K. L. et Edwards, 2023; Chen, C.-H. *et al.*, 2014). One of a key advantage of SECCM is its ability to create a three-phase boundary where the gas–liquid interface is positioned near the electrode. This configuration enhances the coupling between gas transfer and electron transfer reactions. Thus, this characteristic makes SECCM mainly effective for studying gas-involved electrochemical processes, such as the hydrogen evolution reaction (HER), hydrogen oxidation reaction (HOR), oxygen reduction reaction (ORR), oxygen evolution reaction (OER), and CO_2 reduction reaction (Chen, C.-H. *et al.*, 2014; Limb *et al.*, 2024; Ryu *et al.*, 2024).

For instance, Chen *et al* employed SECCM in combination with electron backscatter diffraction (EBSD) to map the kinetics of ORR on polycrystalline platinum electrodes. Their findings demonstrated that (111) and (100) grains exhibited higher ORR activity than (110) oriented grains, and contrary to expectations, grain boundaries did not enhance ORR activity, suggesting that crystallographic orientation is the dominant factor (Chen, C.-H. *et al.*, 2014). Going further in electrocatalytic activity and selectivity, Ryu and Ren introduced a hybrid SECCM-SECM approach,

enabling simultaneous mapping of electrocatalytic activity and product selectivity (Ryu, C. Hyun et Ren, Hang, 2024). Their method employed a dual-channel nanopipet to measure local electrochemical activity while detecting reaction products with high precision (more than 95% collection efficiency). Using polycrystalline platinum and gold electrodes, they revealed that specific crystal facets, despite exhibiting high activity, favored incomplete reduction products (H_2O_2 instead of H_2O). This study emphasizes the importance of localized selectivity mapping, and sets a benchmark for quantitative SECCM applications, demonstrating how activity-selectivity relationships, which are often masked in ensemble measurements, can be explained at the nanoscale.

Lu, Xiaoxi with there coworkers extended SECCM applications to the oxygen evolution reaction (OER), using single-particle analysis to investigate $NiFe_2O_4$-based catalysts. Their study revealed that OER activity increased as particle size decreased due to increase in active site exposure. By establishing size and composition activity correlations, this work highlights the usefulness of SECCM in optimizing multicomponent electrocatalysts (Lu, Xiaoxi *et al.*, 2021). Furthermore, SECCM has already been applied to probe the electrocatalytic activity of HER. These studies include spatially resolve HER kinetics at different Pt grain orientations (Wang, Y. *et al.*, 2022). The findings revealed that HER activity varies significantly across Pt grains, correlating with crystallographic orientation and local surface characteristics. High-index facets demonstrated enhanced activity, consistent with single-crystal studies. Tetteh *et al* reassessed the intrinsic HER activity of platinum using SECCM, revealing that conventional techniques underestimate the catalytic efficiency of platinum due to mass transport limitations (Tetteh, Emmanuel Batsa *et al.*, 2023). Their study demonstrated that SECCM enhanced mass transport rates while minimizing concentration gradients and gas accumulation effects. The exchange current density of Pt was 200 times higher than RDE values. Moreover, they demonstrated that pipet size significantly influenced kinetic measurements, with smaller pipet achieving higher limiting currents density and more accurate Tafel analysis. This work supports the potential of SECCM as a powerful tool for kinetic investigations which can overcome transport limitations in electrocatalysis.

While gas evolution reactions introduce mass transport complexities, Zhao *et al* investigated another structural factor of strain effects on single-nanoparticle electrocatalysis (Zhao, Jiao *et al.*, 2023). Using Pd nanocrystals with well-defined structures, they compared the HER activity of Pd

icosahedra and Pd octahedra with Pd icosahedra exhibited higher HER activity, attributed to their inhomogeneous strain distribution. Pd octahedra, despite having the same surface facets, showed lower activity that can be explained by the strain effect. In summery, by integrating SECCM with SEM, EBSD, transmission electron microscopy (TEM), and finite element method (FEM) modeling, researchers have achieved remarkable insights into electrocatalytic behaviours. SECCM continues to expand its applications in electrochemical activity screening, and electrocatalysis which leads to advancements in energy conversion and electrochemical research.

1.2.4 Single Entity Electrocatalysis

Nanoparticles (NPs) have drawn significant attention in catalysis, sensing, and energy conversion due to their specific chemical and physical properties (Seh *et al.*, 2017; Stamenkovic *et al.*, 2017). Since NPs are widely used in various (electro)catalytic applications to enhance the efficiency (Song et Zhou, 2022), recent researches have shifted toward studying the electrocatalytic behavior of individual nanoparticles to surpass the traditional ensemble or bulk material approaches. The main focus of research in this area has been exploring the relationship between the size and the structure of nanoparticles and their catalytic activity. However, most studies rely on ensembles of nanoparticles, which inherently involve variations in size and shape. These variations limit the precision of the information obtained, making it challenging to fully understand the catalytic behavior of individual nanoparticles (Lai *et al.*, 2011). Ensemble measurements often assume uniform distribution and full electrical contact of nanoparticles with the electrode surface, which is rarely the case. This oversimplification can lead to misinterpretations since not all nanoparticles within an ensemble are equally active or electrically connected (Zhang, L. *et al.*, 2024). As a result, the influence of nanoparticle size and morphology on electrocatalytic activity remains insufficiently understood. Moreover, the electrode exhibits heterogeneity across its surface, but traditional measurement methods tend to average the activity over the entire interface. This averaging process masks the specific activity occurring at individual sites. (Rahman *et al.*, 2022; Saha *et al.*, 2018). In certain cases, a few highly active sites can dominate the overall activity, yet these localized effects are often undetectable in ensemble measurements. Consequently, conventional electrochemical techniques face significant challenges in accurately identifying the true relationship between surface structure and catalytic activity (Ryu, C. Hyun et Ren, Hang, 2024).

Single-entity electrochemistry (SEE) offers a transformative approach to address these challenges by isolating and investigating the catalytic properties of individual nanoparticles. By avoiding averaged measurements of bulk, SEE provides a clearer understanding of unique contributions to the overall electrocatalytic performance. This approach not only enhances the fundamental knowledge of nanoparticles behavior but also helps for designing more effective and efficient electrocatalysts. The main reason for studying single-entity responses is to understand how they contribute to the overall bulk or ensemble response observed in experiments. In the case of a catalyst, understanding how a single particle interacts and reacts at an individual catalytic site could help optimize the chemical adjustment of the catalyst (Baker, 2018; O'Mullane, 2014).

While theoretical models provide valuable predictions, they often struggle to incorporate the inherent heterogeneity and imperfections of actual nanoparticles. Recent advances in synthesizing well-defined, ligand-free nanoparticles have improved the ability to compare theory with experiment, yet challenges remain in characterizing very small particles and correlating their structure with electrocatalytic behavior. SEE can deal these challenges by providing detailed insights and consequently help design of improved catalysts (Trindell *et al.*, 2020; Wahab *et al.*, 2020). This bottom-up perspective enables researchers to analyse complex systems and understand the interactions between individual entities, so it is useful for more precise control and optimization of electrocatalytic processes (Ma et Li, 2025).

Experimentally, SEE is challenging due to the need for nanoscale probes and electrodes, the detection of weak signals with high time resolution, and the requirement for repetitive measurements across multiple entities to build reproduceable data. However, advancements in complementary microscopy and spectroscopy techniques, such as scanning electron microscopy (SEM) and transmission electron microscopy (TEM), have greatly enhanced the capabilities of SEE (Clarke *et al.*, 2024).

1.2.5 SECCM for Single Entity Electrocatalysis

One of the revolutionary methods that can be used for single entity electrochemistry is scanning electrochemical cell microscopy (SECCM). When nanoparticles are supported on an electrochemically inert substrate to create a *particle-on-support* electrode, they serve as an

excellent example of nanostructured electrodes. SECCM is a powerful technique, offering localized electrochemical measurements with nanoscale resolution. Incorporating SECCM into studies of single particles overcomes challenges posed by their small size and complex nature. The technique simplifies single-particle measurements by bringing the droplet at the end of the pipet into contact with specific particles on support, enabling a more precise analysis of structure–activity relationships. This capability is especially important in electrocatalysis, where even minor differences in atomic arrangements or surface can significantly impact nanoparticle reactivity. By leveraging SECCM, researchers can achieve a comprehensive understanding of electrochemical fluxes and interfacial reactivity on a scale proper with the structural heterogeneities of nanostructured materials (Clarke *et al.*, 2024). In SECCM, a droplet at the end of the pipet tip is brought into contact with the surface of the substrate and creating a nano or micro scale electrochemical cell. This method ensures precise and well-defined contact areas, referred to as droplet footprints. The droplet footprint can be seen ex-situ using techniques such as optical microscopy, atomic force microscopy (AFM) (Bentley, Cameron L *et al.*, 2017), scanning electron microscopy (SEM) (Chen, C.-H. *et al.*, 2015a), transmission electron microscopy (TEM) or the techniques like Raman spectroscopy, and electron backscatter diffraction (EBSD) (Chen, C.-H. *et al.*, 2014). Thus, this approach enables accurate normalization of electrochemical data. By integrating multiple analytical techniques, it provides a comprehensive understanding of the relationship between material properties and their electrochemical function. This versatility makes it highly valuable for studies in electrocatalysis, energy storage, sensors, and beyond. For instance, Scanning Electrochemical Cell Microscopy (SECCM) has been utilized to investigate the electrochemical behavior of individual nanoparticles, revealing how variations in morphology, crystallinity, size, and nanoparticle-support interactions influence both activity and stability (Bentley, Cameron L., 2022; Choi *et al.*, 2020; Ma et Li, 2025). The combination of SECCM and SEM offers significant benefits for studying single-particle electrocatalysis. SECCM enables localized, high-resolution electrochemical measurements by confined droplet, ideal for analyzing individual nanoparticles. SEM complements this by providing detailed imaging of particles morphology, including size, shape, surface defects, and their distribution. These techniques together, allow to establish direct correlations between the structure of particle and its electrochemical activity (Jeong, Soojin *et al.*, 2022; Kang *et al.*, 2023). The ability of SECCM to resolve single-particle behavior, avoids the averaging effects in bulk measurements, while SEM

ensures precise visualization and targeting of specific particles (Choi *et al.*, 2020). The combined use of SECCM and SEM is applicable to a broad range of materials and provides complementary data for modeling and simulation, enabling a comprehensive understanding of mass transport and reaction kinetics. Overall, the combination of SECCM and SEM represents a strong and useful method for advancing electrocatalysis research. It provides a detailed understanding of the relationships between structure and electrocatalytic behavior, supporting the design of efficient and stable electrocatalysts for applications in energy conversion and storage (Baker, 2018).

Furthermore, SECCM combines principles of classical electrochemistry while it is able to do hundreds or thousands of spatially resolved measurements across a surface. This technique provides flexibility in the choice of working electrodes, including materials that cannot be fabricated into conventional electrode formats, such as layered materials or on transmission electron microscopy TEM supports (Bentley, Cameron L., 2022; Choi *et al.*, 2020). SECCM allows precise control over the position of its pipet probe, enabling many measurements at targeted surface area (Kang *et al.*, 2016). The small dimensions of the pipet tip ensure minimal exposure of the underlying substrate that allows clear distinction of individual nanoparticle reactions (Bentley, Cameron L., 2022).

1.3 Quantitative Measurements using SECCM

The conical geometry of the pipets used in SECCM significantly influences mass transport within the system, primarily controled by quasi-radial diffusion. This configuration facilitates near steady-state conditions, particularly when employing small pipets with a tip radius r_p of less than 500 nm and using moderate voltammetric scan rates ($\nu \leq 1$ V/s) (Bentley, Cameron L., 2022). For precise current values, finite element method (FEM) simulations with known pipet geometries are recommended. To approximate SECCM behavior, the system can be compared to mass transport at a hemispherical electrode and through a conical pipet while the SECCM geometry represents only a fraction of the hemispherical surface which is defined by the half angle of the pipet (γ). Although the SECCM substrate surface is typically planar and involves a droplet, deviations from the idealized hemispherical model contribute minimally to total mass-transport resistance. Thus, the concentration and current density in SECCM align closely with those of a hemispherical

electrode with an equivalent radius, adjusted by the area ratio that can be calculate by the limiting factor of mass transport which is the half angle of the pipet (Anderson, K. L. et Edwards, 2023).

$$I_{lim}^{SECCM} = i_{lim}^{hemi}(1 - \cos(\gamma)) \quad (1.5)$$

$$I_{lim}^{hemi} = 2\,\pi R_{hemi} nFDC \quad (1.6)$$

In SECCM, the mass transport-limited current (i_{lim}^{SECCM}) corresponds to the electrochemical response controlled by diffusion within the electrolyte droplet. This can be compared to the mass transport-limited current of a hemispherical microelectrode (I_{lim}^{hemi}) where R_{hemi} represents the radius of the hemispherical electrode. The parameters include *n* (number of electrons transferred), *F* (Faraday's constant), *D* and *C* are the diffusion coefficient and concentration of the redox species, respectively.

The transport of electroactive species to the electrode, as illustrated in Figure 1.4A, occurs in a spherically symmetric manner when described in polar coordinates centered at the hemisphere. This means that the radial coordinate (ρ) is the only direction in which concentration gradients exist. Similarly, the conical SECCM pipet positioned above a hemispherical electrode, as shown in Figure 1.4B, also shows radial mass transport, but only to a fraction of the hemispherical surface that can be determined by the half-angle of the pipet (γ), typically ranging between 5° and 15° (Anderson, K. L. et Edwards, 2023; Bentley, Cameron L., 2022). The current density and concentration profile for SECCM is expected to align with those of a hemispherical electrode with an equivalent radius (R_{eq}), with the total current differing by a factor proportional to the surface area ratio, given by (1−cos(γ)) (Anderson, K. L. et Edwards, 2023; Edwards *et al.*, 2009).

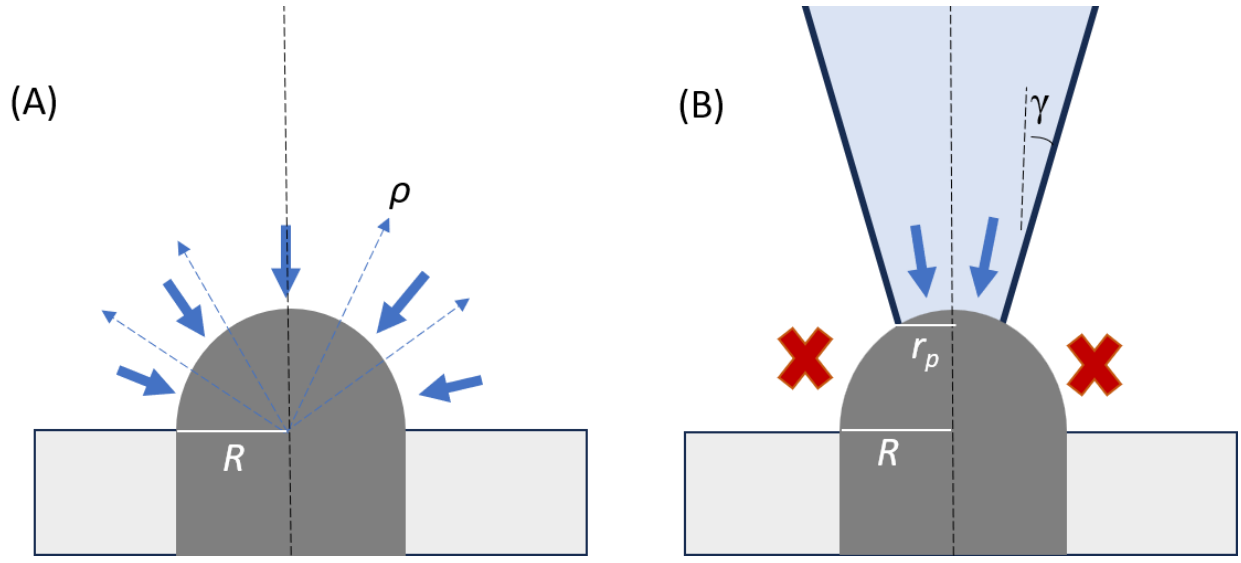

Figure 1.4 (A) Mass transport to a hemispherical electrode and (B) mass transport through a conical pipet, which serves as an approximation for the SECCM tip. Both figures exhibit spherical symmetry. However, in the SECCM setup, the pipet limits mass transport to a specific area of the hemispherical surface, rather than the entire hemisphere. Adapted from (Anderson, K. L. et Edwards, 2023)

Mass transfer coefficient (m) can be defined by the mass transport limited current using the following equation (Lebègue, 2023):

$$m = \frac{i_{lim}^{SECCM}}{nFAC} \tag{1.7}$$

Where using SECCM, A represents the wetting area of the droplet in contact with the electrode surface (Alzahrani *et al.*, 2018; Saxena *et al.*, 2024). Therefore, the mass transfer coefficient can be utilized to determine the surface area or the concentration of the redox species if it is unknown. Going further, m makes relationships between current, potential, and electron-transfer kinetics under steady-state voltammetry conditions (Lebègue, 2023). By fitting experimental current-potential $i(E)$ data to theoretical models, kinetic parameters can be extracted. In cases where there is no bulk concentration of the reaction product, the transport rates of both reactants and products

are equal, and ohmic drop is negligible, the current-potential relationship follows the expression given in following quation (Lebègue, 2023).

$$i(E) = \frac{FAm_0C\exp\left(\alpha f\left(E-E^{0\prime}\right)\right)}{\frac{m}{k^0}+\exp\left(-(1-\alpha)f\left(E-E^0\right)\right)+\exp\left(\alpha f\left(E-E^0\right)\right)} \quad (1.8)$$

In this expression, f represents F/RT, R is the gas constant, and T is the temperature. The formal potential is denoted as $E^{0\prime}$, while α and k^0 correspond to the charge transfer coefficient and the standard rate constant, respectively. Anderson and Edward demonstrated by simulation that equation (1.8), originally derived under the assumption of a uniformly accessible electrode, such as in the case of a hemispherical microelectrode, can be effectively applied to the SECCM response. They also showed that by fitting SECCM experimental data to equation (1.8), where α and k^0 are the only unknown parameters, these kinetic values can be determined with high accuracy, (with a maximum error 7%). However, potential sources of error may arise from uncertainties in the geometric characterization of the pipet, or the wetting area of the droplet (A) (Alzahrani *et al.*, 2018; Anderson, K. L. et Edwards, 2023).

1.4 Experimental Techniques and Characterization Methods

1.4.1 Electrodeposition, Principle and Application

Electrodeposition is a widely employed technique for depositing a thin layer of material onto a conductive substrate by using an external source of energy. This method is important for the synthesis of nanomaterials, coatings, and thin films, offering precise control over the deposited material's thickness, composition, and structure. It is highly proved for being cost-effective, rapid, and easily controllable, making it a simple yet powerful approach to synthesize nanostructures on a substrate (Crespo-Yapur *et al.*, 2022). The process begins by negatively polarizing the working electrode with respect to the equilibrium reduction potential of the species to be deposited. This polarization reduces the metal cations in the electrolyte solution to adatoms. Then these adatoms cluster form nuclei. However, if these nuclei do not achieve the critical size required for stability,

they will dissolve back into the electrolyte. To ensure that the nuclei reach the critical size, the applied potential must exceed a specific critical value E_{crit} (Crespo-Yapur *et al.*, 2022).

Electrodeposition is achievable with the application of an electromotive force supplied by an external power source. The process can be controlled either by the applied potential or current, while monitoring the parameters recorded during deposition. Based on the mode of control, electrodeposition techniques are categorized into two main classes including potentiostatic (controlled-potential) and galvanostatic (controlled-current). Electrodeposition in general employs a three-electrode electrochemical cell where the potential of the working electrode is maintained constant relative to a reference electrode. Potentiostatic method is preferred for its precision in controlling the deposition process. However, it requires careful cell design, including potentiostats with large output capabilities and a stable reference electrode. Additionally, uncompensated resistance and polarization effects must be minimized for accurate results. In contrast, galvanostatic methods apply a constant current to the cell, which can be applied in either continuous or pulsed modes (Nasirpouri, 2017).

The electrodeposition process typically occurs in an electrochemical cell consists of a cathode (the working electrode, which is our conductive substrate, where the material is deposited), an anode (which may dissolve or remain inert), and an electrolyte containing the metal ions to be deposited such as Ag^{+} or Ni^{2+} (Figure1.5). Deposition occurs as the metal ions are reduced at the cathode to form a solid metallic layer. The driving force for this reduction is the applied potential or current, which must overcome the reduction potential of the ions as defined by the Nernst equation (Nasirpouri, 2017):

$$E = E^{0} - \frac{RT}{nF} ln\left(\frac{a_{Red}}{a_{Ox}}\right) \tag{1.9}$$

Where E is the reduction potential, E^{0} is standard reduction potential, R is gas constant, T is temperature, n is number of electrons transferred in the cell reaction. F is Faraday constant, a_{red} and a_{ox} are the activity of reduced and oxidized species respectively. During electrodeposition, metal ions are transported to the electrode surface by diffusion (movement due to concentration gradients), migration (movement in response to the electric field), and convection (bulk motion of

the electrolyte). Key parameters influencing the process include the applied potential or current, electrolyte composition, substrate properties, and temperature. For example, higher overpotentials can enhance the deposition rate but may affect the smoothness of the resulting films, while higher temperatures can improve ion mobility and film uniformity (Nasirpouri, 2017).

Electrodeposition has many applications in various fields. It is commonly used to synthesize nanoparticles (Hu *et al.*, 2020), nanowires (Xiang *et al.*, 2008), thin films for catalysis (Morales-Guio *et al.*, 2016), sensing (Tonelli *et al.*, 2019), and energy storage (Wang, Shixin *et al.*, 2024). It is also essential for the fabrication of electrocatalysts for reactions like oxygen reduction reactions (ORR) and hydrogen evolution reactions (HER), as well as for creating conductive layers in microelectronics and electrodes for energy devices like batteries, fuel cells, and supercapacitors (Kim, K. *et al.*, 2021; Li, Q. *et al.*, 2022).

Compared to other synthesis methods, electrodeposition offers several advantages. It can be performed under ambient conditions, unlike chemical vapor deposition (CVD) or sputtering, which require high temperatures or vacuum environments. Electrodeposition is an effective and versatile method for synthesizing nanoparticles, offering precise control over their size, shape, and distribution by adjusting parameters like current density and electrolyte composition. It produces high-purity, crystalline nanoparticles without the need for surfactants, ensuring clean materials. The technique is cost-effective, scalable for industrial applications, and capable of creating uniform, conformal coatings on complex 3D structures, making it valuable for catalysis, energy devices, and advanced coatings (Gurrappa et Binder, 2008; Lee, S. A. *et al.*, 2021).

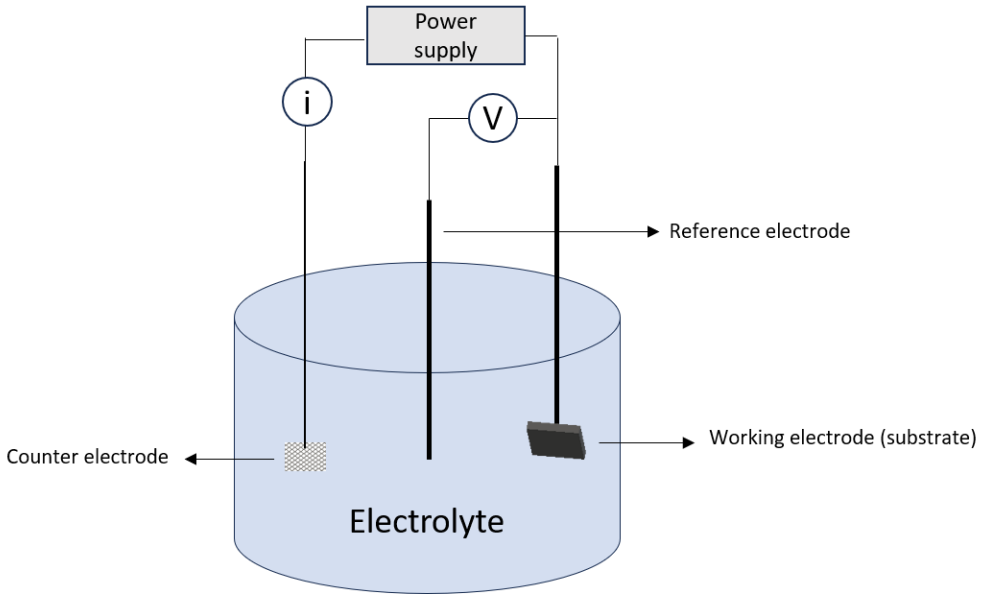

Figure 1.5 A three-electrode electrochemical cell consists of a working electrode which serves as the substrate for electrodeposition, an electrolyte containing metal cations to be deposited, and a reference electrode and a counter electrode to complete the circuit and control the potential.

1.4.2 Electrodeposition Process

Before beginning the electrodeposition process, the electrolyte must be prepared by dissolving the appropriate reactants. Key element such as temperature, reactant concentration, pH, and the presence of additives play a crucial role in shaping the morphology of the electrodeposits. Deposition occurs near the electrode surface, specifically within the electric double layer, where a sharp potential gradient facilitates the reduction of metal complexes. This process begins with nucleation on the electrode surface, followed by the growth of stable nuclei into a continuous film. The method of deposition whether using direct current (DC) or pulsed potentiostatic method significantly impacts the uniformity and structure of the resulting films. For instance, pulse electrodeposition enhances ion renewal during off-times, reducing concentration gradients that can lead to improve film quality (Nasirpouri, 2017) .

The morphology of electrodeposits can also be tailored by adjusting the overpotential, which is the difference between the applied deposition potential and the potential associated with crystal growth.

Controlling this parameter influences nucleation rates and film characteristics, enabling the fabrication of materials optimized for specific applications.

1.4.2.1 Nucleation and Growth

The process of electrodeposition involves two main stages including deposition and electrocrystallization (Nasirpouri, 2017). These stages include several intermediate steps. Initially, hydrated metal ions in aqueous electrolytes, are transported toward the cathode by mass transport mechanisms such as migration, diffusion, and convection. Upon reaching the outer Helmholtz plane (OHP) at the boundary of the double layer, the main deposition process begins as the ion crosses the electrified interface. At this point, the hydrated ion loses its water molecules in a charge-transfer reaction, allowing it to attach to the cathode surface. This attachment results in the formation of ad-ions and, subsequently, ad-atoms (Figure 1.6). The behavior of these species depends mainly on the substrate's surface energy and the specific growth sites available. When an ion partially contacts the substrate, it initially forms an ad-ion at a specific site. This ad-ion retains some charge and is surrounded by fewer hydration water molecules than it had in solution. As it transitions to a growth site like a flat surface, step, kink, or edge the number of surrounding water molecules decreases. Finally, the hydration water molecules are replaced entirely by coordinating metal atoms, creating a charge-neutral ad-atom embedded in the lattice. This stepwise replacement of water molecules marks the progression of the deposition process (Nasirpouri, 2017).

Surface diffusion is a critical stage during electrodeposition. In this process, ad-atoms move across the substrate surface via a random-walk mechanism, transitioning between different growth sites. These movements, which are influenced by the type of site such as terrace, step, or kink, determine the final accommodation of the metal atoms in the lattice. The transition from one site to another finally results in the formation of stable atomic clusters, marking the nucleation phase.

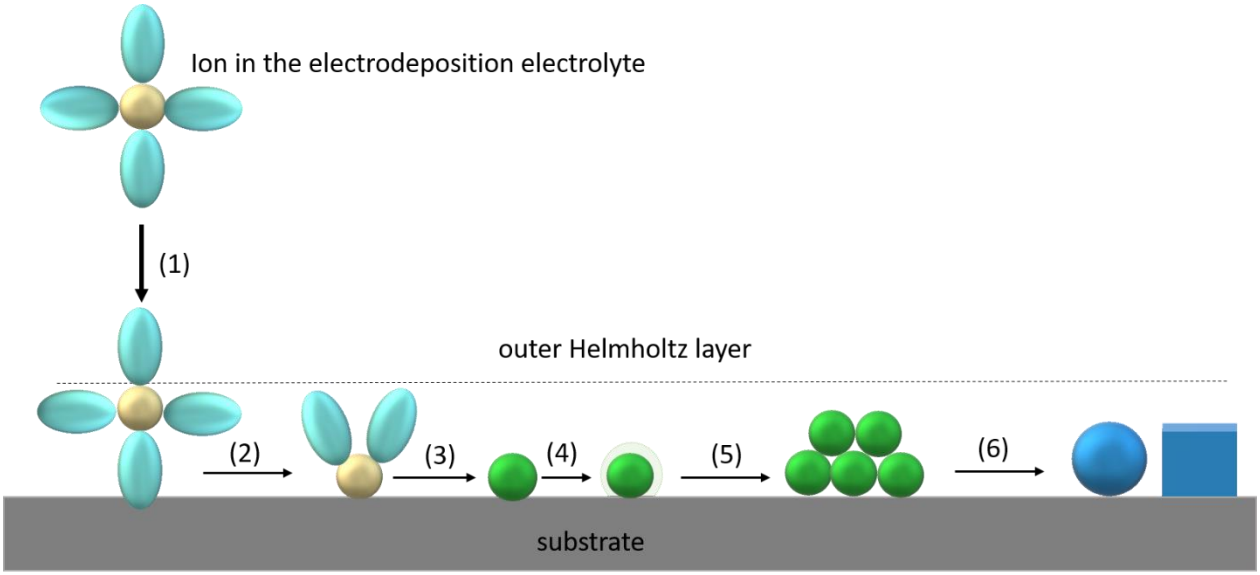

Figure 1.6 A schematic representation of nucleation and growth during a typical electrodeposition process that involves following steps: (1) Ion transport from the bulk electrolyte to the outer Helmholtz plane (OHP), (2) Transfer of ions across the electrical double layer, (3) Partial or complete dehydration leading to the formation of ad-ions and ad-atoms, (4) Surface diffusion of ad-atoms, (5) Nucleation of stable atomic clusters, and (6) Irreversible incorporation of ad-atoms into the atomic lattice, resulting in the development of a specific crystallographic texture and morphology, a process known as electrocrystallization.

1.4.2.2. Growth and Distribution of Metal Particles

The growth of individual metal particles on the electrode surface depends on the number and proximity of neighboring particles. As nucleation is intrinsically random, it naturally leads to a broad distribution of particle sizes. In diffusion-controlled growth (step 4 and 5 in Figure 1.6), particles rapidly develop different diameters due to interparticle diffusional coupling (Figure 1.7). This phenomenon occurs because the diffusion layers surrounding individual particles overlap, altering the availability of reactants. To narrow the size distribution, the overpotential can be reduced, slowing the growth rate and minimizing diffusion effects. By carefully controlling these parameters, it is possible to produce more uniform particles (Liu, H. *et al.*, 2001; Liu, H. et Penner, 2000a).

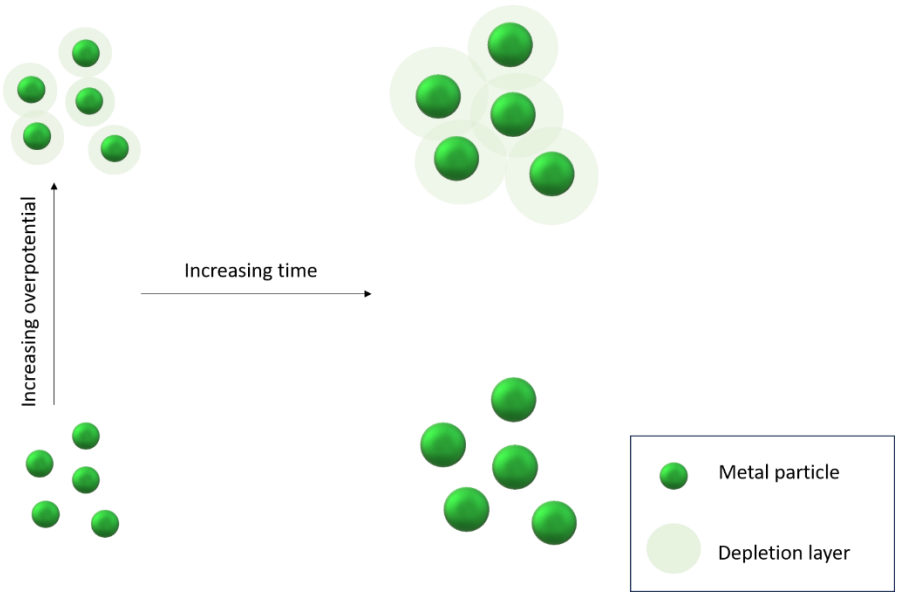

Figure 1.7 Effect of deposition overpotential on expansion of the depletion layer around growing metal particles. A higher overpotential extends the depletion layer further. This affects nucleation and growth, leading to bigger particle size and variation. In contrast, a lower overpotential maintains a more uniform ion distribution, resulting in more controlled growth and reduced particle size dispersion. Based on (Xiang *et al.*, 2008)

1.4.2.3 Single Particle Fabrication using Electrodeposition

To study the behavior of single particles, it is essential to synthesize nanoparticles that are well-separated on the substrate. As already discussed in previous section, in electrodeposition, the morphology of the resulting materials can be controlled by adjusting deposition parameters. Cyclic voltammetry of a glassy carbon electrode in an aqueous $AgNO_3$ solution indicates that silver nucleation initiates at an onset potential of -70 mV vs. Ag/AgCl, signifying the formation of initial nuclei on the electrode surface (Figure 1.8). As the potential is further reduced from -70 mV to -200 mV, the nucleation process transitions into gradual particle growth, which continues with increasing cathodic potential. During the reverse scan, an anodic peak observed at 0.1 V corresponds to the oxidation of deposited silver, confirming the redox behavior of the system.

During the second cycle, the onset potential in the cathodic region shifts to a lower potential, indicating that not all silver was oxidized in the first cycle, leaving some reduced Ag on the surface. This causes subsequent electrodeposition to occur at a lower overpotential, leading to deposition on the remaining Ag particles.

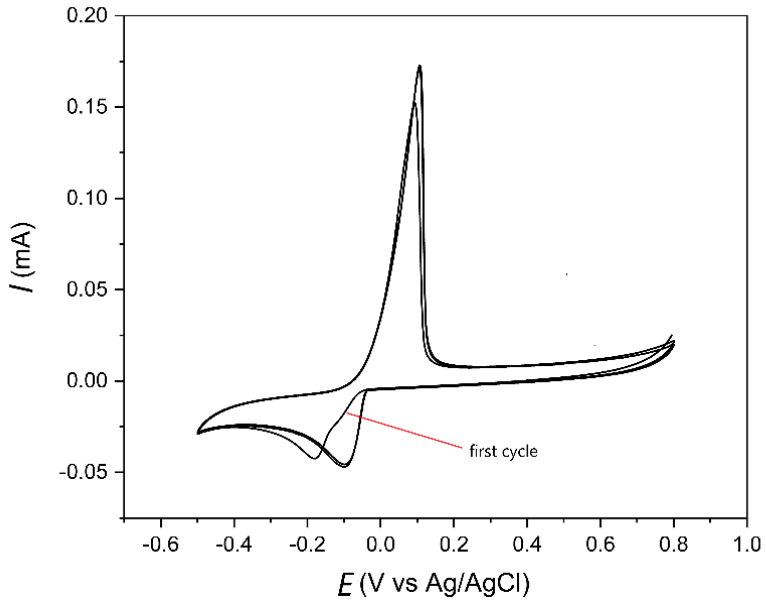

Figure 1.8 Cyclic voltammogramme of a glassy carbon working electrode in 1 mM $AgNO_3$ and 0.1 M KNO_3 using a Pt mesh counter electrode at a sweep rate of 20 mV/s.

Figure 1.9 Shows galvanostatic electrodeposition at low overpotentials by applying constant current densities of -1 µA/cm², -2 µA/cm², -4 µA/cm², and -5 µA/cm² for 5 minutes in 1 mM $AgNO_3$ and 0.1 M KNO_3. Applying a lower current density, which corresponds to a lower overpotential, results in well-dispersed silver particles with increasing the distance between the particles, so there is strong relation between the applied current and the density of silver particle on the substrate surface. By increasing current density, more particles appear on the substrate that are smaller in size (Crespo-Yapur *et al.*, 2022; Isaev *et al.*, 2017).

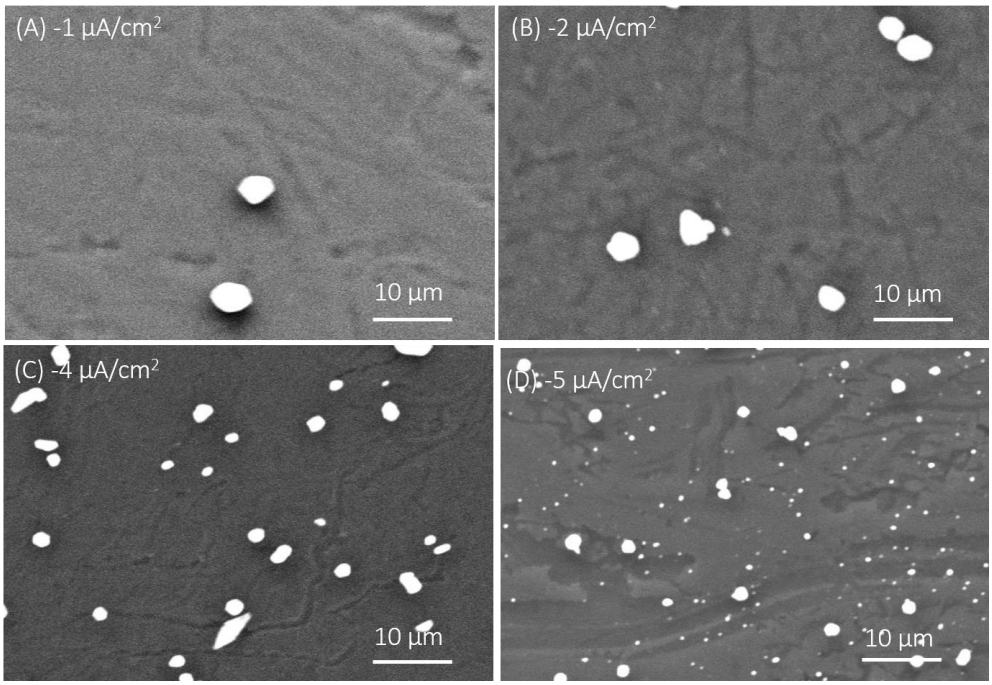

Figure 1.9 Galvanostatic electrodeposition of individual silver particles applying different current density of (A) -1 µA/cm², (B) -2 µA/cm² (C) -4 µA/cm² (D) -5 µA/cm² for 5 minutes in 1 mM $AgNO_3$ and 0.1 M KNO_3.

1.4.3 X-ray Diffraction (XRD)

Before exploring the characterization technique of X-ray diffraction (XRD), it is beneficial to first develop a fundamental understanding of crystal structure in the following sections.

1.4.3.1 Crystal Structure and Space Lattice

A crystal consists of repeating structural motifs, which can be atoms, molecules, or ions. These motifs are arranged in a space lattice (Figure 1.10). A space lattice is an infinite three-dimensional arrangement of points, where each point shares the same spatial relationship with its surrounding neighbors. The overall crystal structure appears when identical structural units, such as atoms or molecules are systematically positioned at each lattice point.

The unit cell is the fundamental structural unit of a crystal lattice, usually taking the form of a parallelepiped (Figure 1.10B). It acts as the basic building block from which the entire crystal is

constructed through translational repetition. The most basic unit cells, known as primitive cells, contain lattice points exclusively at their corners (Figure 1.10C).

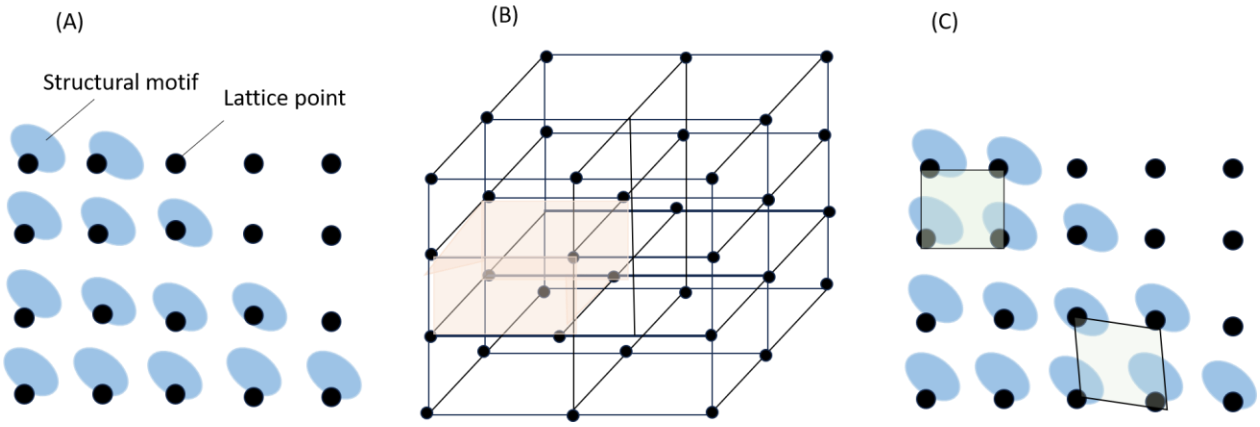

Figure 1.10 (A) The crystal lattice consists of a systematic arrangement of lattice points, while the crystal structure is formed by the placement of structural motifs in accordance with this lattice framework. (B) A unit cell which is a parallel-sided fundamental unit. (C) A unit cell that can be chosen in different ways. Adapted from (Atkins et de Paula, 2010).

Non-primitive unit cells can also contain lattice points at the center or on the faces. The unit cell is defined by six parameters: three edge lengths (a, b, and c) and three interaxial angles (α, β, and γ). (Figure 1.11).

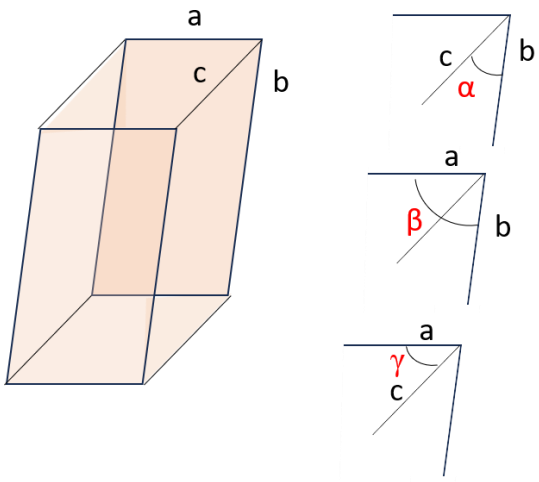

Figure 1.11 The notation for the sides and angles of a unit cell.

Crystals are classified into seven distinct crystal systems based on their rotational symmetry. For instance, the cubic system features four threefold rotational axes, the monoclinic system has a single twofold axis, and the triclinic system exhibits no rotational symmetry. In three-dimensional space, there are only 14 unique space lattices, referred to as Bravais lattices. These can be represented using different unit cell types, including primitive (P), body-centered (I), face-centered (F), and side-centered (A, B, or C) (Figure 1.12).

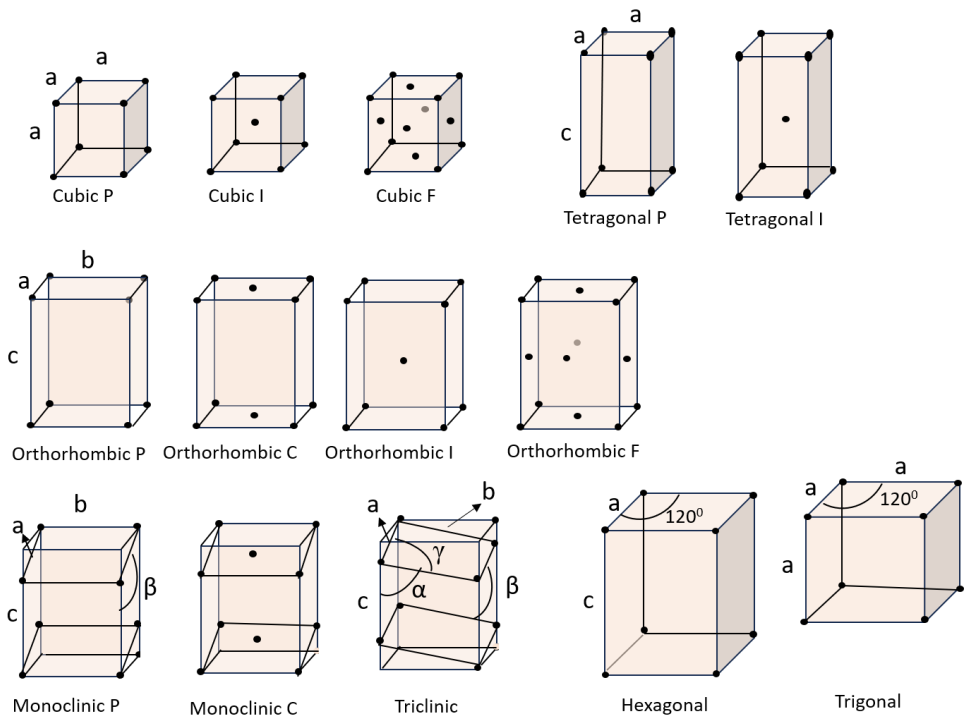

Figure 1.12 The fourteen Bravais lattices define possible three-dimensional arrangements of lattice points, which do not necessarily correspond to atomic positions. P is primitive unit cell. A body-centered unit cell is labeled as I, a face-centered unit cell as F, and a unit cell with lattice points on two opposite faces as C. Adapted from (Atkins et de Paula, 2010)

1.4.3.2 Identification of Lattice Planes: Miller Indices

Crystal planes are identified using Miller indices (*hkl*), where (*hkl*) refers to a specific plane and represents a family of parallel planes. Lower absolute values of *h*, *k*, and *l* indicate planes that are closer to being parallel to the respective a, b, and c axes. For instance, the separation of the (*hkl*) planes in the cubic lattice is given by:

$$\frac{1}{d_{hkl}^2} = \frac{h^2+k^2+l^2}{a^2} \qquad (1.10)$$

The parameters are depicted in Figure 1.13, for the separation of the (*hk0*) planes in the square lattice.

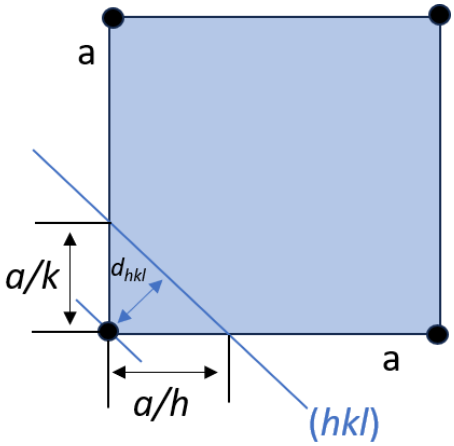

Figure 1.13 The dimensions of a unit cell which determine its geometric parameters and define how it extends through the lattice points.

1.4.3.3 X-ray Diffraction and Structure Determination

In 1895, Wilhelm Röntgen discovered X-rays, and by 1912, Max von Laue proposed that because X-ray wavelengths are comparable to the distances between atomic planes in crystals, they could undergo diffraction when interacting with a crystalline structure. This insight became the beginning of using X-ray diffraction to study the internal arrangement of atoms in solids. This theory was experimentally validated by Walter Friedrich and Paul Knipping, establishing X-ray diffraction as a key technique for determining crystal structures. X-rays (electromagnetic waves with wavelengths near 10^{-10} m) are produced by directing high-energy electrons onto a metal target, resulting in a broad-spectrum emission known as Bremsstrahlung, accompanied by distinct intensity peaks (Figure 1.14A). These peaks arise from electronic transitions within atomic shells (Figure 1.14B and C). Today, synchrotron radiation is extensively employed due to its superior intensity and enhanced analytical capabilities (Atkins et de Paula, 2010).

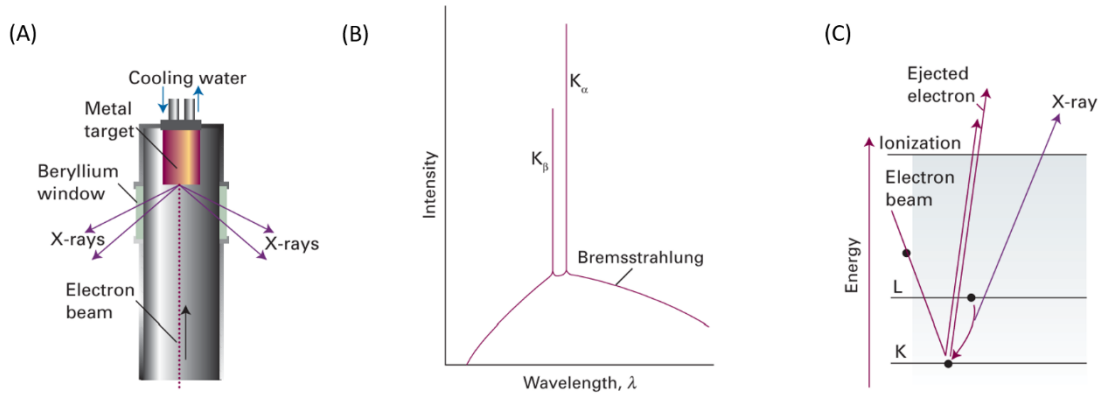

Figure 1.14 (A) Illustrates the production of X-rays by striking a cooled metal target with a focused electron beam. (B) X-ray emission from a metal contains a broad, continuous Bremsstrahlung background with distinct sharp peaks corresponding to electronic transitions. The label K indicates that the radiation results from an electron filling a vacancy in the K shell of the atoms. (C) X-ray generation involves multiple processes. When an incoming electron collides with an electron and eject from the K shell, a vacancy is created. Another electron (from the L shell in) falls into the vacancy and emits its excess energy as an X-ray photon. Adapted with permission from (Atkins et de Paula, 2010).

1.4.3.4 X-ray Diffraction Techniques

Several techniques exist for structural analysis. The first one is *Laue Method*. This technique uses a broad X-ray beam on a single crystal to produce diffraction patterns photographically. Modern synchrotron sources have brought back the interest in this method. Another widely used approach is *powder X-ray diffraction* (*PXRD*), pioneered by Debye, Scherrer, and Hull, where monochromatic radiation is used on powdered samples. Modern powder diffractometers electronically detect diffraction from many randomly oriented crystallites, allowing the measurement of diffraction patterns from all crystallographic planes (Figure 1.15). PXRD is extensively employed to identify phases, phase diagram determination, and quantification of crystalline phases. The *Bragg's Method* developed by William and Lawrence Bragg. It remains the principle method in modern X-ray crystallography, enabling precise determination of crystal

structures. This technique involves rotating a single crystal in monochromatic beam and detecting reflections at various angles.

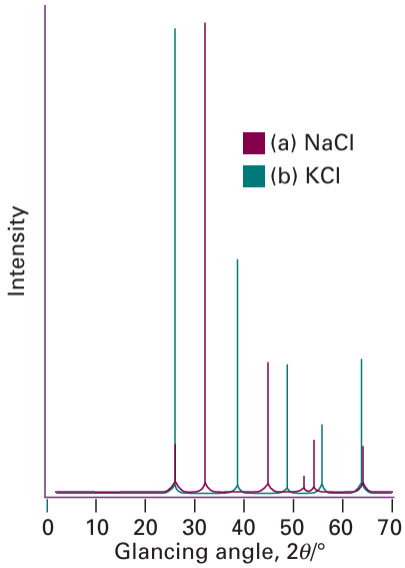

Figure 1.15 X-ray powder diffraction patterns of NaCl (a) and KCl (b). Adapted with permission from (Atkins et de Paula, 2010).

1.4.3.5 Bragg's Law and Constructive Interference

Bragg's law describes diffraction based on crystal planes acting as semi-transparent mirrors (Figure 1.16). It says that constructive interference occurs when:

$$n\lambda = 2d\ sin\theta \qquad (1.11)$$

Where n is the order of reflection, λ is X-ray wavelength, d is interplanar spacing, and θ is glancing angle. This equation shows that constructive interference and therefore an observable diffraction peak occurs when the path-length difference equals an integer number of the wavelength. Higher-order reflections arise from (*nh, nk, nl*) planes. Bragg's law is primarily used to determine the spacing between lattice layers which are crucial for crystallographic analysis and material

characterization. Once the reflection angle (θ) is identified, the interplanar distance (*d*) can be easily calculated.

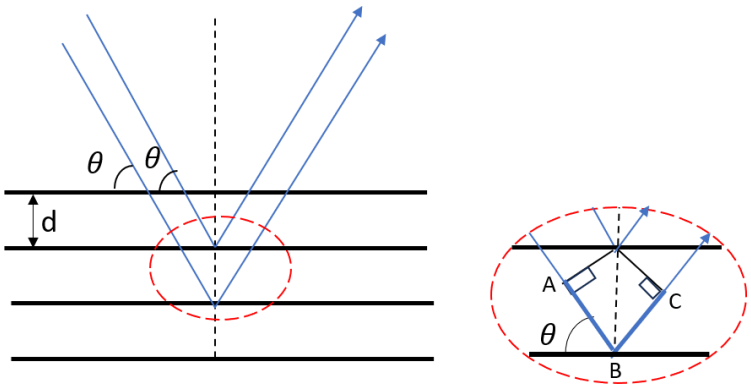

Figure 1.16 The standard approach to deriving Bragg's law involves analyzing the constructive interference of X-rays reflected from parallel crystal planes. The path lengths vary by AB+BC, which depends on the glancing angle, θ. A reflection happens when AB+BC is equal to an integer number of wavelength.

1.4.4 Scanning Electron Microscopy (SEM)

Scanning Electron Microscopy (SEM) is a powerful imaging technique that uses a focused beam of high-energy electrons to scan the surface of a sample, providing detailed information about its topography, composition, and other material properties. By capturing various signals such as secondary electrons (SE), backscattered electrons (BSE), and X-rays, SEM generates high-resolution images and enables elemental analysis. Its resolution is determined by the wavelength of the electrons and the quality of the electron optics, allowing for structural details to be studied at the nanometer scale (Zhou *et al.*, 2007).

Elastic scattering involves the refraction of incident electrons by the atomic nuclei or outer shell electrons of the specimen with minimal energy loss. Electrons scattered at angles greater than 90° are termed backscattered electrons (BSE) and are useful for imaging. In contrast, inelastic scattering occurs when incident electrons transfer significant energy to the specimen, exciting or ionizing its atoms. This process generates secondary electrons (SE), which have energies below 50

eV and are commonly used for imaging and analysis. Moreover, electron interactions with the sample produce other signals, such as characteristic X-rays, Auger electrons, and cathodoluminescence, that can offer further analytical insights. Different signals are detected from specific regions of the sample, as illustrated in Figure 1.17.

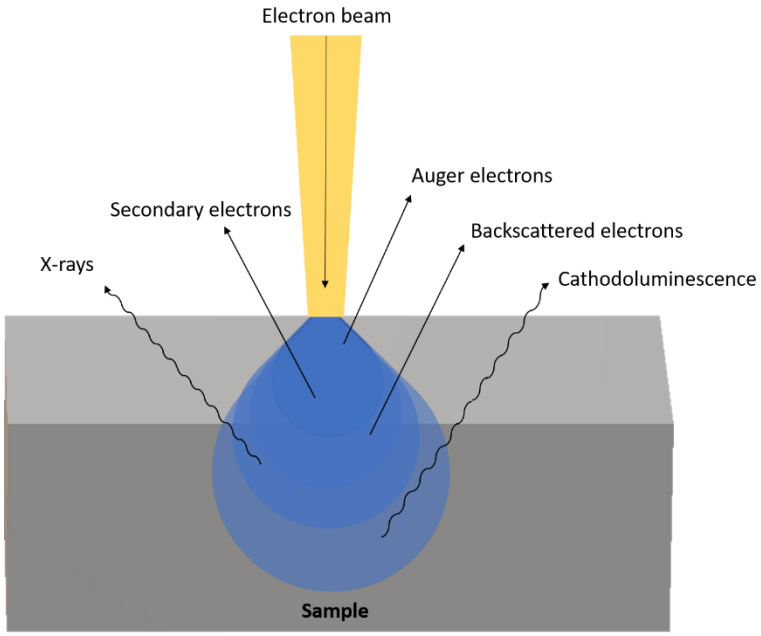

Figure 1.17 The interaction between the electron beam and the specimen, along with the signals emitted from the sample.

1.4.4.1 Configuration of SEM

A typical SEM consists of several essential components designed for functionality and adaptability with applications. The electron gun (electron source), located at the top of the microscope, generates a focused beam of electrons. Depending on the application, SEMs use either thermionic emitters (such as tungsten or LaB_6 filaments) or field emission guns (FEGs), the latter providing higher brightness and resolution. The electron column contains electromagnetic lenses and apertures that focus and shape the electron beam. Condenser lenses control merging the beam and intensity, while the final objective lens focuses the beam onto the sample at a small spot size,

enabling high-resolution imaging. Scanning coils within the column allow the beam to be scanned in every direction across the sample surface, allowing point-by-point imaging. The sample is placed on a motorized stage within a vacuum chamber (Figure 1.18). This stage can move in the X, Y, and Z directions and rotate or tilt, enabling imaging from various angles. Detectors in the SEM capture signals emitted during electron-sample interactions. The Secondary Electron Detector (SED) provides high-resolution images of surface texture, while the Backscattered Electron Detector (BSED) captures compositional contrast based on atomic number. Energy-Dispersive X-ray Spectroscopy (EDS) enables elemental analysis by detecting characteristic X-rays, and will be explained in section (1.4.5) (Zhou *et al.*, 2007).

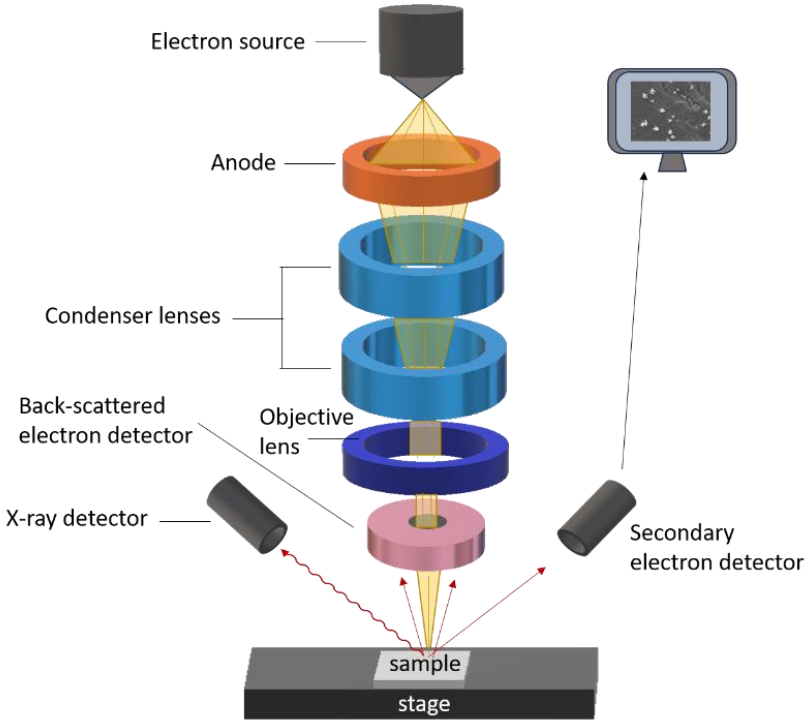

Figure 1.18 Schematic illustration of a scanning electron microscope (SEM). The main components of an SEM, includes the electron gun, condenser lenses, scan coils, and electron detectors. To maintain a stable electron beam and prevent scattering, SEM operates under high vacuum conditions. Some modern systems also include low-vacuum or environmental modes for imaging non-conductive or hydrated samples. The entire system is controlled through a computer interface, which manages beam parameters, stage movement, and real-time image acquisition.

1.4.5 Energy Dispersive X-ray Spectroscopy

Energy Dispersive X-ray Spectroscopy (EDS), also known as EDX, is a powerful analytical technique commonly integrated with SEM to provide elemental composition analysis of materials. While SEM primarily offers high-resolution imaging of surface morphology, EDS extends its capabilities by enabling qualitative and quantitative elemental analysis at the microscale.

When a high-energy electron beam from the SEM interacts with the sample, it not only generates secondary and backscattered electrons for imaging but also excites atoms within the specimen. This excitation leads to the ejection of inner-shell electrons, creating vacancies that are subsequently filled by electrons from higher energy levels. The energy difference between these levels is released in the form of characteristic X-rays, which are unique to each element. EDS detectors capture these X-rays, allowing for elemental identification and mapping (Girão *et al.*, 2017).

The process of X-ray generation includes two primary components, the first one is X-rays characteristic which are emitted due to electronic transitions between specific energy levels of an atom and use it as the fundamental analytical signal in EDS, and the second one, Bremsstrahlung Radiation (Continuous Spectrum), that produces when the incident electron beam slows down upon interacting with the atomic nucleus, generating a broad background X-ray spectrum (Subramanian *et al.*, 2022). The region within the sample where X-rays are generated is crucial for obtaining high-quality EDS spectra. Factors influencing signal generation include the energy of the X-rays, The average atomic weight of the sample, and the absorption properties of specific elements (Girão *et al.*, 2017). EDS is extensively employed in microstructural characterization across various field including material science, biology, and environmental science (Girão *et al.*, 2017).

1.4.5.1 EDS for Single-Particle Analysis

When EDS combined with Scanning Electron Microscopy (SEM) or Scanning Transmission Electron Microscopy (STEM), enables the elemental characterization of single nanoparticles with high spatial resolution. Unlike bulk analysis, where the sample composition is assumed to be homogeneous, EDS for single particles requires careful consideration of sample morphology, X-ray interaction volume, and signal-to-noise ratios. When a high-energy electron beam interacts with

a nanoparticle and excites core electrons to provide an elemental fingerprint of the sample, the efficiency of X-ray detection depends on factors such as:

1. Beam accelerating voltage: Higher voltages increase X-ray generation but also enlarge the interaction volume, potentially including signals from the substrate.
2. Atomic number of the sample: Heavier elements generate stronger X-ray signals, while lighter elements may require specialized detectors.
3. Sample thickness: Nanoparticles must be thin enough to allow electron transmission if analyzed in STEM mode (Hodoroaba, 2020).

The application of EDS includes *chemical differentiation*, where EDS can distinguish between mixed nanoparticles, such as SiO_2 and TiO_2. This capability is particularly valuable in material science and catalysis, where precise identification of nanoparticle components is essential. Another important use of EDS is in the analysis of *core-shell nanoparticles*, where elemental mapping helps confirm the presence and uniformity of coatings. For example, it can validate whether a gold nanoparticle is encapsulated by a silica shell, ensuring proper synthesis and functionality in applications such as drug delivery or catalysis. Furthermore, EDS combined with Scanning Transmission Electron Microscopy (STEM) allows for *nanoparticle morphology classification*, distinguishing between solid, porous, and hollow structures. While STEM provides high-resolution images of nanoparticle morphology, it cannot directly reveal elemental composition. Thus, by combining STEM with EDS, both structural and chemical information are obtained, enabling accurate classification of nanoparticles. This information is crucial in fields like battery, energy conversion researches and nanomedicine, where the internal structure of nanoparticles influences their performance and behavior (Hodoroaba, 2020).

Overall, single-particle EDS provides a powerful analytical approach for understanding the elemental composition and structural properties of nanoparticles, contributing to advancements across various scientific and industrial domains

In summary, the transition toward sustainable energy technologies requires the development of efficient and durable electrocatalysts for reactions such as the oxygen reduction and hydrogen

evolution reactions. To gain a fundamental understanding of these systems, it is crucial to employ advanced methodologies that can bridge the gap between catalyst structure and electrochemical function. Scanning electrochemical cell microscopy (SECCM) provides such a capability, allowing localized electrochemical measurements with high spatial resolution. When combined with structural characterization techniques such as X-ray diffraction (XRD), scanning electron microscopy (SEM), and energy dispersive spectroscopy (EDS), this approach establishes a comprehensive framework for clarifying nanoscale structure–activity relationships. The subsequent chapters of this thesis build on this foundation, applying SECCM to investigate nanoscale electroanalysis, guiding the design of next-generation energy conversion materials.

CHAPTER 2

Influence of Particle Size on Mass Transport During the Oxygen Reduction Reaction of Single Silver Particles using Scanning Electrochemical Cell Microscopy

2.1 Résumé

Les mesures électrochimiques sur entités uniques permettent d'analyser l'activité électrocatalytique de particules individuelles en fonction de leur composition, de leur forme et de leur orientation cristallographique. En plus des effets structurels, la taille des particules peut également influencer l'activité électrocatalytique et les mécanismes réactionnels à travers les effets de transport de masse. Dans cette étude, l'électrodéposition a été utilisée pour fabriquer des particules d'argent bien séparées, de tailles variées, allant de 100 nm à 500 nm de rayon. En combinant la microscopie électrochimique en cellule de balayage (SECCM) avec la microscopie électronique à balayage (SEM), le courant électrocatalytique des particules d'argent individuelles pour la réduction de l'oxygène a été évalué en fonction de leur taille. Les résultats ont montré que la densité de courant augmentait à mesure que le rayon des particules diminuait, ce qui a été corrélé au transport de masse de l'oxygène vers la particule d'argent. Cette observation met en évidence l'importance des effets de transport de masse dépendants de la taille au niveau de particules individuelles et ouvre de nouvelles perspectives pour des mesures quantitatives en électrocatalyse à l'aide de la SECCM.

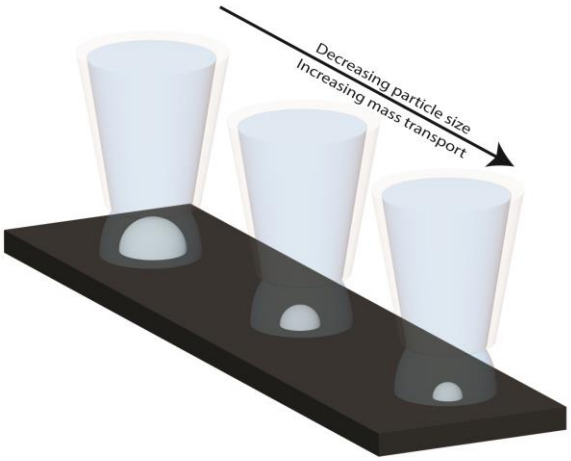

Figure 2.1 Graphical abstract, demonstrating through SECCM in individual particle voltammetry measurements, that decreasing particle size enhances mass transport.

Salek, S., & Byers, J. C. Influence of Particle Size on Mass Transport during the Oxygen Reduction Reaction at Single Silver Particles Using Scanning Electrochemical Cell Microscopy. *The Journal of Physical Chemistry Letters* **(2024)**, *15*(33), 8494-8500. DOI: 10.1021/acs.jpclett.4c01832

The supplementary information can be found in **ANNEXE A**

2.2 Authors Contribution

Samaneh Salek

First author conducted the experimental measurements, processed and interpreted the results, created the figures, carried out the literature review, and wrote the first draft of the manuscript and made corrections.

Joshua Byers

Co-author supervised the study, contributed to result interpretation, participated in discussions, and reviewed the manuscript.

2.3 ABSTRACT

Single entity electrochemical measurements enable insight into the electrocatalytic activity of individual particles based on composition, shape, and crystallographic orientation. In addition to structural effects, particle size can further influence electrocatalytic activity and reaction mechanisms through mass transport effects. In this work, electrodeposition was used to grow well-separated silver particles of varying sizes from 100 nm to 500 nm in radius. Using a multi-microscopy approach of scanning electrochemical cell microscopy combined with scanning electron microscopy, the electrocatalytic current of individual silver particles towards the oxygen reduction reaction was evaluated as a function of their size. It was found that the current density

increased with decreasing particle radius, which was correlated to the mass transport of oxygen to the silver particle, demonstrating the importance of size dependent mass transport effects that can occur at the single particle level using scanning electrochemical cell microscopy, and opening new opportunities for quantitative electrocatalysis measurements.

2.4 Introduction

The measurement of the electrocatalytic activity of an individual electrocatalyst particle combined with correlative microscopy is an emergent technique in the field of single entity electrochemistry enabling new insight into the structure-activity relationship of nanomaterials.(Zhang, L. *et al.*, 2024) Scanning probe electrochemical microscopy, and in particular scanning electrochemical cell microscopy (SECCM), has emerged as a powerful tool, enabling the measurement of electrocatalytic activity down to the single particle level (Wahab *et al.*, 2020). SECCM uses an electrolyte filled pipet probe to create a local electrochemical cell that can be brought into contact with any surface and where working electrode dimensions, determined by the pipet diameter and surface wetting of the droplet, can range from several tens of nanometers to several tens of micrometers (Jayamaha *et al.*, 2024). As a consequence, SECCM has been used to study functional materials at the single particle level for a variety of (photo)electrocatalytic reactions, (Bentley, C. L., 2022; Jin, 2023; Santana Santos *et al.*, 2023; Wahab *et al.*, 2020) such as the oxygen evolution reaction (OER), (Kang *et al.*, 2023; Li, M. *et al.*, 2022; Liu, C. *et al.*, 2023; Lu, X. *et al.*, 2021; Mefford *et al.*, 2021; Mena-Morcillo *et al.*, 2023; Quast, T. *et al.*, 2021; Tarnev *et al.*, 2019) hydrogen evolution reaction (HER), (Bentley, C. L. et Unwin, P. R., 2018; Choi *et al.*, 2020; Gao *et al.*, 2020; Hill, J. W. *et al.*, 2020; Zhao, J. *et al.*, 2023) oxygen reduction reaction (ORR), (Byers *et al.*, 2014; Lai *et al.*, 2011; Tetteh, E. B. *et al.*, 2022; Ustarroz *et al.*, 2018) carbon dioxide reduction reaction (CO_2RR), (Jeong, S. *et al.*, 2022) as well as hydrazine and borohydride oxidation (Saha *et al.*, 2018; Saha *et al.*, 2022, 2023). These single particle studies have encompassed various shapes including nanoplates (Peng *et al.*, 2023), metal organic frameworks (Liu, C. *et al.*, 2023), nanorods(Li, M. *et al.*, 2022; Saha *et al.*, 2018), nanotubes (Byers *et al.*, 2014), nanocrystals (Choi *et al.*, 2020; Jeong, S. *et al.*, 2022; Zhao, J. *et al.*, 2023), and two-dimensional materials (Hill, J. W. et Hill, 2021) providing insight into the role of particle composition, crystallographic orientation, shape, strain, as well as discriminating between the roles of edge sites, defects and basal planes towards electrocatalytic activity.

Single entity measurements using SECCM can be carried out using pipet diameters that are smaller or larger than the active material being evaluated. In the former case, mass transport is defined by the *pipet geometry*, whereas in the latter case, *particle geometry* within the droplet may further influence mass transport. While the role of particle size on mass transport hasn't been evaluated using SECCM, size dependent mass transport effects have been observed during the ORR for individual Pt particles grown on microelectrodes (Chen, S. et Kucernak, A., 2004). Unlike microelectrodes, in SECCM measurements, the working electrode surface is not immersed in electrolyte and is instead exposed to the surrounding atmosphere, either standard atmospheric conditions or a controlled environment using an environmental chamber. Only the area of the working electrode surface brought into contact with the pipet probe is wetted by the electrolyte solution leading to the formation of a three-phase boundary between the solid electrode surface, the solution filled probe, and the surrounding gaseous atmosphere. This has made it a particularly powerful technique for studying gas consuming reactions such as the ORR and CO_2RR as well as gas evolving reactions such as the HER and OER (Mariano *et al.*, 2021a; Mariano *et al.*, 2017a; Mefford *et al.*, 2021). Furthermore, the SECCM configuration enables mass transport rates comparable to gas diffusion electrodes used in CO_2 electrolyzers, fuel cells, and metal air batteries (Jeong, S. *et al.*, 2022; Mariano, R. G. *et al.*, 2022). Methods that enable electrocatalytic activity to be evaluated under high rates of mass transport are becoming increasingly important as common techniques such as the rotating disk electrode do not always translate into equivalent improvements in assembled devices, due, in part, to the lower rates of mass transport that can be achieved using hydrodynamic voltammetry (Lazaridis *et al.*, 2022). In addition to electrocatalytic activity, the rate of mass transport can further impact the selectivity and reaction mechanisms for the ORR and CO_2RR (Chen, S. et Kucernak, A., 2004; Goyal *et al.*, 2020). Given the importance of mass transport in the evaluation of electrocatalyst materials, in this work, silver particles of varying sizes (100 nm – 500 nm radius) were prepared using electrodeposition and their activity towards the ORR was evaluated using SECCM to understand how particle loading and mass transport affect the overall electrocatalytic current.

2.5 Results and discussion

A common challenge in the preparation of nanoparticles for single entity electrochemical measurements is their solution phase synthesis, which requires the use of surface directing agents

to control particle shape as well as their dispersion onto a substrate surface, which can interfere with the evaluation of electrocatalytic activity (Gaudin, L. F. *et al.*, 2024; Saha *et al.*, 2018). To avoid these complications, silver particles with low surface coverage and large interparticle separation were deposited across a glassy carbon substrate using electrodeposition at a low current density (low overpotential) to enable subsequent single entity electrochemical measurements using SECCM (Figure 2.2). This contrasts with usual multi-step metal (nano)particle electrodeposition processes that can include a surface activation step, a particle nucleation step at a large overpotential followed by a particle growth step to create electrode surfaces with high particle loading and high surface coverage (Liu, H. et Penner, 2000b; Walter *et al.*, 2002). In this work, a single step galvanostatic electrodeposition procedure (Figure 2.2A), using a current density of - 50 $\mu A\ cm^{-2}$ for 2 seconds, was used to grow silver particles on a glassy carbon electrode surface with an average interparticle separation that was larger than the diameter of the SECCM pipet probe (1.8 μm). Due to the low current density used, the potential of the working electrode barely exceeded the onset potential for the electrodeposition of silver (Figure A.1). By omitting a surface activation step and using a low overpotential, this approach limited the number of nucleation sites formed on the glassy carbon electrode surface leading to a low silver particle coverage with large interparticle separation. As shown in Figure 2.2B and Figure 2.2C, it was possible to grow small clusters or individual silver particles, free from surface ligands, of different sizes that were separated by several micrometers. EDX spectra (Figure 2.2C) showed a small amount of chloride on the silver particles, likely from the Ag/AgCl (3M KCl) reference electrode, which could also play a role in the growth of silver particles.

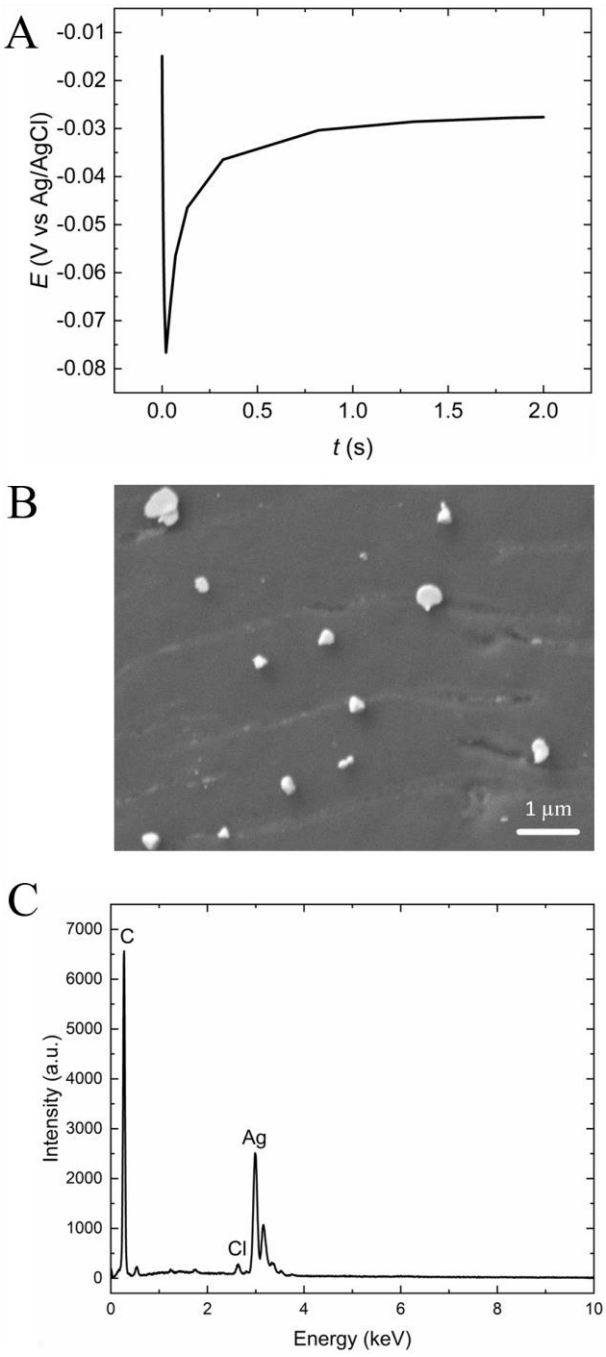

Figure 2.2 (A) Potential-time graph for the galvanostatic electrodeposition of silver on a glassy carbon substrate at a constant current density of - 50 µA cm^{-2} in a 0.1 M KNO_3 and 0.001 M $AgNO_3$ electrolyte using a Ag/AgCl (3M KCl) reference electrode. (B) Scanning electron microscope image and (C) Energy dispersive X-ray spectroscopy measurement of a silver particle electrodeposited on glassy carbon substrate.

The local electrocatalytic activity of the as-prepared carbon supported silver particle substrate was measured using SECCM as illustrated in Figure 2.3A. A pipet probe, with an outer diameter of 1.8 μm (Figure A.2) containing 10 mM KOH and 50 mM KCl and a chloridized silver wire quasi reference counter electrode (QRCE), was used to form a local electrochemical cell that was brought into contact with the working electrode substrate. Voltammetric hopping mode SECCM was used to carry out linear sweep voltammograms (LSVs) for the ORR at each landing site across the heterogeneous electrode surface (Chen, C.-H. *et al.*, 2015b). The total scan area was 100 μm x 100 μm using a spacing of 9 μm between individual approach sites for a total of 121 data points. The measured diameter of the residual electrolyte was approximately 2 μm and is comparable to the value for the outer diameter of the pipet (1.8 μm). Due to the large interparticle separation, most local electrochemical measurements were of the underlying bare carbon surface. However, in some cases, the pipet landed on an area that contained one or more silver particles. Three characteristic regions are highlighted in Figure 2.3B that contain (i) a single particle (yellow circle), (ii) multiple silver particles (blue circle), or (iii) the particle-free carbon substrate (white circle). Where an individual silver particle was contacted by the pipet, its radius is indicated in Figure 2.3B. Figure 2.3C presents a typical LSV for the ORR in the presence of a single silver particle. In this work, LSVs were carried out at a sweep rate of 500 mV s^{-1} by sweeping the potential from - 0.65 V (vs Ag/AgCl QRCE) to - 0.1 V (vs Ag/AgCl QRCE), where sweeping of the potential in the anodic direction is the standard approach for ORR electrocatalysis on metal surfaces to limit the effect of surface oxides on electrocatalytic activity (Mayrhofer *et al.*, 2008; Wang, Q. *et al.*, 2022). LSVs at more negative potentials, beginning at −0.8 V (vs Ag/AgCl QRCE) were also obtained (Figure A.3). Under these conditions, a limiting current was not visible, and in some cases the droplet area was less reproducible. It was found that a cathodic potential limit of −0.65 V (vs Ag/AgCl QRCE) was sufficient to analyze the current under kinetic control while maintaining the integrity of the droplet throughout the measurements.

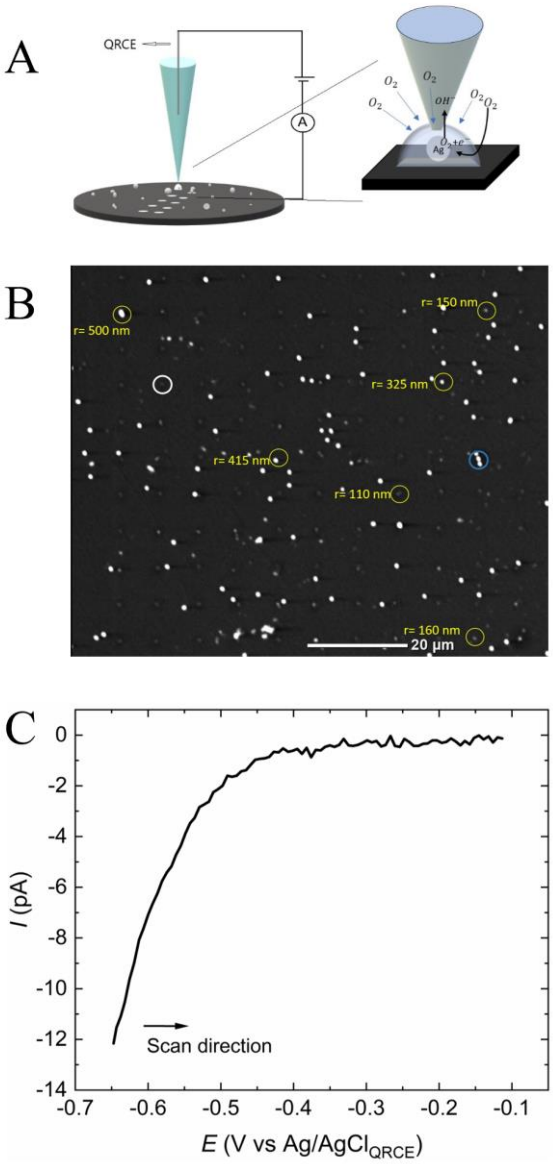

Figure 2.3 (A) Schematic of SECCM configuration for measuring the ORR. (B) Scanning electron microscope of region where electrochemical mapping was carried out using SECCM. (C) Local LSV of ORR on electrodeposited Ag particles on glassy carbon substrate using an Ag/AgCl QRCE in an aqueous solution of 0.01 M KOH and 0.05 M KCl.

In alkaline conditions, both carbon and silver are active towards the ORR (Ge *et al.*, 2015). On silver, the ORR proceeds via a 4-electron reduction to hydroxide (reaction 2.1), while carbon promotes the 2-electron reduction of oxygen to peroxide (reaction 2.2):

$$O_2 + 2\ H_2O + 4\ e^- \rightarrow 4\ OH^- \qquad E^0 = +\ 0.401\ V\ (vs.\ SHE) \qquad (2.1)$$

$$O_2 + H_2O + 2\ e^- \rightarrow HO_2^- + OH^- \qquad E^0 = -\ 0.076\ V\ (vs.\ SHE) \qquad (2.2)$$

The generated peroxide may undergo a second 2-electron reduction step to form hydroxide (reaction 2.3):

$$HO_2^- + H_2O + 2\ e^- \rightarrow 3\ OH^- \qquad E^0 = +\ 0.878\ V\ (vs.\ SHE) \qquad (2.3)$$

Figure 2.4A presents an electrochemical map obtained at a working electrode potential of – 0.65 V (vs Ag/AgCl QRCE) for the area presented in Figure 2.4B. At this potential, the entire substrate surface is electrochemically active towards the ORR including regions that do not contain any silver. An electrochemical map of a bare glassy carbon substrate (control) was measured under the same conditions and is available in the Annex A (Figure A.4). To distinguish between regions that contained silver particles and regions that were free from silver particles, histograms for the ORR current measured at – 0.65 V (vs. Ag/AgCl QRCE) are presented for the carbon substrate (Figure 2.4B) and the carbon supported silver substrate (Figure 2.4C). The histogram for the carbon substrate shows one narrow distribution of current values centered around - 6.4 ± 0.4 pA due to the ORR via reaction 2 for measurements carried out at – 0.65 V (vs Ag/AgCl QRCE). For the carbon supported silver substrate, the histogram (Figure 2.4C) shows a distribution of current values, with most current values being centered around - 7.1 ± 0.5 pA. These current values closely match those obtained using the bare glassy carbon substrate and their high proportion on the carbon supported silver substrate are consistent with a low surface coverage of well-separated silver particles that were prepared through the electrodeposition approach used here. In addition to the response for the underlying carbon substrate, a distribution of current values up to – 42.0 pA were observed, which correspond to silver containing regions, with some areas containing individual silver particles that had current values between – 8.1 pA and – 13.6 pA. In order to isolate the contribution of the silver particles toward the overall current, first the geometric current density and the current density corrected for the electrochemical active surface area (ECSA) are obtained to demonstrate the role

of silver particle loading on the overall measured current. Subsequently, the partial current density for individual silver particles, which only requires their geometric area, is obtained as a function of particle size. By comparing these two different measurements of the current, it is observed that while the overall current density of the entire surface (carbon and silver) increases with increasing silver loading (or particle size) due to an electrocatalytic effect, the partial current density at individual silver particles decreases, which can be attributed to differences in the mass transport of oxygen to the silver particles as a function of their size .

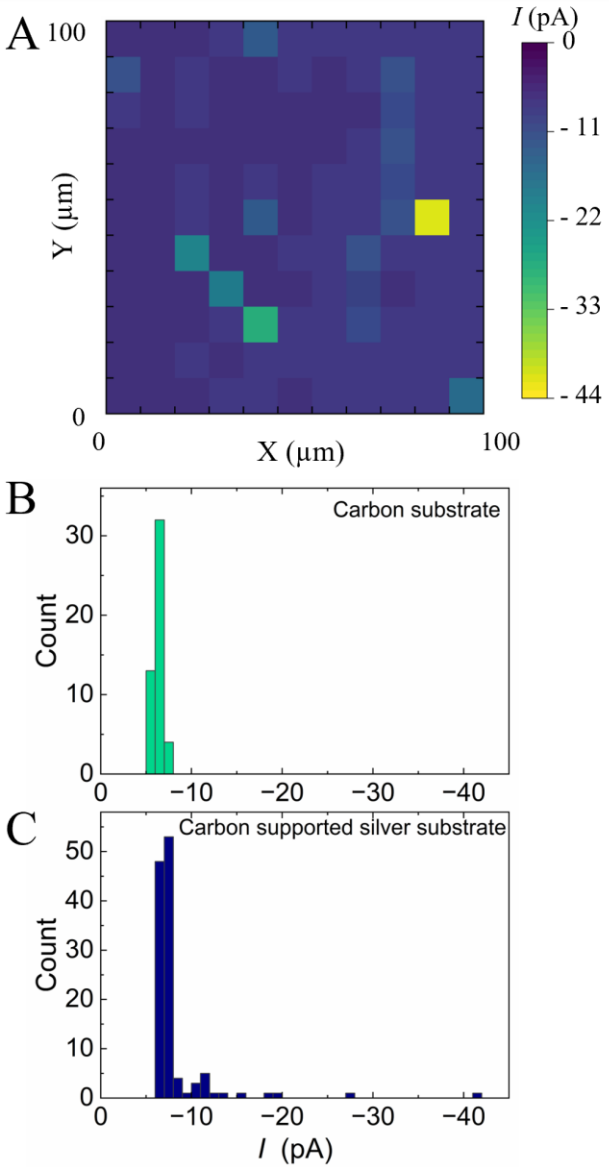

Figure 2.4 SECCM electrochemical map of ORR obtained at (A) -0.65 V (vs Ag/AgCl QRCE) across a carbon supported silver substrate. Histograms for (B) a bare carbon substrate and (C) the carbon supported silver substrate at - 0.65 V (vs Ag/AgCl QRCE) in an aqueous solution of 0.01 M KOH and 0.05 M KCl.

Figure 2.5 presents a magnified SEM image for the three distinct locations that were measured using SECCM: (i) a particle-free region containing only the underlying carbon substrate (Figure 2.5A), (ii) an individual silver particle (Figure 2.5B) and (iii) multiple silver particles (Figure 2.5C). Figure 2.5D presents the corresponding LSVs for each location with the left ordinate displaying the total current (I_T) and the right ordinate displaying the geometric current density (j_{geo}) that was calculated using the droplet diameter (a constant droplet diameter of 2 μm was used). A shift to a less negative (more positive) onset potential (defined by a current density of 0.1mA cm^{-2}) as well as a larger value of the overall current were observed with increasing silver loading (Figure 2.5D) As both the underlying carbon substrate and the silver particles are active towards the ORR in alkaline media, there are two contributing factors to the measured current: (i) the electrochemical surface area and/or (ii) an electrocatalytic effect from the silver particles. A knowledge of particle loading and the ECSA are required to assign a shift of onset potential to an electrocatalytic effect (Masa *et al.*, 2014; Voiry *et al.*, 2018). While a general methodology to measure the ECSA of an electrocatalyst surface is not available, a common approach is the use of the double layer capacitance measured in a region where no Faradaic processes are occurring (Lukaszewski *et al.*, 2016; Trasatti et Petrii, 1991). A limitation of this approach is that the number of sites determined using capacitance measurements may not be a true representation of the number of sites that are electrocatalytically active. This difficulty becomes more pronounced when measuring surfaces that contain more than one material with different values for their double layer capacitance. In addition, in the case of carbon supported particles in alkaline conditions, the electrocatalytic activity of the underlying substrate towards the ORR cannot always be ignored, especially under low loading conditions. Using a SECCM-SEM multi-microscopy approach it is possible to distinguish between the two different electrochemically active surfaces (carbon and silver). Due to the well-defined region outlined by the droplet where electrocatalytic measurements were carried out using SECCM, the surface area of the carbon support as well as the silver particles at each location could be determined from SEM images to define the ECSA of each material, with the surface area of

each silver particle being calculated assuming a hemispherical shape. For regions where only the underlying carbon support was measured, both j_{geo} and j_{ECSA} are the same, while for silver containing regions, the overall surface area is greater than the geometric area due to the presence of the silver particles leading to a decrease of the current density for j_{ECSA} compared with j_{geo}. In all cases, I_T, j_{geo}, and j_{ECSA} increase with silver loading, which can be unambiguously attributed to an electrocatalytic effect and not simply due to an increase in surface area.

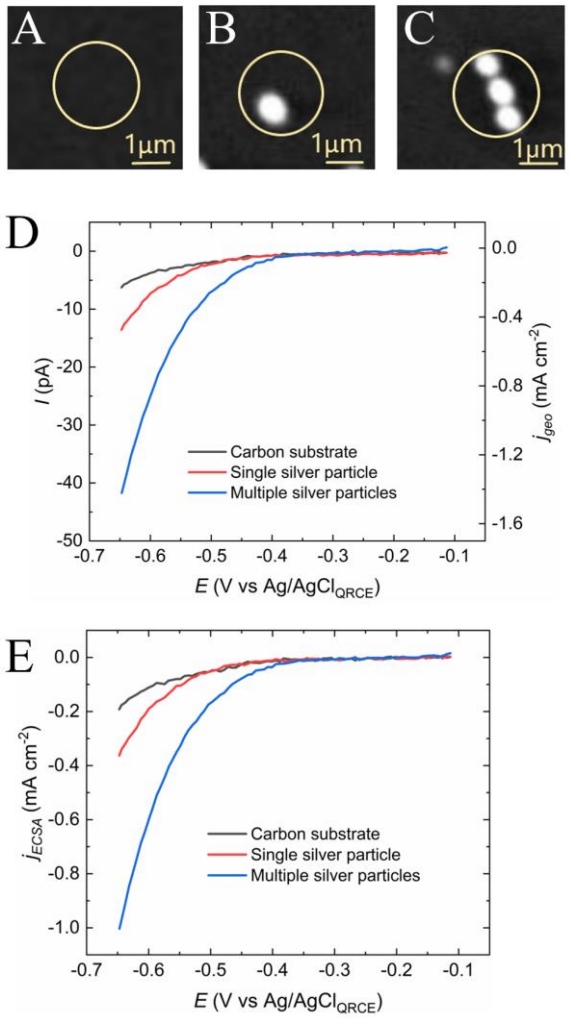

Figure 2.5 Scanning electron microscope image of (A) bare glassy carbon substrate, (B) a single Ag particle, and (C) multiple Ag particles. Corresponding linear sweep voltammograms (D) and (E). Measurements were made using an Ag/AgCl QRCE in an aqueous solution of 0.01 M KOH and 0.05 M KCl.

The total current, I_T, measured at a region containing an individual silver particle is made up of partial currents for the ORR from the carbon support (I_C) and the silver particle (I_{Ag}). As demonstrated above, I_T increases with increasing silver content due to an electrocatalytic effect. To quantify the ORR current for an individual silver particle, I_{Ag}, the fraction of the current from the carbon support, I_C, was subtracted from the total measured current, I_T. The value for the current from the carbon support was obtained from a region on the substrate free from silver particles. By isolating the current contribution from the individual silver particles and accounting for their surface area, it is possible to obtain a current density (j_{Ag}) for silver without the contribution of the carbon support. LSVs showing the partial current densities for the carbon substrate, j_C (black trace) and a silver single particle, j_{Ag} (red trace) are shown in Figure 2.6A. By separating the partial current densities of the two materials, the corresponding LSVs for the carbon and the single silver particle show much clearer potential dependent variations. The current density for the carbon substrate increases gradually with increasing overpotential whereas the current density on the single silver particle increases rapidly with increasing overpotential reflecting its higher rate of reaction for the ORR compared to carbon. Differences in the shape of the LSVs can also be attributed to the different mechanisms occurring for the ORR on these two different materials, where carbon promotes the two-electron reduction of oxygen to peroxide (reaction 2.2), while silver promotes the four-electron reduction to water (reaction 2.1). Figure 2.6B presents LSVs for particles with different radii which show a decrease in current density with increasing particle radius. This is opposite to the trend observed for $I_{Ag,}$ which increased with increasing particle radius due to an increase in silver loading (Figure A.5). The current density, j_{Ag}, depends on the flux of oxygen to the silver electrocatalyst particle surface, which increases with decreasing particle size due to an increase in oxygen mass transport. Thus, in the case of single entity measurements, where the pipet diameter is larger than the particle being interrogated, mass transport is further enhanced and increases with decreasing particle dimensions as observed here. Figure 2.6C presents the current density obtained at – 0.65 V (vs Ag/AgCl QRCE) as a function of the particle radius (closed circles). Additional data points from separate electrochemical maps (open circles) are also included. Further experimental details are available in the Annexe A (Figure A.6 and A.7). The current density is calculated assuming a hemispherical shape. In some cases, the particles are not perfectly spherical, and a minor (shorter length) and major axis (longer length) are defined to obtain an average radius. The error bars in Figure 2.6C represent the standard deviation of the current

density values calculated assuming the radius of the hemisphere is defined by either the minor axis or major axis for each particle. The right ordinate of Figure 2.6C presents the corresponding values for an apparent mass transport coefficient that were calculated using a modified expression (equation 2.4) for the radial diffusion of oxygen to a hemisphere, where D is the diffusion coefficient of oxygen (1.93×10^{-5} cm^2 s^{-1}) to a hemispherical silver particle of radius r:

$$m_0^* = 0.3D/r \tag{2.4}$$

When the pipet dimensions are equal in size to the area of the electrode surface being measured, the mass transport of reactants down the pipet barrel is quasi-radial and is determined by the pipet geometry, most notably the pipet diameter and half cone angle (Anderson, K. L. et Edwards, 2023; Snowden, M. E. *et al.*, 2012). Under these conditions, mass transport is about one tenth the value observed for an equivalent size inlaid disk microelectrode in bulk electrolyte (Snowden, M. E. *et al.*, 2012). On the other hand, in the case of the ORR, due to the three-phase boundary formed between the droplet, the electrode surface, and the surrounding air atmosphere, oxygen can also diffuse from the air to the electrode surface, increasing its mass transport to the substrate surface (Chen, C. H. *et al.*, 2014; Mariano, R. G. *et al.*, 2022; Ustarroz *et al.*, 2018). Chen *et al.* carried out numerical modeling for the ORR at a platinum electrode surface and found that the flux of oxygen at the air/droplet interface increased mass transport by a factor of three compared to the case when only considering oxygen mass transport down the pipet barrel (Chen, C. H. *et al.*, 2014). For these reasons, the apparent mass transport coefficient in equation 2.4 is reduced by a factor of 0.3 compared to radial diffusion to a hemispherical particle in bulk solution to take into consideration the flux of oxygen down the pipet barrel as well as at the air/electrolyte interface. The plotted trace (blue line) is not a fit to the experimental data and represents apparent mass transport coefficient values that were calculated using eq 2.4 to illustrate the relationship between the flux of oxygen, the current density and oxygen mass transport as a function of particle radius. The mass transport coefficient values for the particle sizes measured here are one to two orders of magnitude larger than what can be achieved using a rotating disk electrode and do not take into account the relationship between the pipet diameter and particle size, which could further affect mass transport as a function of particle size. A more complete description of the mass transport of oxygen as function of particle size and pipet diameter using numerical techniques such as finite element modelling (Anderson, K. L. et Edwards, 2023; Chen, C. H. *et al.*, 2014; Choi *et al.*, 2020) combined

with an appropriate kinetic model, should make it possible to establish a relationship for the current density as a function of particle size under high rates of mass transport of oxygen to enable quantitative analysis through a Koutecky-Levich type relationship of key parameters such as the heterogeneous rate constant, k^0, the number of electrons transferred, n, and the transfer coefficient, α, at the single particle level (Kim, J. et Bard, 2016a).

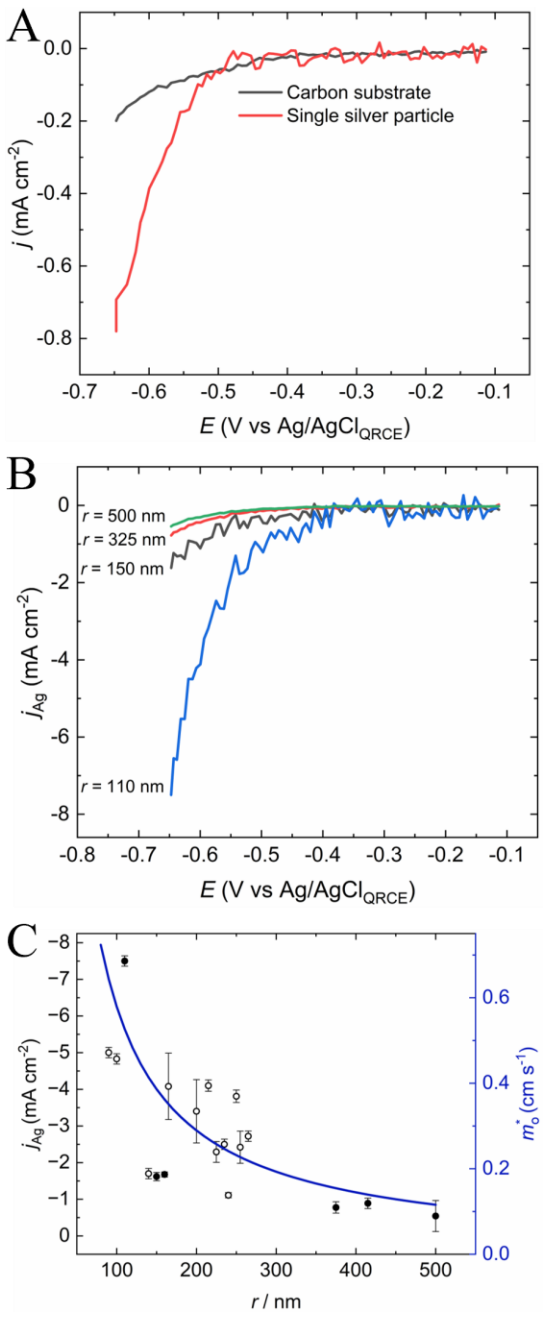

Figure 2.6 (A) LSV of a single Ag particle following background correction and the bare glassy carbon substrate. (B) LSVs of individual silver particles of varying radii following background correction. (C) Current density (left ordinate) and calculated apparent mass transport coefficient values (right ordinate) as a function of the silver particle radius at - 0.65 V (vs Ag/AgCl QRCE).

2.6 Conclusion

In conclusion, electrodeposition was used to prepare well-separated particles of varying sizes (100 nm – 500 nm radius) for single particle studies using SECCM. Electrodeposition can be used to prepare a range of materials (alloys, oxides, faceted particles, etc.) that are free from surface ligands that are often used during solution phase synthesis of nanomaterials. As shown here, when electrodeposition is combined with a SEM-SECCM multi-microscopy approach, it is possible to carry out single entity electrochemical measurements to access a range of particle sizes across a single substrate surface. It was shown that the partial current for silver, I_{Ag}, increased with an increase in silver loading (or particle size), whereas the current density, j_{Ag}, decreased with increasing particle size due to changes in the mass transport of oxygen to the individual electrocatalyst particle, which are important factors to consider when comparing the electrocatalytic of single entities of varying sizes using SECCM. In the future, hybrid probes (Nadappuram *et al.*, 2015) such as those recently demonstrated by Ryu *et al.* (Ryu, C. H. et Ren, H., 2024) could be used to quantify the amount of peroxide generated during the ORR, which can provide further insight into the effects of mass transport on reaction mechanisms at the single particle level. Taken together with the three-phase boundary formed using SECCM, measurements can be carried out at high rates of mass transport, even exceeding those of a gas diffusion electrode (Mariano, R. G. *et al.*, 2022), making the approach a natural bridge between rotating disk (or ring-disk) electrode and membrane electrode assembly measurements (Lazaridis *et al.*, 2022).

CHAPTER 3

Single-Particle Electrocatalysis and Kinetic Insights with Scanning Electrochemical Cell Microscopy (SECCM)

3.1 Résumé

Dans cette étude, la microscopie électrochimique à cellule de balayage (SECCM), combinée à la microscopie électronique à balayage (SEM), a été utilisée pour effectuer une analyse cinétique détaillée de la réaction d'évolution de l'hydrogène (HER) et de la réduction de l'oxygène (ORR) sur des particules individuelles de platine de différentes tailles. La cinétique des réactions a été systématiquement évaluée sur des particules individuelles dont les rayons varient de 90 nm à 500 nm. La variation des conditions de transport de masse a permis d'examiner leur effet sur les performances électrochimiques. Les paramètres cinétiques, incluant la constante de vitesse apparente (k^0_{app}) et la densité de courant d'échange apparente ($j_{0(app)}$), ont été extraits pour quantifier l'activité électrocatalytique.

Les résultats montrent également que les plus petites particules de platine présentent un décalage du potentiel à mi-onde ($E_{1/2}$) vers des potentiels plus négatifs pour l'ORR, ce qui suggère des limitations cinétiques accrues malgré un transport de masse amélioré. Une tendance dépendante de la taille a été observée pour la cinétique de la HER, les plus petites particules présentant des densités de courant d'échange apparentes plus élevées et des surtensions plus faibles. Cette amélioration est attribuée à des conditions de transport de masse optimisées autour des petites particules, ce qui réduit les limitations de diffusion et permet ainsi une évaluation plus précise de la cinétique intrinsèque.

Il est démontré que les paramètres cinétiques des particules individuelles peuvent être obtenus de manière quantitative grâce à une analyse directe et rigoureuse par SECCM. Cette étude établit une base pour des mesures cinétiques détaillées à l'échelle de la particule unique, faisant progresser l'utilisation de la SECCM comme outil analytique en électrochimie.

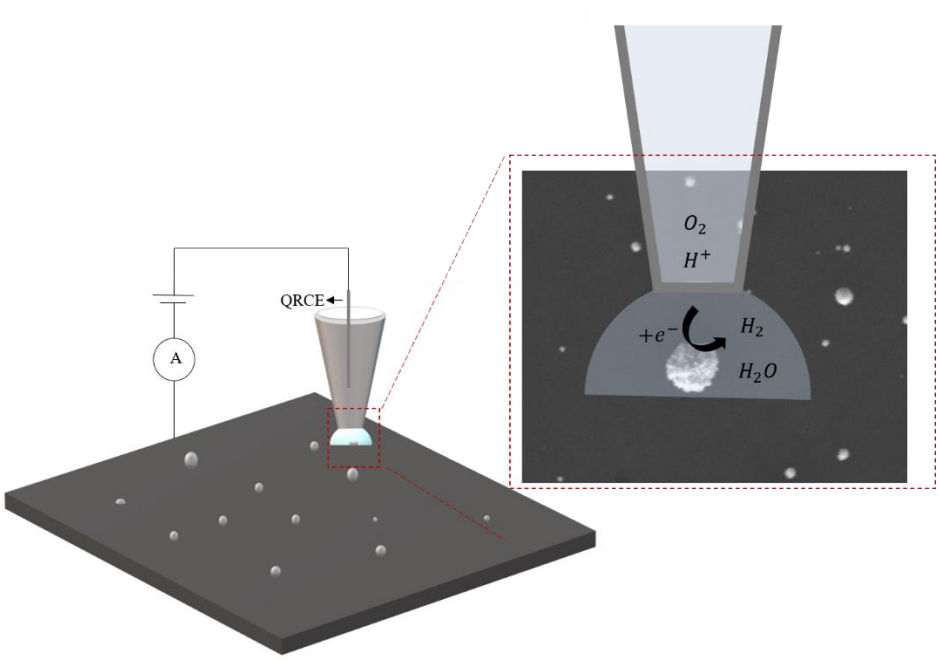

Figure 3.1 Graphical abstract illustrating the probing of individual Pt particles in the presence of protons and oxygen to measure both the hydrogen evolution reaction (HER) and oxygen reduction reaction (ORR).

The supplementary information can be found in **ANNEXE B**

3.2 Authors Contribution

Samaneh Salek

First author conducted the experimental measurements, processed and interpreted the results, created the figures, carried out the literature review, and wrote the first draft of the manuscript and made corrections.

Joshua Byers

Co-author supervised the study, contributed to result interpretation, participated in discussions, and reviewed the manuscript.

3.3 ABSTRACT

In this study, Scanning Electrochemical Cell Microscopy (SECCM) is combined with Scanning Electron Microscopy (SEM) in order to provide a detailed kinetic analysis of the Hydrogen Evolution Reaction (HER) and Oxygen Reduction Reaction (ORR) on individual platinum particles of different sizes. The kinetic of the reaction were systematically evaluated at individual particles different in radii from 90 nm to 500 nm. Variation in mass transport conditions, enabling investigation of their effect on electrochemical performance. The kinetic parameters including the apparent standard rate constant (k^0_{app}) and apparent exchange current density ($j_{0(app)}$) extracted to quantify the electrocatalytic activity. The results also indicate that smaller Pt particles exhibit a shift in half-wave potential ($E_{1/2}$) to more negative potentials for ORR, suggesting increased kinetic limitations despite enhanced mass transport effects. A size-dependent trend in HER kinetics was observed, with smaller particles showing higher apparent exchange current densities and lower overpotentials. This enhancement is attributed to improved mass transport conditions at smaller particles, which reduce mass transport limitations, thereby allowing the intrinsic kinetics to be more accurately measured. It is demonstrated that kinetic parameters for individual particles can be obtained quantitatively through a straightforward quantitative analysis using Scanning Electrochemical Cell Microscopy (SECCM). This study establishes a basis for detailed quantitative measurements, enabling the extraction of kinetic information at the single-particle level, further advancing the use of SECCM for electrochemical analysis.

3.4 Introduction

Electrocatalysis is fundamental to electrochemical energy conversion and storage technologies, such as fuel cells, metal-air batteries, and electrolyzers. (Stamenkovic *et al.*, 2017; Wang, Y. *et al.*, 2022) These technologies are crucial for the transition to a sustainable and hydrogen-based economy. While extensive research has been conducted to understand electrocatalyst performance under various conditions, further advancements require a detailed investigation of nanoscale interactions between catalysts and electrolytes (Jiao *et al.*, 2015; Seh *et al.*, 2017).

The hydrogen evolution reaction (HER) is a critical process in water electrolysis, involving a two-electron transfer mechanism (Gasteiger et Marković, 2009).

$$2H^+ + 2e^- \rightarrow H_2 \qquad E^0 = 0 \text{ V vs RHE} \qquad (3.1)$$

Conversely, the oxygen reduction reaction (ORR) serves as the cathodic process in low-temperature fuel cells and metal-air batteries, converting hydrogen fuel into electrical energy. However, ORR kinetics are inherently sluggish, even on platinum (Pt) catalysts, leading to significant overpotentials that reduce overall system efficiency (Siahrostami *et al.*, 2013). Yet, among various electrocatalysts, Pt exhibits the highest intrinsic activity for oxygen reduction reaction via a four-electron pathway, making it a widely studied material for energy conversion applications. Platinum has long been regarded as the benchmark catalyst for HER and ORR due to its exceptional electrocatalytic activity. In acidic environments, Pt enables HER with negligible overpotential, while for ORR, it remains the most active catalyst due to its stability under oxidizing and acidic conditions (Debe, 2012). Pt has been extensively employed in commercial fuel cells, typically in the form of nanoparticles supported on conductive carbon black (Debe, 2012; Gewirth et Thorum, 2010; Zhao *et al.*, 2022). However, to fully understand platinum intrinsic catalytic activity, single-particle studies are required to isolate fundamental electrochemical properties from ensemble averaged effects. Nanoparticle based catalysts exhibit significant heterogeneity in terms of size, shape, and surface structure (Benck *et al.*, 2014; Kamat *et al.*, 2022; Trindell *et al.*, 2020). This variability complicates the determination of intrinsic catalytic activity, as conventional bulk electrochemical techniques provide only an averaged response that masks individual particle behavior (Clarke *et al.*, 2024). To overcome this limitation, fundamental studies must focus on individual particles to eliminate the influence of neighboring interactions. Establishing a direct correlation between nanoparticle properties and catalytic activity is essential for designing high-performance electrocatalysts (Baker, 2018; Mayrhofer *et al.*, 2005).

Single-entity electrochemistry (SEE) has emerged as a powerful approach for investigating individual electroactive particles and linking their intrinsic properties to ensemble behavior. Recent advances in nanoscale electrochemistry have led to the development of scanning electrochemical probe microscopy techniques, which enable localized electrochemical measurements and eliminate ensemble averaging effects (Kim, J. *et al.*, 2016; Quast, Thomas *et al.*, 2021). One such technique, scanning electrochemical cell microscopy (SECCM), is particularly effective for probing electrochemical fluxes at the nanoscale. SECCM utilizes a nanopipet filled with electrolyte and

containing a quasi-reference counter electrode (QRCE). When the pipet tip makes contact with an electrode surface, a confined electrochemical cell is formed via a small electrolyte droplet, allowing for localized electrochemical activity measurements (Daviddi *et al.*, 2019). SECCM has been successfully applied to study various functional material (Unwin *et al.*, 2016; Yu *et al.*, 2022) including battery materials (Tao *et al.*, 2019), and (photo)electrocatalytic systems (Bentley, Cameron L., 2022; Beugré *et al.*, 2019; Gao *et al.*, 2020; Li, Mingyang *et al.*, 2022; Lu, Xiaoxi *et al.*, 2021; Makarova *et al.*, 2022; Tetteh, Emmanuel Batsa *et al.*, 2023; Wang, Y. *et al.*, 2020; Wang, Yufei *et al.*, 2022).

By focusing on single particles, SECCM provides critical insights into the relationship between individual particle properties and overall catalytic performance (Bentley, Cameron L., 2022; Choi *et al.*, 2020; Lu, Xiaoxi *et al.*, 2021; Roehrich et Sepunaru, 2024; VarhadeTetteh*, et al.*, 2023; Wahab *et al.*, 2020). In this study, we utilize Scanning Electrochemical Cell Microscopy (SECCM) in combination with Scanning Electron Microscopy (SEM) to conduct a comprehensive quantitative kinetic analysis of the Hydrogen Evolution Reaction (HER) and Oxygen Reduction Reaction (ORR) on individual platinum particles of varying sizes. Variations in particle size led to differences in mass transport conditions, enabling the extraction of kinetic parameters providing new insights into the quantitative application of SECCM for single particle electroanalysis. The ability to assess individual particles, rather than relying on ensemble-averaged measurements, advances our understanding of the intrinsic catalytic properties of Pt and highlights the role of mass transport in electrocatalytic reactions.

3.5 Results and discussion

Electrodeposition is a widely used and effective method for synthesizing platinum electrocatalysts, as it facilitates the direct growth of Pt particles on a conductive substrate, ensuring strong electrical contact and efficient charge transfer. However, in studies where particle size consistency is essential achieving a uniform size distribution remains a significant challenge (Chen, S. et Kucernak, 2003; Ornelas et al., 2019). To facilitate the individual analysis of each Pt particle, a glassy carbon substrate was modified with well-spaced Pt particles through electrodeposition aligned with previous studies (Salek et Byers, 2024), ensures adequate interparticle spacing and

allows for precise single-entity electrochemical analysis using scanning electrochemical cell microscopy (SECCM).

In this method, a low current density was used to electrodeposit Pt particles onto a glassy carbon substrate in a bulk three-electrode electrochemical cell. This approach limits the available sites for particle growth, resulting in ligand-free, well-dispersed individual particles of varying sizes. The as-prepared particles were characterized using scanning electron microscopy (SEM), energy dispersive X-ray spectroscopy (EDX), and X-ray diffraction (XRD). Characterization analysis confirmed the presence of spherical particles with sizes ranging from 70 nm to 700 nm, exhibiting a broad size distribution. (See section B.1 in Annexe B)

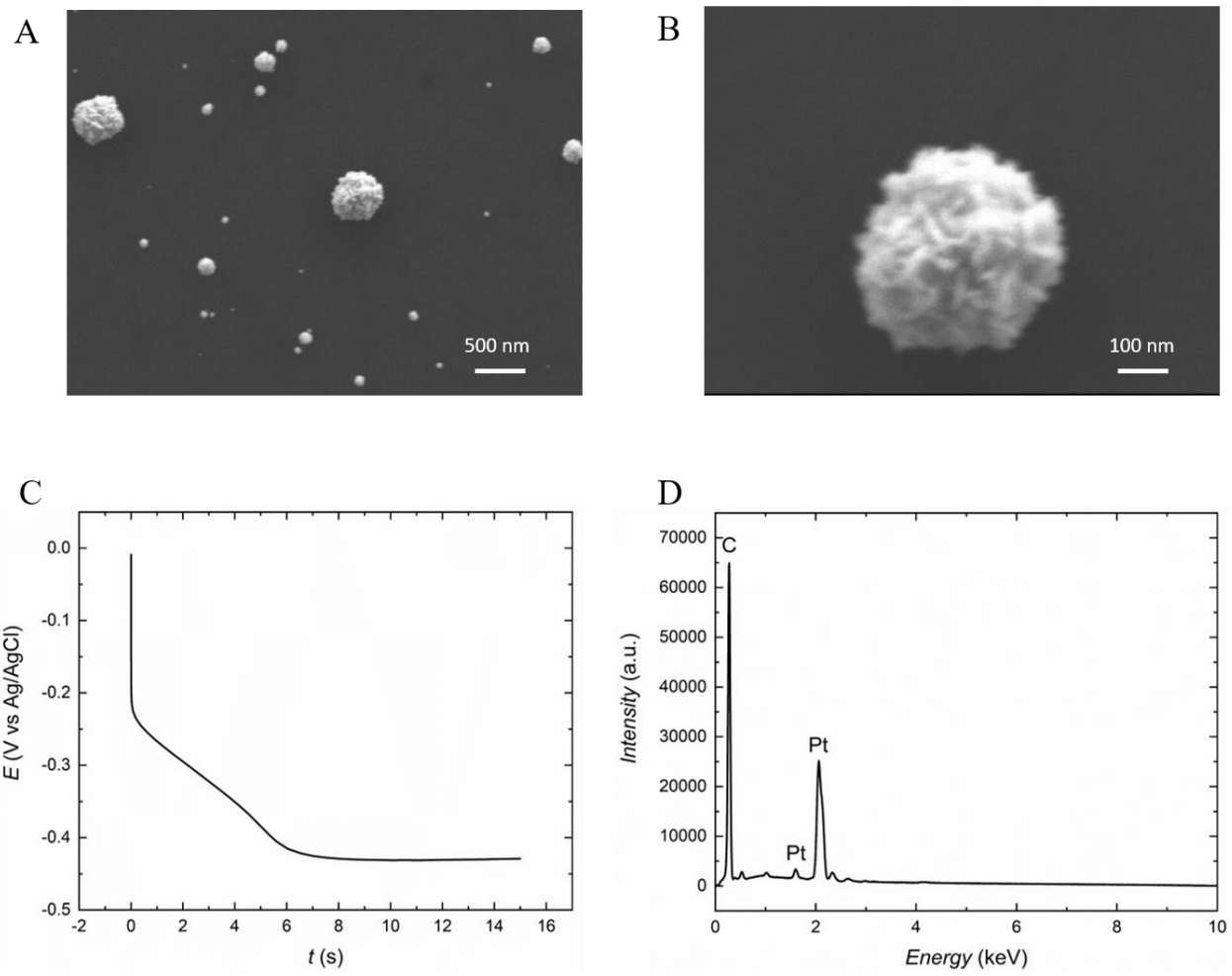

Figure 3.2 (A) Scanning electron microscope image of platinum particles electrodeposited on glassy carbon substrate varying in size from 70 nm to 700 nm. (B) Magnified electron micrograph of an individual particle that shows the morphology of the electrodeposited particles. (C) Potential-time graph for the galvanostatic electrodeposition of platinum on a glassy carbon substrate at a constant current density of – 1 mA cm^{-2} in a 5 mM K_2PtCl_6 and 100 mM HCl electrolyte using an Ag/AgCl (3M KCl) reference electrode. (D) Energy dispersive X-ray spectroscopy measurement of a platinum particle electrodeposited on glassy carbon substrate.

SECCM was performed on a glassy carbon substrate modified with Pt particles to conduct kinetic analysis for the ORR and HER at the level of individual Pt particles. The SECCM electrocatalytic activity map for ORR is shown in Figure 3.3B. A single-barrel pipet with a tip opening radius of approximately 2 μm (Figure B.3) was filled with 100 mM H_2SO_4 to probe the glassy carbon modified with Pt particle sample, while a Pd/H_2 wire (which has 50 mV shift in potential versus RHE (Chen, C.-H. *et al.*, 2014)) inserted into the pipet as a quasi-reference counter electrode (QRCE). During the measurements, a piezoelectric precisely controlled the pipet along the z-axis, allowing it to approach the substrate. Upon contact between the electrolyte droplet at the pipet tip and the substrate, a micrometer-scale electrochemical cell was formed, enabling linear sweep voltammetry (LSV) measurements to be conducted from -0.15 V to 0.55 V vs RHE at a scan rate of 20 mV/s. To further map the electrochemical activity across the glassy carbon substrate, which contains individual Pt particles, a hopping mode was used to measure a 100 μm x 100 μm area with an 8.25 μm spacing between measurement points, resulting in a total of 169 measured points. The footprint of the droplet corresponds to an area approximately matching the diameter of the pipet tip, which is around 2 μm.

A detailed comparison between SECCM maps and SEM images allows for the correlation of current responses with the diameters of the individual particles. In this study, only the areas containing single particles are considered. The ORR performance of individual Pt particles revealed that at 0.08 V vs RHE, higher ORR activity is observed in regions containing one or more Pt particles (Figure 3.3B), while no current signal is detected in areas where only the glassy carbon substrate is present.

At 0.08 V vs RHE, the current response becomes mass transport limited for oxygen reduction reaction (Figure 3.3C). Larger Pt particles generate higher current responses. For example, Pt particle with 500 nm radius producing a current of -12 pA at 0.08 V vs RHE, compared to the smallest particle in the study (90 nm in radius) which yields a current of -820 fA at same potential. This potential is chosen for several reasons as it allows easy differentiation of electrocatalytic activity toward ORR in particles of varying sizes, and at this potential, the linear sweep voltammogram is mass-transport limited, resulting in a diffusion-limited current for ORR (Figure 3.3C). Additionally, at this potential, the glassy carbon substrate does not contribute to the ORR current response (Figure B.5). Previous studies have shown that while larger particles generate higher overall currents due to enhanced electrocatalytic activity, the current density per particle decreases as the particle size increases, and this reduction is likely attributed to variations in oxygen mass transport to the particles, which depend on their size (figure 3.3D) (Salek et Byers, 2024). Figure 3.3C displays steady-state linear sweep voltammograms (LSVs) recorded for Pt particles of varying radii. For larger particles, the diffusion-limited current of ORR is more clearly defined. However, for smaller particles, particularly those with radii below 200 nm, with higher mass transport rate, the LSVs exhibit extended voltammograms due to increased irreversibility of the ORR. In the case of smaller particles, the rapid replacement of oxygen at the surface effectively balances its consumption, thereby mitigating diffusion limitations at more negative potentials. Consequently, a higher overpotential is required to reach the point where mass transport becomes the rate-determining step (Chen, Shengli et Kucernak, Anthony, 2004a).

The mass transport-limited current can be used to determine the mass transfer coefficient (m) for oxygen reduction based on the following equation:(Compton et Banks, 2011)

$$I_{lim} = nAFmC_{O_2} \tag{3.2}$$

Where n is the number of electrons, A is the surface area of the electrode (area of the hemisphere Pt particle), F is Faraday constant, m is mass transfer coefficient, and C_{O_2} is the bulk concentration of oxygen in 0.1 M H_2SO_4, which is ~0.27 mM. Since the diffusion-limited current I_{lim} is directly proportional to the electroactive surface area (A), the measured I_{lim} values were used as a reliable proxy for determining particle radii. This electrochemical estimation provided higher precision

than only SEM-based measurements (Figure B.6). Figure 3.4A presents the calculated mass transfer coefficients for platinum particles of varying radii, illustrating how particle size influences the efficiency of oxygen transport to the catalytic surface. As the radius decreases, the mass transfer coefficient increases, consistent with the enhanced mass transport associated with smaller hemispherical geometries. This trend supports previous findings (Salek et Byers, 2024).

To further evaluate the mass transport behavior using micropipet to individual hemispherical particles, the mass transfer coefficient (m) obtained via scanning electrochemical cell microscopy (SECCM) using micropipet were compared with those predicted by the analytical expression for a hemispherical microelectrode, where the mass transfer coefficient scales as D/r with r being the particle radius and D is diffusion coefficient of oxygen in 0.1M sulfuric acid (1.8×10^{-5} cm^2/s). Across a range of particle sizes form 90 nm to 500 nm in radius, the experimental values from SECCM showed a consistent deviation of approximately $2.4 \pm 0.1\%$ from the theoretical mass transport predicted for hemispherical microelectrodes. This deviation can be attributed to several limiting factors inherent in the SECCM configuration. One key factor is the pipet half angle (13° in this work), which alters the diffusion geometry from ideal radial diffusion to quasi-radial or mixed-mode diffusion. Additionally, the ratio of the particle diameter to the pipet diameter plays a critical role; when this ratio increases, the diffusion field approaches to radial symmetry, resulting in enhanced mass transport. This trend is consistent with observations using a constant pipet diameter across different particle sizes, where smaller particles exhibit relatively higher mass transfer coefficients (Anderson, K. L. et Edwards, 2023; Snowden, Michael E. *et al.*, 2012).

Since above mentioned, the LSVs for smaller particles stretched out to reach limiting current, the half-wave potential ($E_{1/2}$) for smaller particles shift to less positive potential (Figure 3.4B). $E_{1/2}$ confirms an increasing irreversibility of the ORR on smaller particles due to higher mass transport of the oxygen. However, for the range of particle diameters studied in this work, all voltammograms still reach to a steady state condition.

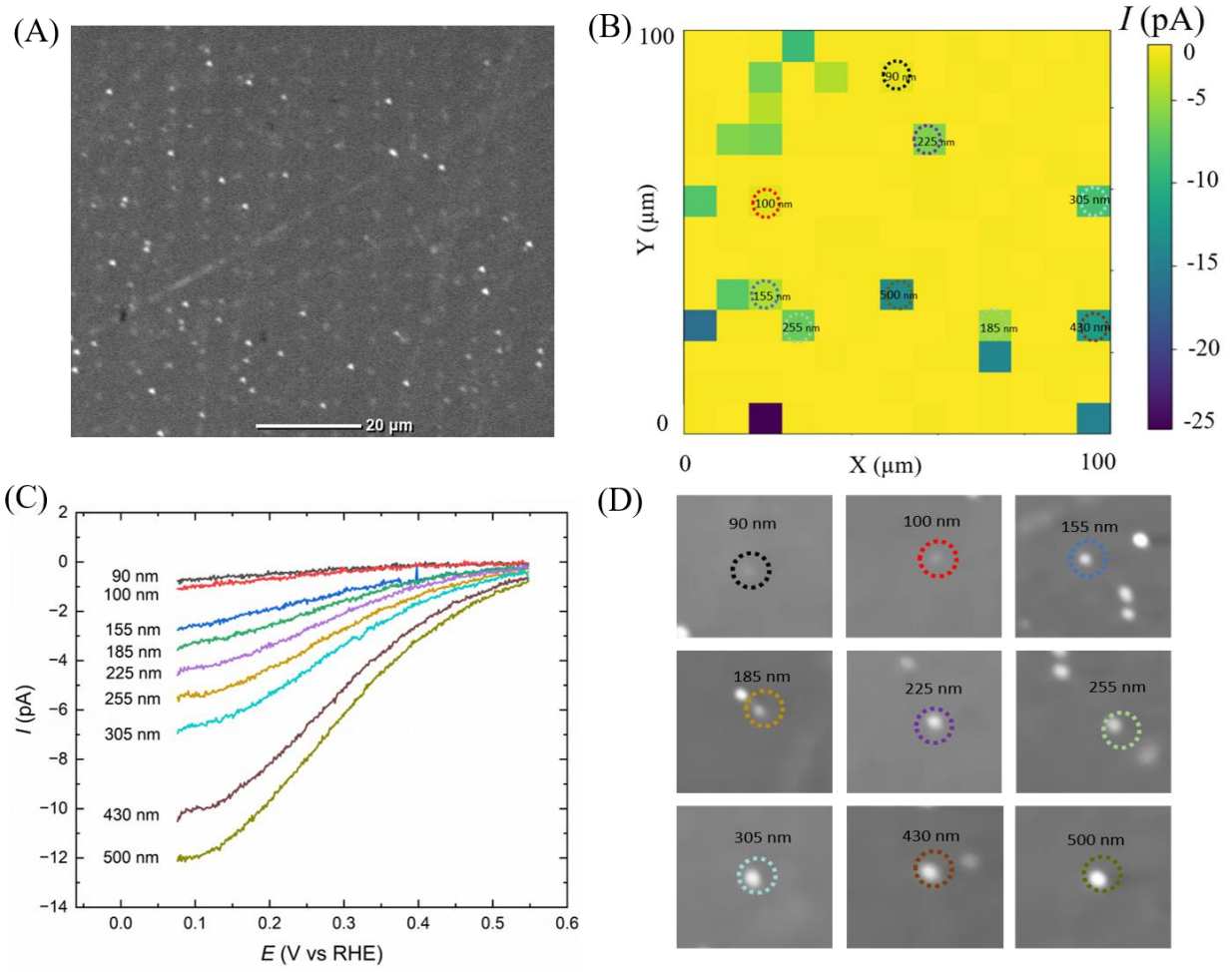

Figure 3.3 (A) Scanning electron microscope image of region where electrochemical mapping was carried out using SECCM. (B) SECCM electrochemical map of ORR obtained at 0.08 V vs RHE across a carbon supported platinum substrate. The studied single particles are indicated with their radius size. (C) SECCM LSVs for ORR on single Pt particles indicated by dashed circles in D in 100 mM H_2SO_4 and using Pd/H_2 as QRCE (D) Scanning electron microscope image of studied single Pt particles.

Unlike the observation of higher mass transport of oxygen through the ORR on the electrocatalytic surfaces using SECCM resulting from the three phase boundary (Chen, C.-H. *et al.*, 2014; Mariano, Ruperto G. *et al.*, 2022), this effect is not observed in the present study on individual particles, as the SECCM pipet, with a diameter of approximately 2 µm, is significantly larger than even the largest particle, which has a maximum diameter of about 1 µm. As a result, the diffusion length between the catalytic surface of platinum and the oxygen in the air increases. In other words, the

oxygen in the air must reach the electrode surface, but its transport is not sufficiently rapid to improve the overall oxygen mass transfer to the particle (Ryu *et al.*, 2024). Note that the three-phase boundary in present SECCM configuration includes the glassy carbon surface as the solid phase which is totally inactive in the studied potential range for ORR (0.5- 0.0 V vs Pd/H_2).

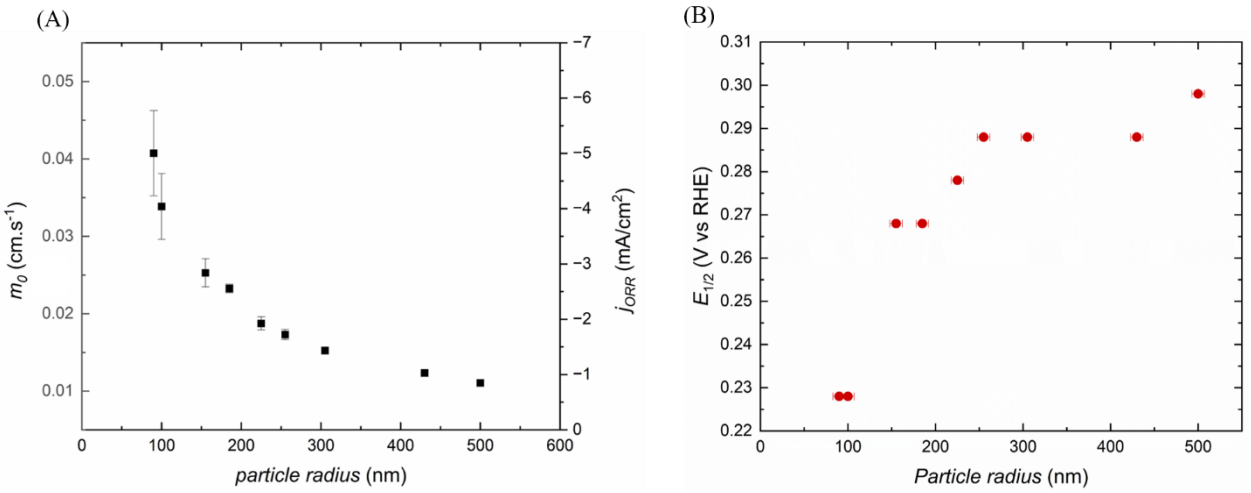

Figure 3.4 (A) Mass transfer coefficient (m) and SECCM current density at the potential of mass transport limited current (0.08 vs RHE) as a function of platinum particles. (B) Half-wave potential ($E_{1/2}$) extracted from steady-state SECCM voltammograms of the oxygen reduction reaction (ORR) on single Pt particles in 0.1 M H_2SO_4.

To analyze the kinetics of the oxygen reduction reaction on individual Pt particles, two approaches were applied. The first approach used the Koutecky-Levich method, which is conventionally used in rotating disk electrode (RDE) experiments, while the second method focused on analyzing the half-wave potential.

For the four-electron reduction of oxygen to water in acidic media, we have (Lebègue, 2023):

$$O_2 + 4H^+ + 4e^- \rightarrow 2H_2O \qquad E^0 = 1.229 \text{ vs RHE} \qquad (3.3)$$

The steady-state current response of this reaction is controlled by the rate of mass transfer of oxygen from the bulk solution to the surface of Pt particle and the rate of electron transfer from Pt particle to oxygen. Thus, for this irreversible reaction it can be written (Kim, J. et Bard, 2016a):

$$\frac{1}{j} = \frac{1}{j_{mt}} + \frac{1}{j_{et}} \tag{3.4}$$

For mass transport limited current we have:

$$j_{mt} = nFmC_{O_2}^{bulk} \tag{3.5}$$

Where n is electron transfer number, F is Faraday constant, and $C_{O_2}^{bulk}$ the bulk concentration of oxygen.

Butler-Volmer model can define electron transfer current by (Kim, J. et Bard, 2016a; Lebègue, 2023):

$$j_{et} = nFkC_{O_2} \tag{3.6}$$

$$k = k^0 e^{-\alpha \frac{nF}{RT}(E-E^0)} \tag{3.7}$$

where k is the forward reaction rates of oxygen reduction to water and k^0 is the heterogeneous standard rate constant, α is the transfer coefficient, and E^0 is the standard reduction potential.

Assuming for the steady-state current at the surface of the Pt particle, and $C_{O_2} = C_{O_2}^{bulk}$, the electron transfer current is given by:

$$j_{et} = nFk^0 C_{O_2}^{bulk} e^{-\alpha \frac{nF}{RT}(E-E^0)} \tag{3.8}$$

Replacing j_{mt} and j_{et} in equation (3.4) results in:

$$\frac{1}{j} = \frac{1}{nFmC_{O_2}^{bulk}} + \frac{e^{\alpha \frac{nF}{RT}(E-E^0)}}{nFk^0 C_{O_2}^{bulk}} \tag{3.9}$$

Varying particles size leads to different mass transfer coefficient (m), thus using the equation (3.9), it is possible to analyze the kinetics of the electron transfer reaction using the obtained LSVs of Pt particles that are different in size. From these voltammograms, plots of $\frac{1}{j}$ versus $\frac{1}{mC_{O_2}^{bulk}}$ can be constructed at various overpotentials. Figure 3.5 shows these plots with a slope of ~ $\frac{1}{4F}$. By extrapolating to $\frac{1}{mC_{O_2}^{bulk}}$ equal to zero, the y-intercept, given by $\frac{e^{\alpha\frac{nF}{RT}(E-E^0)}}{nFk^0C_{O_2}^{bulk}}$, allowing the determination of the kinetic parameters for the electron transfer reaction and find out the k_{app}^0 value of the oxygen reduction reaction on individual Pt particle in 0.1M H_2SO_4 which is equal to 1.62 x 10^{-5} $\pm$0.1 cm.s^{-1}. It is also possible to calculate the transfer coefficient α, from the plot of intercepts at different overpotential (Figure B.8) that gives the value of 0.3 which is in close agreement to the value already reported for the ORR on individual Pt particles (Chen, Shengli et Kucernak, Anthony, 2004a). The advantage of this method lies in its ability to eliminate the influence of mass transport (Kim, J. et Bard, 2016b). It should be mentioned that for the Koutecky-Levich analysis the two particles with the smallest radius (90 nm and 100 nm) were excluded due to demonstrating different behaviour compering to the rest of the particles.

A key point to consider is that Tafel analysis is less versatile than the Koutecký–Levich method due to the very low oxygen concentration in this SECCM configuration under atmospheric conditions. Although under specific conditions, kinetic details such as the rate-determining step, can be derived from the Tafel slope value. To obtain accurate kinetic information, the Tafel slope should ideally be measured under high reactant concentrations, which can provide deeper insights into the fundamental kinetics. Oxygen has a very low solubility in water under standard conditions (0.27 mM in 0.1M acid sulfuric droplet at the end of the pipet tip which is exposed to air), which significantly restricts its interaction with the Pt particle surface. The negative applied potential and the high acidity of the solution can enhance the reaction rate, however, the availability of O_2 to the Pt surface still remains limited due to its low solubility and weaker interaction with Pt surface (van der Heijden *et al.*, 2024; Wang, Shiyi *et al.*, 2021)

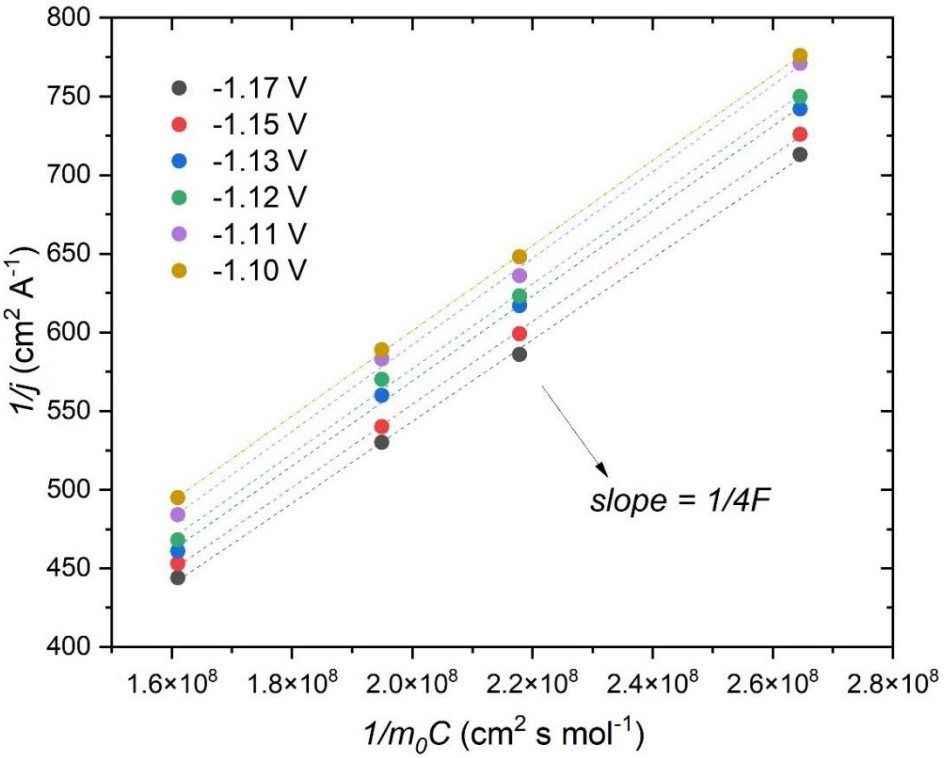

Figure 3.5 Plots of $1/j$ vs $1/mC$ at various overpotentials from SECCM LSVs for ORR on individual platinum particles varying in radii from 155 nm to 500 nm in 100 mM H_2SO_4 as the electrolyte. A slope of all lines is constantly $1/4F$ in the range of -1.06 to -1.12 V for $E - E^0$.

As the standard rate constant (k^o) decreases, larger overpotentials are required to drive the reaction, leading to a noticeable shift of the voltammetric wave toward more negative potentials (Figure 3.4B). This behavior is characteristic of kinetically sluggish systems. Therefore, kinetic limitations contribute to the broadening of the wave, as illustrated in Figure 3.2C. This shift reflects the activation energy needed for the reaction to proceed. Therefore, analyzing the half wave potential can provide a good estimation for the kinetic of the reaction. At the half-wave potential ($E_{1/2}$), the current reaches half of the maximum value observed under mass transport-limited conditions ($j = 0.5\ j_{mt}$ in equation 3.4) that results in correlation of kinetic at the half-wave potential to the mass transfer of the reactant, so rearranging Butler-Volmer equation at $E_{1/2}$ where $k_{1/2}$ is equal to m yields to (Lebègue, 2023; Oldham et Zoski, 1988):

$$E_{1/2} - E^0 = \frac{RT}{\alpha F} \ln\left(\frac{k^0_{app}}{m}\right) \quad (3.10)$$

The obtained apparent rate constant values for ORR on individual Pt particles using half-wave potential can be find in Table 3.1.

Table 3.1 Values of the Standard Rate Constant (k^0_{app}) and mass transfer coefficient (m) obtained from the SECCM LSVs of the Oxygen Reduction Reaction in 0.1 M H_2SO_4 on individual Pt Particles of Different Sizes.

Pt Particle Radius (nm)	**Rate constant, k^0_{app} (from half wave) (cms^{-1})**	**Mass transfer coefficient, m (cms^{-1})**
90	2.10×10^{-5}	4.91×10^{-2}
100	1.90×10^{-5}	4.30×10^{-2}
155	1.27×10^{-5}	2.82×10^{-2}
185	1.07×10^{-5}	2.36×10^{-2}
225	8.90×10^{-6}	1.92×10^{-2}
255	7.90×10^{-6}	1.72×10^{-2}
305	6.60×10^{-6}	1.43×10^{-2}
430	4.70×10^{-6}	1.03×10^{-2}
500	4.08×10^{-6}	0.86×10^{-2}

When the potential is more negative than 0.08 V vs RHE, the hydrogen evolution reaction (HER) becomes increasingly dominant. As the particle size increases, the onset potential for HER shifts slightly toward more negative values. This trend is supported by the overpotential values at a current density of -10 mA/cm², as presented in Table 3.2. Similar to what was observed for ORR, the current response increases with particle size. However, compared to the difference in mass transport-limited current for ORR, the variation in current for particles larger than 100 nm in radius is less pronounced. For example, the current at -0.15 V vs RHE for particles with radii of 430 nm and 500 nm is identical at 510 pA (Figure 3.6), confirming the reduced influence of mass transport on HER. The electrochemical activity map for HER at -0.15 V vs RHE is shown in Annexe B, Figure B.9.

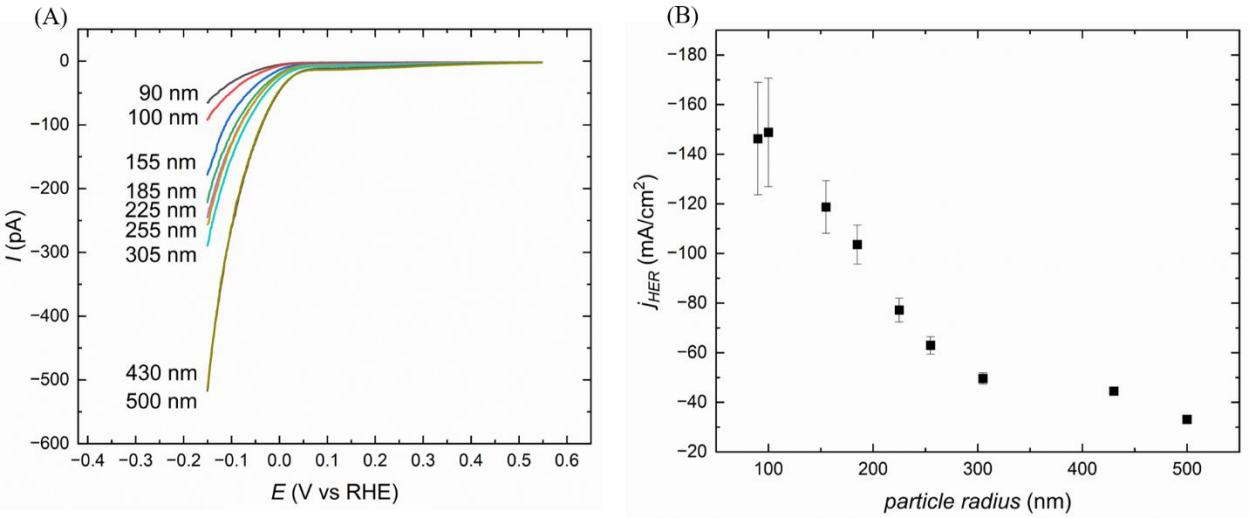

Figure 3.6 (A) SECCM LSVs for HER on single Pt particles in 100 mM H_2SO_4 and using Pd/H_2 as QRCE, the radius of pipet is around 1 µm. (B) SECCM current density at -0.15 V vs RHE as a function of platinum particles.

A distinct trend is observed in how the current density response varies with particle size in HER. The variation in ORR response versus HER can be attributed to differences in the mass transport of H^+ and O_2 reactants down to the micropipet tip. The low concentration of oxygen may also limit

full surface coverage of the Pt particles with reactants, thereby influencing the current density response (Gómez-Marín *et al.*, 2014). As the concentration of hydrogen ion is relatively high in 100 mM H_2SO_4, no steady-state mass-transport limited current is observed for HER within the studied potential range. Out of 169 total landing points, 130 correspond to the glassy carbon substrate without any Pt particles. These points exhibit an average current of -4.26 $\pm$ 0.11 pA at -0.15 V vs RHE, which correlate to a current density of 0.13 $\pm$ 0.003 mA/cm². This value is negligible compared to the hydrogen evolution reaction (HER) current observed on Pt particles (Figure B.10).

The overpotential (η) required to achieve a current density of −10 mA/cm² decreases with decreasing particle size, with smaller platinum particles exhibiting less negative η values compared to their larger ones. This behavior indicates that mass transport effects, which are more favorable for smaller particles due to enhanced diffusion, play a non-negligible role in the overall electrocatalytic performance. These observations suggest that the hydrogen evolution reaction (HER) under these conditions is not controlled only by charge-transfer kinetics but is also influenced by the mass transport of the hydrogen to the catalytic surface.

Tafel analysis was utilized to extract kinetic information for the hydrogen evolution reaction (HER) on individual Pt particles (Figure 3.7). By examining the appropriate region of the linear sweep voltammograms (LSVs) in a high acid concentration (100 mM H_2SO_4), where kinetic analysis is valid, and mass transport effects are minor, the Tafel slope and apparent exchange current density ($j_{0(app)}$) were accurately determined. These parameters are essential for evaluating the catalytic efficiency of a well-defined electrode (Zhang, Y. *et al.*, 2022).

To obtain fundamental kinetic insights, it is essential to identify a potential region where the Tafel slope remains unaffected by non-kinetic factors. This can be verified by the presence of a horizontal region in the Tafel slope plot, indicating that the reaction rate is controlled mostly by electron transfer kinetics, without interference from mass transport limitations or other external influences (van der Heijden *et al.*, 2024). A well-defined horizontal Tafel slope between 94 and 110 mV/dec was observed for Pt particles of different sizes, confirming the reliability of these values in characterizing intrinsic reaction kinetics (Figure B.11). Moreover, the consistent horizontal region

across varying mass transport conditions further validates the accuracy of the kinetic analysis. A previous study reported a similar Tafel slope of 105 mV/dec using SECCM with a pipet an approximately 960 nm diameter on a polycrystalline platinum surface which is approximately in agreement with our individual particles.(Wang, Yufei *et al.*, 2022)

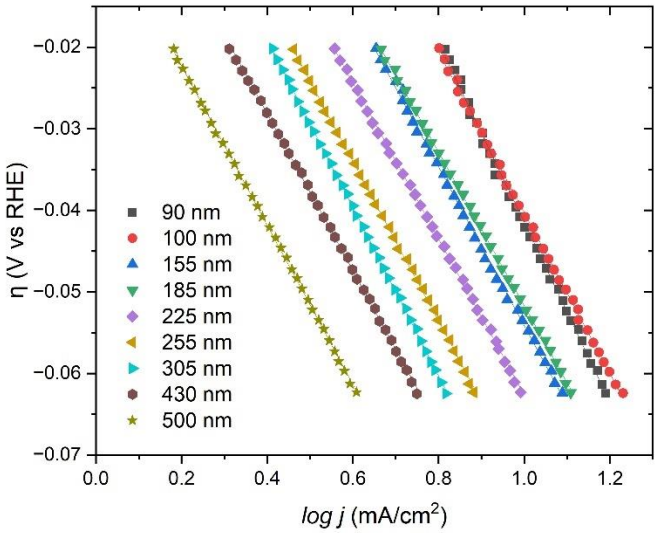

Figure 3.7 Tafel plots for HER on individual platinum particles of different radii with 100 mM H_2SO_4 as the electrolyte.

The apparent exchange current density ($j_{0(app)}$) and apparent rate constant (k^0_{app}) were determined by extrapolation of the Tafel plot (Table 3.2). Higher apparent exchange current density is observed for the smaller Pt particles. The fact of extracting higher value for apparent exchange current densities as well as apparent standard rate constants for smaller particles form Tafel analysis was already observed for individual particles (Chen, Shengli et Kucernak, Anthony, 2004a, 2004b). Higher mass transport related to smaller particles results in measuring the current more directly related to the intrinsic catalytic activity. This allows for more accurate extraction of kinetic parameters such as exchange current density and heterogenous rate constant. In contrast, when mass transport is poor, the current becomes limited by mass transport that can lead to underestimation of the intrinsic rate constant and incorrect conclusions about catalytic activity.

Table 3.2 Values of the Tafel slope, overpotential (η), apparent exchange current density ($j_{0(app)}$), and apparent Standard Rate Constant (k^0) obtained from the SECCM LSVs of the Hydrogen Evolution Reaction in 0.1 M H_2SO_4 on individual Pt Particles of Different Size.

Pt particle Radius **(nm)**	***Tafel slope*** **(mV/dec)**	η **(mV) at -10 mA/cm^2**	$j_{0(app)}$**(mA/cm^2)**	k^0_{app} **(cm/s)**
90	-110	6	14.45	6.2 x 10^{-3}
100	-98	8	12.06	5.2 x 10^{-3}
155	-97	10	9.09	3.9 x 10^{-3}
185	-94	10	9.06	3.9 x 10^{-3}
225	-95	15	7.06	3.0 x 10^{-3}
255	-98	28	5.55	2.4 x 10^{-3}
305	-103	37	4.82	2.0 x 10^{-3}
430	-96	45	3.96	1.7 x 10^{-3}
500	-97	62	2.87	1.2 x 10^{-3}

Finite element modeling was used to simulate the linear sweep voltammograms (LSVs) for the hydrogen evolution reaction (HER), supporting the experimentally extracted kinetic parameters. To investigate the role of mass transport, the simulations were extended to more negative potentials, accessing the mass transport-limited regime (Figure B.14). The results reveal that mass transport effects become significant only at overpotentials beyond –0.6 V, indicating that the kinetic analysis remains unaffected in the lower overpotential region where Tafel slopes were extracted. However, the diffusion limitations are reflected in a shift of the half-wave potential toward more negative values for smaller particles. This shift highlights the higher mass transport for smaller particles, while larger particles, with a lower particle-to-droplet size ratio, exhibit enhanced diffusion contributions. These findings confirm that although HER kinetics dominate at small overpotentials, mass transport begins to influence the observed activity at higher overpotential.

3.6 Conclusion

In summery, this study demonstrates the power of Scanning Electrochemical Cell Microscopy (SECCM) combined with Scanning Electron Microscopy (SEM) to quantitatively analyze the kinetics of the Oxygen Reduction Reaction (ORR) and Hydrogen Evolution Reaction (HER) at the level of individual platinum particles. For ORR, smaller Pt particles showed a shift in half-wave potential ($E_{1/2}$) toward more negative values, indicating increased irreversibility due to rapid oxygen mass transport. The analysis also showed that while larger Pt particles generate higher overall currents, their current density decreases, highlighting the influence of particle size on catalytic performance. The variation in mass transfer coefficients, resulting from differences in particle size, enabled application of the Koutecký–Levich model to quantify the apparent standard rate constant (k^0_{app}) for ORR.

For HER, the kinetic parameters were extracted using Tafel analysis, revealing a clear size-dependent trend in apparent exchange current density ($j_{0(app)}$) and overpotential. Enhanced mass transport reduces the influence of diffusion limitations, enabling more precise kinetic measurements. The data confirm that larger particles require higher overpotentials to reach the same current density due to lower mass transport.

This work establishes a robust methodology for extracting kinetic parameters at the single-particle level using SECCM, paving the way for precise structure–activity relationships in electrocatalysis. The approach here emphasises the quantitative application of SECCM, and can be applied to other catalytic materials, facilitating a quantitative understanding of reaction kinetics in various energy systems, including fuel cells, electrolyzers, and metal–air batteries.

CHAPTER 4

Quantitative Electroanalysis in Ionic Liquids using Scanning Electrochemical Cell Microscopy

4.1 Résumé

La voltammétrie en régime stationnaire du médiateur rédox ferrocène, réalisée dans le liquide ionique à température ambiante 1-éthyl-3-méthylimidazolium tétrafluoroborate, est effectuée à l'aide de la microscopie électrochimique par cellule à balayage (SECCM) sur un substrat en carbone vitreux. Les voltammogrammes linéaires enregistrés (LSV) sont analysés à l'aide d'expressions analytiques récemment développées et validées par modélisation numérique, afin d'extraire le coefficient de diffusion, D, et la constante de vitesse hétérogène, k^o. Pour cela, seuls l'angle semi-ouverture et le rayon de la pipette, mesurés par microscopie électronique, sont nécessaires pour déterminer les paramètres cinétiques et de transport.

Un ensemble de données suffisant a été collecté pour quantifier ces paramètres par analyse statistique, donnant des valeurs de D de 4,1 × 10^{-7} cm^2 s^{-1} et de k^0 de 1,0 × 10^{-2} cm s^{-1}, en bon accord avec les valeurs rapportées dans la littérature. L'utilisation de plusieurs diamètres de pipettes permet d'ajuster la vitesse de transport de masse du ferrocène, et il est démontré que l'analyse de Koutecký–Levich peut être utilisée pour extraire le courant cinétique en SECCM, fournissant une valeur de k^0 de 1 × 10^{-2} cm s^{-1}, cohérente avec celle obtenue à partir de l'expression analytique.

Enfin, des LSV individuels présentant des courants ultrafaibles dans la gamme des femtoampères et picoampères ont été ajustés avec succès à l'aide de l'expression analytique, permettant ainsi de cartographier k^0 à la surface d'un substrat de carbone.

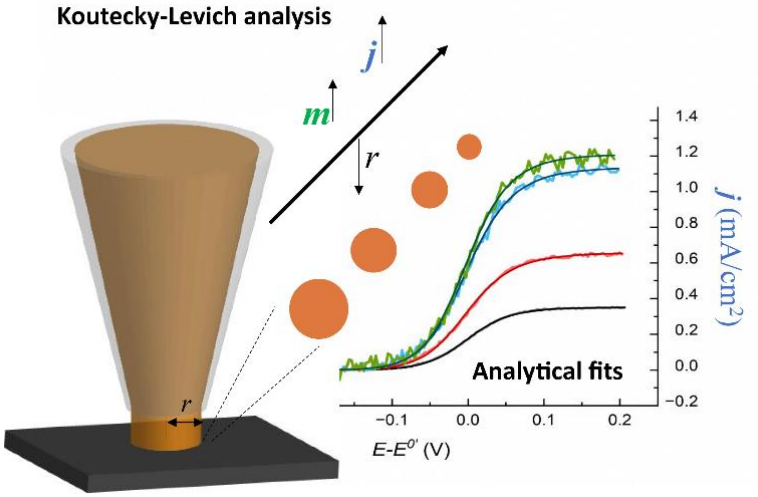

Figure 4.1 Graphical abstract illustrating that both the mass transfer coefficient and current density increase as the size of the pipet tip decreases.

4.2 Authors Contribution

Samaneh Salek

First author conducted the experimental measurements, processed and interpreted the results, created the figures, carried out the literature review, and wrote the first draft of the manuscript and made corrections.

Joshua Byers

Co-author supervised the study, contributed to result interpretation, participated in discussions, and reviewed and corrected the manuscript.

4.3 ABSTRACT

Steady-state voltammetry of the redox mediator ferrocene in the room temperature ionic liquid, 1-ethyl-3-methylimidazolium tetrafluoroborate is carried using scanning electrochemical cell microscopy (SECCM) on a glassy carbon substrate. The measured linear sweep voltammograms (LSVs) are analyzed using recently developed analytical expressions, and validated using numerical modelling, to extract the diffusion coefficient, D, and heterogeneous rate constant, k^0, where only the pipet half-angle and pipet radius, measured using electron microscopy, are needed to determine the kinetic and transport parameters. Sufficient data were collected to quantify these parameters using statistical analysis providing values for D, of 4.1×10^{-7} cm^2 s^{-1}, and k^0, of 1.0×10^{-2} cm s^{-1}, which are in good agreement with literature values. Through the use of several different pipet diameters, it is possible to adjust the rate of mass transport of ferrocene, and it is shown that Koutecký–Levich analysis can be used to extract the kinetic current using SECCM, providing a value of k^0 of 1×10^{-2} cm s^{-1}, matching the results obtained using the analytical expression. Finally, individual LSVs exhibiting ultralow currents in the femtoampere and picoampere range were successfully fit using the analytical expression to map k^0 across a carbon surface.

4.4 Introduction

Room temperature ionic liquids (RTILs) are electrolytes composed entirely of organic cations and inorganic or organic anions that form a liquid at or near room temperature. They exhibit wide potential windows, low vapor pressures, and chemical tunability, motivating their development for a variety of electrochemical applications such as charge storage and electrodeposition. (Basile *et al.*, 2016; Fortunati *et al.*, 2023; Liu, F. *et al.*, 2016; Miao *et al.*, 2021) An ongoing challenge in the electrochemical analysis of RTILs arises from their inherently high viscosities, which limit mass transport and decrease the diffusivity of electroactive species. (Lovelock *et al.*, 2010) Although RTILs consist entirely of ions, their elevated viscosity can reduce ionic conductivity and redox mediator diffusivity, resulting in non-neglible *iR* drops that can complicate the analysis of electrochemical measurements. One strategy to overcome these limitations is the use of microelectrodes. Their reduced dimensions enhance the rate of mass transport of redox species through radial diffusion, and the correspondingly small currents minimize *iR* effects, allowing for more reliable measurements. While microelectrodes offer significant advantages for electroanalysis in room-temperature ionic liquids, their fabrication is typically restricted to noble

metals or carbon. However, as RTILs are increasingly employed in electrocatalysis and battery systems that use diverse and often heterogeneous substrates, there is a growing need for new methodologies capable of measuring transport and kinetic parameters on a wide range of surfaces.

Scanning electrochemical cell microscopy (SECCM), uses a glass pipet filled with an electrolyte to form a meniscus confined electrochemical cell, where the electrode dimensions are determined by the droplet contact area with the working electrode. (Anderson, Kamsy Lerae et Edwards, 2025; Gaudin, Lachlan F. *et al.*, 2024; Jayamaha *et al.*, 2024) This droplet-based configuration requires only minimal solvent volumes, making SECCM valuable for studies in RTILs, where electrolytes are often expensive. SECCM offers additional advantages for electrochemical studies in ionic liquids, including high rates of mass transport of reactants to the electrode surface and the measurement of small currents to minimize *iR* effects. In addition, the probe can be positioned over virtually any surface, facilitating measurements of complex and heterogeneous substrates. (Gaudin, Lachlan F. *et al.*, 2024) As a consequence, SECCM has been used to map an array of electrochemical processes across a multitude of substrate surfaces in RTILs including photo(electrocatalytic) reactions at platinum electrodes (Aaronson *et al.*, 2014) and conjugated polymers, (AaronsonGaroz-Ruiz*, et al.*, 2015) battery electrode materials, (Dayeh *et al.*, 2019) as well as ultrasensitive analytical measurements such as single molecule electrochemical detection. (Byers *et al.*, 2015)

A common practice in the quantitative analysis of SECCM data is the use of finite element modelling to account for the quasi-radial mass-transport that depends on the geometry of the pipet. (Snowden, Michael E. *et al.*, 2012) While this is a useful approach for analysing individual voltametric measurements such as linear sweep voltammograms (LSV) and cyclic voltammograms (CV), it is not amenable to analyzing large datasets. For example, in the hopping mode operation of SECCM, the droplet cell is repeatedly approached to different locations across a substrate surface ten, hundreds or even thousands of times, where at each location an individual measurement, such as an LSV, is carried out. (Bentley, Cameron L. *et al.*, 2019) This has enabled remarkable advances in visualising the flux of electroactive species across heterogeneous substrate surfaces, including the generation of potential dependent electrochemical movies. (Bentley, Cameron L. et Unwin, Patrick R., 2018) At the same time, these large datasets are rich in information that could be further analyzed using analytical expressions to rapidly fit individual

measurements to extract kinetic and transport parameters. While analytical expressions have been widely applied to analyze the steady state response of microelectrodes to determine D, k0, n the number of electrons transferred, and α the charge transfer coefficient, (Mirkin et Bard, 1992; Sun et Mirkin, 2006) they were only recently developed to analyze voltammograms obtained using SECCM (Anderson, K. L. et Edwards, 2023) and have not yet been applied to experimental data.

In this work, we carry out steady state voltammetry measurements of ferrocene in the RTIL 1-ethyl-3-methylimidazolium tetrafluoroborate [EMIM][BF_4], which was selected as a model system as its low vapour pressure and moderate viscosity enable stable droplet formation to carry out electroanalytical measurements under well-defined conditions. The hopping mode of SECCM was used to acquire LSVs across a glassy carbon substrate using four different pipet sizes and the results were analyzed using the recently developed analytical expressions to extract transport and kinetic parameters. While good agreement was found across all pipet sizes for the determination of k0, there was a larger spread in the values for the determination of *D*, that was attributed to a pipet geometry that may not be perfectly conical. The use of four different pipet geometries enabled the rate of mass transport to be systematically adjusted, enabling Koutecký–Levich analysis for the determination of k^0 and α, with the results matching those obtained using the analytical fitting procedure. Finally, individual LSVs were fit using the analytical equations, enabling LSVs in the femtoampere range to be analyzed with high fidelity, leading to the generation of electrochemical maps of k^0. The results presented here demonstrate that voltammograms measured using SECCM can be analyzed using complementary steady-state approaches that show good agreement in the determination of kinetic parameters. This work presents the integration of SECCM with analytical modeling offers a new route to quantify charge-transfer and diffusion processes in RTILs, opening up new opportunity for mapping heterogeneous substrate surfaces.

4.5 Experimental section

4.5.1 Chemical Reagents and Electrode Materials

1-ethyl-3-methylimidazolium tetrafluoroborate >98% [EMIM][BF4] and Ferrocene 98% (C5H5)2Fe were purchased from Io.li.tec GmbH and Sigma-Aldrich, respectively. A glassy carbon substrate was used as a working electrode, and a silver wire served as a quasi-reference counter electrode (QRCE). The surface of glassy carbon electrode was sequentially polished using

monocrystalline diamond suspensions with particle sizes of 3.0, 1.0, 0.5, and 0.25 µm. Following each polishing step, the electrode was sonicated for 1 min in a 1:1 ethanol-water solution and subsequently for 5 min in deionized water. Finally, the electrode was dried under argon before use. The QRCE was prepared by cutting approximately 10 cm of high-purity silver wire. The wire was lightly polished using a polishing pad, rinsed with a 1:1 ethanol-water solution, and then dried before use. Pipets varying in diameter (220 nm, 270 nm, 510 nm and 760 nm) were fabricated using quartz capillaries (0.8 ID x 1.00 OD VitroCom) and a laser puller (P2000, Sutter instrument). Pulling parameters are available in the Annexe C. A JEOL JSM-IT800 scanning electron microscope was used to characterize the geometry of the pulled pipets. The distribution and arrangement of the SECCM droplet footprints on the substrate surface were visualized using an optical microscope (Olympus DSX1000).

4.5.2 Electrochemical measurements with Scanning Electrochemical Cell Microscopy (SECCM)

Each pipet was filled with an electrolyte solution containing [EMIM][BF_4] with 2 mM ferrocene. An Ag wire quasi-reference counter electrode located in the pipets to form a local electrochemical cell in contact with the glassy carbon electrode substrate. The pipet positioning, localized electrochemical measurements, and data collection were conducted using a HEKA ElProScan scanning electrochemical microscope. The voltammetric hopping mode of SECCM was used to carry out linear sweep voltammograms (LSVs) for the oxidation of ferrocene at each landing site across the glassy carbon electrode surface with a scan rate of 100 mV s^{-1}. The total scanned area was 50 µm × 50 µm, with 25 data points collected for each pipet size.

4.5.3 Finite Element Modeling

SECCM steady state voltammograms for ferrocene oxidation in [EMIM][BF_4] using a nanopipette were simulated using a two-dimensional axisymmetric model in COMSOL Multiphysics v5.4, based on finite element analysis. Additional simulation details are provided in the Supporting Information.

4.6 Results and discussion

4.6.1 Steady-state voltammetry of ferrocene in [EMIM][BF_4]

Linear sweep voltammetry was carried out using the hopping mode of SECCM across a glassy carbon substrate using 2 mM ferrocene as a redox mediator in the RTIL 1-ethyl-3-methylimidazolium tetrafluoroborate [EMIM][BF_4]. Ferrocene was used as a redox mediator, as it shows a well-defined redox potential across a variety of organic solvents, as well as room-temperature ionic liquids (RTILs), making it widely used as an internal standard in nonaqueous electrochemistry. (Bentley, Cameron L. *et al.*, 2020; Bentley, Cameron L. *et al.*, 2016; Gagne *et al.*, 1980) A challenge in carrying out voltametric measurements in RTILs is obtaining a steady-state response. Often, peak-shaped responses, characteristic of a time-dependent response are obtained at higher scan rates. (Walsh *et al.*, 2010) To balance a steady-state response and the throughput of the hopping mode operation of SECCM, a series of cyclic voltammograms were carried out between 5 mV s^{-1} and 100 mV s^{-1} for a 520 nm pipet diameter (Figure C.1 and Figure C.2). LSVs recorded for all scan rates in the positive scan direction showed a well-defined plateau, as well as a similar waveshape and limiting current. To optimize throughput, a scan rate of 100 mV s^{-1} was used for all measurements and analysis. Specifically, the pipet was approached at a potential of – 0.6 V, then potential was swept in a positive direction to + 0.6 V until the tip was retracted from the surface and moved to a new location. Figure 4.2A presents an average LSV (solid black line) based on 25 individual measurements (solid grey lines) using the same pipet at different locations on a glassy carbon substrate. Specifically, a pipet with a radius (r_p) of 380 nm was used and showed a stable limiting current value of 1.58 pA and standard deviation of 0.072 pA. Similar to microelectrodes, the limiting current depends on the redox mediator concentration, diffusion coefficient and electrode area. In addition, for SECCM measurements, the limiting current depends on the pipet geometry, including the pipet radius and the pipet half angle (γ), meniscus height (h), and droplet wetting radius (r_p) formed with the working electrode (Figure 4.2B). Both the pipet radius and half angle can be determined from electron microscopy measurements (Figure 4.2C). The droplet contact area can, in some cases, be determined ex-situ using optical and/or electron microscopy measurements. Optical microscopy measurements were used as a qualitative measurement to visualize the droplet across the surface, which showed similar sizes (Figure 4.2D). The droplet contact area depends on several factors including the relative humidity, (Ebejer, Neil

et al., 2010) the solvent used, (VarhadeMeloni*, et al.*, 2023) and the electrode-electrolyte surface energy. (Li *et al.*, 2020) (Gateman *et al.*, 2021) Optimization of these parameters is critical to enable high-fidelity measurements and quantitative analysis. (Saxena *et al.*, 2024) RTILs are ideal solvents for controlling contact area as the low vapour pressure combined with elevated viscosity enable stable droplet formation. It has been shown using AFM and SEM that the droplet footprint for SECCM corresponds closely to pipet diameter. (AaronsonByers*, et al.*, 2015; AaronsonGaroz-Ruiz*, et al.*, 2015; Byers *et al.*, 2015) In this work, the droplet diameter during contact with the substrate is taken to be equal to the pipet outer diameter when analyzing the electrochemical data. Comparing the droplet size across the electrode surface for each measurement, it was found that they are nearly identical in size at each location (Figure 4.2D). The consistency of the droplet size between individual landing sites is consistent with the small deviation of the limiting current (Figure 4.2E). The reversibility of the ferrocene voltammetry was assessed using the Tomeš criterion ($E_{3/4}$-$E_{1/4}$), which for a one electron transfer process, should be 56.4 mV. A value of 62 mV for a pipet radius of 380 nm was found for the Tomeš criterion indicating that the average LSV is slightly quasi-reversible (Table 4.1).

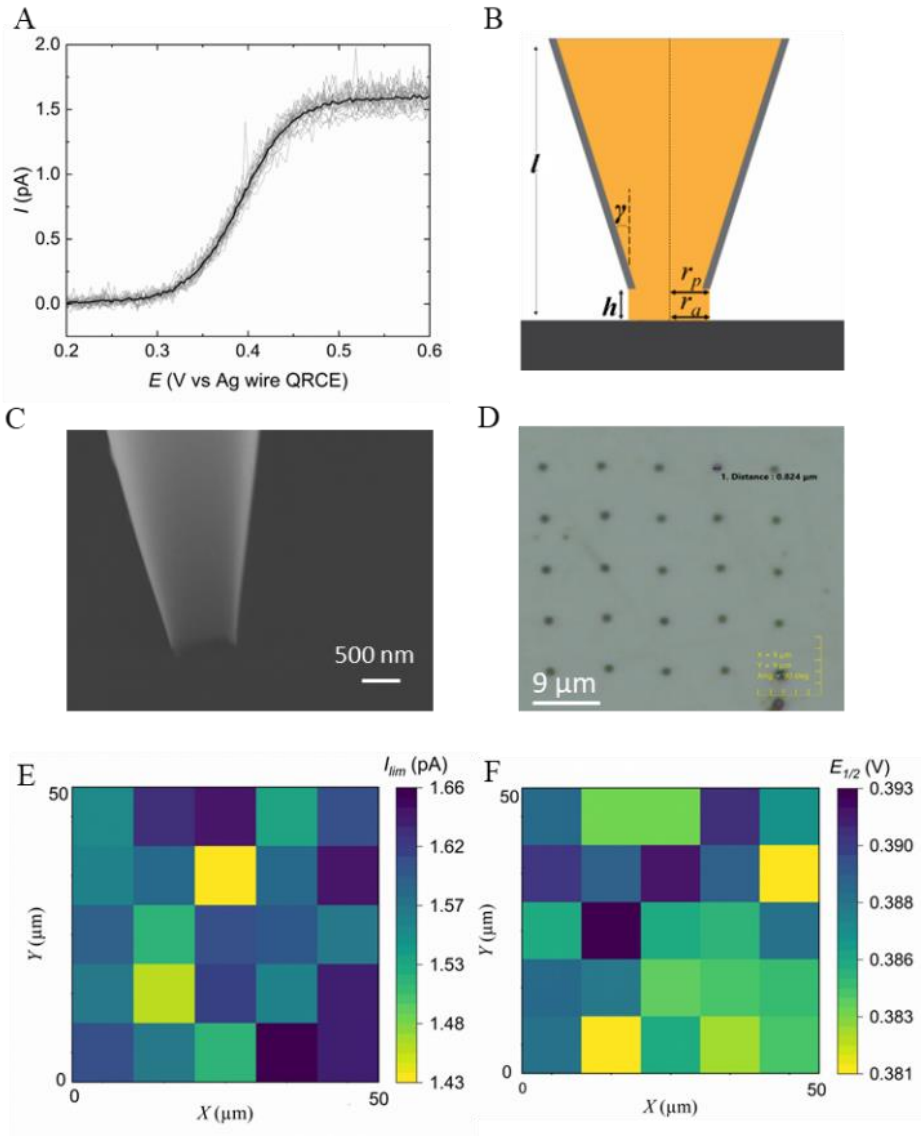

Figure 4.1 (A) SECCM linear sweep voltammograms (25 independent LSVs) and their average (solid black line) for the oxidation of 2 mM ferrocene in [EMIM][BF_4] at a glassy carbon electrode with a pipet tip radius of 380 nm at a scan rate of 100 mV s^{-1}. (B) Schematic representation of the conical SECCM pipet, indicating the half-angle (γ) and tip radius (r_p). The droplet meniscus is defined by its contact radius (r_a) and height (h). (C) Scanning electron microscopy (SEM) image of the SECCM pipet with r_p = 380 nm. (D) Optical image of the droplet footprint on the glassy carbon surface corresponding to the 25 SECCM measurement sites shown in A. (E) Electrochemical maps of the limiting current (I_{lim}) obtained from 25 localized linear sweep

voltammograms in A at (E-$E^{0'}$ = 0.15 V). (F) Corresponding electrochemical map related to half-wave potential ($E_{1/2}$) for the same set of LSVs.

Figure 4.3A presents LSVs that correspond to four different pipet radii (110 nm, 135 nm, 255 nm, and 380 nm). Each LSV presents the average of 25 independent measurements (solid line) and the corresponding standard deviation (shaded area). Optical images of the surface and SEM images of the pipet are presented in the Supporting Information (Figure C.3). Analysis of the average LSVs enabled determination of $E_{3/4}$-$E_{1/4}$, $E_{1/2}$ and I_{lim} for each pipet radius (Table 4.1). A slight shift in $E_{3/4}$-$E_{1/4}$ with decreasing pipet diameter suggest the shape of the LSVs could be affected by changes in the rates of mass transport. In addition to changes in the geometry of the pipet (diameter and half-angle), there are several factors that can influence the position and shape of the LSV. For example, unequal values of the diffusion coefficients of the uncharged form of ferrocene in the reduced state and the charged form of ferrocenium in the oxidized state could cause a shift in the position of the half-wave potential. Rogers et al previously measured the diffusion coefficient for ferrocene and ferrocenium in a related ionic liquid that had the same anion used here and a slightly different cation, specifically, [BMIM][BF_4], and found that the diffusion coefficient of ferrocenium was approximately 30% lower than ferrocene. (Rogers *et al.*, 2008) This could lead to an offset (about 20 mV) that would be constant and independent of tip diameter and contained within the $E^{0'}$ value. Time-dependent effects could affect the wave-shape. However, as shown in Figure C.1 and Figure C.2, for LSVs carried out in the positive scan direction, a significant effect was not observed. On the other hand, an iR drop would be expected to lead to systematic changes in the shape of the LSV. The resistance of the pipet is determined by the size of the tip opening and the conductivity of the electrolyte. A decreasing pipet diameter would give a larger resistance, and larger iR drop, leading to a broadening of the LSV. Blount et al developed an analytical equation for evaluating the resistance of pipets based on their geometry: (Blount *et al.*, 2022)

$$R_s = \frac{h}{\kappa\pi r^2} + \frac{1}{\kappa\pi r \tan\gamma} \tag{4.1}$$

where h is the height of the droplet, which is assumed to be equal to the radius of the pipet, and κ is the electrolyte conductivity. For [EMIM][BF_4], the electrolyte conductivity is 1.55 S m^{-1}, (Stoppa *et al.*, 2010) giving a resistance of 3 MΩ to 15 MΩ for tip radii from 380 nm to 110 nm. Considering

a limiting current of 1.62 pA for a 380 nm radius pipet and a limiting current of 0.46 pA for a 1100 nm radius pipet, the potential drop would be less than 1 mV in both cases and would not affect the shape of the LSV. This reinforces the benefits of using SECCM for nanoscale measurements in ionic liquids, where *iR* drops are not significant due to the small currents measured. If there was a significant contribution of time-dependent effects, this could also affect the waveshape. For this reason, we suggest that the broadening of the waveshape with decreasing pipet diameter is due to an increase in mass transport. Overall, for each pipet radius, the small value of the standard deviation in the limiting current value, reproducible current waveshape for a given pipet diameter, and consistent droplet size at each individual landing site enable high fidelity steady state voltammetric measurements to be obtained on a glassy carbon substrate using ferrocene as a redox mediator in [EMIM][BF_4].

Table 4.1 Summary of Electrochemical Parameters Measured for each Pipet Diameter using SECCM

r_p (nm)	Half-angle (γ)	I_{lim} (pA)	D (cm^2 s^{-1})	$E_{1/2}$ (V)	$E_{3/4}$ - $E_{1/4}$ (mV)	m (cm s^{-1})	k^0 (cm s^{-1})
110	8	0.45	5×10^{-7}	0.398	74	0.0062	0.009
135	11	0.64	4.2×10^{-7}	0.391	70	0.0058	0.012
255	13	1.32	3.8×10^{-7}	0.385	66	0.0034	0.010
380	12	1.58	3.3×10^{-7}	0.387	62	0.0018	0.009

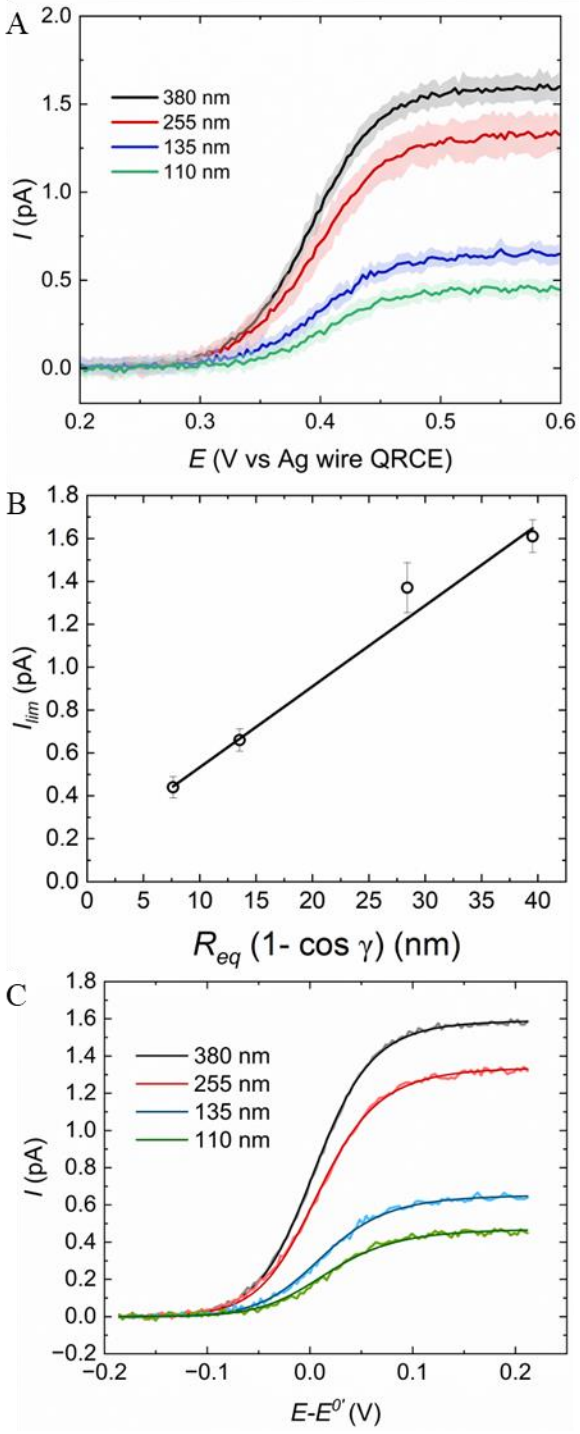

Figure 4.3 (A) Average SECCM LSVs with standard deviations for the oxidation of 2 mM ferrocene in [EMIM][BF_4] on a glassy carbon electrode. Each curve is the average of 25 individual LSVs obtained using pipets with tip radii of 380 nm (black), 255 nm (red), 135 nm (blue), and 110 nm (green) at a scan rate of 100 mV s^{-1}. (B) Plot of the average limiting current from (A) as a

function of an equivalent hemispherical microelectrode geometry. (C) Fit of the average LSVs using equation 4.4.

4.6.2 Quantitative analysis of the limiting current and waveshape

Recently, Anderson et al. (Anderson, K. L. et Edwards, 2023) developed analytical expressions for the evaluation of steady-state LSVs obtained using SECCM where it was shown that the limiting current could be expressed as a combination of an equivalent sized hemi-sphere electrode and the fraction of its area that is contacted by the droplet at the end of the pipet through the following expression:

$$I_{lim} = 2\pi nFCDR_{eq}(1 - \cos\gamma) \tag{4.2}$$

Where n is the number of electrons transferred, F is Faraday's constant, C is the bulk redox mediator concentration, D is the diffusion coefficient, and R_{eq} is a geometrical parameter that corresponds to a hemisphere with an equivalent radius that can be defined using the pipet radius and pipet half angle through the expression, $R_{eq} = (r_p/tan\ \gamma)$. The final term (1 - cosγ) represents the fraction of an equivalent size hemi-sphere electrode surface that is in contact with the droplet of the SECCM pipet. The values for the pipet radius, r_p, and pipet half angle, γ, that make up R_{eq}, were determined from SEM images enabling the use of equation 4.2 to calculate the diffusion coefficient, D, for each pipet based on the limiting current from the average LSV (Table 4.1). Diffusion coefficient values, D, between 3.3×10^{-7} cm^2 s^{-1} to 4.9×10^{-7} cm^2 s^{-1} were obtained, with an average value of $D_{avg} = 4.1\times10^{-7} \pm 0.6$ cm^2 s^{-1}. While current variations for a given pipet size are minor, a larger variation between D values was obtained between different pipet diameters. The diffusion coefficient is a constant that is independent of the pipet geometry and variations in this value reflects uncertainty in the pipet geometry that affects the limiting current and the value of D extracted. The pipet geometry, pipet diameter and half-angle were determined using a representative side-view image obtained using SEM (Figure 4.2C and C.1). The use of a side-view image assumes that the pipet is perfectly conical. However, this is not always the case, and if the geometry is not perfectly conical, the effective electrode geometry, which is contained within the term $R_{eq}(1 - cos\gamma)$ will have some uncertainty as the side-view SEM image could overestimate or underestimate the apparent half-angle and radius of the pipet. Figure C.4 illustrates the changes in

the relative uncertainty for different values of the half-angle and pipet radius. Even modest deviations in the assumed half-angle (e.g. 0.5° - 1°) can lead to relatively large uncertainties, especially for smaller half-angles. This could explain the larger value of the diffusion coefficient for the smallest pipet radius of 110 nm, where the half-angle measured was only 8°, compared to the other pipets that had half-angles in the range of 11°-13°. For a pipet half-angle of this size, even an 8° error can lead to over 20% error in R_{eq}. For such small pipets, transmission electron microscopy has been used to resolve the inner tip radius and the conical geometry of the pipet to improve quantitative precision for scanning ion conductance microscopy probes, and future work could include this type of analysis of the SECCM probe to improve the precision in the determination of D for an individual pipet. (Perry *et al.*, 2016) Time-dependent finite element modelling of CVs measured at different scan rates were also carried out (Figure C.3) as the analytical equations are based on a steady-state model. As shown in Figure C.3, the same value of k^0 was used as the steady state model, whereas D was found to be 10% larger for the time-dependent model. Overall, the similarity in the results obtained using the time-dependent model and the analytical model suggest that the use of a steady-state model to analyze the data is acceptable. An alternative approach to extracting the diffusion coefficient is through the relationship between the limiting current measured using SECCM and the value $R_{eq}(1 - cos\gamma)$, which considers the specific geometry of the pipet in contact with the electrode surface (Figure 4.3B). A linear relationship is observed, as given by equation 4.2, and was used to determine the diffusion coefficient, D_{fit}, using least squares fitting of the linear plot, giving a value across all pipet measurements of $(3.1 \pm 0.2)\times10^{-7}$ cm^2 s^{-1}. The linear fit of Figure 4.3B has a non-zero offset of 0.15 pA, which is slightly larger than the background noise. An intercept of zero is expected based on equation 4.2 and a positive offset reduces the slope, leading to an underestimation of the diffusion coefficient. Nevertheless, previous reports of measured values of the diffusion coefficient of ferrocene in [EMIM][BF_4] were $(1.6 - 3.2)\times10^{-7}$ cm^2 s^{-1} and 5.1×10^{-7} cm^2 s^{-1}, (Barrado *et al.*, 2014; Blount *et al.*, 2022) placing the values reported here within these ranges.

The limiting current can also be used to determine the mass transport coefficient, m, for each pipet diameter:

$$m = \frac{I_{lim}}{nFAC} \tag{4.3}$$

Where A is the droplet contact area, and the other parameters are as defined previously. The average limiting current value was used for I_{lim} while the outer pipet diameter was used to calculate A, which approximates the droplet contact area to calculate m values (Table 4.1).

4.6.3 Quantitative analysis of the waveshape

In addition to the steady-state current, Anderson et al (Anderson, K. L. et Edwards, 2023) also introduced an analytical expression to evaluate the current as a function of potential to extract k^0 through the following equation:

$$I = \frac{I_{lim} e^{\alpha f(E-E^{0\prime})}}{\frac{m}{k^0} + e^{\alpha f(E-E^{0\prime})} + e^{-(1-\alpha) f(E-E^{0\prime})}} \quad (4.4)$$

Where $E^{0'}$ is the formal potential, and $f = F/RT$, R is the universal gas constant and T is the temperature. Ferrocene is used an internal redox standard and the value of apparent formal potential, $E^{0'}$, used for ferrocene was 0.387 V, which corresponds to the $E_{1/2}$ for the 760 nm pipet, which showed a nearly reversible response among the four different pipet geometries used in this work. Figure 4.3C presents average LSVs obtained for each pipet diameter and the fit to the data using equation 4.4, while the mass transfer coefficient was determined using equation 4.3. The only parameter that was adjusted to fit the data was the heterogeneous rate constant, with the constraint that the value of $E_{3/4}$-$E_{1/4}$ for the fitted LSV could not be less than the value of the average LSV. The value of the charge transfer coefficient, α, was assumed to be 0.5. Using this approach, k^0 was found to be between 0.9×10^{-2} cm s^{-1} and 1.2×10^{-2} cm s^{-1} for the different pipet diameters used as summarized in Table 4.1. Reported values of k^0 in the literature can vary widely, with solvent viscosity being a primary factor for the observed differences. (Bentley, Cameron L. *et al.*, 2016) Previous reports of k^0 in the same RTIL, [EMIM][BF_4], are 1.2×10^{-2} cm s^{-1} 1.6×10^{-2} cm·s^{-1}, (Barrado *et al.*, 2014; Frenzel *et al.*, 2017) which closely match our results. Analysis of the average steady-state LSVs using analytical expressions enabled determination of D and k^0, which were found to be $(4.1 \pm 0.4)\times10^{-7}$ cm^2 s^{-1} and $(1.0 \pm 0.1)\times10^{-2}$ cm s^{-1}, respectively (Table 4.1). In addition, using equation 4.2 to determine D across all pipet sizes (Figure 4.3B) using linear fitting provided a slightly smaller value of $(3.1 \pm 0.2)\times10^{-7}$ cm^2 s^{-1}.

4.6.4 Koutecky-Levich analysis

Comparison of the mass transport coefficient and the standard heterogeneous rate constant shows that they are similar in magnitude, consistent with the observed quasi-reversible behaviour. (Compton et Banks, 2011; Lebègue, 2023) This observation is supported by steady-state finite element modelling (Figure 4.4A). The geometry for the numerical simulation and further details are provided in the SI (Section C.6). Figure 4.4A presents LSVs obtained using three different values of the standard heterogeneous rate constant (k_1^0 = 1 cm s^{-1}, k_2^0 = 0.012 cm s^{-1}, and k_3^0 = 0.0055 cm s^{-1}). The numerical simulations show a Nernstian response for the largest k^0 value and a slight broadening with decreasing k^0, consistent with the quasi-reversible response for the k^0 values measured above. Figure 4.4B plots the experimental steady-state LSVs as a current density illustrating the effect of increasing mass transport, which leads to a broadening of the LSVs that becomes more pronounced with decreasing pipet diameter (Figure C.5).

Koutecký–Levich analysis is a useful approach to isolate the kinetic component of the current from steady-state voltammograms. (Lebègue, 2023) It was originally developed for hydrodynamic voltammetric measurements where the rate of mass transport is adjusted by controlling the convective flux towards the working electrode's surface by varying its rotation rate. (Treimer *et al.*, 2002) Through systematic variation of the mass transport using different rotation rates, a series of steady state voltammograms with different limiting current densities can be obtained and Koutecký–Levich analysis can be used to extract k^0. Recently, Kim et al, have shown that this analysis can be extended to microelectrodes, whereby the dimensions of several microelectrodes were systematically adjusted to vary the mass transport rates. (Kim, J. et Bard, 2016a) In an analogous fashion to rotating disk electrode measurements, analysis of the current as a function of mass transport enables determination of kinetic parameters. (Hill, C. M. *et al.*, 2015) In the case of a quasi-reversible reaction for a one electron transfer oxidation, it was shown that the inverse of the total current density could be separated into their mass transport and kinetic components in through the following expression:

$$\frac{1}{j} = \frac{1}{nFmC} + \frac{1}{nFk^0Cb^{\alpha}} \qquad (4.5)$$

Where j is the current density, $b = e^{\frac{F}{RT}\left(E - E^{0\prime}\right)}$, and the other variables are as defined previously. The first term on the right-hand side is the mass transport limited contribution, while the second term on the right-hand side represents the kinetic component of the current as a function of potential. Based on the observations above, Koutecký–Levich analysis was carried out using the average LSVs for each pipet diameter. Figure 4.4C presents $1/j$ at a given overpotential, $E - E^{0'}$, as a function of $1/mC$, which depends on the pipet geometry. Values of $E - E^{0'} \geq 60$ mV and less than potentials corresponding to the limiting current were selected, which extrapolate to small, positive kinetic current density values, $1/j_k$, that are free from mass transport effects and depend on the value of $E - E^{0'}$. In addition, equation (4.5) predicts a slope nearly equal to $1/F$ for a one electron oxidation of ferrocene. Individual plots ($R^2 > 0.99$) are presented in the SI (Figure C.7) and give values of F from 96 300 C mol^{-1} for $E - E^{0'} = 0.15$ V down to 87 489 C mol^{-1} for $E - E^{0'} = 0.06$ V, which is a change of less than 10 % over the entire potential range considered here. (Kim, J. et Bard, 2016a) Figure 4.4D presents the values of $\ln(1/j_k)$ as a function of $E - E^{0'}$, where extrapolation to zero overpotential enables determination of the exchange current density, j_0. Through the relationship $j_0 = k^0CFn$, the heterogenous rate constant k^0, was found to (0.01 ± 0.001) cm·s^{-1}. This value is in good agreement with the average value of k^0 measured for the different pipet diameters using the analytical expression. Analysis of the slope enabled determination of the transfer coefficient α, which was found to 0.58. The same results were obtained, with an $R^2 > 0.99$ for all plots, when constraining the slope to $1/F$ and maintaining the same intercept as obtained in Figure C.7 suggesting the shift in F with potential did not introduce significant error into the calculated values of k^0 and α.

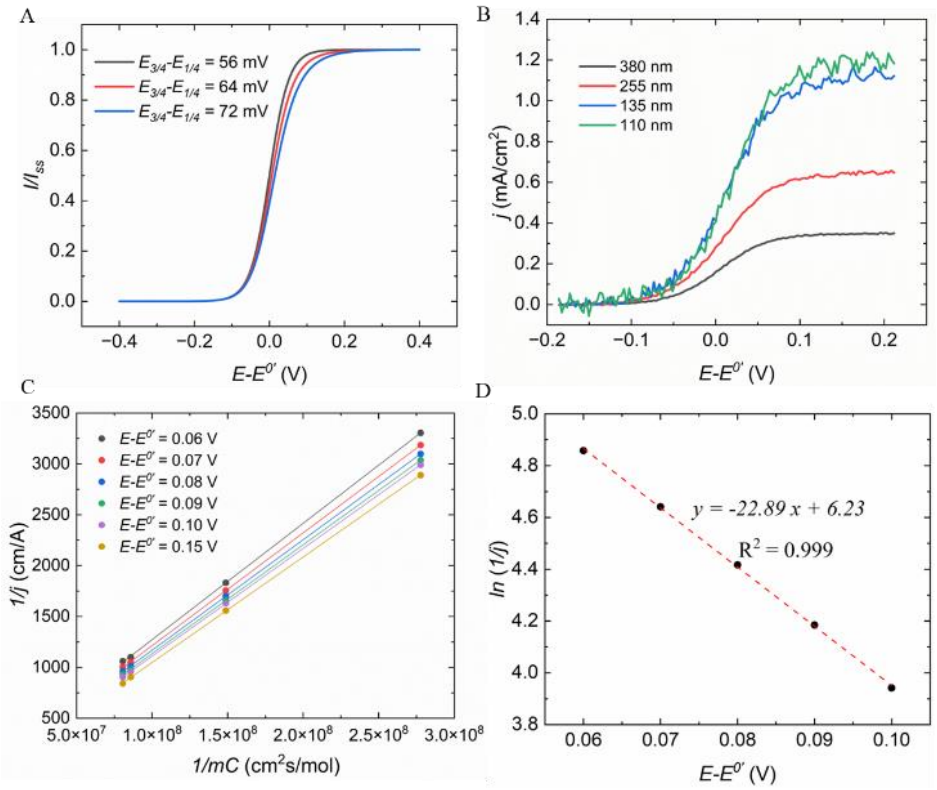

Figure 4.4 (A) Simulated steady-state voltammograms for the oxidation of 2 mM ferrocene in [EMIM][BF_4] using COMSOL Multiphysics, illustrating the effect of electron transfer kinetics on wave shape. Curves with $E_{3/4}$–$E_{1/4}$ values of 56 mV (black), 64 mV (red), and 72 mV (blue) correspond to increasing kinetic limitations (decreasing standard rate constants, k^o). All voltammograms are normalized to their respective mass transport limiting currents. (B) Experimentally obtained average current density LSVs (using pipets of tip radii 110 nm, 135 nm, 255 nm, and 380 nm. (C) Koutecký–Levich plots derived from the LSVs in part B, showing $1/j$ vs $1/mC$ at varying overpotentials ($E - E^{0'}$). (D) Linear plot of $\ln(1/j_k)$ versus $E - E^{0'}$, enabling extraction of the standard rate constant k^o and transfer coefficient α from the intercept and slope, respectively.

Analysis of individual landing sites

The magnitude of the current values measured here are in the femto- and picoampere range, where instrumental noise can become a limiting factor when analyzing the waveshape of the individual

LSVs. This problem is removed when using the average current from all LSV measurements, which smooths out fluctuations in the current values. In order to analyze the waveshape of the individual LSVs, the data were initially filtered using a Savitzky–Golay filter to reduce the effects of instrumental noise when fitting the data. The filtered data were then fit using equations 4.3 and 4.4 to determine m and k^0 at each location for each pipet diameter. Figures 4.5A – 4.5D present the raw experimental data overlaid with the fit based on equation 4.4 for an individual LSV for each pipet diameter, along with the residual current, which shows a negligible value across the entire potential range, indicating a good fit between the experimental data and equation 4.4 despite the instrumental noise, particularly for the smaller pipet sizes. Figures 4.5E and 4.5F present electrochemical maps for the Tomeš criterion and k^0, respectively, at each location for a 380 nm radius. The individual values measured here match closely the average values reported above. Electrochemical maps for the other pipets are presented in the Supporting Information (Figures C.6) along with fits for each LSV (Figure C.9 to C.12). Figure 4.5G presents histograms of the Tomeš criterion for all pipet diameters, which increase in value with decreasing pipet size, consistent with an increase in the quasi-reversible response with increasing mass transport. Finally, histograms presenting the individual values of k^0 for all pipet diameters at each location are presented in Figure 4.5H, where most values of k^0 fall in the range of 0.5×10^{-2} cm s^{-1} to 3×10^{-2} cm s^{-1}. Overall, fitting of the histogram for all LSVs measured across four different pipet diameters, provides a mean value of $(0.98 \pm 0.3)\times10^{-2}$ cm s^{-1}, which matches the values obtained using the average response for an individual pipet diameter, Koutecký–Levich analysis, as well as literature values. In this work, a glassy carbon surface was used in [EMIM][BF_4], with ferrocene as an outer-sphere redox mediator to minimize the influence of surface heterogeneity on the electrochemical response. This approach enabled the acquisition of data sets using four different pipet sizes, allowing both the average and individual responses to be analyzed and subjected to statistical evaluation as a function of pipet geometry. As the electrochemical mapping measurements demonstrate, a single value of the rate constant was obtained using four different pipets at different substrate locations, which is consistent with ferrocene being an outer-sphere redox mediator. In the future, inner-sphere redox mediators and more complex electrode surfaces could be investigated using SECCM in combination with analytical fitting.

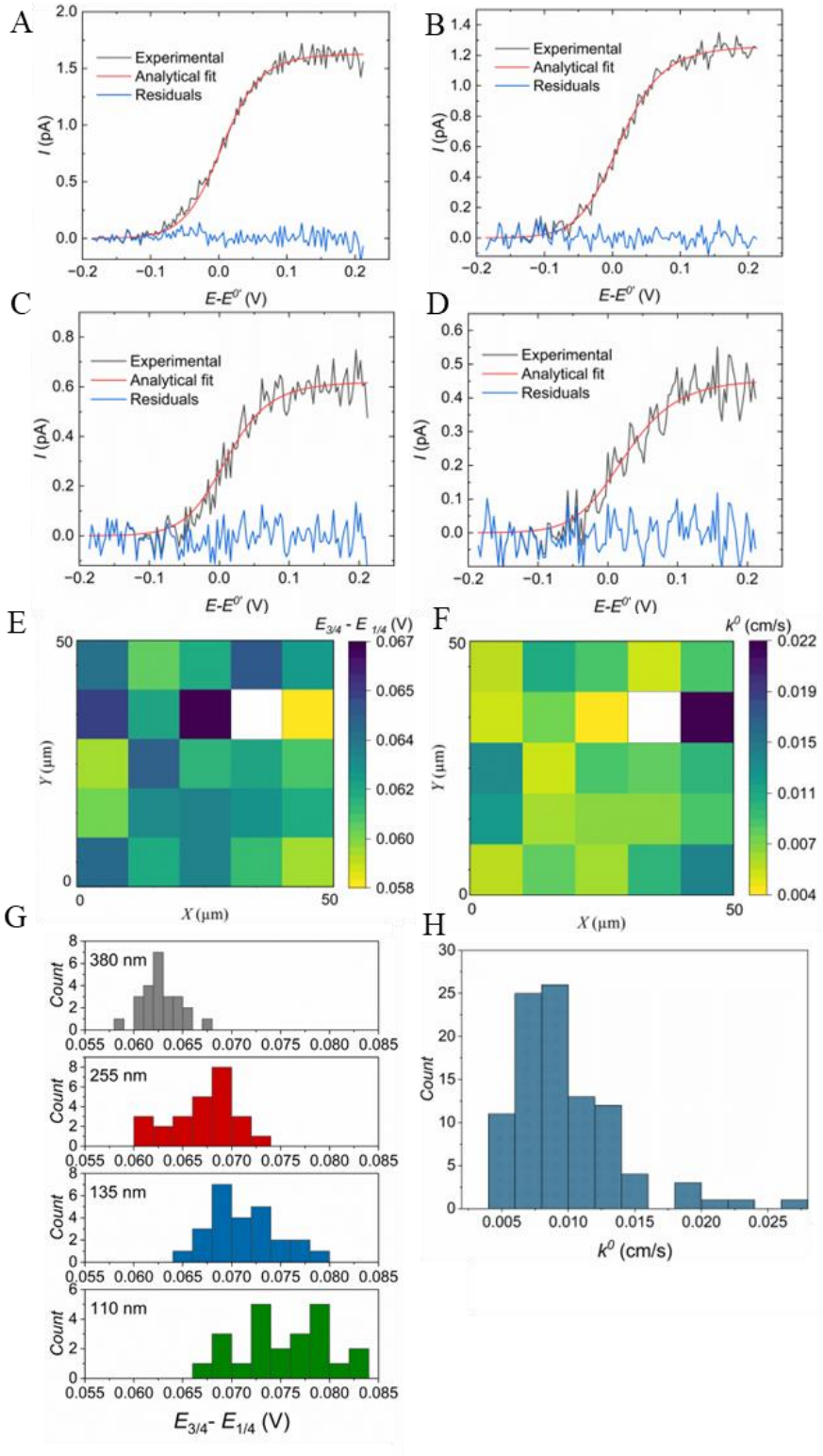

Figure 4.5 Analytical fit (red line) to a representative voltammogram (black line) selected from 25 individual linear sweep voltammograms (LSVs) for the oxidation of 2 mM ferrocene in

[EMIM][BF_4] on a glassy carbon electrode at a scan rate of 100 mV s^{-1}, using a SECCM pipet with tip radii of (A) 380 nm, (B) 255 nm, (C) 135 nm, and (D) 110 nm. Residuals (blue line) from each fit are included to evaluate the fit accuracy. (E, F) Electrochemical maps of the Tomeš criterion and the heterogeneous electron transfer rate constant (k^0), derived from 25 independent SECCM measurements using a 380 nm radius pipet. The white regions in the map correspond to locations where fitting analysis were not successful due to external noise. Histograms of Tomeš criterion (G) and k^0 (H) collected from 97 total measurements.

4.7 Conclusion

In conclusion, LSVs on a glassy carbon surface using four different pipet radii ranging in size from 110 nm to 380 nm in the RTIL [EMIM][BF_4], containing ferrocene as a redox mediator were measured using SECCM. For each pipet diameter, using the hopping mode of SECCM, 25 separate LSVs were obtained providing a statistical average and standard deviation of the current response. Fitting of the averaged voltammograms using recently developed analytical expressions enabled determination of D and k^0 values that are in good agreement with literature reports for ferrocene in [EMIM][BF_4] using other techniques. The mass-transport coefficient, m, and k^0 were found to be of similar magnitude, which was confirmed using finite-element numerical modeling. Moreover, the use of different pipet diameters, enabled the systematic control of the mass transport of ferrocene allowing for Koutecký–Levich analysis to be used to remove the effects of mass transport when determining the heterogeneous rate constant. Recent examples in aqueous solutions have shown that kinetic analysis, including Tafel analysis, can reveal new insights into the intrinsic activity of well-known materials such as platinum as well as new high entropy alloys. (Tetteh, Emmanuel Batsa *et al.*, 2023; Tetteh, Emmanuel Batsa *et al.*, 2024) In the future, variations in surface activity could be correlated with crystallographic orientation to map surface kinetics for electrocatalytic reactions in RTILs. This approach could be particularly useful for the kinetic analysis of electrocatalytic materials at the single particle level, (Kim, J. et Bard, 2016b; Salek et Byers, 2024) or in combination with hybrid SECM-SECCM probes. (Ryu, C. Hyun et Ren, Hang, 2024; Zerdoumi *et al.*, 2024)

New methodology for the accurate determination of k^0 and D in ionic liquids is of ongoing importance where these solvent systems continue to be of broad interest due to their wide electrochemical windows, negligible vapor pressure, and tuneable properties for electrochemical

applications. In this regard, SECCM presents several advantages, including high rates of mass transport that can be challenging to obtain using other methods due to complications from the higher viscosities of ionic liquids. Moreover, SECCM's droplet-based approach uses minimal solvent volume allowing for reduced sample consumption of often expensive ionic liquids. Finally, the hopping mode of SECCM, enabling high-throughput analysis of electrode surfaces, combined with the recently developed analytical equations enables the generation of spatially resolved maps of k^0. While this work focused on ferrocene, an outer-sphere redox species, the approach could be extended to the study of heterogeneous electrocatalytic reactions for the mapping of local variations in k^0 at a material's surface where differences in active sites and electrode inhomogeneities could be visualized. (Aaronson *et al.*, 2014)

CONCLUSION

The studies presented in this thesis demonstrate the power of Scanning Electrochemical Cell Microscopy (SECCM) as a high-resolution, quantitative tool for understanding fundamental structure activity relationships in electrocatalysis. By combining advanced electrochemical measurement technique and getting help from finite element modeling, these works contribute a comprehensive basis for kinetically analysis of catalytic behavior at the single particle level and/or at heterogenous electrode surface with high resolution under high and well-defined mass transport regimes.

In the first study, the use of electrodeposited silver particles of varying sizes on glassy carbon substrates enabled systematic investigation of the oxygen reduction reaction (ORR) on single Ag particles. Electrodeposition provided a clean, ligand-free surface, enabling intrinsic catalytic behavior to be probed without interference from stabilizing agents. The SECCM hopping mode, combined with correlative SEM imaging, made it possible to directly link particle geometry to electrochemical response. It was observed that as the size and loading of Ag particles increased, the total current increased but the current density decreased. This behavior highlighted the critical influence of particle dimensions on mass transport during ORR, emphasizing the need for careful interpretation in single-particle electrocatalysis. These findings are especially important for the evaluation of catalyst behaviour, and linking the electrocatalytic behaviour by precise measurements to materials different in size, shape, or surface structures.

The second study extended this approach to platinum nanoparticles, focusing on both the oxygen reduction reaction (ORR) and the hydrogen evolution reaction (HER). Building on the previous finding that smaller particles benefit from higher mass transport of redox species, this study extracted main kinetic parameters such as the apparent standard rate constant for ORR and HER, and the exchange current density for HER. Smaller Pt particles exhibited more favorable kinetic responses due to enhanced accessibility and higher mass transport, while larger particles showed higher overall currents but lower current densities. By separating kinetic and mass transport contributions using the Koutecký–Levich model and Tafel analysis, the study confirmed that

SECCM is a reliable platform for quantitative kinetic analysis. These results are crucial in advancing the understanding of how individual particles influence the performance of platinum based electrocatalysts, particularly in applications related to energy conversion.

The third study focused on the measurement of electron transfer kinetics in the room temperature ionic liquid [EMIM][BF_4], using ferrocene as a redox mediator. Here, SECCM offered a unique advantage for studying viscous, expensive electrolytes that are otherwise challenging to handle in conventional electrochemical setups. Linear sweep voltammetry was performed using four different pipet diameters, and statistical analysis of 25 individual measurements per pipet enabled reliable determination of the diffusion coefficient (D) and standard heterogeneous rate constant (k^0). The agreement of these values with finite element simulations and literature data validated the method, while the ability to control mass transport by varying the SECCM pipet size allowed the application of Koutecký–Levich analysis. This work not only provided new benchmarks for electrochemistry in ionic liquids, but also highlighted the potential of SECCM to generate spatially resolved maps of electrochemical kinetics, offering a pathway toward local activity mapping on heterogeneous surfaces.

Together, these studies illustrate how SECCM can connect the gap between classical ensemble measurements and nanoscale electrochemistry. Whether investigating individual particles, or redox chemistry in ionic liquids, the methodology enables kinetic measurements in nanoscale conditions with high spatial resolution. The insights gained here are highly relevant for the development of next-generation energy materials, including those used in fuel cells, electrolyzers, and batteries, where understanding and optimizing reaction kinetics at the microscale and nanoscale is essential.

Looking forward, these studies open several exciting directions for future research. The integration of SECCM with hybrid probes such as SECM-SECCM combinations could enable simultaneous mapping of the activity and chemical composition or intermediate detection. Electrodeposition strategies can be further advanced synthesizing the size controlled or alloyed nanoparticles to be investigated electrochemically. In ionic liquids and other unconventional electrolytes, SECCM provides a unique platform to study electrocatalysis under non-aqueous conditions.

In conclusion, these studies advance our ability to extract intrinsic electrochemical kinetics at the single-particle level or at a heterogenous surface. SECCM appears not only as a powerful characterization technique but also as a guiding tool in design and optimization of electrocatalytic materials for sustainable energy technologies.

ANNEXE A Supporting Information

Influence of Particle Size on Mass Transport During the Oxygen Reduction Reaction of Single Silver Particles using Scanning Electrochemical Cell Microscopy

A.1 Growth of silver particles using electrodeposition

Silver nitrate ($AgNO_3$ 99%), potassium nitrate (KNO_3 99%), potassium chloride (KCl 99 %) and potassium hydroxide (KOH 90 %) were purchased from Sigma-Aldrich. All chemicals were used as received. Deionized water (18.2 MΩ cm) was used for electrodeposition. A glassy carbon electrode was used as a working electrode. Prior to electrodeposition, the glassy carbon electrode was cleaned by polishing with alumina powder (1.0, 0.3, 0.05 μm diameter). The electrode was sonicated in a 1:1 (*v:v*) mixture of ethanol and water for 1 minute following sonication in deionized water for 5 minutes followed by drying the electrode under Argon flow. A three-electrode arrangement was employed using a Biologic (SP-300) potentiostat, Pt mesh counter electrode, glassy carbon working electrode, and Ag/AgCl (3 M KCl) reference electrode. An aqueous solution of $AgNO_3$ (1mM) and KNO_3 (100 mM) was used for the electrodeposition. Galvanostatic electrodeposition was carried out at a constant current density of - 50 $\mu A/cm^2$ for 2 seconds. Following electrodeposition, the electrode was rinsed three times with deionized water. SEM images were acquired using a scanning electron microscope (JEOL JSM-7600F) equipped with a detector for energy dispersive spectroscopy (Oxford Instruments).

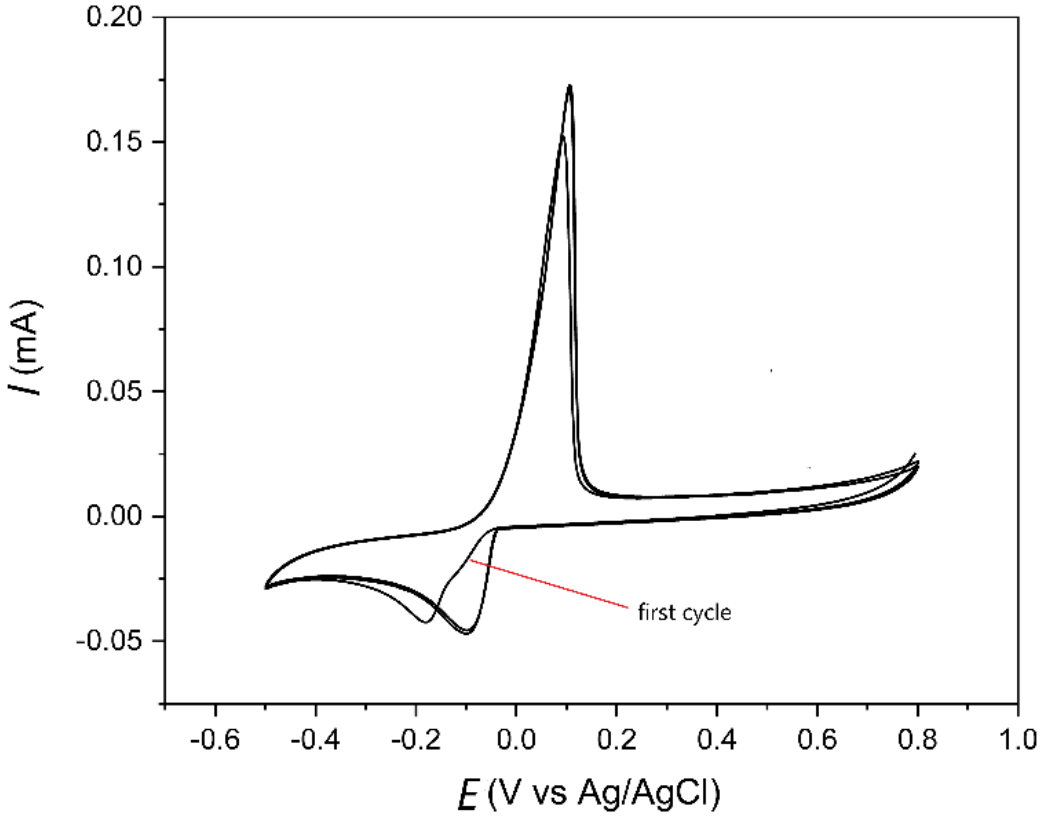

Figure A.1 Cyclic voltammogram of a glassy carbon working electrode in 1 mM $AgNO_3$ and 0.1 M KNO_3 using a Pt mesh counter electrode at a sweep rate of 20 mV/s

A.2 Pipet preparation

Pipets were fabricated using quartz capillaries (0.8 ID x 1.00 OD VitroCom) and a laser puller (P-2000, Sutter instrument). A one step program (HEAT 700, FIL 4, VEL 55, DEL 130, and PUL 55) was used to create pipets with a tip diameter of 1.8 µm. The outer sidewall of the pipet was silanized in dimethyldichlorosilane $Si(CH_3)_2Cl_2$ (99.5%) to increase its hydrophobicity and confine the aqueous droplet at the end of the tip (Ebejer, N. *et al.*, 2013).

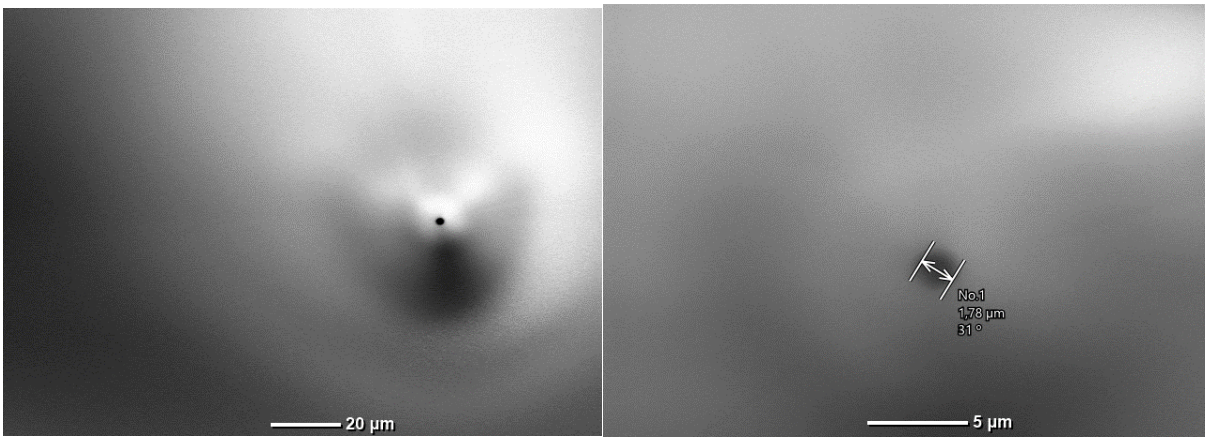

Figure A.2 SEM image of the SECCM pipet with a tip diameter of around 1.8 µm.

A.3 Scanning Electrochemical Cell Microscopy (SECCM)

The pipets were backfilled with a 10 mM KOH and 50 mM KCl electrolyte solution. An Ag/AgCl quasi-reference counter electrode (QRCE) was prepared by anodizing a silver wire in an aqueous saturated KCl solution. A scanning electrochemical microscope (HEKA ElProScan) was used for pipet positioning, local electrochemical measurements, and data acquisition. A JEOL JSM7600F scanning electron microscope was used to acquire SEM images of the substrates following electrochemical mapping.

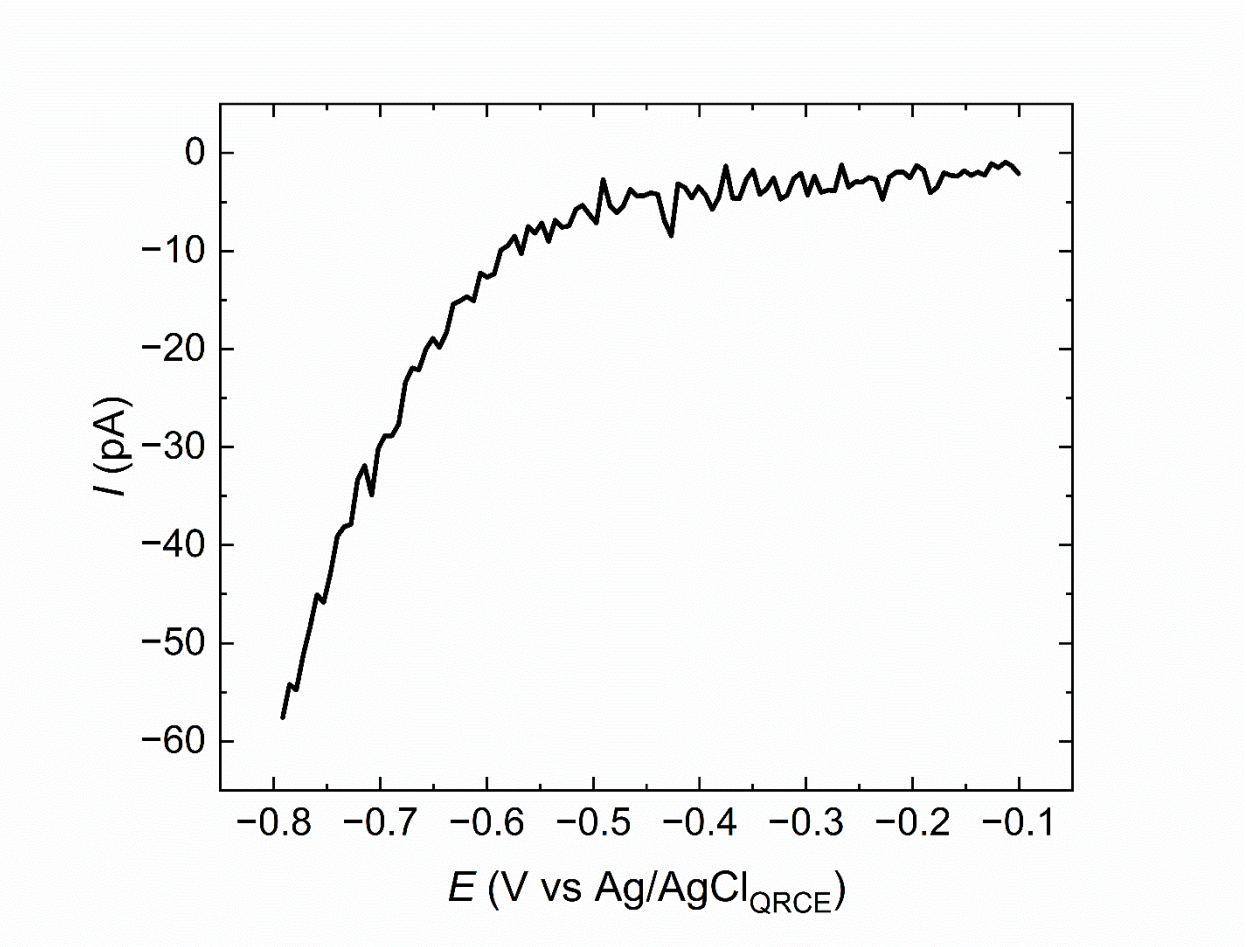

Figure A.3 LSV (I_{Ag}) of individual silver particle started at more negative potential – 0.8 V (vs Ag/AgCl QRCE). The electrolyte solution was 0.01 M KOH and 0.05 M KCl and the scan rate was 500 mV/s.

A.3.1 Electrochemical map of a bare glassy carbon substrate

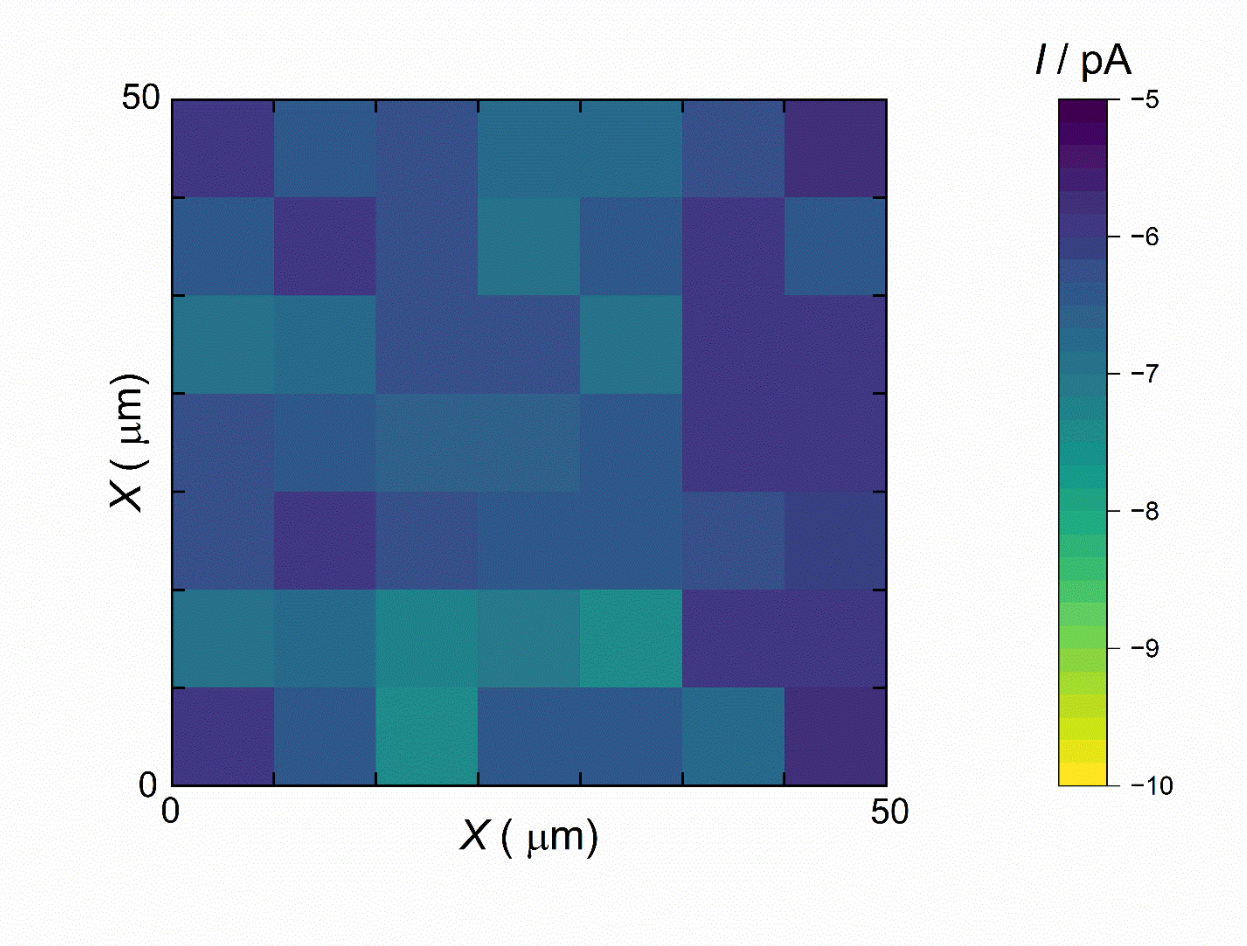

Figure A.4 SECCM map of blank carbon substrate at - 0.65V vs Ag/AgCl QRCE in an aqueous solution of 0.01 M KOH and 0.05 M KCl. Scan area was 50 µm x 50 µm with total of 49 voltammetry measurements.

A.3.2 LSVs of individual silver particles

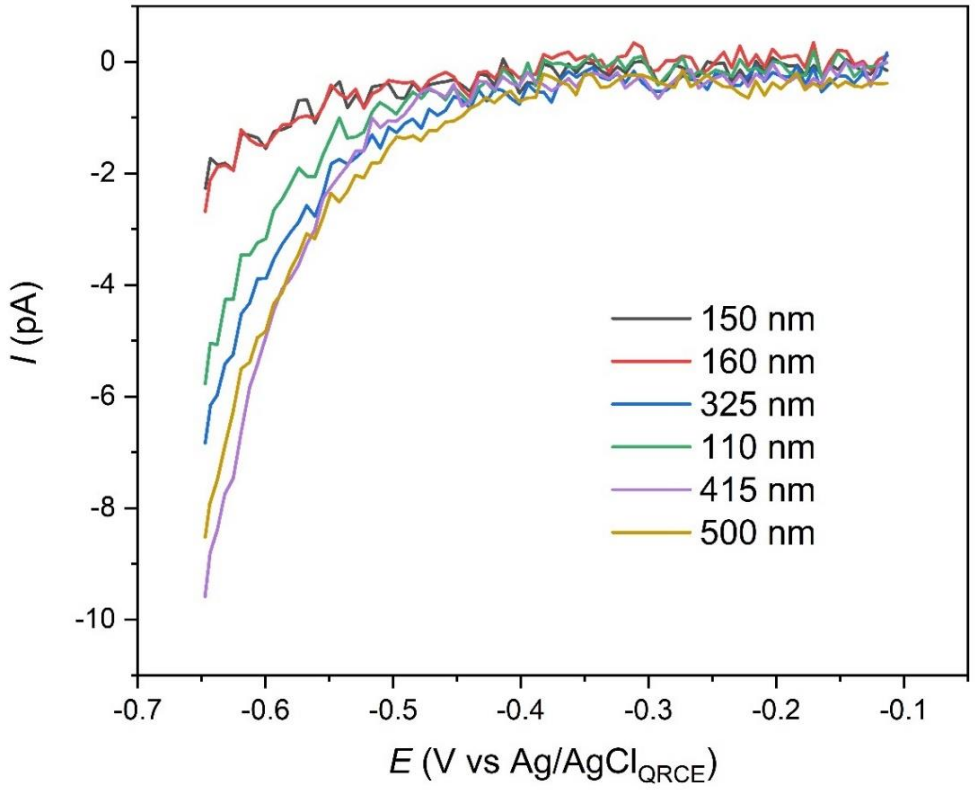

Figure A.5 LSVs (I_{Ag}) of individual silver particles of varying radii following background correction. The electrolyte solution was 0.01 M KOH and 0.05 M KCl and the scan rate was 500 mV/s.

A.3.3 Additional SECCM maps

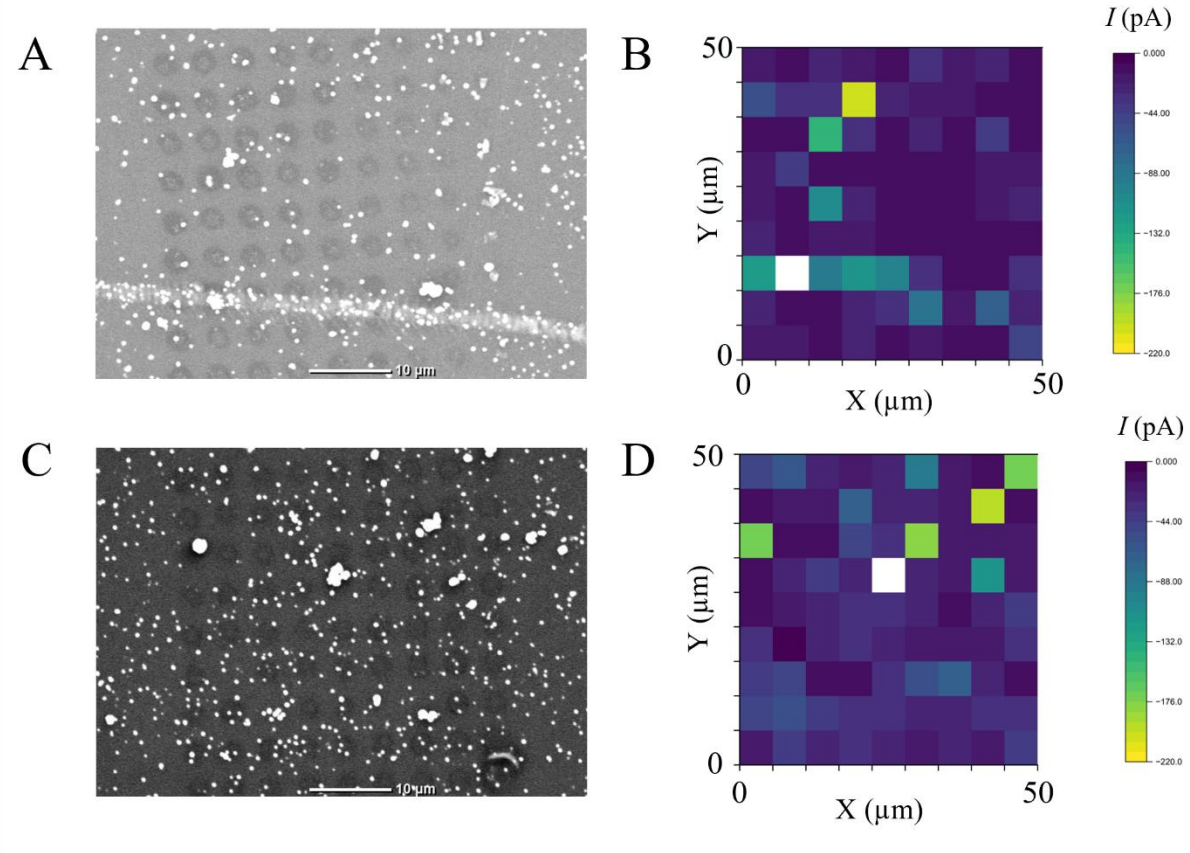

Figure A.6 (A and C) Scanning electron microscope images and corresponding SECCM electrochemical maps (B and D) (scan size of 50 µm by 50 µm for a total of 81 data points) for the ORR obtained at -0.65 V (vs Ag/AgCl QRCE). The electrolyte solution was 0.01 M KOH and 0.05 M KCl and the scan rate was 500 mV/s.

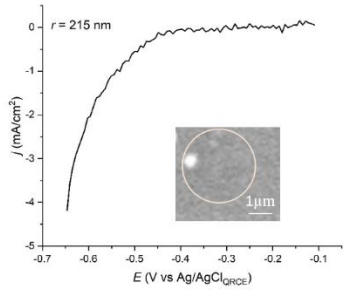
r = 215 nm
j (mA/cm²)
E (V vs Ag/AgCl_QRCE)
1µm

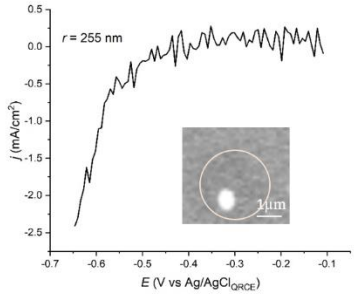
r = 255 nm
j (mA/cm²)
E (V vs Ag/AgCl_QRCE)
1µm

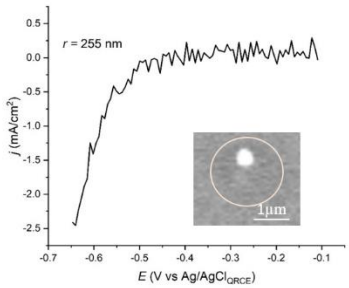
r = 255 nm
j (mA/cm²)
E (V vs Ag/AgCl_QRCE)
1µm

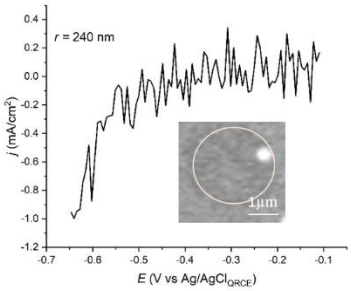
r = 240 nm
j (mA/cm²)
E (V vs Ag/AgCl_QRCE)
1µm

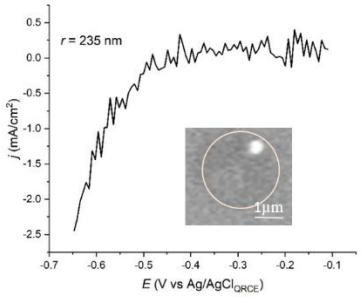
r = 235 nm
j (mA/cm²)
E (V vs Ag/AgCl_QRCE)
1µm

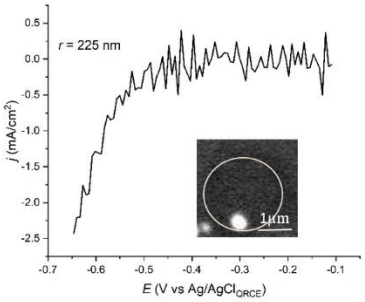
r = 225 nm
j (mA/cm²)
E (V vs Ag/AgCl_QRCE)
1µm

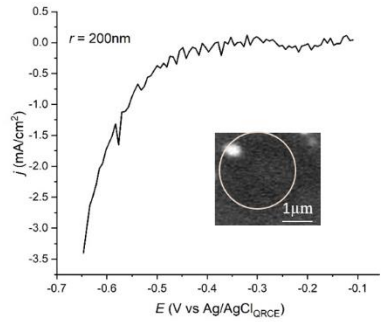
r = 200nm
j (mA/cm²)
E (V vs Ag/AgCl_QRCE)
1µm

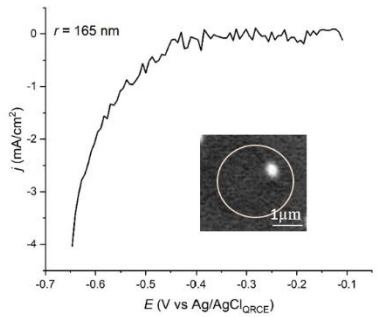
r = 165 nm
j (mA/cm²)
E (V vs Ag/AgCl_QRCE)
1µm

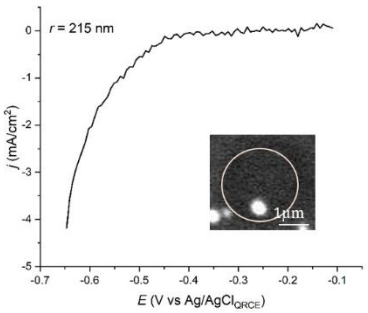
r = 215 nm
j (mA/cm²)
E (V vs Ag/AgCl_QRCE)
1µm

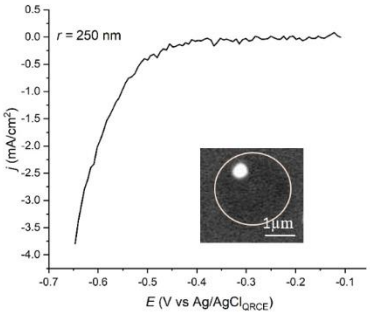
r = 250 nm
j (mA/cm²)
E (V vs Ag/AgCl_QRCE)
1µm

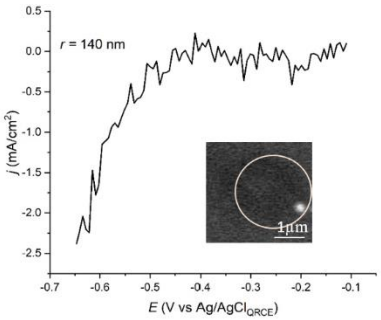
r = 140 nm
j (mA/cm²)
E (V vs Ag/AgCl_QRCE)
1µm

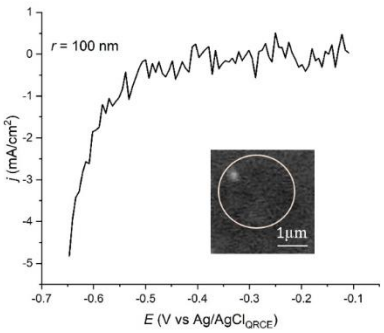
r = 100 nm
j (mA/cm²)
E (V vs Ag/AgCl_QRCE)
1µm

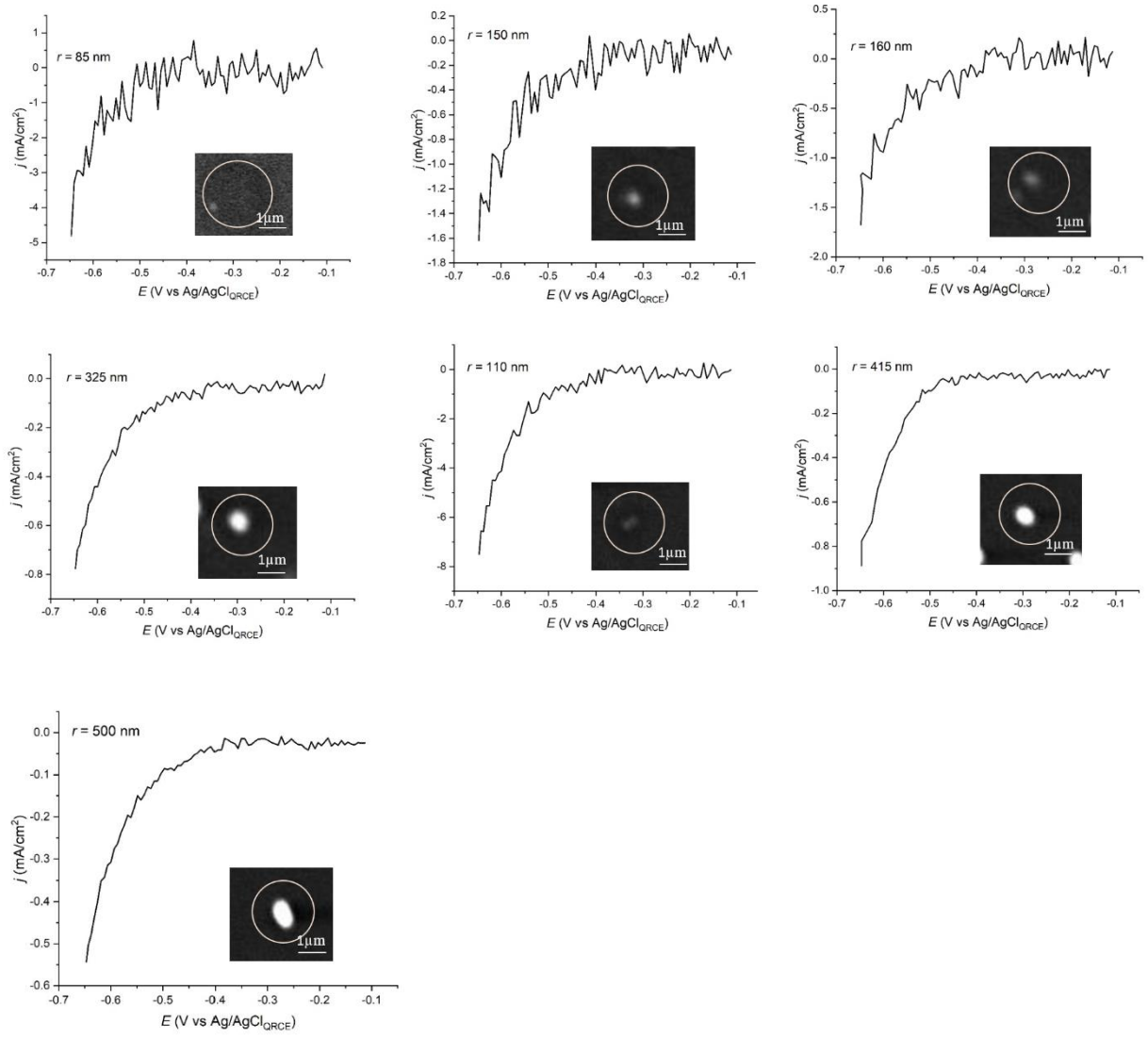

Figure A.7 SECCM LSVs of individual silver particles and their corresponding SEM image.

ANNEXE B Supporting Information

Single-Particle Electrocatalysis and Kinetic Insights with Scanning Electrochemical Cell Microscopy (SECCM)

B.1 Growth of Platinum particles using electrodeposition

Potassium hexachloroplatinate IV (K_2PtCl_6 98%) from Sigma-Aldrich, and hydrochloric acid (HCl 36.5 to 38.0%) were purchased from Fisher Scientific. Glassy carbon used as a substrate, and deionized water (18.2 MΩ cm) was used for electrodeposition.

Before electrodeposition, the electrode was cleaned by sequential polishing with monocrystalline diamond suspension of decreasing particle sizes (3.0, 1.0, 0.5, and 0.25 μm). After each polishing, it was sonicated first in a 1:1 ethanol-to-water mixture for 1 minute, followed by 5 minutes in deionized water. The electrode was then dried under a flow of argon gas.

A three-electrode setup was used, comprising a Biologic (SP-300) potentiostat, a platinum mesh as the counter electrode, the glassy carbon as the working electrode, and an Ag/AgCl (3 M KCl) as a reference electrode. The electrodeposition was performed in an aqueous solution containing 5 mM K_2PtCl_6 and 100 mM HCl using a galvanostatic method with a constant current density of -1 mA/cm^2 for 15 seconds. After deposition, the electrode was rinsed three times with deionized water and subsequently characterized by scanning electron microscopy (SEM) using a JEOL JSM-IT800 microscope equipped with an energy-dispersive X-ray spectroscopy (EDS) detector (Oxford Instruments) (Figure B.1). Structural analysis was further performed using X-ray diffraction (XRD) (Figure B.2).

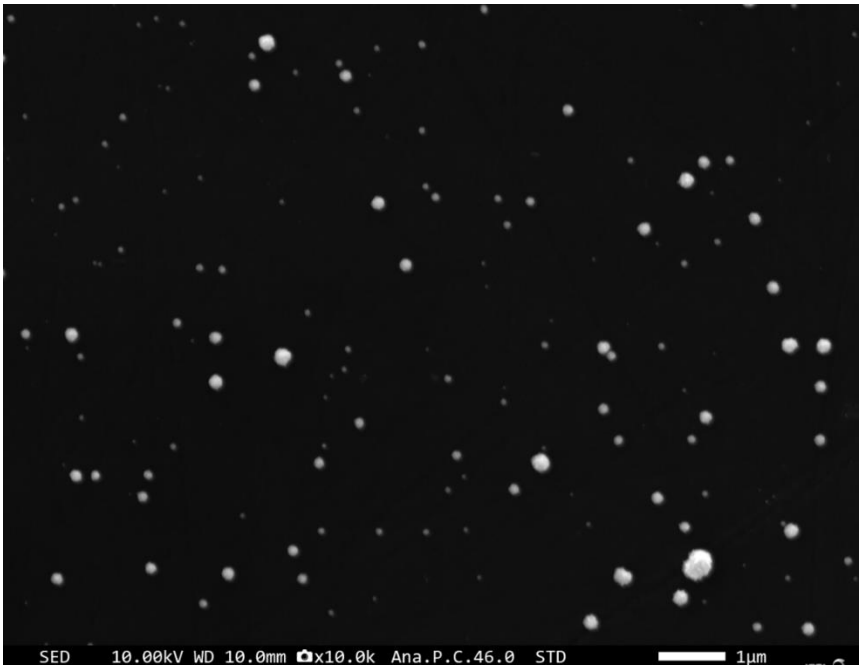

Figure B.1 Scanning electron microscope image of glassy carbon substrate modified with Pt particles

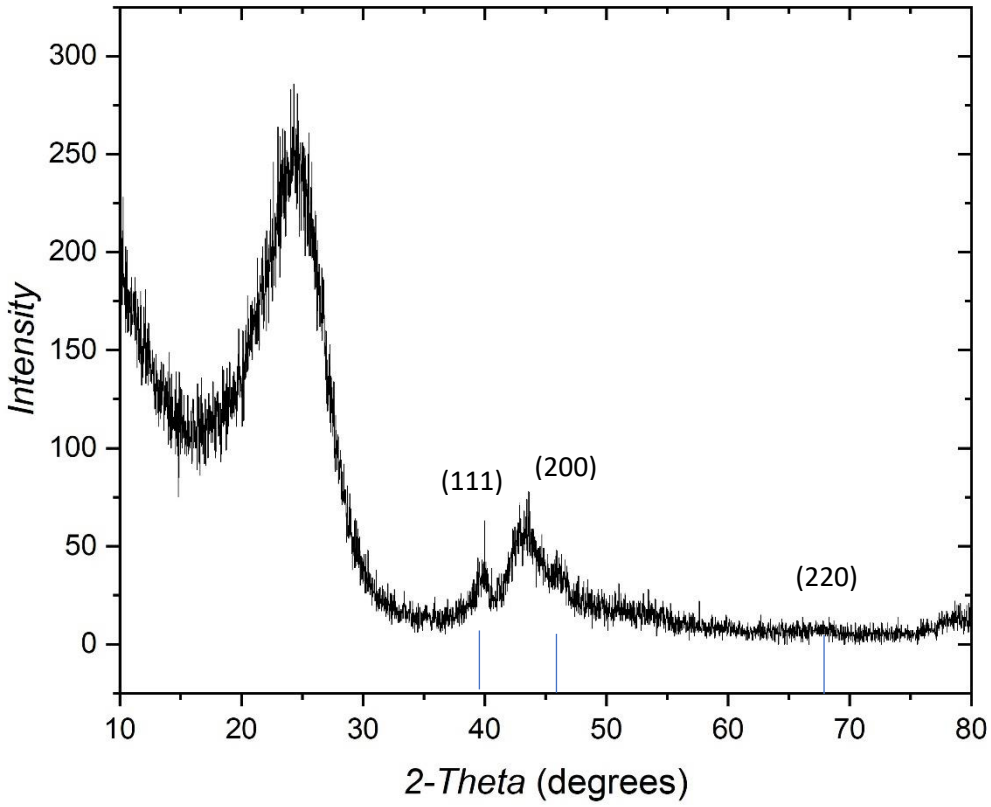

Figure B.2 XRD analysis of glassy carbon substrate modified with Pt particles. The sample were prepared using the same method explained above; electrodeposition in an aqueous solution containing 5 mM K_2PtCl_6 and 100 mM HCl using a galvanostatic method with a constant current density of -1 mA/cm^2. The current was applied for an extended duration to ensure the formation of a uniform film suitable for XRD analysis.

B.2 Pipet preparation

Quartz capillaries (0.8 mm ID × 1.00 mm OD, VitroCom) were used to fabricate pipets with a laser puller (P-2000, Sutter Instrument). A single-step program (HEAT 700, FIL 4, VEL 55, DEL

130, PUL 55) was employed to produce pipets with a tip diameter of around 1.8 µm that were characterized using JEOL JSM-IT800 Scanning electron microscope (Figure B.3). To enhance hydrophobicity and confine the aqueous droplet to the tip, the outer sidewall of the pipet was

silanized with dimethyldichlorosilane ($Si(CH_3)_2Cl_2$, 99.5%) by connecting the back of the pipet (wide end) to a fine piece of tubing that's connected to a regulated dry N_2 line.

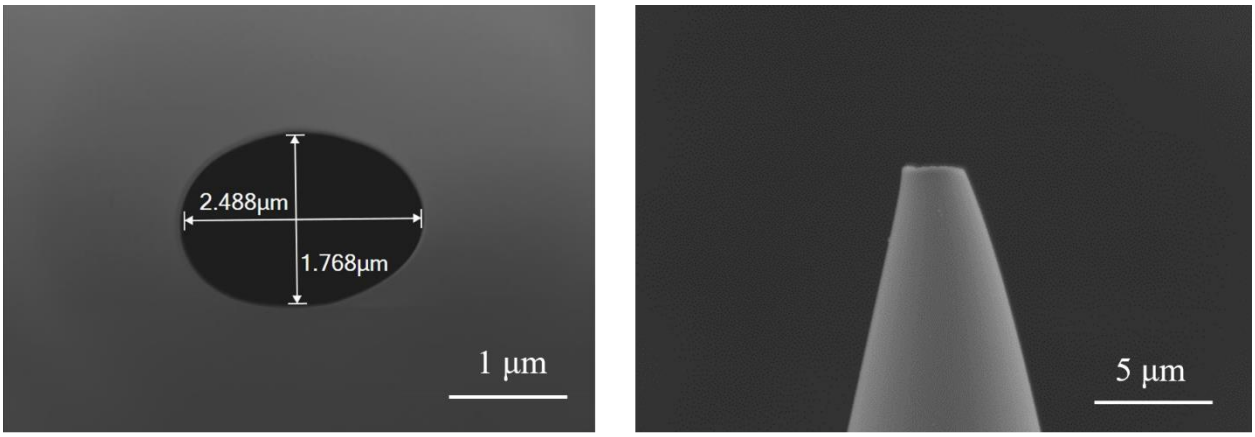

Figure B.3 SEM image of the SECCM pipet with a tip diameter of around 2 µm.

B.3 Scanning Electrochemical Cell Microscopy (SECCM)

The pipet was filled with an electrolyte solution containing 100 mM H_2SO_4 and a Pd/H_2 wire as a QRCE, which was prepared by applying a -3.0 V bias between a palladium electrode and a platinum wire counter electrode for 10 minutes in a two-electrode configuration with 0.05 M sulfuric acid. The initiation of the hydrogen evolution reaction (HER) on the palladium electrode was confirmed by the formation of hydrogen bubbles, indicating its saturation with hydrogen.

Pipette positioning, localized electrochemical measurements, and data acquisition were conducted using a HEKA ElProScan scanning electrochemical microscope. A hopping mode was employed to perform a matrix scan of 13 × 13 for a total of 169 measurement points over a 100 µm × 100 µm area on a glassy carbon substrate containing Pt particles. The diameter of the residual electrolyte droplet after measurement was approximately 2 µm matching the outer diameter of the pipette for a well-confined electrochemical cell to perform localized measurements.

After completing the electrochemical mapping, SEM images of the substrates were captured using a JEOL JCM6000plus scanning electron microscope.

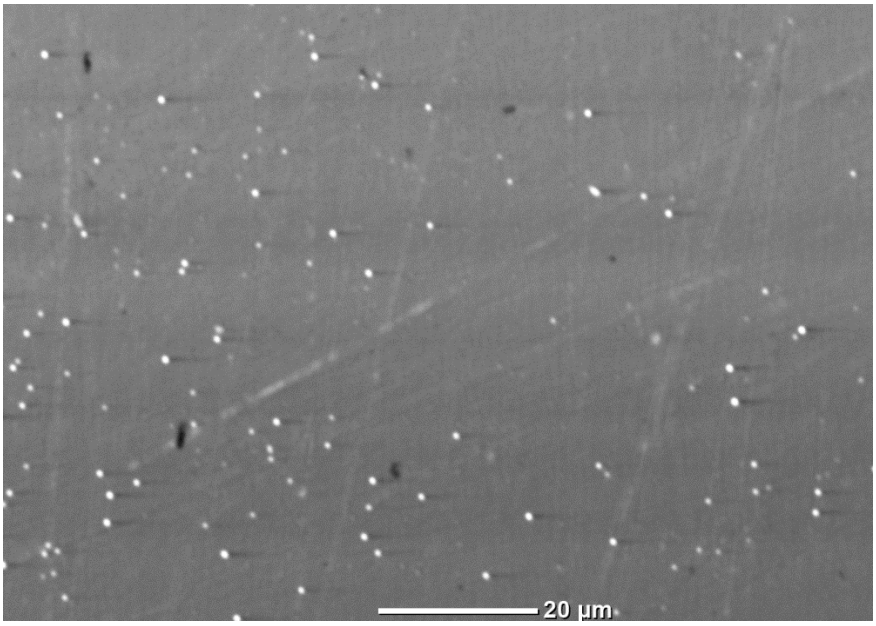

Figure B.4 The area of the glassy carbon substrate where the SECCM was performed.

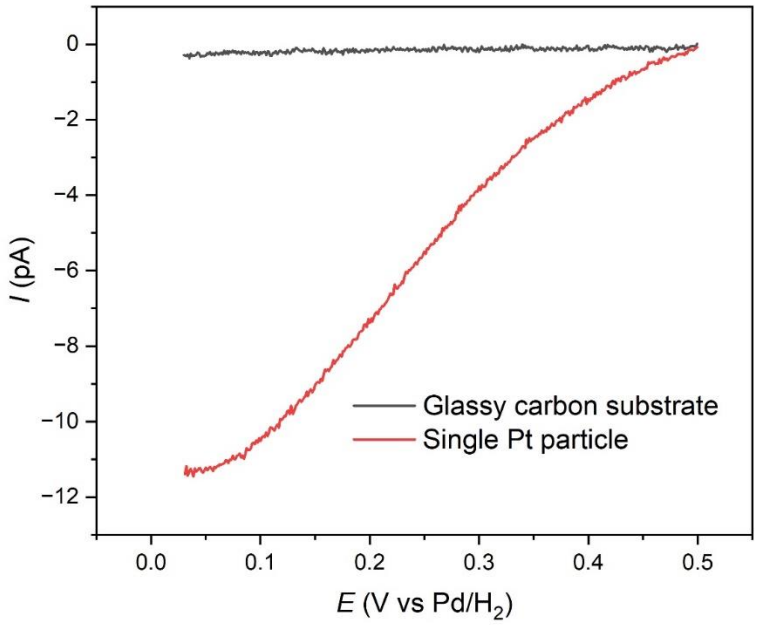

Figure B.5 SECCM LSVs of ORR (black) on glassy carbon substrate, and (Red) on glassy carbon substrate containing Pt particle. Demonstrating no current activity for glassy carbon substrate at this range of potential.

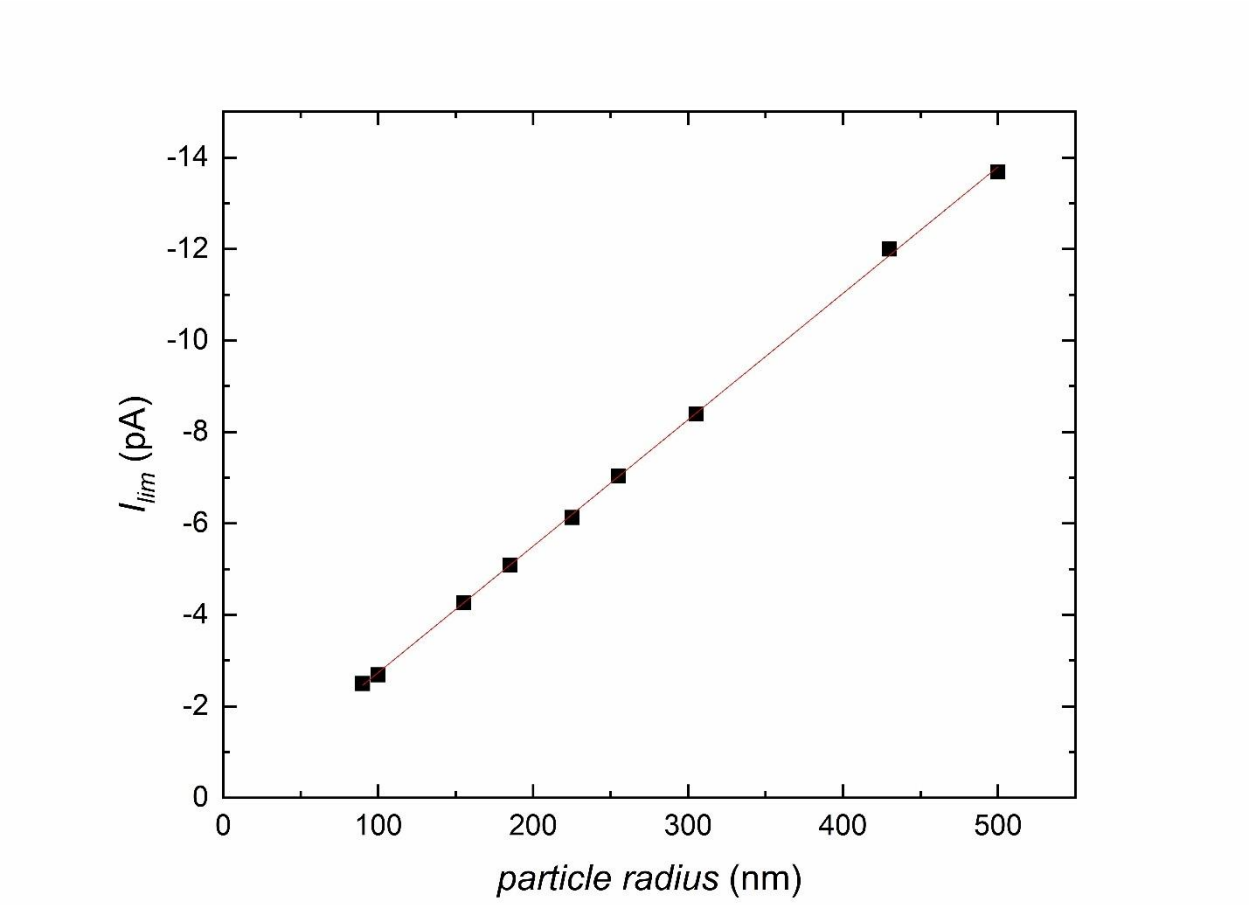

Figure B.6 Dependence of diffusion-limited current on platinum particle radius during the oxygen reduction reaction (ORR) measured using SECCM. Each data point represents the limiting current extracted from LSVs at 0.08V vs RHE at individual particles. The observed increase in limiting current (I_{lim}) with particle radius (r) reflects the direct relation between particles surface area and diffusion limiting current.

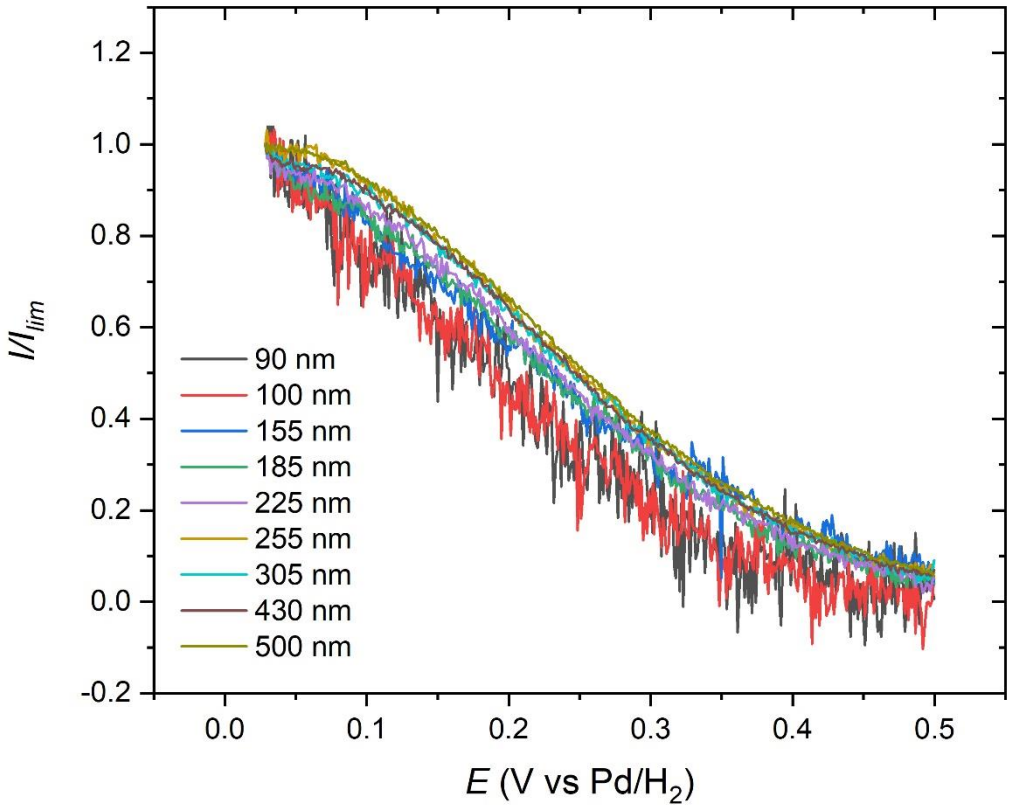

Figure B.7 Normalized SECCM LSVs (the ORR currents were normalized by mass transport limited current.

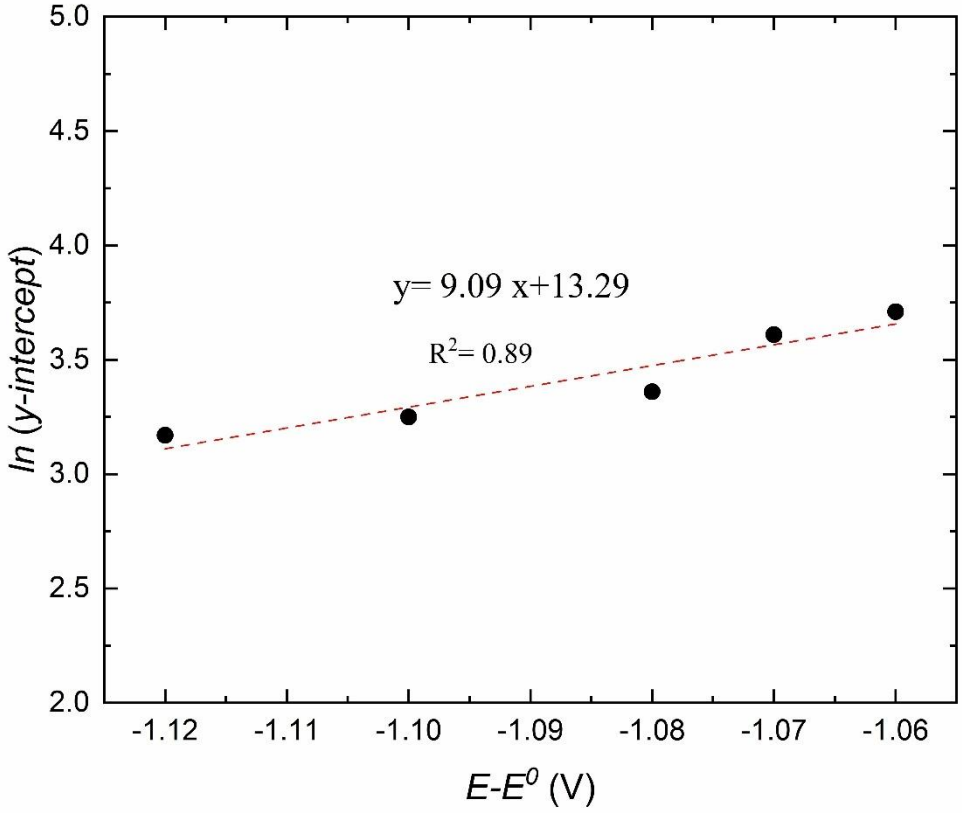

Figure B.8 Linear plot of ln(*y*-intercept) vs ($E - E^0$) obtained from K-L analysis for ORR. Both α and k^0 can be determined from the slope and the intercept respectively based on $\ln(y - intercept) = \ln\left(\frac{1}{Fk^0 C_{O_2}}\right) + \frac{\alpha F}{RT}(E - E^0)$.

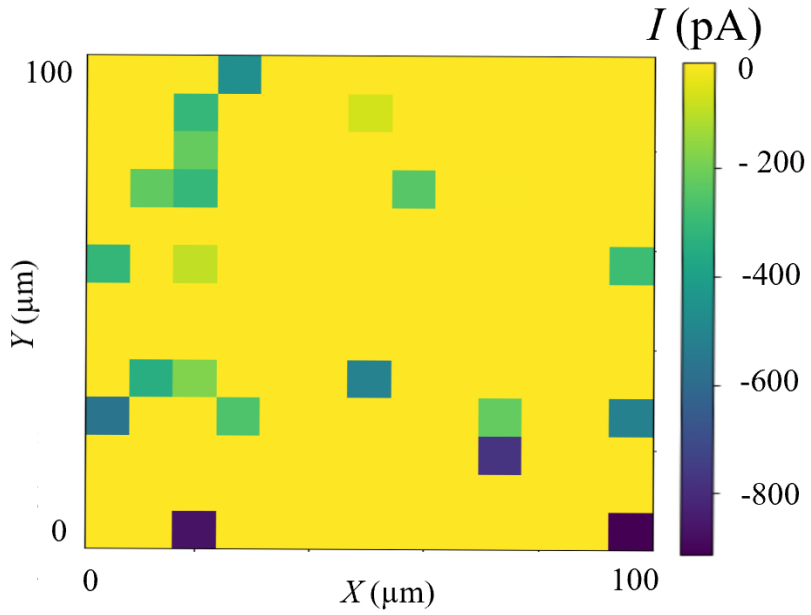

Figure B.9 SECCM electrochemical map of HER obtained at -0.2 V (vs Pd/H_2 QRCE) across the carbon supported platinum substrate.

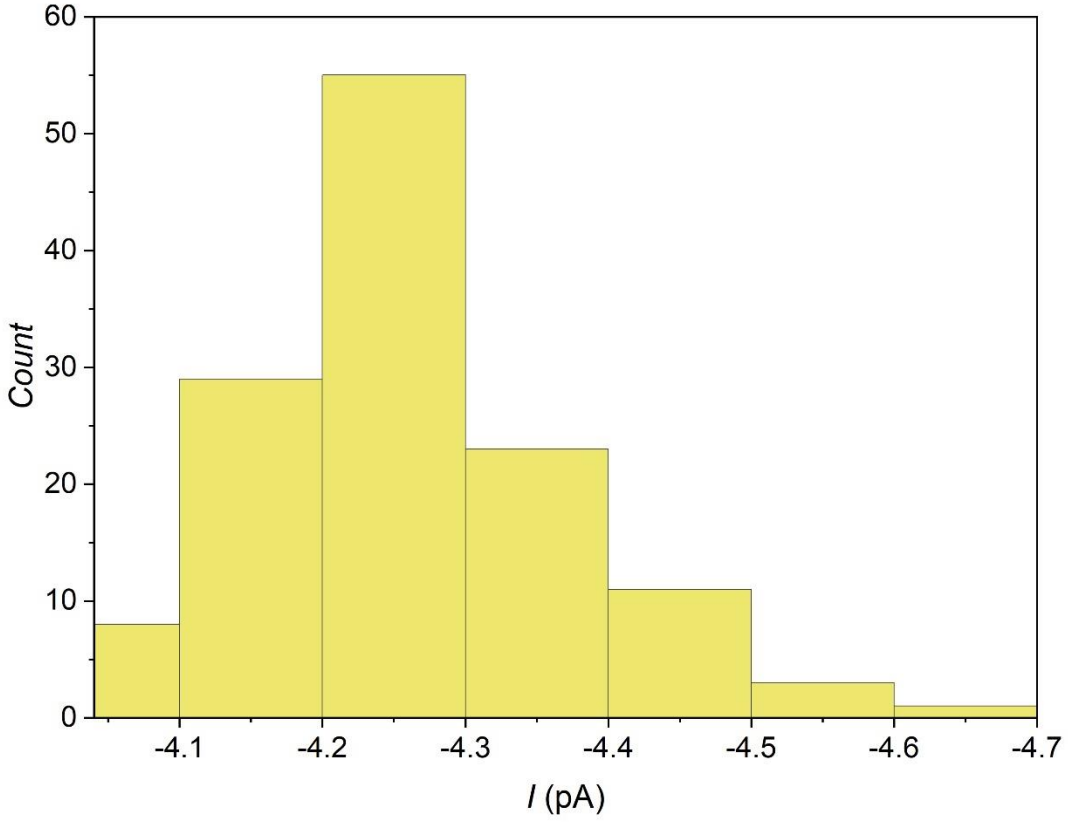

Figure B.10 Histograms of current at -0.2 V vs Pd/H_2 for the scanned area, where the pipet landed on bare carbon substrate in an aqueous solution of 0.1 M H_2SO_4.

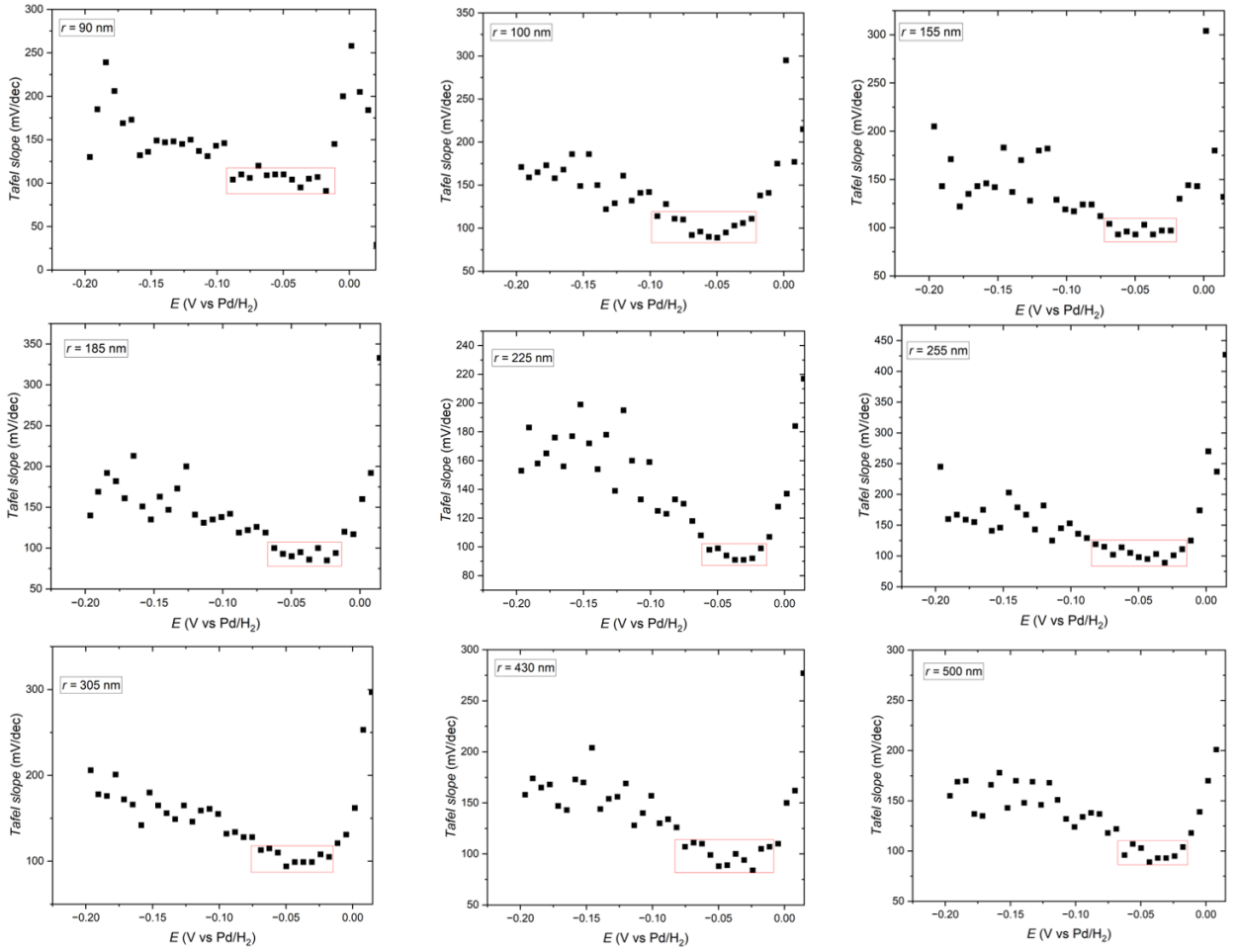

Figure B.11 Tafel slope plot as a function of potential of the SECCM HER on individual platinum particle on glassy carbon substrate in 0.1 M H_2SO_4.

B.4 Finite element modeling

Finite element modeling (FEM) was used to simulate the hydrogen evolution reaction (HER) on individual Pt particle supported on a glassy carbon substrate. The model was designed to mimic the geometry of SECCM, incorporating a pipet tip with a 2 μm diameter filled with electrolyte (100 mM H_2SO_4). By solving the coupled Butler–Volmer equations at the electrode-electrolyte interface, we were able to reproduce the LSVs for particles (90 nm to 500 nm in diameter) and visualize local proton concentration gradients, supporting the experimentally extracted kinetic parameters. Boundary conditions are applied to regions 1 to 5. (1) Electrolyte and glassy carbon substrate interface when the surface of substrate remains inactive, insulating glass walls (2), bulk

condition (3), the active electrode surface which is the surface of hemisphere particle (4), and droplet-air interface.

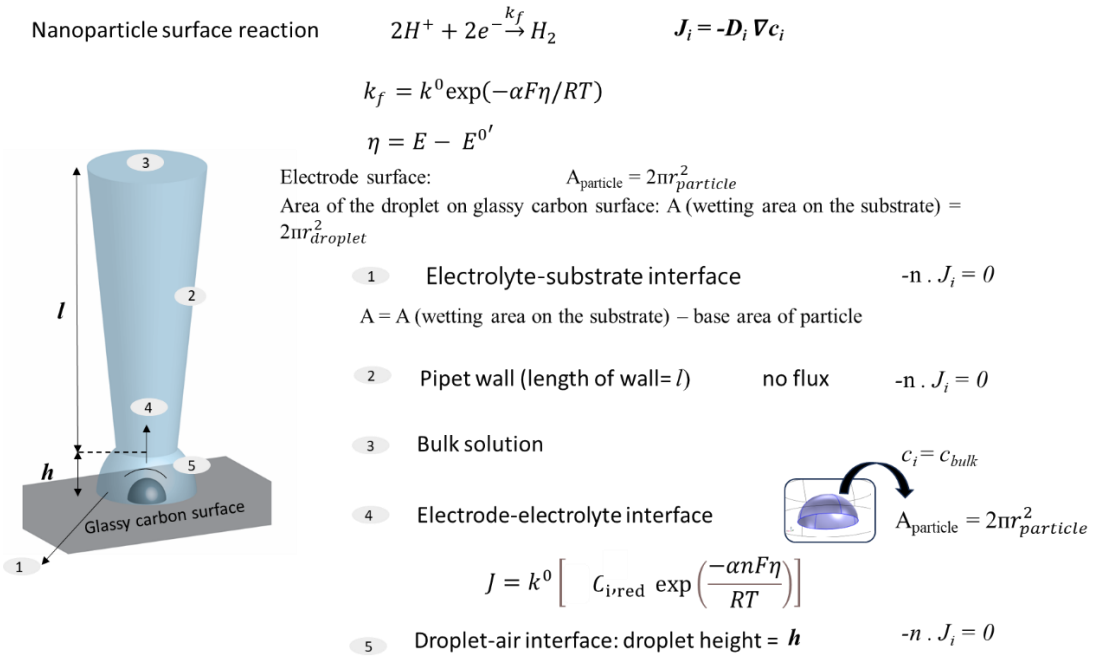

Figure B.12 Geometric model and boundary conditions used in COMSOL simulations of nanoparticle-catalyzed HER under a droplet. The geometry represents a nanodroplet confined between the pipet tip and a glassy carbon substrate partially covered by a single particle. The simulation domain includes: (1) the electrolyte–substrate interface, where the electrochemically active area is the exposed surface of the nanoparticle where $A_{particle}=2\pi r_{particle}^2$, and the total wetted area is $A=\pi r_{droplet}^2$ (2) the pipet glass wall of length l with no-flux boundary condition, (3) the bulk solution of the droplet, with species concentrations $c_i=c_{bulk}$ (4) the electrode–electrolyte interface, where HER follows Butler–Volmer kinetics, and (5) the droplet–air interface of height h, also defined as a no-flux boundary. Species flux is by Fick's law, $J_i=-D_i \nabla c_i$, with $\eta=E-E^0$ representing the overpotential.

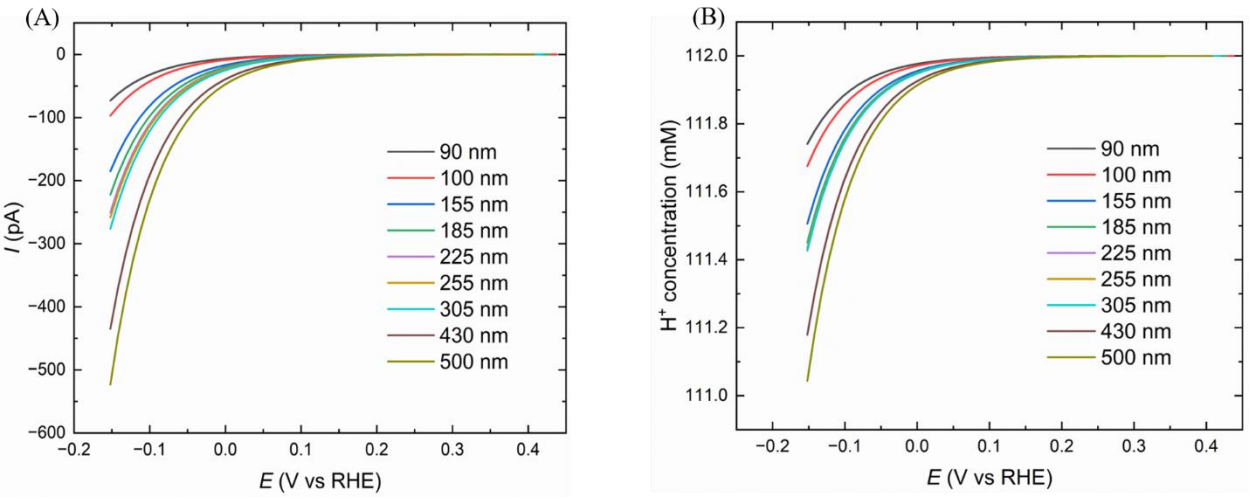

Figure B.13 Finite element simulations of the hydrogen evolution reaction (HER) on individual Pt particles (90–500 nm in diameter) supported on a glassy carbon substrate in 100 mM H_2SO_4. Simulations were performed using a SECCM configuration with a pipet tip diameter of 2 μm and a scan rate of 20 mV s^{-1}. (A) Simulated LSV curves (B) Corresponding profiles of proton (H^+) concentration, illustrating local depletion near the particle surface during HER.

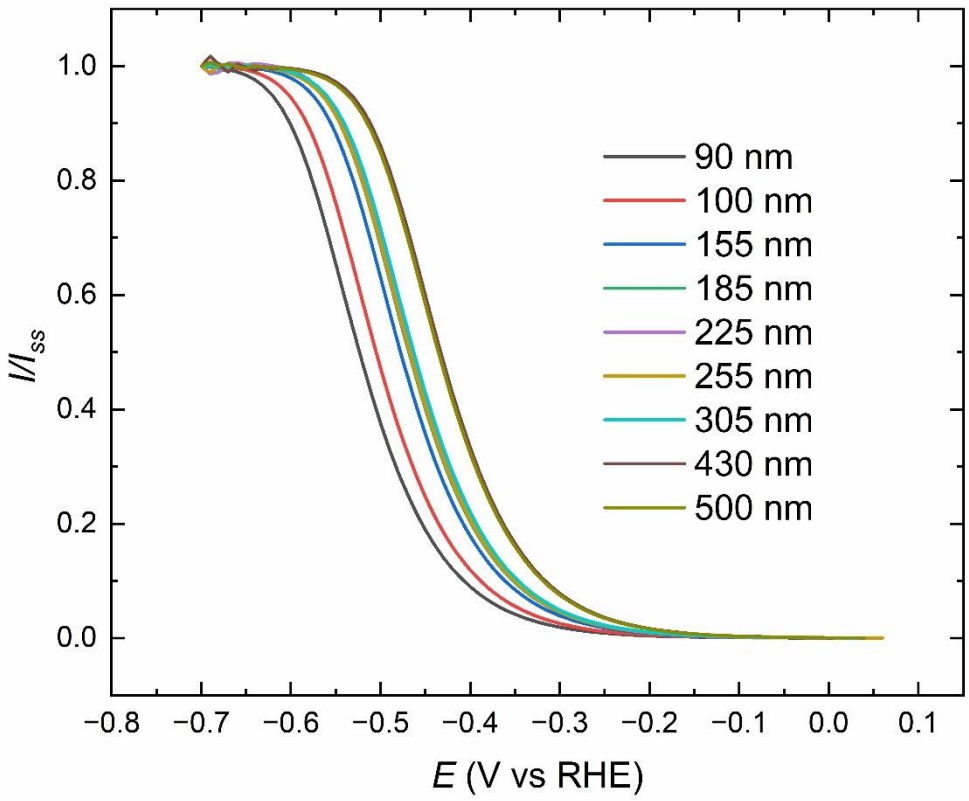

Figure B.14 Finite element simulations of the hydrogen evolution reaction (HER) LSVs on individual platinum particles (90–500 nm) on a glassy carbon substrate in 100 mM H_2SO_4, using kinetic parameters extracted from SECCM experiments. Simulations were performed using a pipet tip diameter of 2 μm and a scan rate of 20 mV s^{-1} over an extended potential range, accessing the mass transport-limited regime and validating the experimentally obtained kinetic parameters.

ANNEXE C Supporting Information

Steady-state Voltammetry in Ionic Liquids using Scanning Electrochemical Cell Microscopy

C.1 Pipet fabrication

Pipets were fabricated using quartz capillaries (0.8 ID x 1.00 OD VitroCom) and a laser puller (P-2000, Sutter instrument). A one step program applied for each pipet diameter as follow:

***r* = 110 nm**

HEAT 485, FIL 1, VEL 30, DEL 145, and PUL 175

***r* = 135 nm**

HEAT 520, FIL 1, VEL 45, DEL 145, and PUL 175

***r* = 255 nm**

HEAT 700, FIL 4, VEL 55, DEL 130, and PUL 70

***r* = 380 nm**

HEAT 730, FIL 4, VEL 55, DEL 130, and PUL 70

C.2 SECCM cyclic voltammograms at different scan rates

To study the effect of scan rate, each voltammetric measurement was initiated by landing the SECCM tip on the substrate at +0.6 V (vs Ag wire QRCE), followed immediately by a potential

sweep from +0.6 V to +0.2 V and then back to +0.6 V to obtain a full cyclic voltammogram (Figures S1A-E). There was no potential hold applied before the scan. The meniscus made contact and the potential sweep started immediately. For the overlaid linear sweep voltammograms (LSVs) shown in Figure C.2F, the anodic sweep from +0.2 V to +0.6 V was extracted from the corresponding CVs directly, and no background subtraction or signal correction was applied. The data are presented as acquired for all cyclic voltammograms (Figures C.2A–E). Scan rates between 5 mV s^{-1} and 100 mV s^{-1} were compared, and even at the slowest scan rate, a slight time dependent response was observed during the negative scan direction. For the slowest scan rate, a slight hysteresis is observed during the negative sweep at potentials less positive than the half-wave potential. This hysteresis becomes more pronounced at higher scan rates, which may, in part, result from the scan protocol used to acquire the cyclic voltammograms (e.g. landing at a positive potential and sweeping the potential to a negative potential. This was not how the LSVs in the main text were obtained. All of the LSVs in the main text were obtained by landing at potential of – 0.6 V and scanning to +0.6 V. Figure C.1G presents overlapping LSVs (positive scan direction) obtained at 10 mV/s and 100 mV s^{-1} where they overlap within error between two separate landing sites. Figure C.1H presents overlapping CVs obtained at 10 mV s^{-1} and 100 mV s^{-1}. For the 10 mV s^{-1} CV, a slight hysteresis is observed during the negative sweep at potentials less positive than the half-wave potential. This hysteresis becomes more pronounced at 100 mVs^{-1}. Because all measurements in the positive scan direction exhibited a similar steady-state response across scan rates, and the hysteresis was most pronounced at the foot of the wave during the reverse scan, a protocol using a scan rate of 100 mV s^{-1}, beginning from a negative potential and scanning in the positive direction was used to reduce the measurement time. Further evaluation of the time-dependent response was done using time-dependent finite element modelling (Figure C.3). Details of the model are included in Section C.6 and a COMSOL model report with full details is included as an additional supplementary file. Figure C.2 presents an overlay of the experimental and time dependent element modelling for CVs obtained at (A) 10 mV s^{-1} and (B) 100 mV s^{-1}. It can be observed that in both cases the shapes of the LSVs are quite similar in the positive scan direction. In the case of the negative scan direction, a more pronounced hysteresis is observed in the experimental CVs compared with the simulated CVs. Attempts were made to use a different value of the diffusion coefficient for the oxidized species, ferrocenium. However, this did not recreate the hysteresis observed during the scan in the negative direction. The time-dependent simulation

used a value $D = 4.3\text{x}10^{-7}$ cm^2 s^{-1} and $k^0 = 0.01$ cm s^{-1}. While the values of the heterogeneous rate constant for charge transfer are the same for both the time-dependent model and the experimental values, the value of the diffusion coefficient was 10% larger for the time-dependent model compared to the analytical model, which is within range of what has been previously reported by Anderson et al.(Anderson, K. L. et Edwards, 2023)

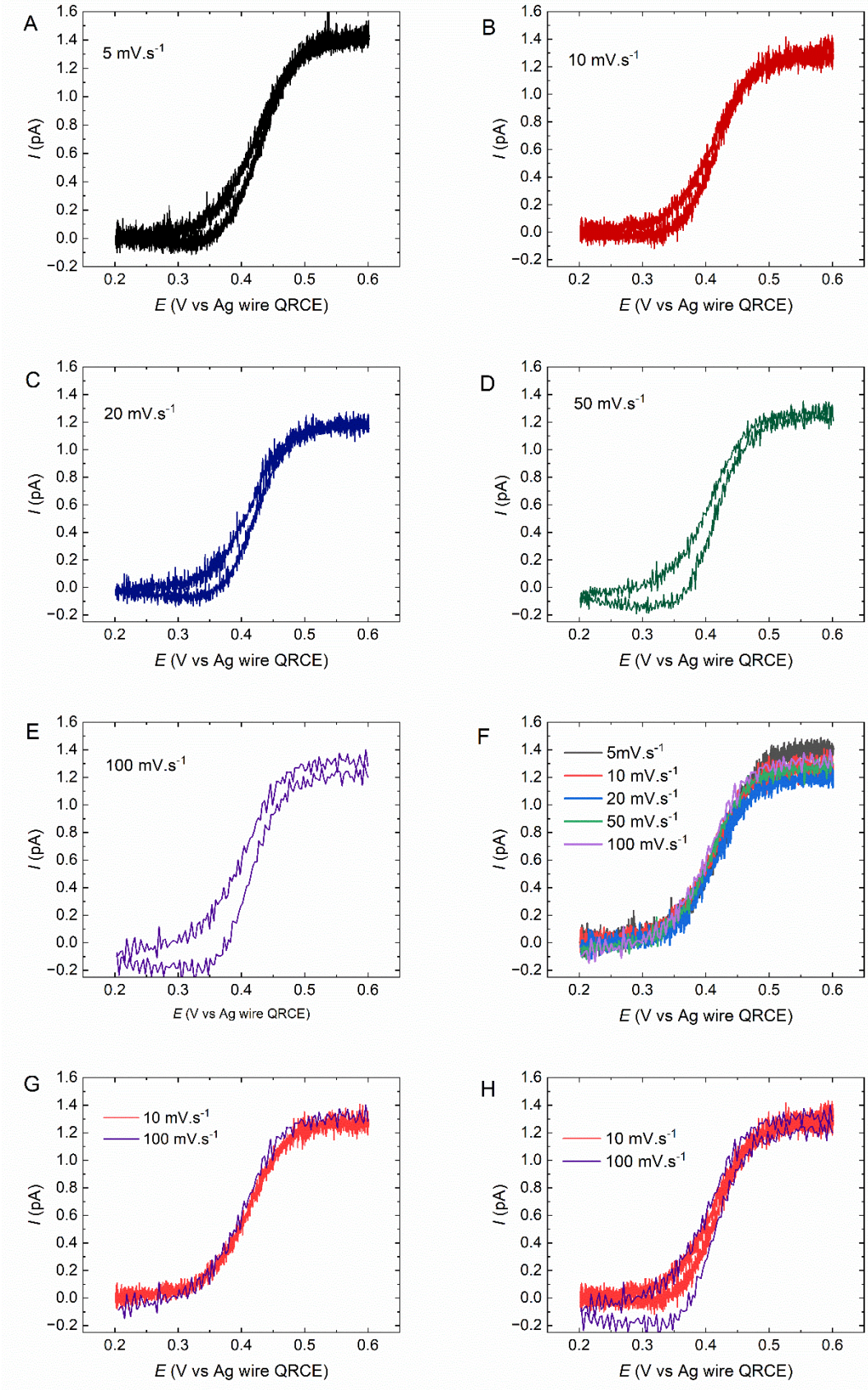
A
5 mV.s-1
B
10 mV.s-1
C
20 mV.s-1
D
50 mV.s-1
E
100 mV.s-1
F
5mV.s-1
10 mV.s-1
20 mV.s-1
50 mV.s-1
100 mV.s-1
G
10 mV.s-1
100 mV.s-1
H
10 mV.s-1
100 mV.s-1
I (pA)
E (V vs Ag wire QRCE)

Figure C.1 SECCM cyclic voltammograms of 2 mM ferrocene/ferrocenium redox couple in [EMIM][BF_4] on a glassy carbon electrode using a pipet with a tip radius of 255 nm. Voltammograms were obtained at scan rates of (A) 5 mV s^{-1}, (B) 10 mV s^{-1}, (C) 20 mV s^{-1}, (D) 50 mV s^{-1}, and (E) 100 mV s^{-1} over a potential range of +0.2 to +0.6 V vs Ag wire QRCE. (F) Overlay of the anodic linear sweep from +0.2 V to +0.6 V was extracted from the corresponding CVs in A-E, highlighting the consistent shape and diffusion limited current plateau for anodic sweep across different scan rates. No background subtraction was applied, and the data are presented as acquired. The slight variations in limiting current (e.g., at 5 mV s^{-1}) are within the expected range for measurements performed using a pipet with a radius of 255 nm. (G) Overlay of anodic sweeps recorded at 10 and 100 mV s^{-1}. (H) Overlay of the cyclic voltammograms at 10 and 100 mV s^{-1}.

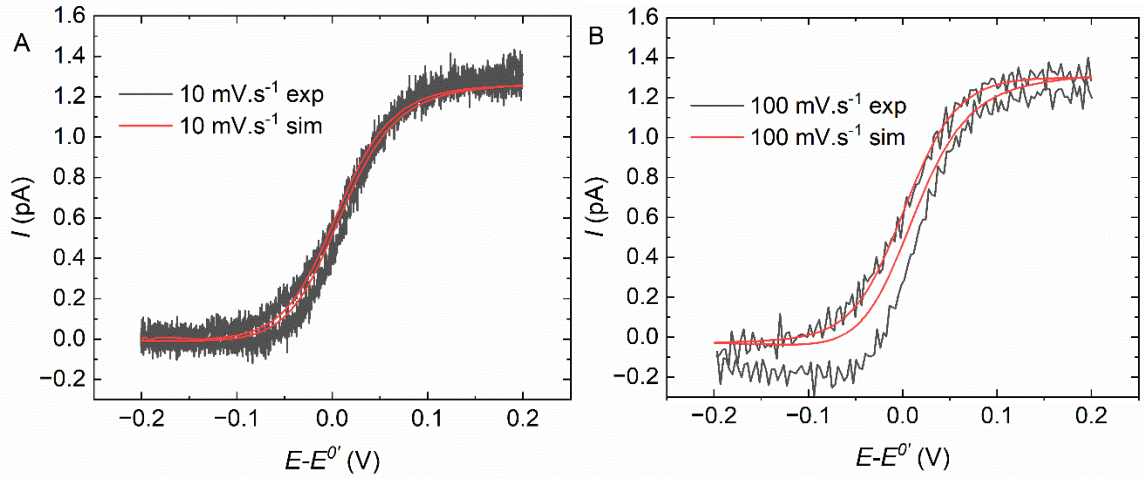

Figure C.2 Comparison of experimental and time-dependent finite element modelling CVs at (A) 10 mV.s and (B) 100 mV.s using a 510 nm diameter pipet. For the finite element modelling, values of $D = 4.3 \times 10^{-7}$ cm^2 s^{-1} and $k^0 = 0.01$ cm s^{-1} were used.

C.3 Characterization and Electrochemical mapping for limiting current and half-wave potential of SECCM Pipet with varying tip radii

The voltammetric hopping mode of SECCM was used to carry out linear sweep voltammogram (LSV) for the oxidation of 2 mM ferrocene in [EMIM][BF_4] at each landing site across the glassy carbon electrode surface with 100 mVs^{-1} scan-rate and Ag wire as QRCE. The total scanned area was 50 µm × 50 µm, with 25 data points collected for each pipet size.

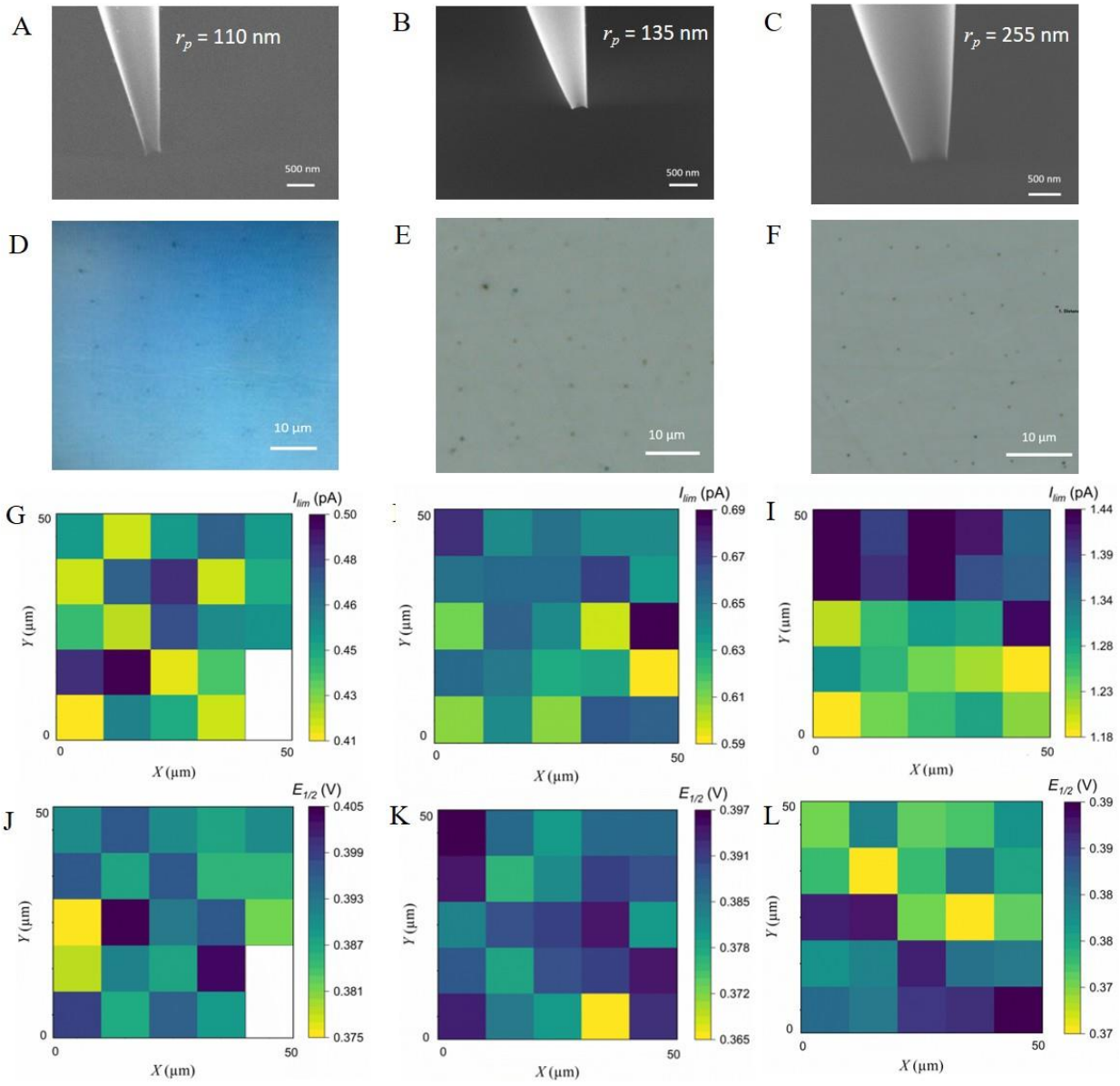

Figure C.3 Characterization of SECCM pipets with three different tip radii and corresponding electrochemical maps for oxidation of 2 mM ferrocene in [EMIM][BF_4] on glassy carbon electrode at a scan rate of 100 mV s^{-1} with Ag wire as QRCE. Columns correspond to pipet with tip radii of 110 nm (left), 135 nm (middle), and 255 nm (right). (A–C) Scanning electron microscopy (SEM) images of each pipet. (D–F) Optical microscope images of droplet contact areas on the glassy carbon surface. (G–I) Electrochemical maps of the limiting current (I_{lim}) obtained from 25 localized linear sweep voltammograms (LSVs) per pipet at (E-$E^{0'}$=0.15 V). (J–L) Corresponding maps

related to half-wave potential ($E_{1/2}$). The white regions in the map indicate unsuccessful measurement.

C.4 Propagation of error in pipet geometry

For the pipet geometry defined by $R_{eq}(1-\cos\gamma)$, the propagation of error, $\sigma_{R_{eq}(1-\cos\gamma)}$ normalized by the geometry is:

$$\frac{\sigma_{R_{eq}(1-\cos\gamma)}}{R_{eq}(1-\cos\gamma)} = \sqrt{\left(\frac{\sigma_{R_{eq}}}{R_{eq}}\right)^2 + \left[\left(\frac{\sin\gamma}{1-\cos\gamma}\right)\sigma_\gamma\right]^2}$$

Assuming a 10% error in the equivalent radius, σ_{Req}, Figure C.4 plots the variation in the relative standard error for the pipet geometry for 3 different errors in the half-angle of 0.25º, 0.5º, and 1º as a function of the pipet half-angle showing that as the pipet half-angle decreases, the relative error in the pipet geometry becomes larger.

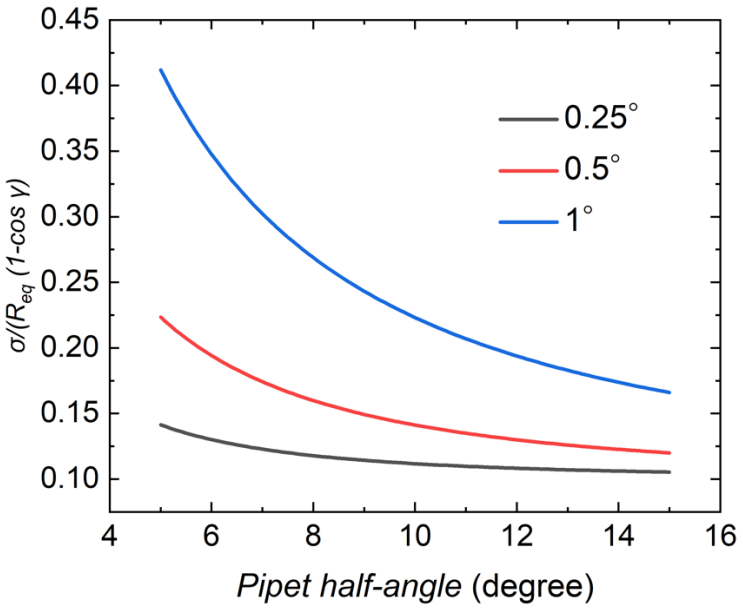

Figure C.4 Relative propagation of error in the pipet geometry as a function of pipet half angle.

C.5 Normalized LSVs

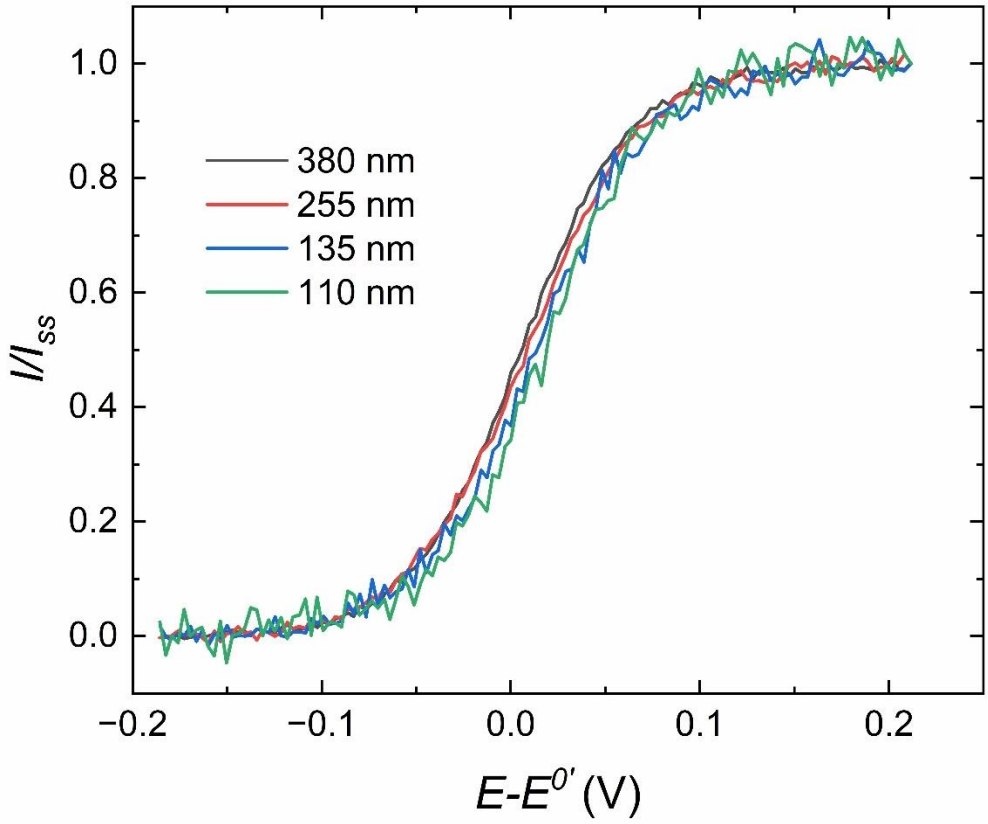

Figure C.5 Normalized average SECCM LSVs using pipets of tip radii 110 nm, 135 nm, 255 nm, and 380 nm for the oxidation of 2 mM ferrocene in [EMIM][BF_4] on a glassy carbon electrode.

C.6 Finite element modeling

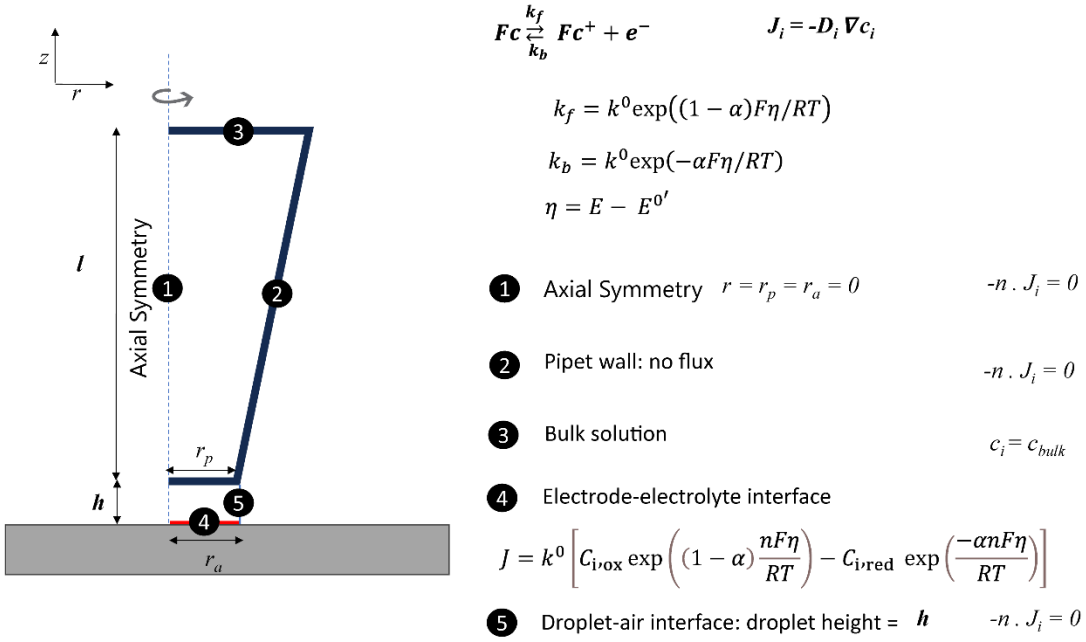

Figure C.6 Axisymmetric simulation domain used to model the SECCM pipet. Full geometry with a uniformly active substrate (region 4, in red), representing a conductive surface with radius r_a separated from the pipet tip by a distance h (droplet height). The pipet has an outer radius of r_p and length l. Boundary conditions are applied to regions 1–5, corresponding to axial symmetry (1), insulating glass walls (2), bulk condition (3), the active electrode surface (4), and droplet-air interface.

C.7 Individual Koutecký-Levich plot at different E-$E^{0'}$

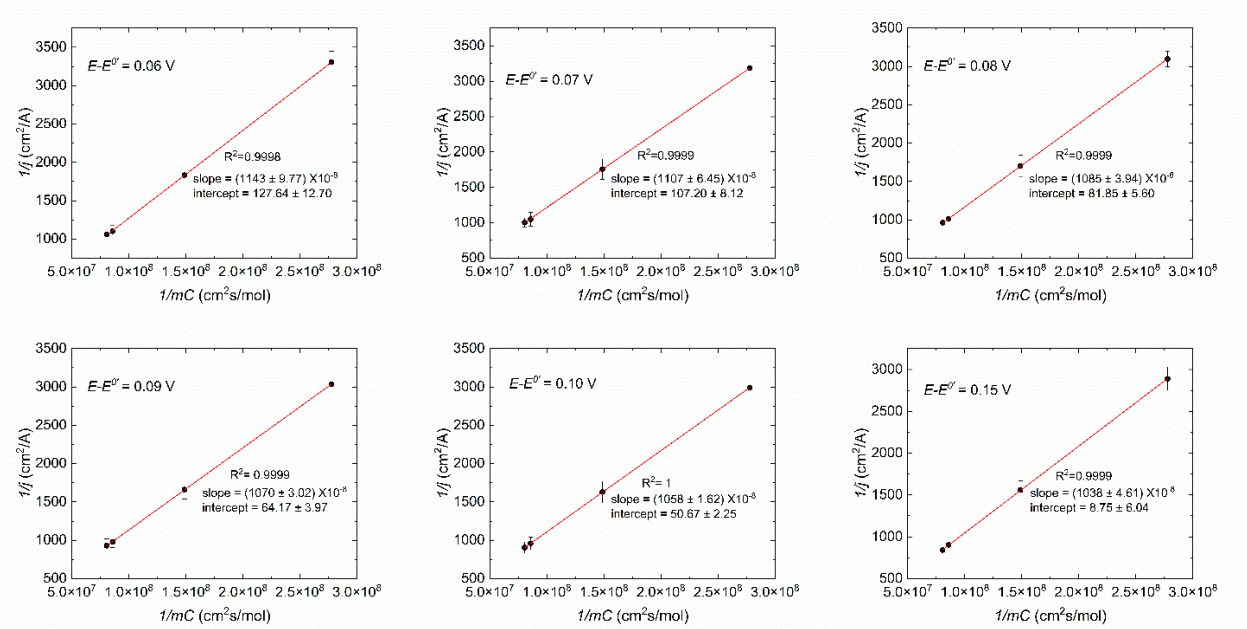

Figure C.7 Koutecký–Levich analysis for the oxidation of 2 mM ferrocene in [EMIM][BF_4] on glassy carbon electrode using SECCM pipets of varying tip radii, resulting in different mass transfer coefficients (m). Plots of $1/j$ versus $1/mC$ are shown at six different overpotentials $E - E_o'$ (from 0.06 V to 0.15 V). At each graph, the slope is constant to ~$1/F$ (Faraday constant) supporting the validity of the selected potential range for Koutecký–Levich analysis, while the intercepts vary with potential, reflecting changes in the kinetic contribution to the overall current. The data points associated with smaller pipets appear at smaller values of $1/mC$ (toward the lower end of the horizontal axis), whereas larger pipets, having smaller mass-transport coefficients (m), yield larger $1/mC$ values.

C.8 Analytical fitting

Each individual LSV was analyzed by fitting to analytical expressions, enabling the extraction of the local mass transport coefficient (m) and the standard heterogeneous rate constant (k^o) at each landing site and electrochemical maps were made to visualize the variation of $E_{3/4}$- $E_{1/4}$ and k^o across the glassy carbon surface using each pipet.

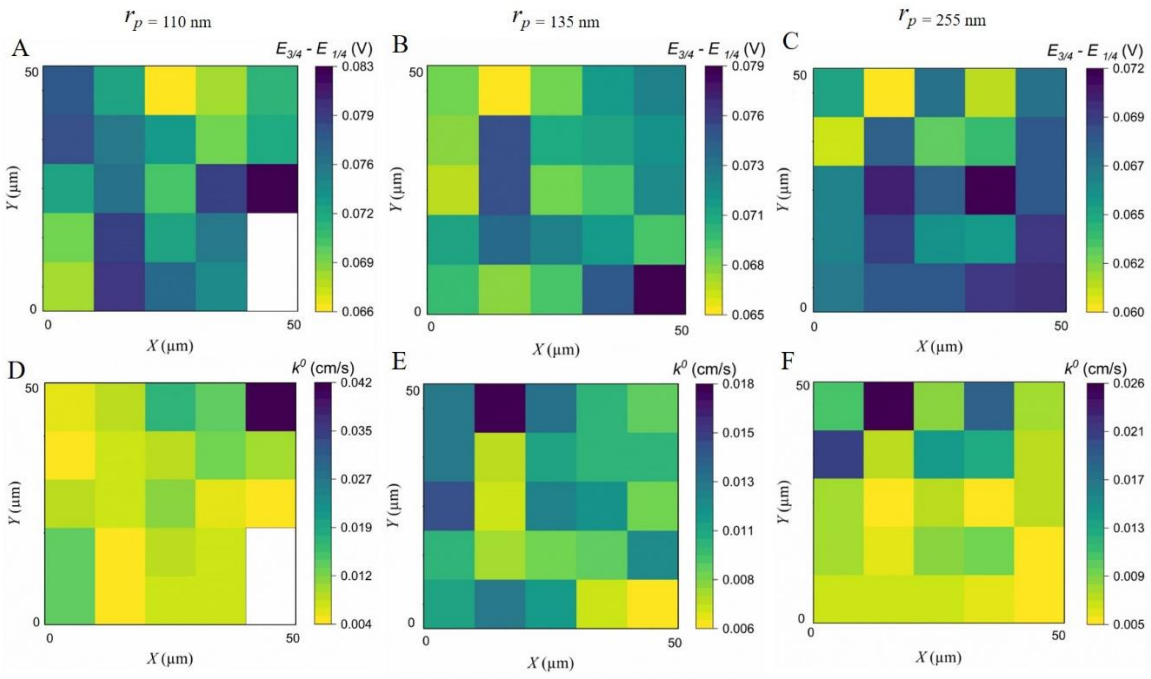

Figure C.8 Electrochemical maps for SECCM LSVs related to oxidation of 2 mM ferrocene in [EMIM][BF_4] on glassy carbon electrode, using pipets of three different radii. (A–C) Maps of $E_{3/4}-E_{1/4}$ extracted from individual linear sweep voltammograms, for pipet radii of 110 nm (A), 135 nm (B), and 255 nm (C). (D–F) Corresponding maps of the standard heterogeneous rate constant k^0, extracted by fitting the voltammograms for the same pipet sizes as in (A–C). The white regions in the map corresponded to locations where measurements or subsequent fitting analysis were not successful due to external noise.

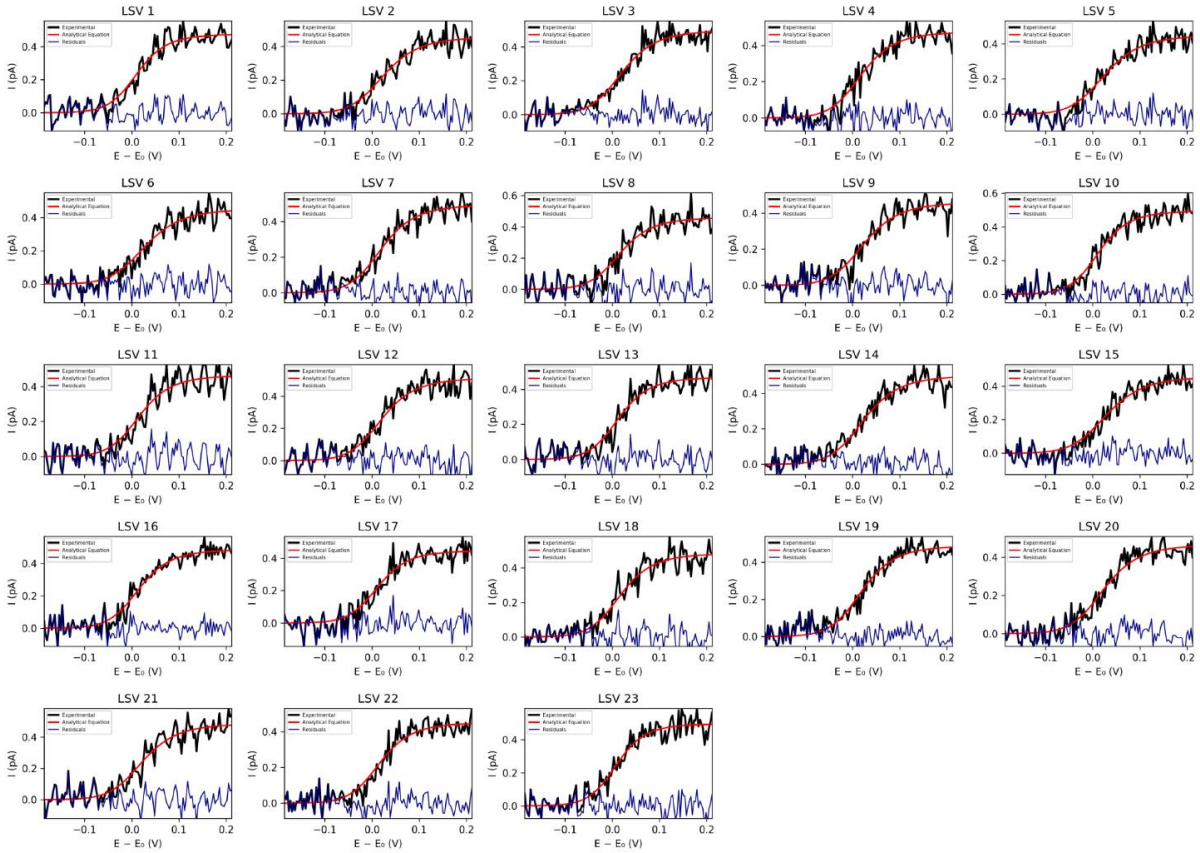

Figure C.9 Overlay of analytical expressions with individual linear sweep voltammograms (LSVs) at 23 distinct landing sites for the oxidation of 2 mM ferrocene in [EMIM][BF_4] on a glassy carbon electrode, using SECCM with a pipet tip radius of 110 nm at a scan rate of 100 mV s^{-1}. Residuals from each overlay are provided to evaluate the accuracy of the analytical representation.

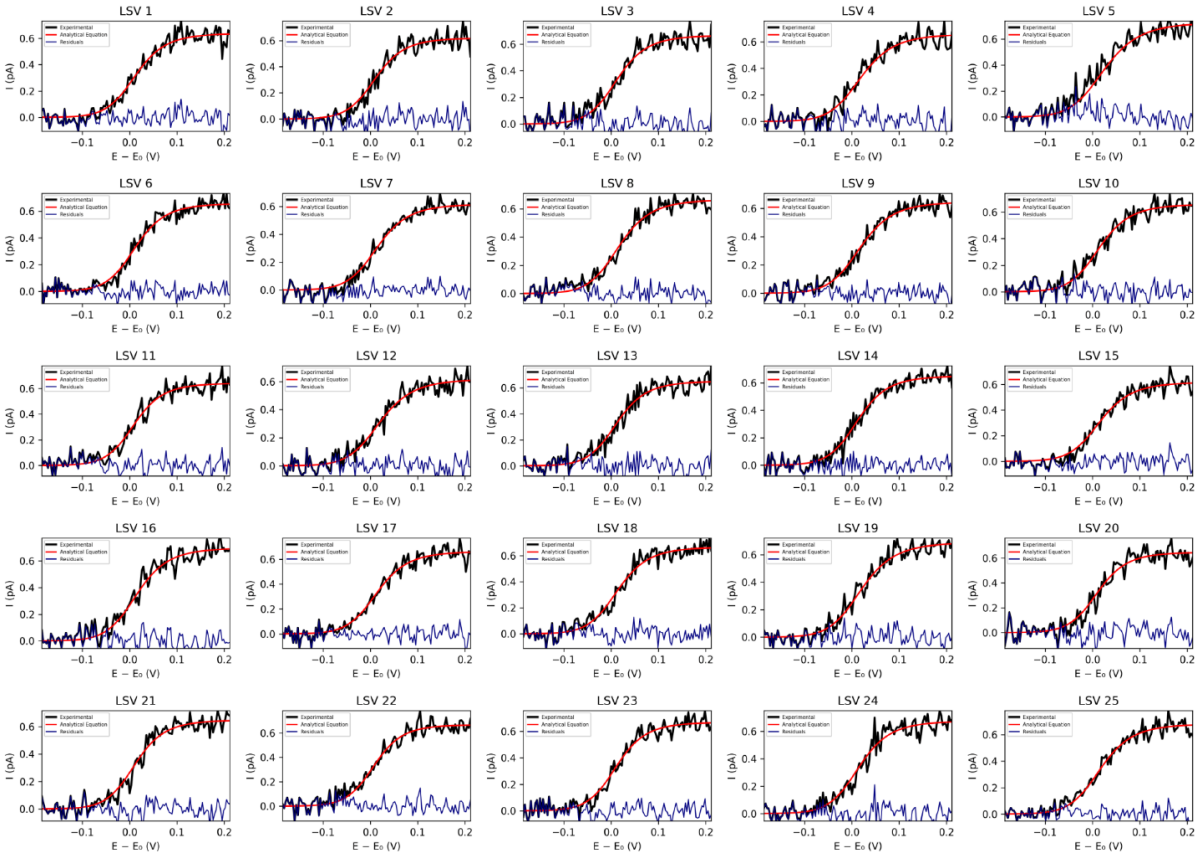

Figure C.10 Overlay of analytical expressions with individual linear sweep voltammograms (LSVs) at 25 distinct landing sites for the oxidation of 2 mM ferrocene in [EMIM][BF_4] on a glassy carbon electrode, using SECCM with a pipet tip radius of 135 nm at a scan rate of 100 mV s^{-1}. Residuals from each overlay are provided to evaluate the accuracy of the analytical representation.

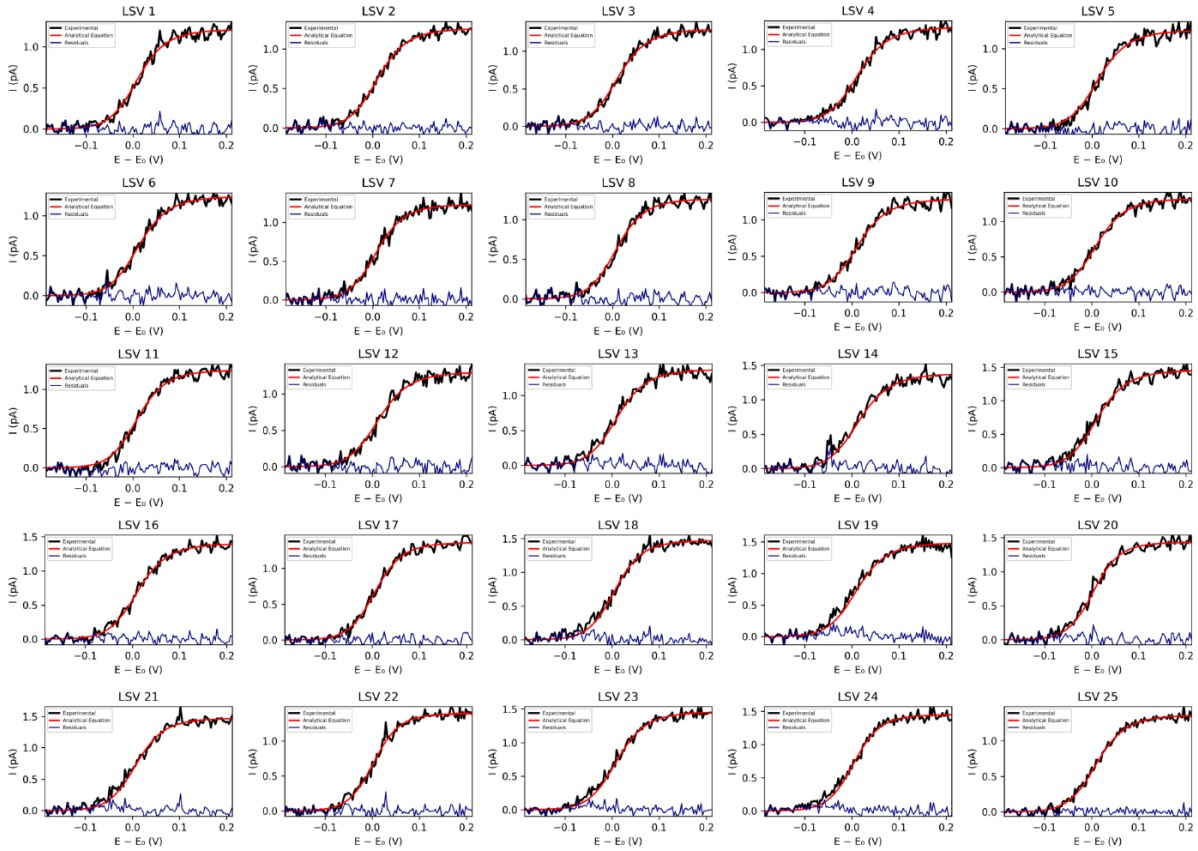

Figure C.11 Overlay of analytical expressions with individual linear sweep voltammograms (LSVs) at 25 distinct landing sites for the oxidation of 2 mM ferrocene in [EMIM][BF_4] on a glassy carbon electrode, using SECCM with a pipet tip radius of 255 nm at a scan rate of 100 mV s^{-1}. Residuals from each overlay are provided to evaluate the accuracy of the analytical representation.

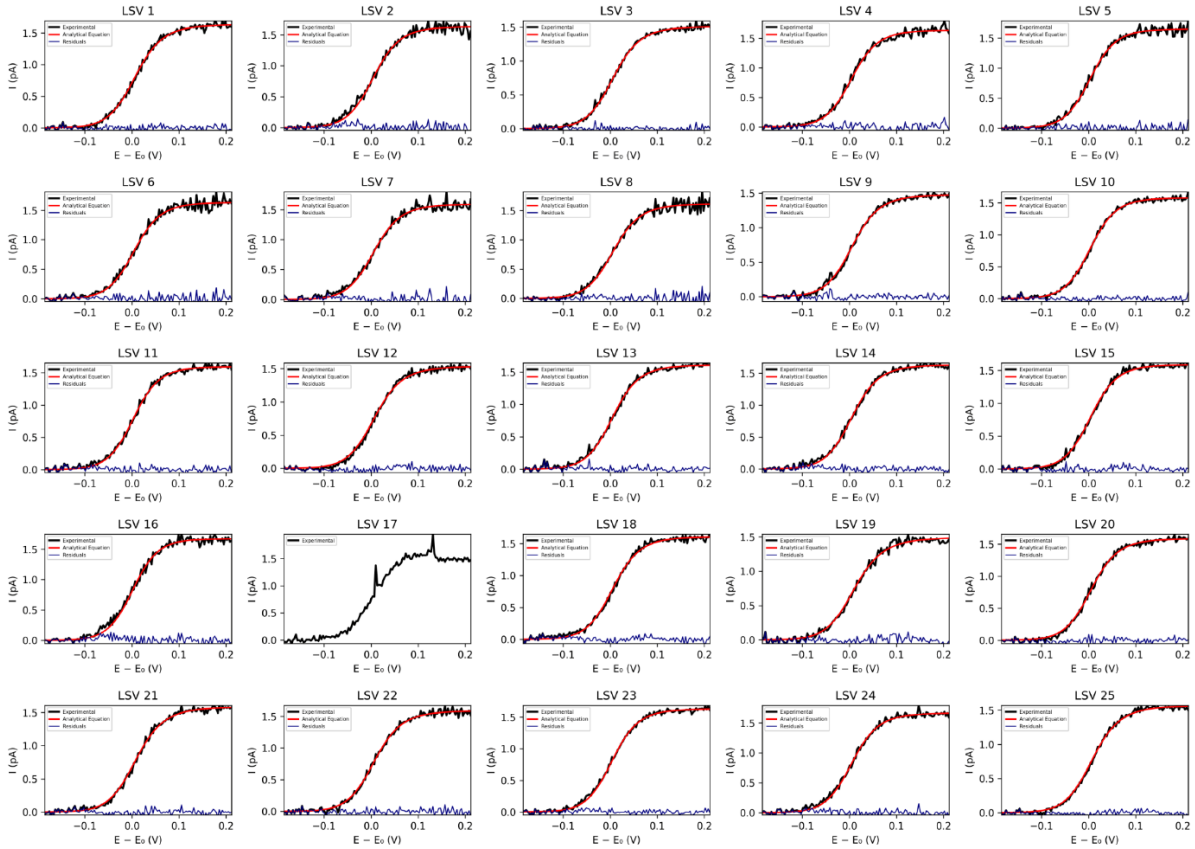

Figure 0.12 Overlay of analytical expressions with individual linear sweep voltammograms (LSVs) at 25 distinct landing sites for the oxidation of 2 mM ferrocene in [EMIM][BF_4] on a glassy carbon electrode, using SECCM with a pipet tip radius of 380 nm at a scan rate of 100 mV s^{-1}. Residuals from each overlay are provided to evaluate the accuracy of the analytical representation.

APPENDICE A

COMSOL Report for Chapter 3

Contents

1 Global Definitions

GLOBAL SETTINGS

USED PRODUCTS

Design Module
CAD Import Module
COMSOL Multiphysics
Corrosion Module

COMPUTER INFORMATION

1.1 PARAMETERS

1.1.1 Parameters 1

PARAMETERS 1

Name	Expression	Value	Description
r_NP	430[nm]	4.3E−7 m	
r_drop	1[um]	1E−6 m	
H_cell	10[um]	1E−5 m	
H_bottom	0.6*r_drop	6E−7 m	
r_bottom	sqrt(r_drop^2 - H_bottom^2)	8E−7 m	
r_top	r_bottom + H_pipette*tan(Pipette_cone_angle)	2.9702E−6 m	
Pipette_cone_angle	13[degree]	0.22689 rad	
H_pipette	H_cell - H_bottom	9.4E−6 m	
gap	30[nm]	3E−8 m	
DelT_R	H_cell*tan(Pipette_cone_angle)	2.3087E−6 m	

1.1.2 Parameters 2

PARAMETERS 2

Name	Expression	Value	Description
DcH	9e-5[cm^2/s]	9E−9 m^2/s	
DcH2	4.5e-5[cm^2/s]	4.5E−9 m^2/s	
cH_bulk	120[mM]	120 mol/m^3	
E_appl	-0.7[V]	−0.7 V	
Ef	0[V]	0 V	Formal potential

Name	Expression	Value	Description
i0ref	1[mol/(m^2*s)]*F_const	96485 A/m²	Reference exchange current density
E_start	-0.7[V]	−0.7 V	Start potential
E_vertex	0.04[V]	0.04 V	Vertex potential
E_step	10[mV]	0.01 V	Potential step (output)
ScanRate	20[mV/s]	0.02 V/s	
c0_H2	0[mM]	0 mol/m³	
c0_O2	0.27[mM]	0.27 mol/m³	

2 Component 1

2.1 DEFINITIONS

2.1.1 Nonlocal Couplings

Average 1

Coupling type	Average
Operator name	aveop1

SELECTION

Geometric entity level	Boundary
Name	Nano Particle Surface Reaction
Selection	Named geom1_difsel1: Geometry geom1: Dimension 2: Boundaries 8, 10, 13–14

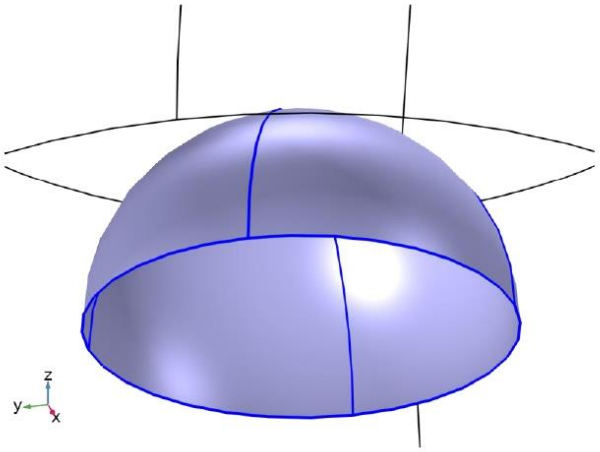

Selection

2.1.2 Coordinate Systems

Boundary System 1

Coordinate system type	Boundary system
Tag	sys1

COORDINATE NAMES

First	Second	Third
t1	t2	n

2.2 GEOMETRY 1

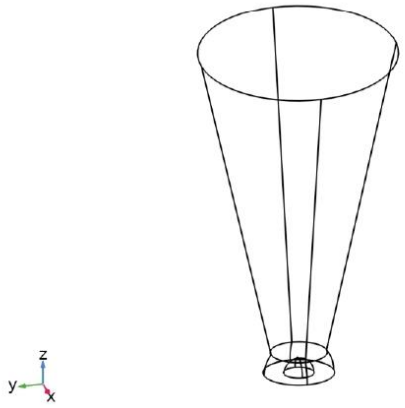

Geometry 1

UNITS

Length unit	nm
Angular unit	deg

2.3 ELECTROANALYSIS

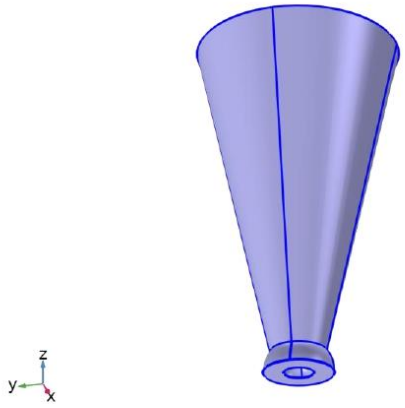

Electroanalysis

EQUATIONS

$$\nabla \cdot \mathbf{J}_i + \mathbf{u} \cdot \nabla c_i = R_i$$

$$\nabla \cdot \mathbf{i}_s = Q_s$$
$$\mathbf{J}_i = -D_i \nabla c_i$$
$$\mathbf{i}_s = -\sigma_s \nabla \phi_s$$
$$\phi_l = 0, \quad \phi_s = \text{phis}$$

FEATURES

Electrolyte 1	Domain
No Flux 1	Boundary
Insulation 1	Boundary
Initial Values 1	Domain
Electrode Surface 1	Boundary
Concentration 1	Boundary

2.4 MESH 1

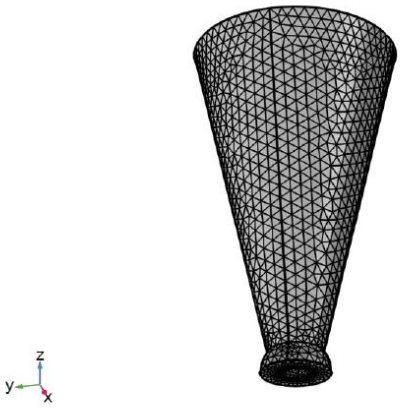

Mesh 1

2.4.1 Size (size)

SETTINGS

Description	Value
Maximum element size	350
Minimum element size	15
Curvature factor	0.3
Resolution of narrow regions	0.85
Maximum element growth rate	1.35
Predefined size	Extra fine

2.4.2 Size 1 (size1)

SELECTION

Geometric entity level	Boundary
Selection	Geometry geom1: Dimension 2: Boundaries 1–16

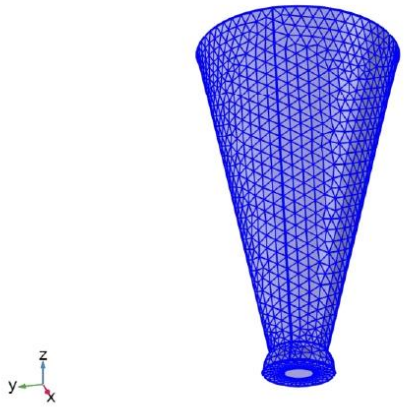

Size 1

SETTINGS

Description	Value
Maximum element size	550
Minimum element size	40
Curvature factor	0.4
Resolution of narrow regions	0.7
Maximum element growth rate	1.4
Predefined size	Finer

2.4.3 Free Tetrahedral 1 (ftet1)

SELECTION

Geometric entity level	Domain
Selection	Geometry geom1: Dimension 3: Domains 1–2

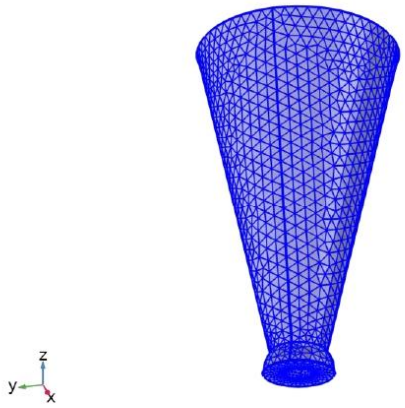

Free Tetrahedral 1

SETTINGS

Description	Value
Avoid inverted curved elements	On

INFORMATION

Description	Value
Last build time	< 1 second
Built with	COMSOL 6.3.0.290 (win64), May 19, 2025, 9:04:06 PM

3 Study 1

COMPUTATION INFORMATION

Computation time	2 min 18 s

3.1 PARAMETRIC SWEEP

Parameter name	Parameter value list	Parameter unit
E_appl	range(E_start,E_step,E_vertex)	V

STUDY SETTINGS

Description	Value
Sweep type	Specified combinations
Parameter name	E_appl
Unit	V

PARAMETERS

Parameter name	Parameter value list	Parameter unit
E_appl	range(E_start,E_step,E_vertex)	V

3.2 STATIONARY

STUDY SETTINGS

Description	Value
Include geometric nonlinearity	Off

PHYSICS AND VARIABLES SELECTION

Key	Solve for
Electroanalysis (tcd)	On

STORE IN OUTPUT

Interface	Output	Selection
Electroanalysis (tcd)	Physics controlled	

MESH SELECTION

Component	Mesh
Component 1	Mesh 1

4 Results

4.1 DATASETS

4.1.1 Study 1/Solution 1

SOLUTION

Description	Value
Solution	Solution 1 (sol1)
Component	Component 1 (comp1)

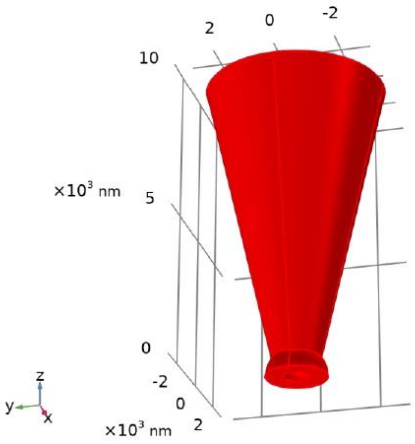

Dataset: Study 1/Solution 1

4.2 DERIVED VALUES

4.2.1 Surface Average 1

DATA

Description	Value
Dataset	Study 1/Solution 1 (sol1)

EXPRESSIONS

Expression	Unit	Description
tcd.Itot_es1	A	Total current

INTEGRATION SETTINGS

Description	Value
Integration order	4

T

4.3 PLOT GROUPS

4.3.1 Concentration, H, Streamline (tcd)

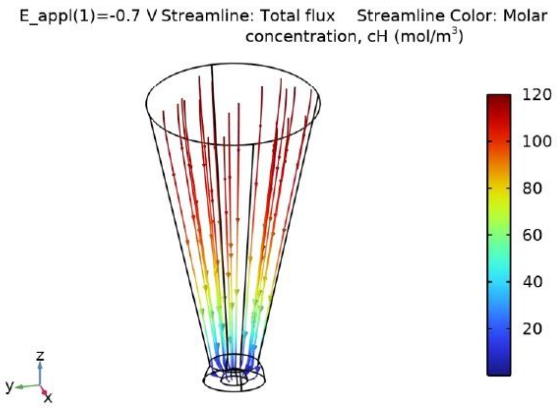

Streamline: Total flux Streamline Color: Molar concentration, cH (mol/m³)

4.3.2 Concentration, H, Surface (tcd)

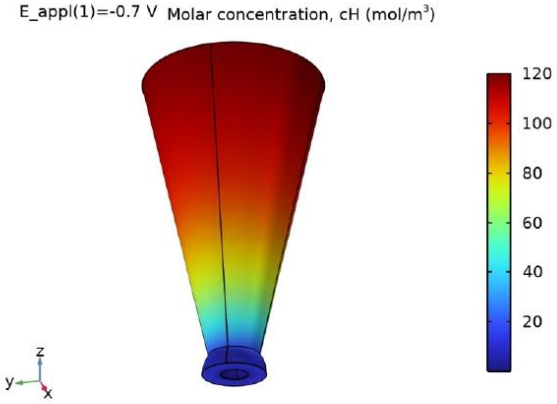

Molar concentration, cH (mol/m³)

4.3.3 Concentration, H2, Streamline (tcd)

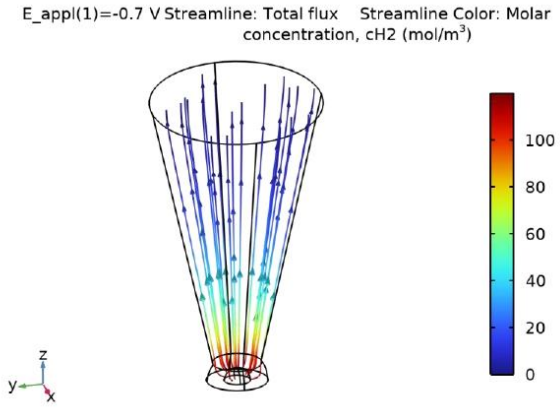

Streamline: Total flux Streamline Color: Molar concentration, cH2 (mol/m³)

4.3.4 Concentration, H2, Surface (tcd)

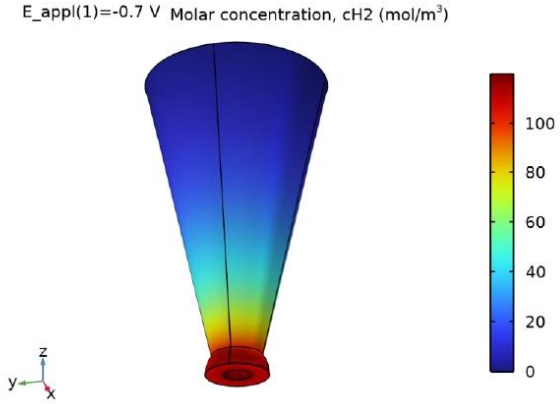

Molar concentration, cH2 (mol/m³)

4.3.5 Total current

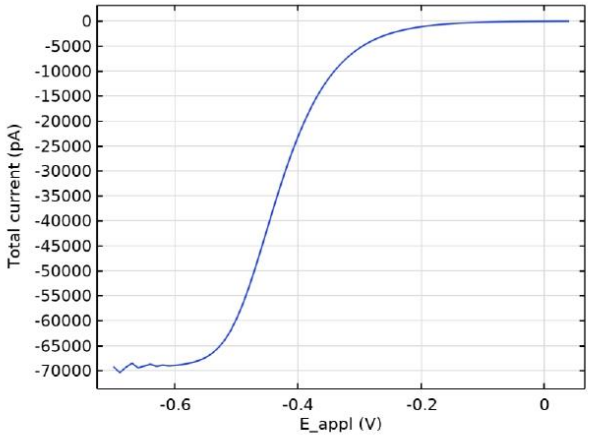

4.3.6 3D Plot Group 6

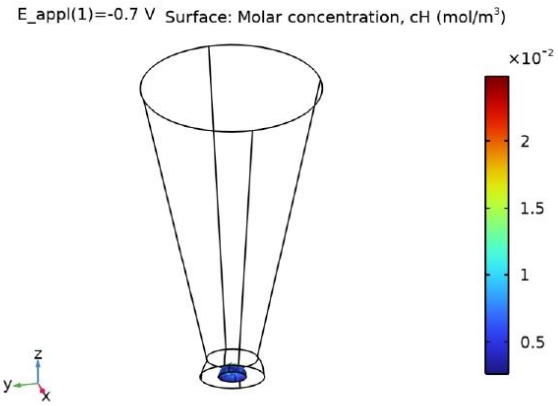

Surface: Molar concentration, cH (mol/m³)

4.3.7 1D Plot Group 7

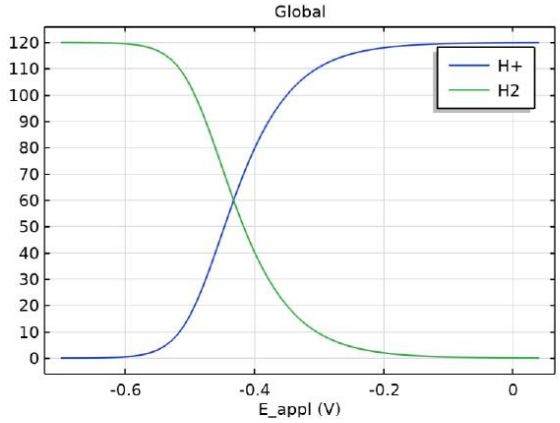

Global

4.3.8 1D Plot Group 8

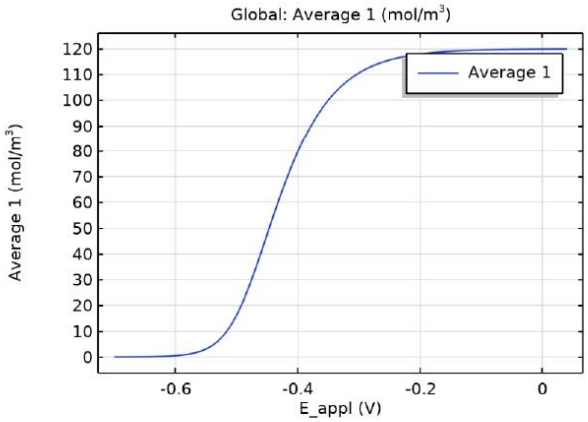

Global: Average 1 (mol/m³)

APPENDICE B

COMSOL report for chapter 4

Contents

1 Global Definitions

USED PRODUCTS

COMSOL Multiphysics
Electrochemistry Module

1.1 PARAMETERS

PARAMETERS 1

Name	Expression	Value	Description
pipetradius	255 [nm]	2.55E−7 m	Pipet radius
pipetlength	1500[um]	0.0015 m	Length of pipet
meniscusheight	pipetradius	2.55E−7 m	Distance between end of pipet and electrode surface
contactradius	pipetradius	2.55E−7 m	Contact radius of droplet with electrode surface
gamma	14[deg]	0.24435 rad	
D1	4.1e-7[cm^2/s]	4.1E−11 m^2/s	
D2	D1	4.1E−11 m^2/s	
conc	2[mM]	2 mol/m^3	
Ef	0[V]	0 V	
E_appl	0[V]	0 V	Applied potential
k0	0.012[cm/s]	1.2E−4 m/s	Reaction rate
E_start	-0.4[V]	−0.4 V	Start potential
E_vertex	0.4[V]	0.4 V	Vertex potential
E_step	1[mV]	0.001 V	Potential step
v	0.1[V/s]	0.1 V/s	Voltammetric scan rate
T	298 [K]	298 K	Temperature
n	1	1	
F	96485[C/mol]	96485 C/mol	
pie	3.14	3.14	

2 Component 1

2.1 DEFINITIONS

2.1.1 Coordinate Systems

Boundary System 1

Coordinate system type	Boundary system
Tag	sys1

COORDINATE NAMES

First	Second	Third
t1	to	n

2.1.2 Domain Properties

Infinite Element Domain 1

Tag	ie1

SELECTION

Geometric entity level	Domain
Selection	Domain 2

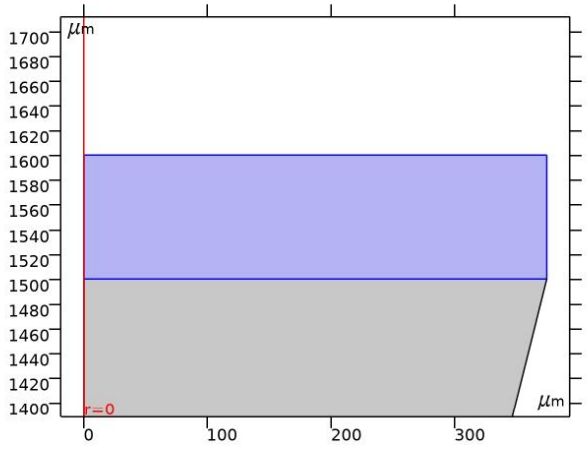

Selection

2.2 GEOMETRY 1

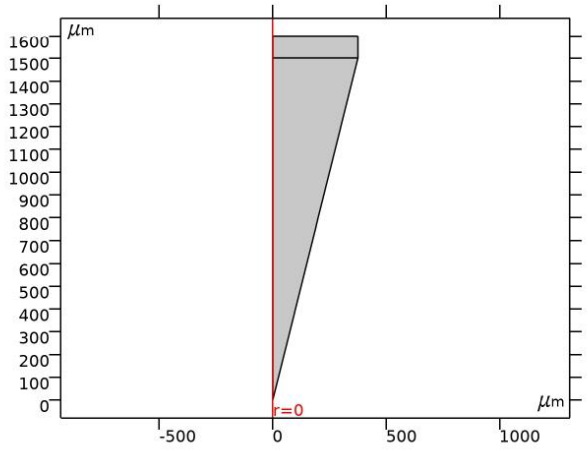

Geometry 1

UNITS

Length unit	µm
Angular unit	deg

2.3 ELECTROANALYSIS

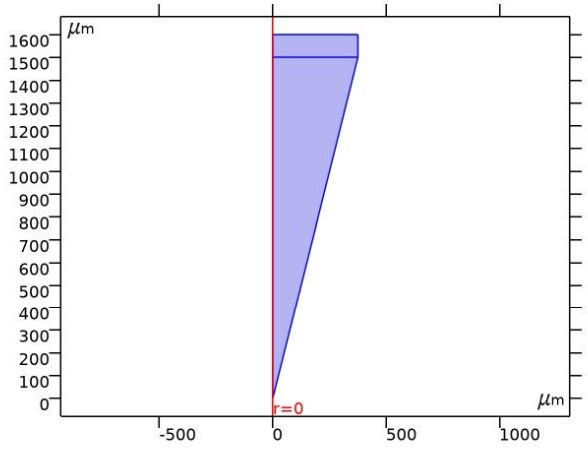

Electroanalysis

EQUATIONS

$$\nabla \cdot \mathbf{J}_i = R_i$$

$$\mathbf{J}_i = -D_i \nabla c_i$$
$$\phi_l = 0$$

FEATURES

Transport Properties 1
Axial Symmetry 1
No Flux 1
Initial Values 1
Electrode Surface 1
Concentration 1

2.3.1 Transport Properties 1

EQUATIONS

$$\nabla \cdot \mathbf{J}_i = R_i$$
$$\mathbf{J}_i = -D_i \nabla c_i$$
$$\phi_l = 0$$

2.3.2 No Flux 1

EQUATIONS

$$-\mathbf{n} \cdot \mathbf{J}_i = 0$$

2.3.3 Electrode Surface 1

EQUATIONS

$$i_{\text{total}} = \sum_m i_{\text{loc},m}$$
$$-\mathbf{n} \cdot \mathbf{J}_i = R_{i,\text{tot}}, \quad R_{i,\text{tot}} = \sum_m R_{i,m}$$

Electrode Reaction 1

EQUATIONS

$$\eta = \phi_{s,\text{ext}} - \phi_l - E_{\text{eq}}$$

2.3.4 Concentration 1

EQUATIONS

$$c_i = c_{0,i}$$

2.4 MESH 1

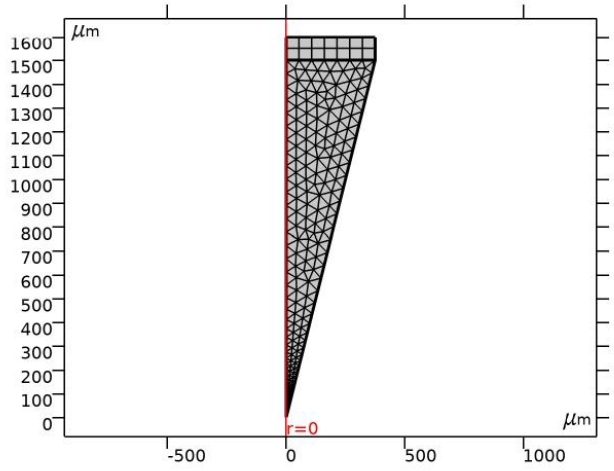

Mesh 1

3 Study 1

COMPUTATION INFORMATION

Computation time	8 s
CPU	Apple M1, 8 cores
Operating system	Mac OS X

3.1 PARAMETRIC SWEEP

Parameter name	Parameter value list	Parameter unit
E_appl	range(E_start,E_step,E_vertex)	V

STUDY SETTINGS

Description	Value
Sweep type	Specified combinations
Parameter name	E_appl
Unit	V

PARAMETERS

Parameter name	Parameter value list	Parameter unit
E_appl (Applied potential)	range(E_start,E_step,E_vertex)	V

3.2 STATIONARY

STUDY SETTINGS

Description	Value
Include geometric nonlinearity	Off

MESH SELECTION

Geometry	Mesh
mesh1	mesh1

PHYSICS AND VARIABLES SELECTION

Physics interface	Discretization
Electroanalysis (elan)	physics

MESH SELECTION

Geometry	Mesh
Geometry 1 (geom1)	mesh1

4 Results

4.1 DATA SETS

4.1.1 Study 1/Solution 1

SOLUTION

Description	Value
Solution	Solution 1
Component	Save Point Geometry 1

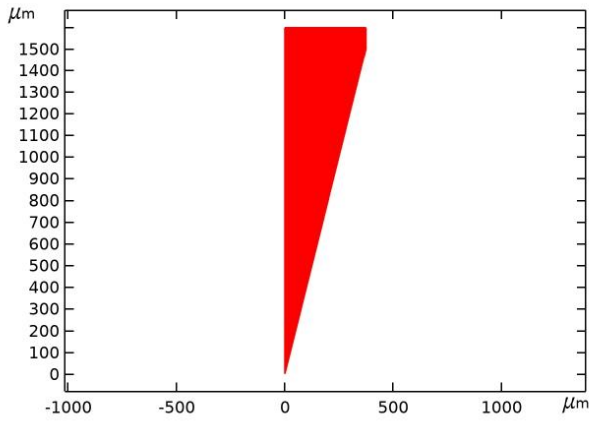

Data set: Study 1/Solution 1

4.1.2 Study 1/Parametric Solutions 1

SOLUTION

Description	Value
Solution	Parametric Solutions 1
Component	Geometry 1

4.1.3 Revolution 2D 1

DATA

Description	Value
Data set	Study 1/Solution 1

AXIS DATA

Description	Value

Description	Value
Axis entry method	Two points
Points	{{0, 0}, {0, 1}}

REVOLUTION LAYERS

Description	Value
Start angle	-90
Revolution angle	225

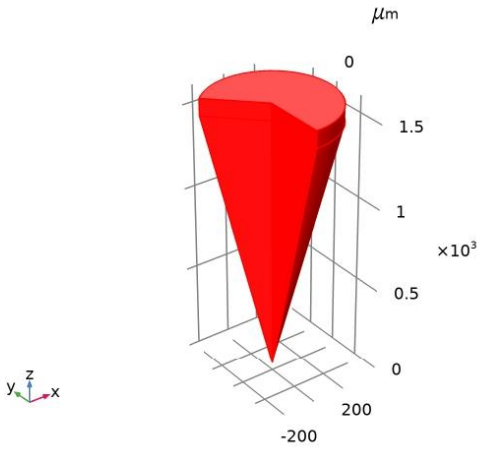

Data set: Revolution 2D 1

4.2 PLOT GROUPS

4.2.1 Concentration (elan)

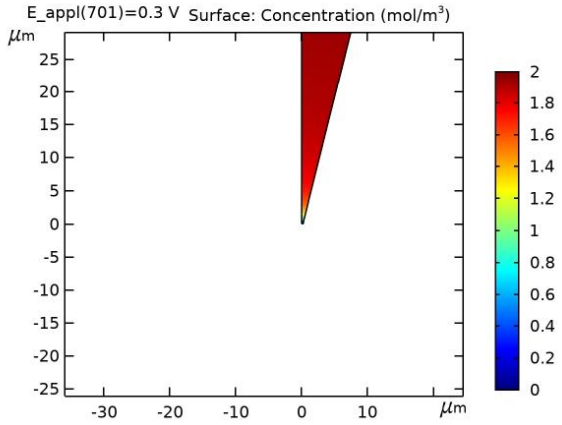

Surface: Concentration (mol/m³)

4.2.2 Concentration, 3D (elan)

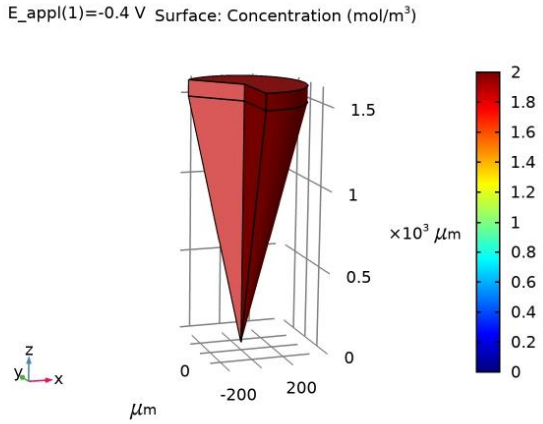

Surface: Concentration (mol/m³)

4.2.3 Total current

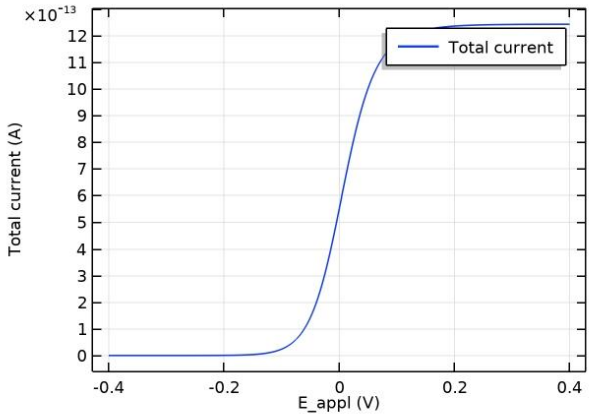

APPENDICE C

Publisher's Permission for Figure Reuse

PLS Clear

PARTIES:

1. **Oxford Publishing Limited** (Licensor); and
2. **Samaneh Salek** (Licensee).

Thank you for your recent permission request. Some permission requests for use of material published by the Licensor, such as this one, are now being facilitated by PLSclear.

Set out in this licence cover sheet (the **Licence Cover Sheet**) are the principal terms under which Licensor has agreed to license certain Licensed Material (as defined below) to Licensee. The terms in this Licence Cover Sheet are subject to the attached General Terms and Conditions, which together with this Licence Cover Sheet constitute the licence agreement (the **Licence**) between Licensor and Licensee as regards the Licensed Material. The terms set out in this Licence Cover Sheet take precedence over any conflicting provision in the General Terms and Conditions.

Free Of Charge Licence Terms

Licence Date:	20/02/2025
PLSclear Ref No:	102655

The Licensor

Company name:	Oxford Publishing Limited
Address:	Rights Department Great Clarendon Street Oxford OX2 6DP GB

The Licensee

Licensee Contact Name:	Samaneh Salek
Licensee Address:	2101 Rue Jeanne-Mance Montreal J0L2K0 Canada

Licensed Material

title:	Instructor's solutions manual to accompany Atkins' Physical Chemistry 9/e
ISBN:	9780199583966
publisher:	Oxford Publishing Limited

Are you requesting permission to reuse the cover of the publication?	No
Figure number & title	chapter 19 figures 19.14, 19.15, 19.16, and 19.17
Page numbers	chapter 19 pages: 700 and 701
Are you the author of the content that you are requesting to reuse?	Yes
Will you be changing or editing the image?	No

For Use In Licensee's Publication(s)

usage type	Book, Journal, Magazine or Academic Paper-Thesis or Dissertation
Author	Samaneh Salek
Language	English
Title of dissertation/thesis	quantitative analysis using Scanning electrochemical cell microscopy
University or institution	university of Quebec in Montreal
Unlimited circulation?	No

Rights Granted

Exclusivity:	Non-Exclusive
Format:	Thesis or Dissertation
Language:	English
Territory:	World
Duration:	Lifetime of Licensee's Edition
Maximum Circulation:	1
Additional Terms:	If at some future date your thesis is published it will be necessary to re-clear this permission. Please also note that if the material to be used is acknowledged to any other source, you will need to clear permission with the rights holder, and for any electronic version the © line must appear on the same page as the OUP material and the OUP material should not be included under a Creative Commons license, or any other open-access license allowing onward reuse.

GENERAL TERMS AND CONDITIONS

1. Definitions and Interpretation

1.1 Capitalised words and expressions in these General Terms and Conditions have the meanings given to them in the Licence Cover Sheet.

1.2 In this Licence any references (express or implied) to statutes or provisions are references to those statutes or provisions as amended or re-enacted from time to time. The term including will be construed as illustrative, without limiting the sense or scope of the words preceding it. A reference to in writing or written includes faxes and email. The singular includes the plural and vice versa.

2. Grant of Rights

2.1 The Licensor grants to Licensee the non-exclusive right to use the Licensed Material as specified in the Licence Cover Sheet.

2.2 The rights licensed to Licensee under this Licence do not include the right to use any third party copyright material incorporated in the Licensed Material. Licensee should check the Licensed Material carefully and seek permission for the use of any such third party copyright material from the relevant copyright owner(s).

2.3 Unless otherwise stated in the Licence Cover Sheet, the Licensed Material may be:

2.3.1 subjected to minor editing, including for the purposes of creating alternative formats to provide access for a beneficiary person (provided that any such editing does not amount to derogatory treatment); and/or

2.3.2 used for incidental promotional use (such as online retail providers' search facilities).

2.4 Save as expressly permitted in this Licence or as otherwise permitted by law, no use or modification of the Licensed Material may be made by Licensee without Licensor's prior written permission.

3. Copyright Notice and Acknowledgement

3.1 Licensee must ensure that the following notices and acknowledgements are reproduced prominently alongside each reproduction by Licensee of the Licensed Material:

3.1.1 the title and author of the Licensed Material;

3.1.2 the copyright notice included in the Licensed Material; and

3.1.3 the statement "Reproduced with permission of The Licensor through PLSclear."

4. Reversion of Rights

4.1 The rights licensed to Licensee under this Licence will terminate immediately and automatically upon the earliest of the following events to occur:

4.1.1 the Licensed Material not being used by Licensee within 18 months of the Licence Date;

4.1.2 expiry of the Licence Duration; or

4.1.3 the Maximum Circulation being reached.

5. Miscellaneous

5.1 By using the Licensed Material, Licensee will be deemed to have accepted all the terms and conditions contained in this Licence.

5.2 This Licence contains the entire understanding and agreement of the parties relating to its subject matter and supersedes in all respects any previous or other existing arrangements, agreements or understandings between the parties whether oral or written in relation to its subject matter.

5.3 Licensee may not assign this Licence or any of its rights or obligations hereunder to any third party without Licensor's prior written consent.

5.4 This Licence is governed by and shall be construed in accordance with the laws of England and Wales and the parties hereby irrevocably submit to the non-exclusive jurisdiction of the Courts of England and Wales as regards any claim, dispute or matter arising under or in relation to this Licence.

APPENDICE D

Copyright Permission for Article

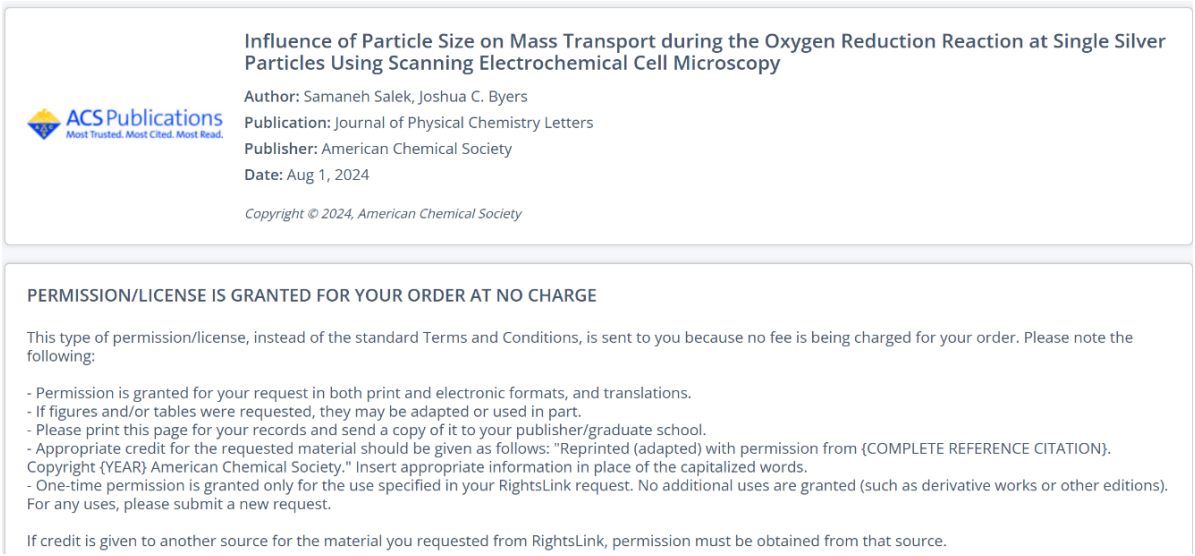

Influence of Particle Size on Mass Transport during the Oxygen Reduction Reaction at Single Silver Particles Using Scanning Electrochemical Cell Microscopy

Author: Samaneh Salek, Joshua C. Byers

Publication: Journal of Physical Chemistry Letters

Publisher: American Chemical Society

Date: Aug 1, 2024

BIBLIOGRAPHIE

Aaronson, B. D. B., Byers, J. C., Colburn, A. W., McKelvey, K. et Unwin, P. R. (2015, 2015/04/21). Scanning Electrochemical Cell Microscopy Platform for Ultrasensitive Photoelectrochemical Imaging. *Analytical Chemistry*, *87*(8), 4129-4133. doi: 10.1021/acs.analchem.5b00288

Aaronson, B. D. B., Garoz-Ruiz, J., Byers, J. C., Colina, A. et Unwin, P. R. (2015, 2015/11/24). Electrodeposition and Screening of Photoelectrochemical Activity in Conjugated Polymers Using Scanning Electrochemical Cell Microscopy. *Langmuir*, *31*(46), 12814-12822. doi: 10.1021/acs.langmuir.5b03316

Aaronson, B. D. B., Lai, S. C. S. et Unwin, P. R. (2014, 2014/02/25). Spatially Resolved Electrochemistry in Ionic Liquids: Surface Structure Effects on Triiodide Reduction at Platinum Electrodes. *Langmuir*, *30*(7), 1915-1919. doi: 10.1021/la500271f

Alzahrani, H., Bentley, C., Burrows, R., Cao, C., Cai, Q., Chikere, C., . . . Ying, Y. (2018). Dynamics of nanointerfaces: general discussion. *Faraday Discussions*, *210*(0), 451-479. doi: 10.1039/C8FD90026D

Anderson, K. L. et Edwards, M. A. (2023). Evaluating Analytical Expressions for Scanning Electrochemical Cell Microscopy (SECCM). *Analytical Chemistry*, *95*(21), 8258-8266. doi: 10.1021/acs.analchem.3c00216

Anderson, K. L. et Edwards, M. A. (2025, 2025/04/16). A Tutorial for Scanning Electrochemical Cell Microscopy (SECCM) Measurements: Step-by-Step Instructions, Visual Resources, and Guidance for First Experiments. *ACS Measurement Science Au*, *5*(2), 160-177. doi: 10.1021/acsmeasuresciau.4c00091

Atkins, P. et de Paula, J. (2010). *Atkins' Physical Chemistry* OUP Oxford.

Baker, L. A. (2018, 2018/11/21). Perspective and Prospectus on Single-Entity Electrochemistry. *Journal of the American Chemical Society*, *140*(46), 15549-15559. doi: 10.1021/jacs.8b09747

Barrado, E., Couto, R. A. S., Quinaz, M. B., Lima, J. L. F. C. et Castrillejo, Y. (2014, 2014/04/15/). Electrochemical behaviour of ferrocene in the ionic liquid 1-ethyl-3-methylimidazolium tetrafluoroborate, EMIMBF4, at 298K. *Journal of Electroanalytical Chemistry*, *720-721*, 139-146. doi: https://doi.org/10.1016/j.jelechem.2014.03.026

Basile, A., Bhatt, A. I. et O'Mullane, A. P. (2016, Jun 13). Stabilizing lithium metal using ionic liquids for long-lived batteries. *Nat Commun*, *7*, ncomms11794. doi: 10.1038/ncomms11794

Benck, J. D., Hellstern, T. R., Kibsgaard, J., Chakthranont, P. et Jaramillo, T. F. (2014, 2014/11/07). Catalyzing the Hydrogen Evolution Reaction (HER) with Molybdenum Sulfide Nanomaterials. *ACS Catalysis*, *4*(11), 3957-3971. doi: 10.1021/cs500923c

Bentley, C. L. (2022). Scanning electrochemical cell microscopy for the study of (nano)particle electrochemistry: From the sub-particle to ensemble level. *Electrochemical Science Advances*, *2*(3), e2100081. doi: https://doi.org/10.1002/elsa.202100081

Bentley, C. L. (2022). Scanning electrochemical cell microscopy for the study of (nano)particle electrochemistry: From the sub-particle to ensemble level. *Electrochemical Science Advances*, *2*(3). doi: 10.1002/elsa.202100081

Bentley, C. L., Kang, M., Maddar, F. M., Li, F., Walker, M., Zhang, J. et Unwin, P. R. (2017). Electrochemical maps and movies of the hydrogen evolution reaction on natural crystals of molybdenite (MoS 2): basal vs. edge plane activity. *Chemical science*, *8*(9), 6583-6593.

Bentley, C. L., Kang, M. et Unwin, P. R. (2019, 2019/02/13). Nanoscale Surface Structure–Activity in Electrochemistry and Electrocatalysis. *Journal of the American Chemical Society*, *141*(6), 2179-2193. doi: 10.1021/jacs.8b09828

Bentley, C. L., Kang, M. et Unwin, P. R. (2020, 2020/09/01). Scanning Electrochemical Cell Microscopy (SECCM) in Aprotic Solvents: Practical Considerations and Applications. *Analytical Chemistry*, *92*(17), 11673-11680. doi: 10.1021/acs.analchem.0c01540

Bentley, C. L., Li, J., Bond, A. M. et Zhang, J. (2016, 2016/08/04). Mass-Transport and Heterogeneous Electron-Transfer Kinetics Associated with the Ferrocene/Ferrocenium

Process in Ionic Liquids. *The Journal of Physical Chemistry C*, *120*(30), 16516-16525. doi: 10.1021/acs.jpcc.6b05545

Bentley, C. L. et Unwin, P. R. (2018). Nanoscale electrochemical movies and synchronous topographical mapping of electrocatalytic materials. *Faraday Discussions*, *210*, 365-379. doi: 10.1039/c8fd00028j

Bentley, C. L. et Unwin, P. R. (2018). Nanoscale electrochemical movies and synchronous topographical mapping of electrocatalytic materials. *Faraday Discussions*, *210*(0), 365-379. doi: 10.1039/C8FD00028J

Beugré, R., Dorval, A., Lavallée, L. L., Jafari, M. et Byers, J. C. (2019, 2019/10/01/). Local electrochemistry of nickel (oxy)hydroxide material gradients prepared using bipolar electrodeposition. *Electrochimica Acta*, *319*, 331-338. doi: https://doi.org/10.1016/j.electacta.2019.06.143

Blount, B., Juarez, G., Wang, Y. et Ren, H. (2022). iR drop in scanning electrochemical cell microscopy. *Faraday Discussions*, *233*(0), 149-162. doi: 10.1039/D1FD00046B

Byers, J. C., Güell, A. G. et Unwin, P. R. (2014). Nanoscale electrocatalysis: Visualizing oxygen reduction at pristine, kinked, and oxidized sites on individual carbon nanotubes. *Journal of the American Chemical Society*, *136*(32), 11252-11255. doi: 10.1021/ja505708y

Byers, J. C., Paulose Nadappuram, B., Perry, D., McKelvey, K., Colburn, A. W. et Unwin, P. R. (2015, Oct 20). Single Molecule Electrochemical Detection in Aqueous Solutions and Ionic Liquids. *Anal Chem*, *87*(20), 10450-10456. doi: 10.1021/acs.analchem.5b02569

Chen, C.-H., Jacobse, L., McKelvey, K., Lai, S. C., Koper, M. T. et Unwin, P. R. (2015a). Voltammetric scanning electrochemical cell microscopy: dynamic imaging of hydrazine electro-oxidation on platinum electrodes. *Analytical chemistry*, *87*(11), 5782-5789.

Chen, C.-H., Jacobse, L., McKelvey, K., Lai, S. C. S., Koper, M. T. M. et Unwin, P. R. (2015b, 2015/06/02). Voltammetric Scanning Electrochemical Cell Microscopy: Dynamic Imaging of Hydrazine Electro-oxidation on Platinum Electrodes. *Analytical Chemistry*, *87*(11), 5782-5789. doi: 10.1021/acs.analchem.5b00988

Chen, C.-H., Meadows, K. E., Cuharuc, A., Lai, S. C. S. et Unwin, P. R. (2014). High resolution mapping of oxygen reduction reaction kinetics at polycrystalline platinum electrodes. *Physical Chemistry Chemical Physics*, *16*(34), 18545-18552. doi: 10.1039/C4CP01511H

Chen, C. H., Meadows, K. E., Cuharuc, A., Lai, S. C. S. et Unwin, P. R. (2014). High resolution mapping of oxygen reduction reaction kinetics at polycrystalline platinum electrodes. *Physical Chemistry Chemical Physics*, *16*(34), 18545-18552. doi: 10.1039/c4cp01511h

Chen, S. et Kucernak, A. (2003, 2003/08/01). Electrodeposition of Platinum on Nanometer-Sized Carbon Electrodes. *The Journal of Physical Chemistry B*, *107*(33), 8392-8402. doi: 10.1021/jp0348934

Chen, S. et Kucernak, A. (2004). Electrocatalysis under Conditions of High Mass Transport Rate: Oxygen Reduction on Single Submicrometer-Sized Pt Particles Supported on Carbon. *Journal of Physical Chemistry B*, *108*(10), 3262-3276. doi: 10.1021/jp036831j

Chen, S. et Kucernak, A. (2004a, 2004/03/01). Electrocatalysis under Conditions of High Mass Transport Rate: Oxygen Reduction on Single Submicrometer-Sized Pt Particles Supported on Carbon. *The Journal of Physical Chemistry B*, *108*(10), 3262-3276. doi: 10.1021/jp036831j

Chen, S. et Kucernak, A. (2004b, 2004/09/01). Electrocatalysis under Conditions of High Mass Transport: Investigation of Hydrogen Oxidation on Single Submicron Pt Particles Supported on Carbon. *The Journal of Physical Chemistry B*, *108*(37), 13984-13994. doi: 10.1021/jp048641u

Choi, M., Siepser, N. P., Jeong, S., Wang, Y., Jagdale, G., Ye, X. et Baker, L. A. (2020). Probing Single-Particle Electrocatalytic Activity at Facet-Controlled Gold Nanocrystals. *Nano Letters*, *20*(2), 1233-1239. doi: 10.1021/acs.nanolett.9b04640

Clarke, T. B., Krushinski, L. E., Vannoy, K. J., Colón-Quintana, G., Roy, K., Rana, A., . . . Dick, J. E. (2024, 2024/08/14). Single Entity Electrocatalysis. *Chemical Reviews*, *124*(15), 9015-9080. doi: 10.1021/acs.chemrev.3c00723

Compton, R. et Banks, C. (2011). *Understanding voltammetry., by Imperial College Press* : London.

Crespo-Yapur, D. A., Elizondo, A. S., Herrera, D. et Videa, M. (2022, 2022/01/01/). Galvanostatic electrodeposition of silver nanoparticles: Nucleation and growth studies. *Materials Today: Proceedings*, *48*, 1-4. doi: https://doi.org/10.1016/j.matpr.2020.04.760

Daviddi, E., Gonos, K. L., Colburn, A. W., Bentley, C. L. et Unwin, P. R. (2019, 2019/07/16). Scanning Electrochemical Cell Microscopy (SECCM) Chronopotentiometry: Development and Applications in Electroanalysis and Electrocatalysis. *Analytical Chemistry*, *91*(14), 9229-9237. doi: 10.1021/acs.analchem.9b02091

Dayeh, M., Ghavidel, M. R. Z., Mauzeroll, J. et Schougaard, S. B. (2019). Micropipette Contact Method to Investigate High-Energy Cathode Materials by using an Ionic Liquid. *ChemElectroChem*, *6*(1), 195-201. doi: https://doi.org/10.1002/celc.201800750

Debe, M. K. (2012). Electrocatalyst approaches and challenges for automotive fuel cells. *Nature*, *486*(7401), 43-51.

Ebejer, N., Güell, A. G., Lai, S. C., McKelvey, K., Snowden, M. E. et Unwin, P. R. (2013). Scanning electrochemical cell microscopy: a versatile technique for nanoscale electrochemistry and functional imaging. *Annu Rev Anal Chem (Palo Alto Calif)*, *6*, 329-351. doi: 10.1146/annurev-anchem-062012-092650

Ebejer, N., Schnippering, M., Colburn, A. W., Edwards, M. A. et Unwin, P. R. (2010, 2010/11/15). Localized High Resolution Electrochemistry and Multifunctional Imaging: Scanning Electrochemical Cell Microscopy. *Analytical Chemistry*, *82*(22), 9141-9145. doi: 10.1021/ac102191u

Edwards, M. A., Williams, C. G., Whitworth, A. L. et Unwin, P. R. (2009, 2009/06/01). Scanning Ion Conductance Microscopy: a Model for Experimentally Realistic Conditions and Image Interpretation. *Analytical Chemistry*, *81*(11), 4482-4492. doi: 10.1021/ac900376w

Fortunati, A., Risplendi, F., Re Fiorentin, M., Cicero, G., Parisi, E., Castellino, M., . . . Hernández, S. (2023, 2023/04/29). Understanding the role of imidazolium-based ionic liquids in the

electrochemical CO2 reduction reaction. *Communications Chemistry*, *6*(1), 84. doi: 10.1038/s42004-023-00875-9

Frenzel, N., Hartley, J. et Frisch, G. (2017). Voltammetric and spectroscopic study of ferrocene and hexacyanoferrate and the suitability of their redox couples as internal standards in ionic liquids. *Physical Chemistry Chemical Physics*, *19*(42), 28841-28852. doi: 10.1039/C7CP05483A

Gagne, R. R., Koval, C. A. et Lisensky, G. C. (1980, 1980/09/01). Ferrocene as an internal standard for electrochemical measurements. *Inorganic Chemistry*, *19*(9), 2854-2855. doi: 10.1021/ic50211a080

Gao, R., Edwards, M. A., Qiu, Y., Barman, K. et White, H. S. (2020, 2020/05/13). Visualization of Hydrogen Evolution at Individual Platinum Nanoparticles at a Buried Interface. *Journal of the American Chemical Society*, *142*(19), 8890-8896. doi: 10.1021/jacs.0c02202

Gasteiger, H. A. et Marković, N. M. (2009). Just a Dream—or Future Reality? *Science*, *324*(5923), 48-49. doi: doi:10.1126/science.1172083

Gateman, S. M., Gharbi, O., Turmine, M. et Vivier, V. (2021, 2021/12/10/). Measuring changes in wettability and surface area during micro droplet corrosion measurements. *Electrochimica Acta*, *399*, 139402. doi: https://doi.org/10.1016/j.electacta.2021.139402

Gaudin, L. F., Funston, A. M. et Bentley, C. L. (2024). Drop-cast gold nanoparticles are not always electrocatalytically active for the borohydride oxidation reaction. *Chemical Science*, *15*(19), 7243-7258. doi: 10.1039/d4sc00676c

Gaudin, L. F., Wright, I. R., Harris-Lee, T. R., Jayamaha, G., Kang, M. et Bentley, C. L. (2024). Five years of scanning electrochemical cell microscopy (SECCM): new insights and innovations. *Nanoscale*, *16*(26), 12345-12367. doi: 10.1039/D4NR00859F

Ge, X., Sumboja, A., Wuu, D., An, T., Li, B., Goh, F. W. T., . . . Liu, Z. (2015, 2015/08/07). Oxygen Reduction in Alkaline Media: From Mechanisms to Recent Advances of Catalysts. *ACS Catalysis*, *5*(8), 4643-4667. doi: 10.1021/acscatal.5b00524

Gewirth, A. A. et Thorum, M. S. (2010, 2010/04/19). Electroreduction of Dioxygen for Fuel-Cell Applications: Materials and Challenges. *Inorganic Chemistry*, *49*(8), 3557-3566. doi: 10.1021/ic9022486

Girão, A. V., Caputo, G. et Ferro, M. C. (2017). Chapter 6 - Application of Scanning Electron Microscopy–Energy Dispersive X-Ray Spectroscopy (SEM-EDS). Dans T. A. P. Rocha-Santos et A. C. Duarte (dir.), *Comprehensive Analytical Chemistry* (vol. 75, p. 153-168). Elsevier.

Gómez-Marín, A. M., Rizo, R. et Feliu, J. M. (2014). Oxygen reduction reaction at Pt single crystals: a critical overview. *Catalysis Science & Technology*, *4*(6), 1685-1698. doi: 10.1039/C3CY01049J

Goyal, A., Marcandalli, G., Mints, V. A. et Koper, M. T. M. (2020). Competition between CO2Reduction and Hydrogen Evolution on a Gold Electrode under Well-Defined Mass Transport Conditions. *Journal of the American Chemical Society*, *142*(9), 4154-4161. doi: 10.1021/jacs.9b10061

Gurrappa, I. et Binder, L. (2008, 2008/12/01). Electrodeposition of nanostructured coatings and their characterization—A review. *Science and Technology of Advanced Materials*, *9*(4), 043001. doi: 10.1088/1468-6996/9/4/043001

Hill, C. M., Kim, J. et Bard, A. J. (2015, 2015/09/09). Electrochemistry at a Metal Nanoparticle on a Tunneling Film: A Steady-State Model of Current Densities at a Tunneling Ultramicroelectrode. *Journal of the American Chemical Society*, *137*(35), 11321-11326. doi: 10.1021/jacs.5b04519

Hill, J. W., Fu, Z., Tian, J. et Hill, C. M. (2020). Locally Engineering and Interrogating the Photoelectrochemical Behavior of Defects in Transition Metal Dichalcogenides. *Journal of Physical Chemistry C*, *124*(31), 17141-17149. doi: 10.1021/acs.jpcc.0c05235

Hill, J. W. et Hill, C. M. (2021). Directly visualizing carrier transport and recombination at individual defects within 2D semiconductors. *Chemical Science*, *12*(14), 5102-5112. doi: 10.1039/d0sc07033e

Hodoroaba, V.-D. (2020). Chapter 4.4 - Energy-dispersive X-ray spectroscopy (EDS). Dans V.-D. Hodoroaba, W. E. S. Unger et A. G. Shard (dir.), *Characterization of Nanoparticles* (p. 397-417). Elsevier.

Hu, S., Yi, J., Zhang, Y.-J., Lin, K.-Q., Liu, B.-J., Chen, L., . . . Ren, B. (2020, 2020/05/20). Observing atomic layer electrodeposition on single nanocrystals surface by dark field spectroscopy. *Nature Communications*, *11*(1), 2518. doi: 10.1038/s41467-020-16405-3

Isaev, V. A., Grishenkova, O. V., Kosov, A. V., Semerikova, O. L. et Zaykov, Y. P. (2017, 2017/02/01). Simulation of the potentiodynamic and galvanostatic phase formation in melts. *Russian Metallurgy (Metally)*, *2017*(2), 146-151. doi: 10.1134/S0036029517020057

Jayamaha, G., Maleki, M., Bentley, C. L. et Kang, M. (2024). Practical guidelines for the use of scanning electrochemical cell microscopy (SECCM). *Analyst*, *149*(9), 2542-2555. doi: 10.1039/d4an00117f

Jeong, S., Choi, M.-H., Jagdale, G. S., Zhong, Y., Siepser, N. P., Wang, Y., . . . Ye, X. (2022, 2022/07/20). Unraveling the Structural Sensitivity of CO2 Electroreduction at Facet-Defined Nanocrystals via Correlative Single-Entity and Macroelectrode Measurements. *Journal of the American Chemical Society*, *144*(28), 12673-12680. doi: 10.1021/jacs.2c02001

Jeong, S., Choi, M. H., Jagdale, G. S., Zhong, Y., Siepser, N. P., Wang, Y., . . . Ye, X. (2022). Unraveling the Structural Sensitivity of CO2Electroreduction at Facet-Defined Nanocrystals via Correlative Single-Entity and Macroelectrode Measurements. *Journal of the American Chemical Society*, *144*(28), 12673-12680. doi: 10.1021/jacs.2c02001

Jiao, Y., Zheng, Y., Jaroniec, M. et Qiao, S. Z. (2015). Design of electrocatalysts for oxygen- and hydrogen-involving energy conversion reactions. *Chemical Society Reviews*, *44*(8), 2060-2086. doi: 10.1039/C4CS00470A

Jin, Z. (2023). High-Spatiotemporal-Resolution Electrochemical Measurements of Electrocatalytic Reactivity. *Analytical Chemistry*, *95*(16), 6477-6489. doi: 10.1021/acs.analchem.2c05755

Kamat, G. A., Zamora Zeledón, J. A., Gunasooriya, G. T. K. K., Dull, S. M., Perryman, J. T., Nørskov, J. K., . . . Jaramillo, T. F. (2022, 2022/02/18). Acid anion electrolyte effects on

platinum for oxygen and hydrogen electrocatalysis. *Communications Chemistry*, *5*(1), 20. doi: 10.1038/s42004-022-00635-1

Kang, M., Bentley, C. L., Mefford, J. T., Chueh, W. C. et Unwin, P. R. (2023, 2023/11/14). Multiscale Analysis of Electrocatalytic Particle Activities: Linking Nanoscale Measurements and Ensemble Behavior. *ACS Nano*, *17*(21), 21493-21505. doi: 10.1021/acsnano.3c06335

Kang, M., Momotenko, D., Page, A., Perry, D. et Unwin, P. R. (2016). Frontiers in nanoscale electrochemical imaging: faster, multifunctional, and ultrasensitive. *Langmuir*, *32*(32), 7993-8008.

Kim, J. et Bard, A. J. (2016a, 2016/02/02). Application of the Koutecký-Levich Method to the Analysis of Steady State Voltammograms with Ultramicroelectrodes. *Analytical Chemistry*, *88*(3), 1742-1747. doi: 10.1021/acs.analchem.5b03965

Kim, J. et Bard, A. J. (2016b, 2016/01/27). Electrodeposition of Single Nanometer-Size Pt Nanoparticles at a Tunneling Ultramicroelectrode and Determination of Fast Heterogeneous Kinetics for Ru(NH3)63+ Reduction. *Journal of the American Chemical Society*, *138*(3), 975-979. doi: 10.1021/jacs.5b11655

Kim, J., Renault, C., Nioradze, N., Arroyo-Currás, N., Leonard, K. C. et Bard, A. J. (2016, 2016/07/13). Electrocatalytic Activity of Individual Pt Nanoparticles Studied by Nanoscale Scanning Electrochemical Microscopy. *Journal of the American Chemical Society*, *138*(27), 8560-8568. doi: 10.1021/jacs.6b03980

Kim, K., Raymond, D., Candeago, R. et Su, X. (2021, 2021/11/12). Selective cobalt and nickel electrodeposition for lithium-ion battery recycling through integrated electrolyte and interface control. *Nature Communications*, *12*(1), 6554. doi: 10.1038/s41467-021-26814-7

Lai, S. C. S., Dudin, P. V., Macpherson, J. V. et Unwin, P. R. (2011, 2011/07/20). Visualizing Zeptomole (Electro)Catalysis at Single Nanoparticles within an Ensemble. *Journal of the American Chemical Society*, *133*(28), 10744-10747. doi: 10.1021/ja203955b

Lazaridis, T., Stühmeier, B. M., Gasteiger, H. A. et El-Sayed, H. A. (2022, 2022/05/01). Capabilities and limitations of rotating disk electrodes versus membrane electrode

assemblies in the investigation of electrocatalysts. *Nature Catalysis*, *5*(5), 363-373. doi: 10.1038/s41929-022-00776-5

Lebègue, E. (2023, 2023/12/01). Allen J. Bard, Larry. R. Faulkner, Henry S. White: Electrochemical Methods: Fundamentals and Applications, 3rd edition, Wiley. *Transition Metal Chemistry*, *48*(6), 433-436. doi: 10.1007/s11243-023-00555-6

Lee, J., Jeong, B. et Ocon, J. D. (2013, 2013/03/01/). Oxygen electrocatalysis in chemical energy conversion and storage technologies. *Current Applied Physics*, *13*(2), 309-321. doi: https://doi.org/10.1016/j.cap.2012.08.008

Lee, S. A., Yang, J. W., Choi, S. et Jang, H. W. (2021). Nanoscale electrodeposition: Dimension control and 3D conformality. *Exploration*, *1*(3), 20210012. doi: https://doi.org/10.1002/EXP.20210012

Li, M., Ye, K.-H., Qiu, W., Wang, Y. et Ren, H. (2022, 2022/03/30). Heterogeneity between and within Single Hematite Nanorods as Electrocatalysts for Oxygen Evolution Reaction. *Journal of the American Chemical Society*, *144*(12), 5247-5252. doi: 10.1021/jacs.2c00506

Li, M., Ye, K. H., Qiu, W., Wang, Y. et Ren, H. (2022). Heterogeneity between and within Single Hematite Nanorods as Electrocatalysts for Oxygen Evolution Reaction. *Journal of the American Chemical Society*, *144*(12), 5247-5252. doi: 10.1021/jacs.2c00506

Li, Q., Chen, A., Wang, D., Zhao, Y., Wang, X., Jin, X., . . . Zhi, C. (2022, 2022/06/27). Tailoring the metal electrode morphology via electrochemical protocol optimization for long-lasting aqueous zinc batteries. *Nature Communications*, *13*(1), 3699. doi: 10.1038/s41467-022-31461-7

Li, Y., Morel, A., Gallant, D. et Mauzeroll, J. (2020, 2020/09/15). Oil-Immersed Scanning Micropipette Contact Method Enabling Long-term Corrosion Mapping. *Analytical Chemistry*, *92*(18), 12415-12422. doi: 10.1021/acs.analchem.0c02177

Limb, J., Gaudin, L. F. et Bentley, C. L. (2024). Structure-dependent CO2 reduction on molybdenite (MoS2) electrocatalysts. *Chemical Communications*, *60*(36), 4781-4784. doi: 10.1039/D4CC00496E

Liu, C., Xu, J., Jiang, C., Gao, H., Ren, X. et Lu, L. (2023). The Microstructure-Activity Relationship of Metal-Organic Framework-Based Electrocatalysts for the Oxygen Evolution Reaction at the Single-Particle Level. *ACS Materials Letters*, *5*(7), 1902-1910. doi: 10.1021/acsmaterialslett.3c00404

Liu, F., Deng, Y., Han, X., Hu, W. et Zhong, C. (2016, 2016/01/05/). Electrodeposition of metals and alloys from ionic liquids. *Journal of Alloys and Compounds*, *654*, 163-170. doi: https://doi.org/10.1016/j.jallcom.2015.09.137

Liu, H., Favier, F., Ng, K., Zach, M. P. et Penner, R. M. (2001, 2001/12/03/). Size-selective electrodeposition of meso-scale metal particles: a general method. *Electrochimica Acta*, *47*(5), 671-677. doi: https://doi.org/10.1016/S0013-4686(01)00747-2

Liu, H. et Penner, R. M. (2000a, 2000/10/01). Size-Selective Electrodeposition of Mesoscale Metal Particles in the Uncoupled Limit. *The Journal of Physical Chemistry B*, *104*(39), 9131-9139. doi: 10.1021/jp0017902

Liu, H. et Penner, R. M. (2000b). Size-selective electrodeposition of mesoscale metal particles in the uncoupled limit. *Journal of Physical Chemistry B*, *104*(39), 9131-9139. doi: 10.1021/jp0017902

Lovelock, K. R. J., Cowling, F. N., Taylor, A. W., Licence, P. et Walsh, D. A. (2010, 2010/04/08). Effect of Viscosity on Steady-State Voltammetry and Scanning Electrochemical Microscopy in Room Temperature Ionic Liquids. *The Journal of Physical Chemistry B*, *114*(13), 4442-4450. doi: 10.1021/jp912087n

Lu, X., Li, M., Peng, Y., Xi, X., Li, M., Chen, Q. et Dong, A. (2021, 2021/10/20). Direct Probing of the Oxygen Evolution Reaction at Single NiFe2O4 Nanocrystal Superparticles with Tunable Structures. *Journal of the American Chemical Society*, *143*(41), 16925-16929. doi: 10.1021/jacs.1c08592

Lu, X., Li, M., Peng, Y., Xi, X., Li, M., Chen, Q. et Dong, A. (2021). Direct Probing of the Oxygen Evolution Reaction at Single NiFe2O4Nanocrystal Superparticles with Tunable Structures. *Journal of the American Chemical Society*, *143*(41), 16925-16929. doi: 10.1021/jacs.1c08592

Lukaszewski, M., Soszko, M. et Czerwiński, A. (2016). Electrochemical methods of real surface area determination of noble metal electrodes - an overview. *International Journal of Electrochemical Science*, *11*(6), 4442-4469. doi: 10.20964/2016.06.71

Ma, Y. et Li, D. (2025, 2025/02/01/). Recent advances in characterization of electrocatalytic nanoparticles at single-particle level. *Current Opinion in Electrochemistry*, *49*, 101623. doi: https://doi.org/10.1016/j.coelec.2024.101623

Makarova, M. V., Amano, F., Nomura, S., Tateishi, C., Fukuma, T., Takahashi, Y. et Korchev, Y. E. (2022, 2022/01/21). Direct Electrochemical Visualization of the Orthogonal Charge Separation in Anatase Nanotube Photoanodes for Water Splitting. *ACS Catalysis*, *12*(2), 1201-1208. doi: 10.1021/acscatal.1c04910

Mariano, R. G., Kang, M., Wahab, O. J., McPherson, I. J., Rabinowitz, J. A., Unwin, P. R. et Kanan, M. W. (2021a). Microstructural origin of locally enhanced CO2 electroreduction activity on gold. *Nature Materials*, *20*(7), 1000-1006. doi: 10.1038/s41563-021-00958-9

Mariano, R. G., Kang, M., Wahab, O. J., McPherson, I. J., Rabinowitz, J. A., Unwin, P. R. et Kanan, M. W. (2021b, Jul). Microstructural origin of locally enhanced CO(2) electroreduction activity on gold. *Nat Mater*, *20*(7), 1000-1006. doi: 10.1038/s41563-021-00958-9

Mariano, R. G., McKelvey, K., White, H. S. et Kanan, M. W. (2017a). Selective increase in CO2 electroreduction activity at grain-boundary surface terminations. *Science*, *358*(6367), 1187-1192. doi: 10.1126/science.aao3691

Mariano, R. G., McKelvey, K., White, H. S. et Kanan, M. W. (2017b, Dec 1). Selective increase in CO(2) electroreduction activity at grain-boundary surface terminations. *Science*, *358*(6367), 1187-1192. doi: 10.1126/science.aao3691

Mariano, R. G., Wahab, O. J., Rabinowitz, J. A., Oppenheim, J., Chen, T., Unwin, P. R. et Dincă, M. (2022, 2022/07/27). Thousand-fold increase in O2 electroreduction rates with conductive MOFs. *ACS Central Science*, *8*(7), 975-982. doi: 10.1021/acscentsci.2c00509

Mariano, R. G., Wahab, O. J., Rabinowitz, J. A., Oppenheim, J., Chen, T., Unwin, P. R. et Dincă, M. (2022). Thousand-fold increase in O2electroreduction rates with conductive MOFs. *ACS Central Science*, *8*(7), 975-982. doi: 10.1021/acscentsci.2c00509

Masa, J., Batchelor-McAuley, C., Schuhmann, W. et Compton, R. G. (2014). Koutecky-Levich analysis applied to nanoparticle modified rotating disk electrodes: Electrocatalysis or misinterpretation. *Nano Research*, *7*(1), 71-78. doi: 10.1007/s12274-013-0372-0

Mayrhofer, K. J. J., Blizanac, B. B., Arenz, M., Stamenkovic, V. R., Ross, P. N. et Markovic, N. M. (2005, 2005/08/01). The Impact of Geometric and Surface Electronic Properties of Pt-Catalysts on the Particle Size Effect in Electrocatalysis. *The Journal of Physical Chemistry B*, *109*(30), 14433-14440. doi: 10.1021/jp051735z

Mayrhofer, K. J. J., Strmcnik, D., Blizanac, B. B., Stamenkovic, V., Arenz, M. et Markovic, N. M. (2008). Measurement of oxygen reduction activities via the rotating disc electrode method: From Pt model surfaces to carbon-supported high surface area catalysts. *Electrochimica Acta*, *53*(7), 3181-3188. doi: 10.1016/j.electacta.2007.11.057

Mefford, J. T., Akbashev, A. R., Kang, M., Bentley, C. L., Gent, W. E., Deng, H. D., . . . Chueh, W. C. (2021). Correlative operando microscopy of oxygen evolution electrocatalysts. *Nature*, *593*(7857), 67-73. doi: 10.1038/s41586-021-03454-x

Mena-Morcillo, E., van der Zalm, J. et Chen, A. (2023, 2023/05/18). Spatially Resolved Optical Spectroscopic Measurements with Simultaneous Photoelectrochemical Mapping Using Scanning Electrochemical Probe Microscopy. *The Journal of Physical Chemistry Letters*, *14*(19), 4600-4606. doi: 10.1021/acs.jpclett.3c00603

Miao, L., Song, Z., Zhu, D., Li, L., Gan, L. et Liu, M. (2021, 2021/05/20). Ionic Liquids for Supercapacitive Energy Storage: A Mini-Review. *Energy & Fuels*, *35*(10), 8443-8455. doi: 10.1021/acs.energyfuels.1c00321

Mirkin, M. V. et Bard, A. J. (1992, 1992/10/01). Simple analysis of quasi-reversible steady-state voltammograms. *Analytical Chemistry*, *64*(19), 2293-2302. doi: 10.1021/ac00043a020

Morales-Guio, C. G., Liardet, L. et Hu, X. (2016, 2016/07/20). Oxidatively Electrodeposited Thin-Film Transition Metal (Oxy)hydroxides as Oxygen Evolution Catalysts. *Journal of the American Chemical Society*, *138*(28), 8946-8957. doi: 10.1021/jacs.6b05196

Nadappuram, P. B., McKelvey, K., Byers, J. C., Güell, A. G., Colburn, A. W., Lazenby, R. A. et Unwin, P. R. (2015). Quad-Barrel Multifunctional Electrochemical and Ion Conductance Probe for Voltammetric Analysis and Imaging. *Analytical Chemistry*, *87*(7), 3566-3573. doi: 10.1021/acs.analchem.5b00379

Nasirpouri, F. (2017). Fundamentals and Principles of Electrode-Position. Dans F. Nasirpouri (dir.), *Electrodeposition of Nanostructured Materials* (p. 75-121). Cham : Springer International Publishing.

O'Mullane, A. P. (2014). From single crystal surfaces to single atoms: investigating active sites in electrocatalysis. *Nanoscale*, *6*(8), 4012-4026. doi: 10.1039/C4NR00419A

Oldham, K. B. et Zoski, C. G. (1988, 1988/11/25/). Comparison of voltammetric steady states at hemispherical and disc microelectrodes. *Journal of Electroanalytical Chemistry and Interfacial Electrochemistry*, *256*(1), 11-19. doi: https://doi.org/10.1016/0022-0728(88)85002-2

Ornelas, I. M., Unwin, P. R. et Bentley, C. L. (2019, 2019/12/03). High-Throughput Correlative Electrochemistry–Microscopy at a Transmission Electron Microscopy Grid Electrode. *Analytical Chemistry*, *91*(23), 14854-14859. doi: 10.1021/acs.analchem.9b04028

Peng, Y., Gao, C., Deng, X., Zhao, J. et Chen, Q. (2023). Elucidating the Geometric Active Sites for Oxygen Evolution Reaction on Crystalline Iron-Substituted Cobalt Hydroxide Nanoplates. *Analytical Chemistry*, *95*(31), 11657-11663. doi: 10.1021/acs.analchem.3c01420

Perry, D., Momotenko, D., Lazenby, R. A., Kang, M. et Unwin, P. R. (2016, 2016/05/17). Characterization of Nanopipettes. *Analytical Chemistry*, *88*(10), 5523-5530. doi: 10.1021/acs.analchem.6b01095

Quast, T., Varhade, S., Saddeler, S., Chen, Y.-T., Andronescu, C., Schulz, S. et Schuhmann, W. (2021). Single Particle Nanoelectrochemistry Reveals the Catalytic Oxygen Evolution

Reaction Activity of Co3O4 Nanocubes. *Angewandte Chemie International Edition*, *60*(43), 23444-23450. doi: https://doi.org/10.1002/anie.202109201

Quast, T., Varhade, S., Saddeler, S., Chen, Y. T., Andronescu, C., Schulz, S. et Schuhmann, W. (2021). Single Particle Nanoelectrochemistry Reveals the Catalytic Oxygen Evolution Reaction Activity of Co3O4 Nanocubes. *Angewandte Chemie - International Edition*, *60*(43), 23444-23450. doi: 10.1002/anie.202109201

Rahman, M. M., Tolbert, C. L., Saha, P., Halpern, J. M. et Hill, C. M. (2022, 2022/12/27). On-Demand Electrochemical Fabrication of Ordered Nanoparticle Arrays using Scanning Electrochemical Cell Microscopy. *ACS Nano*, *16*(12), 21275-21282. doi: 10.1021/acsnano.2c09336

Roehrich, B. et Sepunaru, L. (2024, 2024/08/21). Impedimetric Measurement of Exchange Currents and Ionic Diffusion Coefficients in Individual Pseudocapacitive Nanoparticles. *ACS Measurement Science Au*, *4*(4), 467-474. doi: 10.1021/acsmeasuresciau.4c00017

Rogers, E., Silvester, D., Poole, D., Aldous, L., Hardacre, C. et Compton, R. (2008). Voltammetric characterization of the ferrocene/ferrocenium and cobaltocenium vertical bar cobaltocene redox couples in RTILs. *JOURNAL OF PHYSICAL CHEMISTRY C*, *112*(7), 2729-2735.

Ryu, C. H., Mandal, D. et Ren, H. (2024, 2024/12/18). Gas–Liquid–Solid Three-Phase Boundary in Scanning Electrochemical Cell Microscopy. *ACS Measurement Science Au*, *4*(6), 729-736. doi: 10.1021/acsmeasuresciau.4c00061

Ryu, C. H. et Ren, H. (2024). Simultaneous Mapping of Electrocatalytic Activity and Selectivity via Hybrid Scanning Electrochemical Probe Microscopy. *Nano Letters*. doi: 10.1021/acs.nanolett.4c01280

Ryu, C. H. et Ren, H. (2024, 2024/05/22). Simultaneous Mapping of Electrocatalytic Activity and Selectivity via Hybrid Scanning Electrochemical Probe Microscopy. *Nano Letters*, *24*(20), 6112-6116. doi: 10.1021/acs.nanolett.4c01280

Saha, P., Hill, J. W., Walmsley, J. D. et Hill, C. M. (2018). Probing Electrocatalysis at Individual Au Nanorods via Correlated Optical and Electrochemical Measurements. *Analytical Chemistry*, *90*(21), 12832-12839. doi: 10.1021/acs.analchem.8b03360

Saha, P., Rahman, M. M. et Hill, C. M. (2022). Borohydride oxidation electrocatalysis at individual, shape-controlled Au nanoparticles. *Electrochemical Science Advances*, *2*(5). doi: 10.1002/elsa.202100120

Saha, P., Rahman, M. M. et Hill, C. M. (2023). Electrocatalysis at Individual Colloidal Nanoparticles: A Quantitative Survey of Four Geometries via Electrochemical Cell Microscopy. *Journal of Physical Chemistry C*, *127*(19), 9059-9066. doi: 10.1021/acs.jpcc.3c01427

Salek, S. et Byers, J. C. (2024, 2024/08/22). Influence of Particle Size on Mass Transport during the Oxygen Reduction Reaction at Single Silver Particles Using Scanning Electrochemical Cell Microscopy. *The Journal of Physical Chemistry Letters*, *15*(33), 8494-8500. doi: 10.1021/acs.jpclett.4c01832

Santana Santos, C., Jaato, B. N., Sanjuán, I., Schuhmann, W. et Andronescu, C. (2023). Operando Scanning Electrochemical Probe Microscopy during Electrocatalysis. *Chemical Reviews*, *123*(8), 4972-5019. doi: 10.1021/acs.chemrev.2c00766

Saxena, N., Mena-Morcillo, E., Tripp, M., Keech, P. G., Behazin, M. et Gateman, S. M. (2024, 2024/10/04). In Situ Quantification of a Wetted Surface Area during Scanning Electrochemical Cell Microscopy Using Retraction Curves. *ACS Measurement Science Au*. doi: 10.1021/acsmeasuresciau.4c00042

Seh, Z. W., Kibsgaard, J., Dickens, C. F., Chorkendorff, I., Nørskov, J. K. et Jaramillo, T. F. (2017). Combining theory and experiment in electrocatalysis: Insights into materials design. *Science*, *355*(6321), eaad4998.

Siahrostami, S., Verdaguer-Casadevall, A., Karamad, M., Deiana, D., Malacrida, P., Wickman, B., . . . Rossmeisl, J. (2013, 2013/12/01). Enabling direct H2O2 production through rational electrocatalyst design. *Nature Materials*, *12*(12), 1137-1143. doi: 10.1038/nmat3795

Snowden, M. E., Güell, A. G., Lai, S. C. S., McKelvey, K., Ebejer, N., O'Connell, M. A., . . . Unwin, P. R. (2012, 2012/03/06). Scanning Electrochemical Cell Microscopy: Theory and Experiment for Quantitative High Resolution Spatially-Resolved Voltammetry and Simultaneous Ion-Conductance Measurements. *Analytical Chemistry*, *84*(5), 2483-2491. doi: 10.1021/ac203195h

Snowden, M. E., Güell, A. G., Lai, S. C. S., McKelvey, K., Ebejer, N., Oconnell, M. A., . . . Unwin, P. R. (2012). Scanning electrochemical cell microscopy: Theory and experiment for quantitative high resolution spatially-resolved voltammetry and simultaneous ion-conductance measurements. *Analytical Chemistry*, *84*(5), 2483-2491. doi: 10.1021/ac203195h

Song, D. et Zhou, Y.-G. (2022). From ensemble electrochemistry to nanoparticle-impact electrochemistry: Altered reaction process and possible applications. *Current Opinion in Electrochemistry*, *34*, 101011.

Stamenkovic, V. R., Strmcnik, D., Lopes, P. P. et Markovic, N. M. (2017, 2017/01/01). Energy and fuels from electrochemical interfaces. *Nature Materials*, *16*(1), 57-69. doi: 10.1038/nmat4738

Stoppa, A., Zech, O., Kunz, W. et Buchner, R. (2010, 2010/05/13). The Conductivity of Imidazolium-Based Ionic Liquids from (−35 to 195) °C. A. Variation of Cation's Alkyl Chain. *Journal of Chemical & Engineering Data*, *55*(5), 1768-1773. doi: 10.1021/je900789j

Subramanian, K., Janavi, G., Marimuthu, S., Kannan, M., Raja, K., Haripriya, S., . . . Moorthy, P. (2022). *A textbook on fundamentals and applications of nanotechnology* ASTRAL INTERNATIONAL PVT.

Sun, P. et Mirkin, M. V. (2006, 2006/09/01). Kinetics of Electron-Transfer Reactions at Nanoelectrodes. *Analytical Chemistry*, *78*(18), 6526-6534. doi: 10.1021/ac060924q

Tao, B., Yule, L. C., Daviddi, E., Bentley, C. L. et Unwin, P. R. (2019). Correlative Electrochemical Microscopy of Li-Ion (De)intercalation at a Series of Individual LiMn2O4 Particles. *Angewandte Chemie International Edition*, *58*(14), 4606-4611. doi: https://doi.org/10.1002/anie.201814505

Tarnev, T., Aiyappa, H. B., Botz, A., Erichsen, T., Ernst, A., Andronescu, C. et Schuhmann, W. (2019). Scanning Electrochemical Cell Microscopy Investigation of Single ZIF-Derived Nanocomposite Particles as Electrocatalysts for Oxygen Evolution in Alkaline Media. *Angewandte Chemie - International Edition*, *58*(40), 14265-14269. doi: 10.1002/anie.201908021

Tetteh, E. B., Kim, M., Savan, A., Ludwig, A., Chung, T. D. et Schuhmann, W. (2023, 2023/12/20/). Reassessing the intrinsic hydrogen evolution reaction activity of platinum using scanning electrochemical cell microscopy. *Cell Reports Physical Science*, *4*(12), 101680. doi: https://doi.org/10.1016/j.xcrp.2023.101680

Tetteh, E. B., Krysiak, O. A., Savan, A., Kim, M., Zerdoumi, R., Chung, T. D., . . . Schuhmann, W. (2024). Long-Range SECCM Enables High-Throughput Electrochemical Screening of High Entropy Alloy Electrocatalysts at Up-To-Industrial Current Densities. *Small Methods*, *8*(7), 2301284. doi: https://doi.org/10.1002/smtd.202301284

Tetteh, E. B., Löffler, T., Tarnev, T., Quast, T., Wilde, P., Aiyappa, H. B., . . . Schuhmann, W. (2022). Calibrating SECCM measurements by means of a nanoelectrode ruler. The intrinsic oxygen reduction activity of PtNi catalyst nanoparticles. *Nano Research*, *15*(2), 1564-1569. doi: 10.1007/s12274-021-3702-7

Tonelli, D., Scavetta, E. et Gualandi, I. (2019). Electrochemical Deposition of Nanomaterials for Electrochemical Sensing. *Sensors*, *19*(5), 1186.

Trasatti, S. et Petrii, O. A. (1991). International Union of Pure and Applied Chemistry Physical Chemistry Division Commission on Electrochemistry: Real Surface Area Measurements in Electrochemistry. *Pure and Applied Chemistry*, *63*(5), 711-734. doi: 10.1351/pac199163050711

Treimer, S., Tang, A. et Johnson, D. C. (2002). A Consideration of the Application of Koutecký-Levich Plots in the Diagnoses of Charge-Transfer Mechanisms at Rotated Disk Electrodes. *Electroanalysis*, *14*(3), 165-171. doi: https://doi.org/10.1002/1521-4109(200202)14:3<165::AID-ELAN165>3.0.CO;2-6

Trindell, J. A., Duan, Z., Henkelman, G. et Crooks, R. M. (2020, 2020/01/22). Well-Defined Nanoparticle Electrocatalysts for the Refinement of Theory. *Chemical Reviews*, *120*(2), 814-850. doi: 10.1021/acs.chemrev.9b00246

Trogisch, N., Hartig-Weiss, A. et El-Sayed, H. A. (2024, 2024/03/13). Limitations of Liquid Electrolyte RDE Experiments for the Determination of OER Catalyst Activity: The Effect of the Catalyst Layer Thickness. *Journal of The Electrochemical Society*, *171*(3), 036506. doi: 10.1149/1945-7111/ad2e7f

Unwin, P. R., Güell, A. G. et Zhang, G. (2016, 2016/09/20). Nanoscale Electrochemistry of sp2 Carbon Materials: From Graphite and Graphene to Carbon Nanotubes. *Accounts of Chemical Research*, *49*(9), 2041-2048. doi: 10.1021/acs.accounts.6b00301

Ustarroz, J., Ornelas, I. M., Zhang, G., Perry, D., Kang, M., Bentley, C. L., . . . Unwin, P. R. (2018). Mobility and Poisoning of Mass-Selected Platinum Nanoclusters during the Oxygen Reduction Reaction. *ACS Catalysis*, *8*(8), 6775-6790. doi: 10.1021/acscatal.8b00553

van der Heijden, O., Park, S., Vos, R. E., Eggebeen, J. J. J. et Koper, M. T. M. (2024, 2024/04/12). Tafel Slope Plot as a Tool to Analyze Electrocatalytic Reactions. *ACS Energy Letters*, *9*(4), 1871-1879. doi: 10.1021/acsenergylett.4c00266

Varhade, S., Meloni, G., Tetteh, E. B., Kim, M., Schumacher, S., Quast, T., . . . Schuhmann, W. (2023, 2023/08/20/). Elucidation of alkaline electrolyte-surface interaction in SECCM using a pH-independent redox probe. *Electrochimica Acta*, *460*, 142548. doi: https://doi.org/10.1016/j.electacta.2023.142548

Varhade, S., Tetteh, E. B., Saddeler, S., Schumacher, S., Aiyappa, H. B., Bendt, G., . . . Schuhmann, W. (2023). Crystal Plane-Related Oxygen-Evolution Activity of Single Hexagonal Co3O4 Spinel Particles. *Chemistry – A European Journal*, *29*(12), e202203474. doi: https://doi.org/10.1002/chem.202203474

Voiry, D., Chhowalla, M., Gogotsi, Y., Kotov, N. A., Li, Y., Penner, R. M., . . . Weiss, P. S. (2018, 2018/10/23). Best Practices for Reporting Electrocatalytic Performance of Nanomaterials. *ACS Nano*, *12*(10), 9635-9638. doi: 10.1021/acsnano.8b07700

Wahab, O. J., Kang, M. et Unwin, P. R. (2020). Scanning electrochemical cell microscopy: A natural technique for single entity electrochemistry. *Current Opinion in Electrochemistry*, *22*, 120-128. doi: 10.1016/j.coelec.2020.04.018

Walsh, D. A., Lovelock, K. R. J. et Licence, P. (2010). Ultramicroelectrode voltammetry and scanning electrochemical microscopy in room-temperature ionic liquid electrolytes. *Chemical Society Reviews*, *39*(11), 4185-4194. doi: 10.1039/B822846A

Walter, E. C., Murray, B. J., Favier, F., Kaltenpoth, G., Grunze, M. et Penner, R. M. (2002). Noble and coinage metal nanowires by electrochemical step edge decoration. *Journal of Physical Chemistry B*, *106*(44), 11407-11411. doi: 10.1021/jp026389p

Wang, Q., Guesmi, H., Tingry, S., Cornu, D., Holade, Y. et Minteer, S. D. (2022). Unveiling the Pitfalls of Comparing Oxygen Reduction Reaction Kinetic Data for Pd-Based Electrocatalysts without the Experimental Conditions of the Current-Potential Curves. *ACS Energy Letters*, *7*(3), 952-957. doi: 10.1021/acsenergylett.2c00181

Wang, S., Guo, Y., Du, X., Xiong, L., Liang, Z., Ma, M., . . . Liu, M. (2024, 2024/08/01). Preferred crystal plane electrodeposition of aluminum anode with high lattice-matching for long-life aluminum batteries. *Nature Communications*, *15*(1), 6476. doi: 10.1038/s41467-024-50723-0

Wang, S., Zhu, E., Huang, Y. et Heinz, H. (2021). Direct correlation of oxygen adsorption on platinum-electrolyte interfaces with the activity in the oxygen reduction reaction. *Science Advances*, *7*(24), eabb1435. doi: doi:10.1126/sciadv.abb1435

Wang, Y., Gordon, E. et Ren, H. (2020, 2020/02/04). Mapping the Potential of Zero Charge and Electrocatalytic Activity of Metal–Electrolyte Interface via a Grain-by-Grain Approach. *Analytical Chemistry*, *92*(3), 2859-2865. doi: 10.1021/acs.analchem.9b05502

Wang, Y., Li, M. et Ren, H. (2022, 2022/08/17). Voltammetric Mapping of Hydrogen Evolution Reaction on Pt Locally via Scanning Electrochemical Cell Microscopy. *ACS Measurement Science Au*, *2*(4), 304-308. doi: 10.1021/acsmeasuresciau.2c00012

Wang, Y., Li, M. et Ren, H. (2022, Aug 17). Voltammetric Mapping of Hydrogen Evolution Reaction on Pt Locally via Scanning Electrochemical Cell Microscopy. *ACS Meas Sci Au*, *2*(4), 304-308. doi: 10.1021/acsmeasuresciau.2c00012

Xiang, C., Kung, S.-C., Taggart, D. K., Yang, F., Thompson, M. A., Güell, A. G., . . . Penner, R. M. (2008, 2008/09/23). Lithographically Patterned Nanowire Electrodeposition: A Method for Patterning Electrically Continuous Metal Nanowires on Dielectrics. *ACS Nano*, *2*(9), 1939-1949. doi: 10.1021/nn800394k

Xing, W., Yin, G. et Zhang, J. (2014). *Rotating electrode methods and oxygen reduction electrocatalysts* Elsevier.

Yu, Y., Zhang, K., Parks, H., Babar, M., Carr, S., Craig, I. M., . . . Bediako, D. K. (2022, Mar). Tunable angle-dependent electrochemistry at twisted bilayer graphene with moiré flat bands. *Nat Chem*, *14*(3), 267-273. doi: 10.1038/s41557-021-00865-1

Zerdoumi, R., Quast, T., Tetteh, E. B., Kim, M., Li, L., Dieckhöfer, S. et Schuhmann, W. (2024, 2024/07/09). Integration of Scanning Electrochemical Microscopy and Scanning Electrochemical Cell Microscopy in a Bifunctional Nanopipette toward Simultaneous Mapping of Activity and Selectivity in Electrocatalysis. *Analytical Chemistry*, *96*(27), 10886-10892. doi: 10.1021/acs.analchem.4c00149

Zhang, L., Wahab, O. J., Jallow, A. A., O'Dell, Z. J., Pungsrisai, T., Sridhar, S., . . . Baker, L. A. (2024, 2024/05/21). Recent Developments in Single-Entity Electrochemistry. *Analytical Chemistry*, *96*(20), 8036-8055. doi: 10.1021/acs.analchem.4c01406

Zhang, Y., Arpino, K. E., Yang, Q., Kikugawa, N., Sokolov, D. A., Hicks, C. W., . . . Li, G. (2022, 2022/12/16). Observation of a robust and active catalyst for hydrogen evolution under high current densities. *Nature Communications*, *13*(1), 7784. doi: 10.1038/s41467-022-35464-2

Zhao, J., Fu, C., Ye, K., Liang, Z., Jiang, F., Shen, S., . . . Jiang, K. (2022, 2022/02/03). Manipulating the oxygen reduction reaction pathway on Pt-coordinated motifs. *Nature Communications*, *13*(1), 685. doi: 10.1038/s41467-022-28346-0

Zhao, J., Wang, M., Peng, Y., Ni, J., Hu, S., Zeng, J. et Chen, Q. (2023). Exploring the Strain Effect in Single Particle Electrochemistry using Pd Nanocrystals. *Angewandte Chemie International Edition*, *62*(30), e202304424. doi: https://doi.org/10.1002/anie.202304424

Zhao, J., Wang, M., Peng, Y., Ni, J., Hu, S., Zeng, J. et Chen, Q. (2023). Exploring the Strain Effect in Single Particle Electrochemistry using Pd Nanocrystals. *Angewandte Chemie - International Edition*, *62*(30). doi: 10.1002/anie.202304424

Zhou, W., Apkarian, R., Wang, Z. L. et Joy, D. (2007). Fundamentals of scanning electron microscopy (SEM). *Scanning microscopy for nanotechnology: techniques and applications*, 1-40.